Black-hole dynamics and their environments

by

Daria D. Gangardt

UNIVERSITY OF BIRMINGHAM

A thesis submitted to the University of Birmingham for the degree of
DOCTOR OF PHILOSOPHY

Institute of Gravitational Waves
Physics and Astronomy Department
College of Engineering and Physical Sciences
University of Birmingham

July 2024

UNIVERSITY OF
BIRMINGHAM

University of Birmingham Research Archive
e-theses repository

This unpublished thesis/dissertation is under a Creative Commons Attribution-NonCommercial-NoDerivatives 4.0 International (CC BY-NC-ND 4.0) licence.

You are free to:

Share — copy and redistribute the material in any medium or format

The licensor cannot revoke these freedoms as long as you follow the license terms.

Under the following terms:

Attribution — You must give appropriate credit, provide a link to the license, and indicate if changes were made. You may do so in any reasonable manner, but not in any way that suggests the licensor endorses you or your use.

NonCommercial — You may not use the material for commercial purposes.

NoDerivatives — If you remix, transform, or build upon the material, you may not distribute the modified material.

No additional restrictions — You may not apply legal terms or technological measures that legally restrict others from doing anything the license permits.

Notices:

You do not have to comply with the license for elements of the material in the public domain or where your use is permitted by an applicable exception or limitation.

No warranties are given. The license may not give you all of the permissions necessary for your intended use. For example, other rights such as publicity, privacy, or moral rights may limit how you use the material.

Unless otherwise stated, any material in this thesis/dissertation that is cited to a third-party source is not included in the terms of this licence. Please refer to the original source(s) for licencing conditions of any quotes, images or other material cited to a third party.

Dedicated to my grandfather, Dr. Mikhail Gangardt. Thank you for asking me about gravitational waves.

Посвящается моему дедушке, Михаилу Гангардту. Спасибо, что ты меня спрашивал про гравитационные волны.

Abstract

Black holes are objects that induce extreme astrophysical phenomena. Several avenues exist to explore how black holes form and how they evolve. In this thesis, I explore the multi-faceted spin dynamics of binary black holes (Part I) and then turn to active galactic nuclei, focussing on theoretical models for the discs around supermassive black holes (Part II). Part I presents a new taxonomy for spin precession of binary black holes, and introduces a new scheme for uncovering different spin precession parameters in gravitational-wave events. Five spin precession parameters are introduced in Ch. 3; one of these is the nutational amplitude which is indicative of two misaligned spins in the black hole binary. A system where the nutational amplitude is maximised is then shown to be recoverable by future gravitational wave detectors in Ch. 4, meaning that spin-spin effects will soon be constrainable. In Part II, I give an outline of active galactic nuclei theory and observations. Chapter 6 investigates two active galactic nuclei disc models by Sirko and Goodman (2003) [1] and Thompson *et al.* (2005) [2]. Migration formulae are applied to these disc models, recovering the presence of migration traps where black hole capture is likely. The thesis is tied together by the want to understand gravitational wave sources better, which I introduce in Ch. 1.

Acknowledgments

Thank you

Although a PhD is supposed to be an independent undertaking, my experience was one of a great unified community that supported me for four years and maybe more. There are so many people who made this possible; I cannot list them all but I am extremely grateful nonetheless.

I will start close to home, with my family. Thank you to my mum Maria Gangardt, my dad Dimitri Gangardt and my sister Sophia Gangardt. I hope I've made you proud. Thank you to my friends from secondary school and university, Ellen Coleman, Owen Evans, Jamie Mair, Ellie Naccarato, Delfina Petersen, Ashleigh Reece, K.M. White and Julie Zhou. Our climbs, our chats and our watch-alongs kept me sane through this long journey. Special shout-out goes to my university friends at 5BB; to James Bradford, Torin Cooper-Bennun, Sam Higginbotham, Dan Hunt, James Nuttall and Evan Ridley. Our adventures are my most treasured memories. Even more special thanks to my best friends S. Stunell and R. Taylor - I am so grateful to have you guys in my life.

Thank you to Joe Robinson, for being my friend and for giving me only happy moments to remember you by.

During my PhD, I had the opportunity to meet many accomplished scientists and friendly people, from not only one but two Physics departments! I would like to thank

the kind people of the Astrophysics Department at the University of Milano-Bicocca for welcoming me and helping me with all things *italiano*. Thank you especially to Viola De Renzis, Giulia Fumagalli and Alice Spadaro. Thank you as well to Floor Broekgaarden, Matt Mould, Isobel Romero-Shaw and Nathan Steinle for showing me the kind of researcher I wanted to be. Back in the UK, I would like to thank Aysha Aamer, Diganta Bandopadhyay, Swetha Bhagwat, Alice Bonino, Cressida Cleland, Eliot Finch, Rory Fraser, Alex Gill, Panagiota Kolitsidou, Simona Pacuraru, Paige Ramsden, Dan Ryczanowski, Xinyue Sheng, Lucy Thomas, Natalie Williams and Isobel Worssam for every time you've helped me and for every time you've distracted me.

Thanks go to Alessandro A. Trani for giving me the best final PhD project on AGNs and for all the help I received from you since. Thank you to my mentor Davide Gerosa, for polishing me into the researcher I am today. Thank you Davide also for your kindness when things were not going according to plan. I couldn't have wished for a better supervisor.

Finally, I would like to thank Bash Mitchell, for being the stellar partner that he is. Thank you for helping me with my code, thank you for the cups of tea, thank you for your reassurances and thank you for your endless support. Thank you for travelling with me, thank you for staying in with me, thank you for doing everything and doing nothing with me.

Funding

The work presented in this thesis was supported by funding from the University of Birmingham and the STFC. Additionally, funding was received from the European Union's H2020 ERC Starting Grant No. 945155-GWmining, the Royal Society Grant

No. RGS-R2-202004, the Cariplo Foundation Grant No. 2021-0555, the Leverhulme Trust Grant No. RPG-2019-350, MUR PRIN Grant No. 2022-Z9X4XS and the ICSC National Research Centre funded by NextGenerationEU. Computational work was performed on the University of Birmingham BlueBEAR cluster.

During my PhD, I was also fortunate to receive travel support from the ‘Study in Italy’ program of the Italian Ministry of Foreign Affairs and International Cooperation and the Turing Scheme of the UK Department of Education.

“There I elected to demur

Beneath a low-slung juniper

That like a blanket on my chin

Kept some dew out and some heat in,

Yet left me freely face to face

All night with universal space.”

Robert Frost, *An Unstamped Letter on our Rural Leather Box.*

Contents

List of Figures

List of Tables

Chapter 1

A general introduction

Summary

This thesis is effectively split into two parts. In the first part, Chapters 3—4, I summarise work on detecting spin precession in black-hole binaries. In the second part, Chapters 5—6, I summarise work on active galactic nuclei discs. The two topics are intrinsically linked by a motivation to better understand gravitational wave sources. Therefore, I introduce gravitational wave theory and current knowledge in Ch. 1 first.

1.1 A brief history of black holes

The idea of a black hole (BH), an object whose gravitational pull would be so great that not even light can escape it, has existed in theory from as early as 1784-1798 [3, 4] (see Montgomery *et al.* (2009) [5] for a review). Using Newtonian gravity, the equating of escape velocity to that of the speed of light gives the radius of such an object as one proportional to its mass:

$$R_\mathrm{s} = \frac{2GM}{c^2}\,, \tag{1.1}$$

where R_s is the Schwarzschild radius, M represents the object mass, G is the gravitational constant and c is the speed of light. However, a physical mechanism for the formation of a black hole was not presented until the seminal work of Chandrasekhar (1931) [6]. In Chandrasekhar (1931) [6], it was proposed that if stars were to gravitationally collapse inward, then the Pauli exclusion principle would create a counteracting pressure due to electrons resisting existing in the same energy states. This pressure, dubbed 'electron degeneracy pressure', could naturally form white dwarves with degenerate cores, astrophysical objects far more compact than stars. Expanding on this idea, Oppenheimer and Volkoff (1939) [7] showed analytically that above a maximum limit, stable neutron stars would be unable to form, and would continue to contract inwards. In Oppenheimer and Snyder (1939) [8], the endpoint of the massive neutron star evolution was shown to be an object so dense, not even light could escape it. The predictions of Oppenheimer and Volkoff (1939) [7], Oppenheimer and Snyder (1939) [8] were formed by going beyond Newtonian gravity and employing general relativity.

In 1915, Einstein published his theory of General Relativity [9–11]. These historic texts suggested that gravity is a result of the interconnectedness of space and time, a warping effect from the presence of compact objects. A year later, Schwarzschild (1916) [12] published the first exact solution to Einstein's field equations by assuming spherical symmetry in a vacuum. This solution presented a singularity at $r = 0$ contained within an event horizon of radius R_s, which Einstein himself doubted the possibilty of [13]. In Penrose (1965) [14], it was demonstrated that irrespective of assumptions of symmetry, a gravitational collapse of matter under Einstein's field equations will form a physical singularity- a black hole.

In general relativity, black holes are described as simple objects with only three internal properties (according to the No-Hair Conjecture)- their mass, spin and charge [15–19]. When studying black holes, we are often more concerned with their mass and their spins than their charge. This is because black holes that are charged are expected to attract the opposite charge and become neutral. The event horizon of a non-spinning black hole is given by the Schwarzschild radius (Eq. (1.1)), but if the black hole is spinning then additional radii must be considered due to the presence of an ergosphere. In Kerr (1963) [20], analytical solutions describing spinning black holes with angular momentum $\vec{S}_i = GM^2\vec{\chi}_i/c$, where $\vec{\chi}_i$ is the dimensionless spin of the black hole, were provided. In Boyer-Lindquist coordinates [21], the boundaries of the ergosphere, $r_\pm$, are given by:

$$r_\pm = \frac{GM}{c^2}\left(1 \pm \sqrt{1-\chi_i^2}\right) . \tag{1.2}$$

If $\chi_i = 0$, we recover Eq. (1.1), i.e., the black hole is non-rotating and there is no ergosphere. At $\chi_i = 1$, the ergosphere boundaries shrink to $r_\pm = R_\mathrm{s}/2$, and we find that objects can get closer to spinning black holes than to non-rotating black holes. If the magnitude of the black hole spin goes above the Kerr limit ($S_i > GM^2/c$, or $\chi_i \geq 1$), the black hole's event horizon will be smaller than its radius, and a distant observer would be able to see the centre of the black hole. This scenario, named a "naked singularity", is considered to be impossible according to the cosmic censorship conjecture [22]; therefore, they are rarely considered when studying astrophysical black holes.

In 1962 and 1963, extra-galactic observations using radio telescopes produced catalogues of "quasi-stellar" objects (quasars) [23]. The observational signatures of quasars could only be explained if they were taken to be extremely luminous objects located at high redshift ($z \sim 0.16$ for the quasar in Schmidt (1963) [23], but we now observe quasars as far away as $z \sim 7$ [24]). This high luminosity was then explained as accretion onto extremely massive and compact sources - supermassive black holes (SMBHs) [25, 26]. A strong radio source that seemed impossibly compact and unusually bright at the centre of the Milky Way Galaxy was reported in Balick and Brown (1974) [27]. In parallel, the observational discovery of pulsars [28] confirmed the work of stellar collapse astronomers- the rapid, regular electromagnetic signatures of the signals were well-explained by assuming that their source was a rapidly spinning neutron star [29]. In 1972, spectroscopic observations of the X-ray and radio source Cygnus X-1 revealed it to be a star with an even more compact companion - a black hole [30, 31]. More recently, by studying stellar orbits near our galactic centre, Ghez *et al.* (1998) [32] and Genzel *et al.* (2000) [33] obtained observations of a massive object ($M > 10^6\,\mathrm{M}_\odot$) in a small volume ($r < 0.01$pc) at the centre of the Milky Way. By the 2000s, black holes were no longer mythical subjects of general relativity, but instead astrophysical objects that could be studied, albeit indirectly.

Direct imaging of black holes, or their event horizons, are difficult and costly. In 2019, the Event Horizon Telescope collaboration released pictures of the "shadow" of the black hole at the centre of the galaxy M87 [34], and later in 2022, similar pictures of our Galaxy's central BH were released [35]. These images are compilations of radio observations of the photon paths around a black hole from multiple telescopes around the globe (effectively creating a very long interferometer). The images provide direct evidence that supermassive black holes exist at the centre of the M87 and the Milky Way galaxies. However, an even more direct method to study black holes exists: gravitational radiation.

1.2 Two black holes are better than one

1.2.1 Formation channels

Applying Einstein's field equations to linearised gravity tells us that gravitational radiation will travel as gravitational waves (GWs) whose amplitudes h are approximately given by:

$$h \sim \frac{R_\mathrm{s}}{r}\frac{v^2}{c^2}\,, \tag{1.3}$$

which is an approximation of the quadrupole formula. For non-relativistic sources, i.e. sources where $v \ll c$, maximising the compactness of a source (M/r) maximises the amplitude of GWs. Thus, in order to detect GWs with our instruments, we must turn to compact objects such as black holes, neutron stars and white dwarves. A proposed powerful source is the merger of two compact sources. If two compact objects are close enough to each other (within a few R_s), then the loss of gravitational radiation through GWs will lead to their orbits shrinking and the two objects merging. Historically, the initial separation was a point of contention - black holes would have to form relatively close to one another so that the expansion of the Universe did not pull them apart. Electromagnetic (EM) observations of stars, the proposed origin of compact sources, did not have the resolution to determine if binaries could form at such small separations.

The task of gravitational wave astronomers became to determine formation channels for binary black holes (BBHs). Traditionally, there are two key categories of formation channels - the isolated formation channel and the dynamic formation channel. For the isolated formation channel, the source of BBHs are stellar binaries. One of the stars in the binary is expected to inflate as it becomes a red giant, introducing a common envelope of gas into the system. This envelope swallows the second star, and gaseous friction hardens the binary. Eventually, the two stars become compact sources with a small enough separation that they can merge within Hubble time (the pathways to this determine subchannels within the isolated formation channel) [36–41]. A key motivator for the isolated channel is that a significant fraction of stars in the sky ($\sim 40\%$ or more) are in binaries or multiple systems [42–44]. The isolated BBHs are expected to be two slowly-spinning, spin-aligned black holes with masses subject to the pair-instability gap [45–48]. Massive stars ($M \gtrsim 130\,\mathrm{M}_\odot$) are theoretically expected to undergo pair-instability supernovae when runaway quantum and chemical processes cause them to rapidly and violently contract under their self-gravity [49], causing singular pair-instability supernovae that blow the original stellar material apart, leaving no BH remnant behind [50]. Stars that have masses greater than $\gtrsim 100\,\mathrm{M}_\odot$ (depending on metallicity) will instead undergo partial contractions, losing their material gradually through violent pulses (the pulsational pair-instability process [50]) that eventually leave behind BH remnants with smaller masses than expected for their original size. With current GW observations, there is uncertainty in the pair instability supernovae process [51, 52].

We turn our attention to a different formation channel for BBHs- the dynamical formation channel. In this case, black holes are assumed to be in dense, dynamic environments such as globular clusters or galactic nuclei. In both cases, it is expected that black holes will migrate through their environments, typically sinking to their centres. The high numerical density of black holes allows them to interact with one another, forming binaries that can merge within Hubble time [53–62]. For dry (gas-poor) environments such as globular clusters, it is expected that the two merging black holes will have spins in random directions [59, 63–65]. For wet (gas-rich) environments, such as active galactic nuclei, the black holes are expected to generally align with the rotation of the accretion disc, thus introducing preferentially spin-aligned or spin-antialigned BBHs [66, 67]. In both cases, the high density of black holes more easily allows for merger products to merge with more black holes in the environment again in a process known as hierarchical merging [68–73].

It is possible that black holes form from a mixture of both formation channels [74–76]. To make such predictions, typically a process known as population synthesis, which compares predictions from different formation channels to detected GW sources, is used. The predictions from these formation channels are also what we use to inform our parametric models of the BBH population.

1.2.2 Gravitational wave detection

On the 14th of September, 2015, the LIGO-Virgo collaboration obtained the first detection of gravitational waves from the merger of two black holes [77]. The signal, emitted by two distant and relatively massive black holes (total mass $\sim 65\,\mathrm{M}_\odot$), had a network signal to noise (SNR) ratio equal to ~ 26 and a significance of 5.1σ. In this section, I describe the methods used to detect and verify GW150914 and the GW events that followed it.

Gravitational waves have extremely small amplitudes, stretching space-time to peak strains of $h \sim 10^{-22}$ in the case of stellar mass BBH mergers at a similar distance and with similar masses to GW150914 [77]. In order to detect such small perturbations, one needs long interferometers. LIGO consists of two interferometers, LIGO Hanford and LIGO Livingston. The two interferometers are identical in design, each composed of two 4km long arms optimised ‘to increase interaction time with a gravitational wave’ [78]. Virgo [78] and KAGRA [79] are enhanced Michelson interferometers with two 3km arms, located in Italy and Japan respectively. The two LIGO interferometers are more sensitive to gravitational waves than Virgo and KAGRA; however, Virgo and KAGRA's locations allow them to help localise signals using triangulation. As well as this, KAGRA is the most recently-built interferometer, and tests advanced instruments that we expect to use for future detectors.

The detectors operate in runs, collecting measurements of laser phase shifts over several months. The arm lengths of the detectors are the determining factor for the frequency of GWs we are sensitive to. Figure 1.1 shows the LIGO and Virgo sensitivity curves as shown in Abbott *et al.* (2023) [80], known as 'sensitivity buckets'. For arm lengths of several kilometres, the GW frequencies we measure best are in the $10 - 10^3$ Hz range. Gravitational waves in this frequency range correspond to stellar-mass BBH mergers (masses below $\sim 2 \times 10^2\,\mathrm{M}_\odot$) and neutron star inspirals. From Fig. 1.1, it can also be seen that the GW detectors are not equally sensitive across the frequencies. The main limiting factors here are seismic noise for low frequencies and quantum noise for high frequencies [81].

The data collected by the detectors are often dominated by instrumental noise; this noise is typically modelled as stationary and Gaussian and removed from the datasets. Noise artefacts, short transient bursts in the data called 'glitches' [82–84] are also expected; these can tamper GW event results, even when identified in the data [85]. Several other methods are then used to model instrumental noise, such as hardware injections which test how the instruments react to a physically simulated GW signal. Monitoring the noise curve during the observing runs aids in noise removal during signal detection and the post-processing stage. For the first observing runs, GW events were always detected by more than one GW detector; consistency between the signals allowed for further removal of instrumental background noise in the strain data.

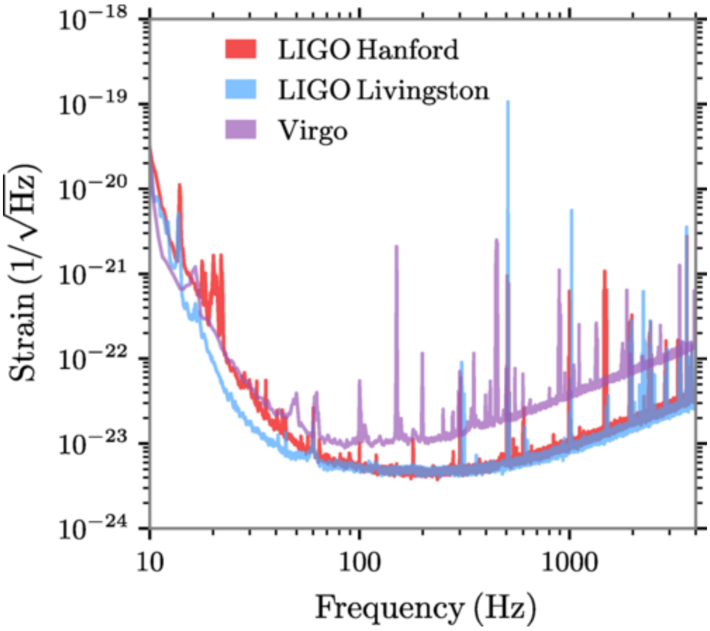

Figure 1.1: Figure 2 from Abbott *et al.* (2023) [80], showing a snapshot of the detectable GW strain for the three interferometers (LIGO Hanford (red), LIGO Livingston (blue) and Virgo (purple)) during the third LIGO-Virgo run in January 2020.

In order to identify GW merger events, matched filtering is used. Matched filtering is the comparison of seconds-long snippets in the time series to a bank of waveform templates, where highly correlated waveforms are retained and form the initial guess for the source parameters and significance of the candidate event. Waveform templates are simulated GW event waveforms, initially generated using effective one-body theory, sometimes combining it with post-Newtonian theory and then calibrated using numerical relativity [86, 87]. There are several matched filter analyses used within the LIGO-Virgo-KAGRA (LVK) collaboration that are used for the GW events, including PyCBC [88] and GstLal [89]. Different pipelines will have different success criteria for detections, will use different waveform template banks and different methods estimating the background noise. The matched filtered analyses can therefore be used independently; sometimes, GW events are found in one search pipeline only. Matched filtering provides a set of triggers, these are then further analysed and added to a catalogue of GW events [80, 90–92] if they pass a certain criteria. The current events reported in the Gravitational-wave Transient Catalogues (GWTCs) use the criterion $p_{\mathrm{astro}} > 0.5$ for the GW events used in detailed analysis (events designated with 'GW'). The parameter p_{astro} is the 'probability of astrophysical origin', a parameter that is made more robust to data with significant marginal detections or non-detections by including both the foreground and background events in its calculations [93, 94]. Groups outside of the LVK collaboration have also performed their own analyses on the publicly released strain data, forming independent GW event catalogues [95–99], which are mostly in agreement with the LVK GW catalogues.

Once a set of candidate events is formed, the priority is to determine the source parameters. Gravitational wave science uses Bayesian statistics to do so; the sparsity of GW measurements and the wealth of information of GW signals makes this an obvious choice. Below I list GW events of interest to this thesis and current population results.

1.2.3 Catalogues of binary black holes

The LVK collaboration is currently in its fourth observing run. Data are publicly available for the first three observing runs, O1-O3, at Trovato (2020) [100]. A new event from O4 was recently announced in The LIGO Scientific Collaboration *et al.* (2024) [101]. The first run, O1, ran from 12/09/2015 until 19/01/2016, and detected 3 BBH mergers with $p_{\mathrm{astro}} > 0.5$. The second run, O2, ran from 30/11/2016 until 25/08/2017, and detected 7 BBH mergers and the first neutron star merger with $p_{\mathrm{astro}} > 0.5$. The third run started after an upgrade to the LIGO detectors, increasing their sensitivities. The results from the third run were split into two sets, O3a and O3b. The first half of the third run, O3a, ran from 01/04/2019 until 01/10/2019, initially reporting 39 confident GW events in Abbott *et al.* (2020) [91], with one event with unusual masses making its source compact objects undeterminable [102]. A later re-release of the O3a results, Abbott *et al.* (2024) [92], updated the confident compact binary coalescence list, claiming 44 GW events with $p_{\mathrm{astro}} > 0.5$ detected in O3a. The second half of the third run, O3b, ran from 01/11/2019 until 27/03/2020, detecting 35 GW events with $p_{\mathrm{astro}} > 0.5$ [80]. The fourth observing run, O4, has been running since 24/05/2023. The results from O4 are currently not publicly available except for GW230529 [101].

As aforementioned, the first GW event reported by the LVK collaboration was GW150914. This event, the merger of a $35^{+4}_{-3}\,\mathrm{M}_{\odot}$ BH with a $30^{+3}_{-5}\,\mathrm{M}_{\odot}$ BH, had an estimated network SNR of ~ 26, a False Alarm Rate (FAR) of $1/203000\,\mathrm{yr}^{-1}$, and a significance greater than 5.1σ [77]. The low FAR legitimised GW150914 as a detection, paving the way for GW data analysis. The signal was detected in the two LIGO detectors. The total mass of the signal, $65\,\mathrm{M}_{\odot}$, corresponds to a merger and ringdown frequency of ~ 250 Hz, which places the event at the centre of the LIGO detectors' sensitivity band (see Fig. 1.1); this coupled with the high significance of GW150914 made it perfect for tests of GR and studies of black hole ringdown [103–107].

The events detected in O1 and O2 were presented in one catalogue, GWTC-1. This catalogue had 11 total events. One of the show-stoppers was GW170817, the first detection of a merger between two neutron stars [108]. This event was detected by all three available detectors at the time, the two LIGO detectors and Virgo. This allowed for good precision in the event's localisation (the signal's 90% credibility region covered only $16\,\mathrm{deg}^2$ across the sky), which aided the EM community in finding EM counterparts to the GW signal. The merger happened only 40^{+7}_{-15} Mpc away, giving it an SNR of 32.4 and making it the closest GW event detected so far. The kilonova explosion that accompanied the merger is the first confident kilonova detection [109–115] (although the GW170817 kilonova light curves confirm a posteriori that the first kilonova detected using EM observations was in 2013, detailed in Tanvir *et al.* (2013) [116]), and the association of the gamma-ray burst GRB 170817A with the GW signal provided key insights into gamma-ray burst sources [115, 117–123]. The combined direct measurements of the luminosity distance from the GW signature and the redshift from the EM counterparts provided an independent measurement of the Hubble constant, H_0 [124]. As more EM counterparts are associated to future GW signals, the error on H_0 measured using this method are expected to decrease [125]. An independent and accurate method of measuring H_0 is currently needed since the two main methods - standard candle supernovae and the cosmological microwave background - disagree [126, 127].

The second GW catalogue, GWTC-2.1 (an updated version of GWTC-2), reported the final findings from the first half of O3, i.e. events detected in O3a. This catalogue (and GWTC-2 before it) revealed two events with improbable masses, GW190521 [128] and GW190814 [102]. GW190521 is the merger of two black holes with large masses, $98^{+34}_{-22}\,\mathrm{M}_\odot$ and $57^{+27}_{-30}\,\mathrm{M}_\odot$, with the resulting black hole having a mass of $147^{+40}_{-16}\,\mathrm{M}_\odot$. Before the detection of GW190521, the maximum mass a stellar-origin black hole could have was predicted to be near $65\,\mathrm{M}_\odot$, depending on its metallicity [50]. This threshold maximum stellar-origin BH mass is set by the pair instability supernovae (see Sec. 1.2). The origin of observed supermassive black holes ($M > 10^4\,\mathrm{M}_\odot$) is elusive, making it difficult to predict the minimum supermassive BH mass. There are key relations between supermassive black hole masses and the properties of their host galaxies. Extrapolating these relations to smaller galaxies such as dwarf galaxies give us supermassive black hole masses as low as $10^4\,\mathrm{M}_\odot$ [129, 130], which still leaves an expected dearth of BH masses in the range $[\sim 65\,\mathrm{M}_\odot\,, \sim 10^4\,\mathrm{M}_\odot]$. Assuming these theoretical predictions for the upper BH mass gap, we see that the two component masses of GW190521 are clear outliers; the primary mass (heavier BH) especially has a mass that is greater than that predicted by the pair instability process in its region of 90% credibility. The mass of the merger remnant, $142^{+28}_{-16}\mathrm{M}_{\odot}$, is also the first direct observation of an intermediate mass BH. Several theories have been put forward for the creation of the components of GW190521 [131]: the two source BHs were possibly formed through hierarchical mergers in a highly dynamic and dense environment [68–73], the two source BHs are actually primordial BHs formed during the inflation of the universe and not stellar-origin [132, 133], the parameter estimation mistook a highly eccentric merger of smaller masses to be a quasi-circular merger of high masses instead [134, 135]. It is also possible that the maximum mass limit of BHs given by the pair instability process is incorrect, something explored in Farmer *et al.* (2020) [52] and Mapelli *et al.* (2020) [136].

On the other side of the BH mass spectrum is the lower mass gap, the gap between the maximum predicted masses for neutron stars ($\sim 2.3\,\mathrm{M}_{\odot}$ depending on the equation of state of the neutron star [108, 137, 138]) and the statistically inferred minimum mass of a BH ($\sim 5\,\mathrm{M}_{\odot}$ from X-ray binaries [139–142]). The detection of GW190814, a merger of a $23^{+1}_{-1}\,\mathrm{M}_{\odot}$ BH with a $2.6^{+0.1}_{-0.1}\,\mathrm{M}_{\odot}$ compact object challenges this predicted mass gap [102]. The secondary mass could represent either a light black hole or a heavy neutron star. The case of the secondary object being a heavy neutron star is currently disfavoured; observations from GW170817, the confirmed neutron star merger event, disfavour the neutron star equation of state necessary for neutron stars as heavy as $2.6^{+0.1}_{-0.1}\,\mathrm{M}_{\odot}$. The secondary mass being a black hole is preferred [143, 144]; if the merger remnant of GW170817 is a black hole, its mass would be $\sim 2.7\,\mathrm{M}_{\odot}$, which is similar to the mass of the secondary object of GW190814. If the secondary mass is a neutron star, GW190814 would be the first detection of a neutron star-black hole merger.

The third GW catalogue, GWTC-3, reported detections from the second half of O3, i.e. results from O3b [80]. In this catalogue were the first two confident detections of neutron star-black hole mergers, GW200105 and GW200115 [145]. These events have light BHs ($8.9^{+1.1}_{-1.3}\,\mathrm{M}_\odot$ and $5.9^{+2.0}_{-2.5}\,\mathrm{M}_\odot$ respectively) and standard neutron star masses ($1.9^{+0.2}_{-0.2}\,\mathrm{M}_\odot$ and $1.4^{+0.9}_{-0.3}\,\mathrm{M}_\odot$ respectively). No tidal deformation or tidal disruption of the neutron stars was observed, which is not unexpected given that the mass ratios of the events were ~ 0.21 and ~ 0.24 for GW200105 and GW200115 respectively - if the masses were more equal, the two objects would spend more time orbiting one another, and thus the black hole would have more time to deform the neutron star [146–149]. No EM counterpart was detected for either of the two NSBH events; this was to be expected - an EM counterpart for an NSBH is theorised to come from the tidal disruption of the neutron star forming an accretion disc [150, 151] from which a relativistic jet can be observed [152, 153].

The third catalogue also contains details for GW200129, a high SNR event (network SNR ~ 26) with possible hints of spin precession [80, 148, 154]. Spin precession is the tilting of the BBH orbital plane due to the spins of the black holes coupling. I further discuss this event and spin precession in the following chapter, Ch. 2.

At the current date, the LVK collaboration is still in its fourth run, O4. However, this run has already yielded another event with a mass in the lower mass gap with the event GW230529 [101]. This event has a primary mass of $3.6^{+0.8}_{-1.2}\,\mathrm{M}_\odot$ and a secondary mass of $1.4^{+0.6}_{-0.2}\,\mathrm{M}_\odot$, a standard neutron star. The signal is the first GW event where the primary mass is in the lower mass gap. Crucially, the primary mass of GW230529 has a probability of being a BH of 99% [101], unlike the secondary mass of GW190814, whose nature is still uncertain. GW230529 further contests the lower mass gap in the astrophysical BH mass distribution.

1.2.4 Gravitational wave detectors of the future

Data for the fourth LVK observing run have yet to be released publicly. The LIGO detectors and Virgo detector were upgraded before their fourth observation run, some upgrades being detailed in Abbott *et al.* (2020) [155] (but see Appendix A in The LIGO Scientific Collaboration *et al.* (2024) [101] for more details). With this upgrade, the sensitivity bucket of the LIGO detectors (Fig. 1.1) has become deeper, thus becoming more sensitive to GWs. Advanced Virgo [156] has also joined the fourth observing run, and will be aiding the localisation of compact object mergers. The GW detector KAGRA was due to join the three interferometers with new cryogenic technology as detailed in Kagra Collaboration (2019) [157]; however due to unexpected issues the sensitivity of KAGRA to GWs is not as good as was originally predicted [79]. There are further plans for a new GW detector in India, LIGO-India, to be built within the next decade [158], which will help with GW detection and localisation alongside Virgo and KAGRA.

As aforementioned, LIGO is only sensitive to $\sim 10 - 1000$ Hz, so it is limited to detecting mergers of neutron stars and black holes. In the 2030s, GW science will take another leap forward as the Laser Interferometer Space Antenna (LISA) becomes operational. LISA will be a triangular laser interferometer in space, with an arm length of 2.5×10^6 km [159]. This arm length means that LISA will be mostly taking information in the $10^{-4} - 1$ Hz frequency window, making it sensitive to inspiralling white dwarves, the mergers of SMBHs, and eccentric inspirals of stellar-mass BBHs [160].

A different way to measure gravitational waves exists in the pulsar timing array method. By timing pulsars across the Milky Way, one can obtain a measurement for the stochastic background signal from in-spiralling supermassive black holes (see Taylor [161] for a review). The longer the pulsars are timed, the better the signal. Several collaborations exist under the umbrella of the International Pulsar Timing Array (PTA) that gather gravitational wave data from pulsars, including: NANOGrav that in 2023 released their 15 years of data that showed evidence for a GW signal [162], the European PTA collaboration which combined their data with the India PTA data in EPTA Collaboration *et al.* (2023) [163] and also found away from the null hypothesis of no GW signal, and the Parkes PTA who report their results in Reardon *et al.* (2023) [164] that agree with the other two claims. The Chinese PTA independently reported results in Xu *et al.* (2023) [165] that are concurrent of evidence for a GW background signal in pulsar measurements.

In the next century, there are further plans for developing top of the art gravitational wave detectors. One of these is the Einstein Telescope [166, 167], whose longer arm length of 10km and improved machinery will increase its sensitivity to gravitational waves for a larger range of frequencies compared to that of LIGO. The other is the Cosmic Explorer, the next evolution of LIGO-style detectors, with new technologies allowing for even higher sensitivities [168, 169]. These new features will allow for several improvements to GW data: the two new interferometers will be able to observe GWs from high redshifts (as high as $z \sim 20$ [168, 170, 171], but see Mancarella *et al.* (2023) [172] for potential limitations), at high precision for a longer time [173].

1.2.5 A population of black holes

The population problem in GW science is a multi-faceted one. The hundreds of events currently available for analysis can be statistically combined to obtain an observed population; then, taking selection effects into account, we can reverse engineer the GW detections into an astrophysical population of black holes and compact objects.

As well as this, as the number of GW events increases, making general statements on the properties of black holes will become more valuable than the specificities of individual events. However, this assumes that the current detections are being combined 'correctly'; the methodology behind black hole population studies is an active field in GW science [76, 174–184].

Alongside every GW catalogue release, the LVK collaboration releases companion publications on the BH and compact object populations [185–187]. In order to infer population parameters, hierarchical Bayesian methods are used. This allows us to statistically marginalise results over individual event uncertainties. However, this method requires parametric models, predictions in the population parameter spaces for how the masses or spins or rates may be distributed. Individual GW events are then weighted and statistically combined to form a posterior, from which distributions for the population parameters are pulled. These are then compared to the priors, and conclusions are then made about the population of BHs.

One of the key parameters one can measure from GW data is the rate of specific merger events and its evolution with redshift. This information is a predictor of the formation channels of BBHs [182, 188–190]. Knowing the rate of events can also motivate expectations for future detections [188, 191]. If the rate of BBH mergers given by LVK collaborations is correct, as future detector sensitivities increase we can expect to measure thousands of BBH mergers in a single observing run. Current population estimates of the BBH merger rate are in the range of $17.9 - 44.0\,\mathrm{Gpc}^{-3}\,\mathrm{yr}^{-1}$ taken at redshift $z = 0.2$. This rate is thought to increase with redshift proportionally to $(1+z)^{\lambda}$, where $\lambda = 2.9^{+1.7}_{-1.8}$ for $z \lesssim 1$ [187].

In GWTC-1, the best fit to the mass distribution of BHs was the power law model, a smooth distribution that inferred that 99% of BH source masses fall under $45\,\mathrm{M}_{\odot}$ [185].

High mass events such as GW190521 in GWTC-2 and GW200220_061928 in GWTC-3 challenged this model, with current parametric models for the mass distribution combining power laws with Gaussian features to account for mass build ups in the distribution. As sensitivities increase for future detections, the distribution of BH masses will have a larger sample size and higher resolution. This consequence has lead to a call for more flexible models of the GW population of black holes, such as Gaussian processes, non-parametric inference methods, and neural networks [75, 179, 183, 184, 192–200]. The most recent work by the LVK collaboration on the topic of BH masses [187] showed that the population of BH masses is clumpy, with buildups at $M \sim 35\,\mathrm{M}_{\odot}$. Abbott *et al.* (2023) [187] also claimed no evidence of an upper mass gap, instead finding that the mass distribution must decrease monotonically for masses greater than $50\,\mathrm{M}_{\odot}$. Masses are well measured in GW detectors, the total mass and mass ratio being dominant terms in the GW phase and strain. Black-hole spins, on the other hand, have a much more subtle effect on the waveform.

Part I

Black holes and spin dynamics

Chapter 2

Spin precession

Summary

According to the no-hair theorem, black holes are described by three intrinsic properties only - their mass, their spin and their charge. The charges of black holes are expected to be negligible, as a charged black hole would attract the opposite charge and self-neutralise. However, black holes are expected to retain some angular momentum. Spinning black holes in binaries induce an effect known as spin precession. In this chapter, I describe the theory behind spin precession, the methods we use to detect them, and the necessary spin precession equations needed to understand Chapters 3-4 further along in this work. In this Chapter, I describe the precession-averaging formalism from Kesden *et al.* (2015) [201], Gerosa *et al.* (2015) [202], which was more recently updated in Gerosa *et al.* (2023) [203]. The spin precession taxonomy presented in Chapter 3, along with the five parameters, were formulated using the old precession averaging formalism of Kesden *et al.* (2015) [201], Gerosa *et al.* (2015) [202], and used the first version of the Python package PRECESSION [204].

2.1 Quantifying spin precession

Spin precession is an effect unique to general relativity. Unlike in Newtonian gravity, the connected curvature of space-time allows for the spins of objects to couple and interact during the inspiral. The coupling of the individual sources' spins to one another and its effect on the orbital motion of the two objects mean that spin precession is detectable as a modulation of the gravitational wave strain.

Measuring spin precession does not guarantee measuring the individual spins of the black holes in the binary. This is because the dominant effects of spin precession on the waveform are mass-weighted combinations of the two spins. These combinations are summarised using two parameters: the effective inspiral spin χ_{eff} [205] and the effective precession spin χ_{P} [206]. The effective inspiral parameter χ_{eff} is the mass-weighted projection of the source spins onto the the orbital angular momentum $\vec{L}$, defined as:

$$\chi_{\mathrm{eff}} = c\left(\frac{\vec{S}_1}{m_1} + \frac{\vec{S}_2}{m_2}\right) \cdot \frac{\hat{L}}{GM}\,, \tag{2.1}$$

where $\vec{S}_i$ is the spin angular momentum of black hole i, m_i is the mass of black hole i and $M \equiv m_1 + m_2$ is now the total mass of the binary (unlike in Ch. 1). The heavier mass in the black hole binary is denoted by the subscript 1, the lighter by subscript 2. The effective inspiral parameter is a useful quantity - this combination of spins has been shown to remain constant during the inspiral in the weak gravitational field regime [205, 207] (see Sec. 2.2 below for more details). Additionally, χ_{eff} has been shown to be correlated with the SNR [208] and to determine the signal length due to the effect of orbital hang up [209]. From Eq. (2.1), it can be seen that if $\chi_{\mathrm{eff}} \neq 0$, then at least one black hole in the system must be spinning. If $\chi_{\mathrm{eff}} > 0$, the total spin of the black holes will be aligned with the orbital angular momentum; if $\chi_{\text{eff}} < 0$ the total spin will be anti-aligned with $\vec{L}$. If the black hole spins obey the Kerr limit, $-1 \leq \chi_{\text{eff}} \leq 1$.

The effective precession spin χ_{P} was designed to summarise the "amount of precession" in the binary. It is a parameter that ranges from 0 to 1, where $\chi_{\text{P}} = 0$ means the spins are either not present or are aligned with the orbital angular momentum, and $\chi_{\text{P}} = 1$ denotes a system with maximal precession. The definition of χ_{P}, as first proposed in Schmidt *et al.* (2015) [206], is:

$$\chi_{\text{P}} = \max\left\{\chi_{1,\perp}, \frac{q(4q+3)}{4+3q}\chi_{2,\perp}\right\}, \tag{2.2}$$

where $\vec{\chi}_i$ is the dimensionless component spin of black hole i, $\chi_{i,\perp}$ is the component of $\vec{\chi}_i$ perpendicular to the orbital angular momentum $\vec{L}$, and $q = m_2/m_1$ is the mass ratio of the black holes. Unlike χ_{eff}, χ_{P} does not stay constant during the inspiral [210]. In order to control for this variation, Gerosa *et al.* (2021) [210] introduce a new χ_{P}, the precession-average of which, $\langle\chi_{\text{P}}\rangle$, can be easily applied to GW event data. This generalised χ_{P}, $\langle\chi_{\text{P}}\rangle$, has a range between 0 and 2 and controls for some of the variations of χ_{P}. The value range $1 \leq \langle\chi_{\text{P}}\rangle \leq 2$ can only be inhabited by binary black holes with two spins misaligned with $\vec{L}$. Due to poor constraints on spin precession in current gravitational wave events, the two χ_{P} parameters currently give results that agree with one another [210], but with better sensitivities the two parameters should become distinguishable [211]. The χ_{P} of Eq. (2.2) is also insufficient in the strong-field regime and a more appropriate parameter was suggested in Thomas *et al.* (2021) [212].

2.1.1 Spin precession inference

We have already detected spin precession in compact object inspirals in pulsar EM signals [213–217]. Pulsars are highly spinning neutron stars; if the spins of the pulsar and its companion star are misaligned, it induces a change in the frequency of pulses received on Earth. We typically observe pulsar pulse timings over longer time periods than GW signals and are thus more sensitive to small changes in the frequency. The spin precession we have detected so far from pulsars is caused by the coupling of the orbital angular momentum with the spin of one of the objects, rather than spin-spin coupling. Spin-spin coupling is unlikely to be detected through pulsar observations: pulsars as we detect them exist in the weak gravitational regime, for spin-spin coupling more compact objects like black hole binaries are necessary (see, e.g., Reynolds (2021) [218]).

While the detection of a black hole spinning in a gravitational wave event was made as early as the first LIGO-Virgo observation run with the event GW151226 [219], spin precession in the form of $\chi_{\mathrm{P}} > 0$ in single-event analysis remains elusive. There are ~ 15 events with posteriors constrained away from $\chi_{\mathrm{eff}} = 0$ with 90% credibility listed in the first three LVK GW catalogs; events with a χ_{P} posterior significantly constrained away from $\chi_{\mathrm{P}} = 0$ are non existent. Spin precession has a subtle effect on the gravitational waveform, and for confident detections we need events with several orbital cycles in-band. Thus, in order to detect spin precession, an event with high SNR (such that the GW signal can be distinguished from noise earlier in the inspiral) is necessary. In Hannam *et al.* (2022) [148], it was claimed that GW200129, a gravitational event with a network SNR ~ 26, showed significant spin precession ($\chi_{\mathrm{P}} \sim 0.9^{+0.2}_{-0.6}$) when the event was re-analysed using the NR surrogate waveform `NRSur7dq4` [148, 154]. However, the evidence for spin precession in the signal is located in the data from the single detector LIGO Livingston, and is undermined by uncertainties in glitch mitigation for the detector, as discussed in Payne *et al.* (2022) [85]. The `IMRPhenomXPHM` analysis of GW200129 also suggested a precessing system in contrast to the `SEOBNRv4PHM` analysis which prefers a non-spinning system; we explore this further in Fig. 4.5 of Ch. 4. These results show promise- spin precession in single events may very well be constrained in future catalogs, when the sensitivity of GW detectors increases and events can be detected with higher SNR.

A different avenue for spin precession detection is statistically combining the posteriors of the current GW events and predicting the spin precession of the astrophysical BBH population. The uncertainties in population measurements decrease as more events are detected. In the GWTC-3 and GWTC-2 population papers, it was shown that the case of perfect spin-orbit alignment in binaries, $\cos\theta_1 = \cos\theta_2 = 1$, was excluded [186, 187]. Additionally, in GWTC-3, the distribution of χ_P is shown to be either broad with a centre at $\chi_\mathrm{P} = 0$, or narrow with a median at $\chi_\mathrm{P} \sim 0.2$ [187] - demonstrating that some of the BBHs detected by the LVK collaboration have misaligned spins, and are precessing. There are still some limitations to the evidence for spin precession; for one, the population posterior shape of fig. 15 in Abbott *et al.* (2023) [187] is replicated in fig. 2 in Mould and Gerosa (2022) [174] when using only the events from GWTC-2 and including spin in selection effects. Additionally, there is a possibility that spin precession detections are driven by the parametrisation of the prior population models. These uncertainties can be reduced through the use of nonparametric models such as the use of flexible spline functions, as was done for the primary mass model in Abbott *et al.* (2023) [187]. Another level of uncertainty stems from the thresholds used to determine a “GW event”. Currently, the LVK GW catalogs apply a threshold in

p_{astro} for the events they consider confident. However, the GWTC-3 population paper instead uses a more relaxed threshold of false alarm rate < 1 per year. Currently, the GWTC-3 catalog contains a total of 35 GW events with $p_{\mathrm{astro}} > 0.5$; the GWTC-3 population paper analyses over 70. Current GW events lack confident detections of spin precession- the effect of different sample sizes, model choices and selection effects will become more pronounced as sensitivities increase.

2.2 The post-Newtonian regime

Spin precession and its effects on the GW waveforms can only be accurately described using complete solutions to the Einstein field equations. These solutions are obtained using numerical relativity, a computationally expensive process. Numerical relativity solutions are used in the strong-field regime, where the compact sources of GWs are close to merger and moving at highly relativistic speeds. There are only ~ 40 numerical relativity simulations that extend to more than 50 orbits before merger [220]; these are used for NR surrogate waveform calibration and for unusual merger cases [221]. A different approach to using NR simulations that is less expensive and accurate up to separations of $r \sim 5R_{\mathrm{s}}$ is the post-Newtonian (PN) regime (see Blanchet (2014) [222] for a review).

The post-Newtonian formalism starts from a metric and stress-energy tensor that both assume a non-relativistic ($v/c \ll 1$) source that is self-gravitating ($(R_{\mathrm{s}}/R)^{1/2} \sim v/c$). One can then expand equations of motion in powers of $(v/c)^2$ (or equivalently M/r), so-called PN 'orders', and obtain a GW waveform accurate up to the specified PN order. By considering higher order PN terms, we introduce effects unique to general relativity to the gravitational waveform, such as spin-orbit coupling and spin-spin coupling [223, 224] up to a measurable accuracy without needing numerical relativity.

Out of the detectable LVK GW sources, BBHs are the most massive type of source translating to high SNR values. Additionally, tidal deformation, an effect which competes with spin-spin coupling at the 2PN order [225], is expected to be negligible for BBHs [226]. Thus, we can expect to constrain spin precession in the mergers of BBHs best. However, a competing effect within BBH mergers and inspirals is orbital eccentricity; some events assumed to be precessing such as GW190521 and GW200129 could be eccentric instead [135, 227]. The distinguishability of eccentricity and spin precession in a GW event has been explored in Romero-Shaw *et al.* (2023) [228]. Currently, GW events are assumed to be quasi-circular, justified by the fact that gravitational radiation is efficient at circularising orbits (see, for example, Peters and Mathews (1963) [229]). In Fumagalli and Gerosa (2023) [230], the spins of a BBH merger have been shown to 'remember' the eccentricity of a binary - this opens an avenue for inferring eccentricity in circularised GW events [231]. In this thesis, I focus on spin precession in circular binaries, assuming that the eccentricity is 0.

By working up to the 2PN order, we obtain analytic expressions for spin precession valid up to separations of $r \sim 5\,R_\mathrm{s}$ [201–203]. These equations are built on the PN work done by Apostolatos *et al.* (1994) [232], Blanchet *et al.* (1995) [233] and Kidder (1995) [224].

2.2.1 Spin precession equations

We now work in geometric units, so that $G = c = 1$. The parameter r is the separation between the two black holes. In this framework, since $G = c = 1$, the total mass of the binary M can be used as a unit or scaling factor for our spin equations.

The motion of the black holes in the binary induces an orbital angular momentum, given by

$$\vec{L} = \eta M^{1/2} r^{1/2} \hat{L} \,, \tag{2.3}$$

where $\eta = m_1 m_2/M$ is the symmetric mass ratio. The black holes also have individual spin angular momenta, denoted by $\vec{S}_i$, which are constrained to have magnitudes $S_i \leq m_i^2$ (i.e., the Kerr limit applies). These angular momenta sum to a total angular momentum $\vec{J} = \vec{L} + \vec{S}_1 + \vec{S}_2$. Similarly, the total spin vector is defined as $\vec{S} = \vec{S}_1 + \vec{S}_2$.

Three timescales govern the motion of two merging black holes. These are:

1. the orbital timescale, $t_{\rm orb}$,
2. the precession timescale, $t_{\rm pre}$,
3. and the radiation reaction timescale, $t_{\rm RR}$.

These three timescales have a different dependency on the orbital separation r. The orbital timescale $t_{\rm orb}$ tracks the time it takes for a black hole to complete an orbit around the other and is proportional to $\sim r^{3/2}$. It is the shortest timescale, and is often averaged over to calculate global binary properties, such as the eccentricity of the orbit. The precession timescale $t_{\rm pre}$ describes the timescale it takes the spins of the black holes, $\vec{S}_{1,2}$, and the Newtonian orbital angular momentum, $\vec{L}$, to precess around the total angular momentum $\vec{J}$. The precessional timescale $t_{\rm pre}$ is proportional to $\sim r^{5/2}$ (see Eqs. (2.5, 2.6) below). The longest timescale, $t_{\rm RR}$, tracks the decrease in the binary's separation r due to the binary losing energy through gravitational waves. The radiation reaction timescale $t_{\rm RR}$ is proportional to $\sim r^4$.

We can separate these timescales, and average over not only $t_{\rm orb}$ but also $t_{\rm pre}$, as proposed in Kesden *et al.* (2015) [201] and Gerosa *et al.* (2015) [202]. To separate these timescales, one needs simply to enter a regime where r is very large (where $r \gg M$), so that $t_{\rm RR} \gg t_{\rm pre} \gg t_{\rm orb}$. Working in the PN limit allows us to do just that.

In Gangardt and Steinle *et al.* (2021) [199], the aim was to study the evolution of $\vec{S}_{1,2}$ and $\vec{L}$ during the inspiral, averaging over the precessional timescale. This requires analytic expressions for the angular momenta on the precession timescale. To obtain these expressions, we first restrict the number of degrees of freedom using constants of motion. The BBH spin precession problem has nine degrees of freedom (each angular momenta, $\vec{S}_{1,2}$ and $\vec{L}$, has three), which are reduced to six when considering that the direction and magnitude of $\vec{J}$ are constant on the precession timescale (these only change on the radiation reaction timescale, or for rare configurations of the binary spins, see Sec. 3.1). The magnitudes of $\vec{S}_{1,2}$ are constant when considering spin effects up to 2PN [224] and the magnitude of $\vec{L}$ also remains constant on the precession timescale (see the dependence of $\vec{L}$ on r in Eq. (2.3)), leaving three degrees of freedom.

In Sec. 2.1, we introduced the projected effective spin parameter, $\chi_{\rm eff}$. As aforementioned, this parameter has been shown to be conserved over all three timescales at 2PN order [205, 207]. Equation (2.1) can be rewritten geometrically, breaking the angular momenta into their vector components:

$$\chi_{\rm eff} \equiv \frac{qS_1 \cos\theta_1 + S_2 \cos\theta_2}{\eta M^2 (1+q)} \,,$$

where θ_1 (θ_2) refers to the angle between $\vec{S}_1$ ($\vec{S}_2$) and $\vec{L}$. In Gerosa *et al.* (2015) [202], the remaining two degrees of freedom are represented by the magnitude of the total spin, S, and the angle φ'. In the updated work of Gerosa *et al.* (2023) [203], the remaining two degrees of freedom are φ' and the weighted spin difference [235]

$$\delta\chi \equiv \frac{\chi_1 \cos\theta_1 - q\chi_2 \cos\theta_2}{1+q} \,.$$

The extrinsic parameter φ' is defined as

$$\varphi' = \frac{\hat{S}_1 \cdot (\hat{y} \times \hat{S})}{|\hat{S}_1 \times \hat{S}|},$$

where $\hat{y}$ is the unit vector orthogonal to the $\vec{J}$-$\vec{L}$ plane. Following Gerosa *et al.* (2015) [202], $\chi_{\rm eff}$ can be rewritten as a function of S and φ' only:

$$\begin{aligned}\chi_{\rm eff}(S, \varphi') = \frac{1}{4qM^2S^2L}\Big[(J^2 - L^2 - S^2)[S^2(1+q)^2 - (S_1^2 - S_2^2)(1-q^2)] \\ - (1-q^2)A(S)\cos\varphi'\Big],\end{aligned} \tag{2.4}$$

where $A(S)$ is a constant that vanishes when the magnitude S is at its minimum ($S = S_{\rm min}$) or maximum ($S = S_{\rm max}$). Equation (2.4) forms a closed oval in the $\chi_{\rm eff} - S$ plane for any binary with defined values of $q\,, S_1\,, S_2\,, r$ and J, which can be seen in Fig. 2.1. The outer boundaries of this loop can be drawn by setting $\cos\varphi' = -1$ for the upper boundary (which we label $\chi_{\rm eff+}$) and $\cos\varphi' = 1$ for the lower boundary ($\chi_{\rm eff-}$). Specific binaries will have a constant value of $\chi_{\rm eff}$, meaning that they will move on horizontal lines within the closed loop of Fig. 2.1 during a precession cycle. The turning points of each binary are labelled S_- and S_+. The behaviour of φ' during a precession cycle depends on where the turning points $S_\pm$ lie on the loop, and are used in Gerosa *et al.* (2015) [202] to define three spin morphologies:

1. if S_+ and S_- lie on $\chi_{\rm eff+}$, φ' oscillates about π and never reaches 0;
2. if S_+ and S_- lie on $\chi_{\rm eff-}$, φ' oscillates about 0 and never reaches π;
3. if one turning point lies on $\chi_{\rm eff+}$ and the other on $\chi_{\rm eff-}$, φ' will monotonically move from $-\pi$ to π.

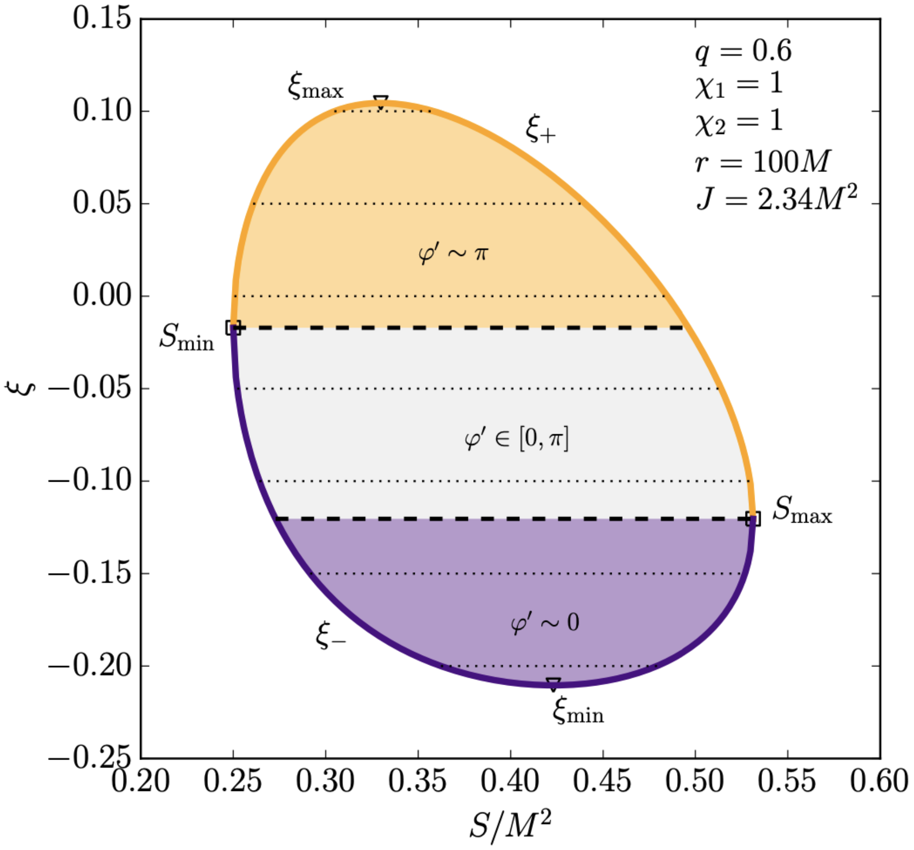

Figure 2.1: Left subplot from figure 2 in Gerosa *et al.* (2015) [202]. This figure shows the "effective potential" drawn when considering the effective inspiral parameter χ_{eff} as a function of the total spin magnitude S and the angle ϕ'. A binary with a defined χ_1, χ_2, q, M at a specific separation r and value of J will move along a horizontal line within the potential in a quasi-periodic fashion.

Moving away from the complicated geometric meaning of the angle φ', three different spin precession morphologies can be found in an $\vec{L}$-aligned frame. In this frame, the basis is formed on the direction of $\vec{L}$ (we label this direction $\hat{z}'$). The plane that runs parallel to $\vec{L}$ and $\vec{S}_1$ is represented by the unit vector $\hat{x}'$ and a unit vector that is the normal to the $\vec{L}$-$\vec{S}_1$ or $\hat{z}'$-$\hat{x}'$ plane completes the set. The angle between $\vec{S}_1$ and $\vec{L}$, θ_1, is by formulation always in the $\hat{z}'$-$\hat{x}'$ plane. The angle between $\vec{S}_1$ and $\vec{S}_2$ that is projected onto the $\hat{x}'$-$\hat{y}'$ plane, $\Delta\Phi$, is an azimuthal angle that tracks the motion of $\vec{S}_1$ and $\vec{S}_2$ around $\vec{L}$ in a similar fashion to φ'. In the $\vec{L}$-aligned frame, a new set of morphologies appears, identified by the azimuthal angle $\Delta\Phi$:

1. if $\Delta\Phi(S_+) = \Delta\Phi(S_-) = 0$, $\Delta\Phi$ oscillates about 0 and never reaches π (we label this case 'L0', meaning 'librating about 0');
2. if $\Delta\Phi(S_+) = \Delta\Phi(S_-) = \pi$, $\Delta\Phi$ oscillates about π and never reaches 0 (we label this case 'Lπ', meaning 'librating about π');
3. if $\Delta\Phi = 0$ at one of the turning points, and $\Delta\Phi = \pi$ at the other turning point, will circulate through the full range of $-\pi$ to π (we label this case 'C', meaning 'circulating').

A BBH with defined values of $q\,, S_1\,, S_2\,, r$ and J will form a unique $\chi_{\rm eff}$ loop in the $\chi_{\rm eff} - S$ plane. Similarly to the φ' case, the $\Delta\Phi$ morphologies will divide the loop into three horizontal sections. A BBH with a constant $\chi_{\rm eff}$ will precess in a singular morphology during a precession cycle. However, unlike the φ' case, not all three $\Delta\Phi$ morphologies will necessarily be available to a binary defined by its $q\,, S_1\,, S_2\,, r$ and J values. The available morphologies, and the divisions between them, will change during the inspiral as r changes. The morphologies a binary is in can tell us about its precessional dynamics without the need of the value of S [236].

In order to calculate the precession-averaged value of a parameter that is a function of S only, we will need a method to integrate over values of S. To do so, one can use eq. (26) from Gerosa *et al.* (2015) [202]:

$$\frac{\mathrm{d}S}{\mathrm{d}t} = -\frac{3(1-q^2)}{2q}\frac{S_1 S_2}{S}\frac{(\eta^2 M^3)^3}{L^5}\left(1-\frac{\eta M^2 \xi}{L}\right) \times \sin\theta_1 \sin\theta_2 \sin\Delta\Phi\,. \tag{2.5}$$

Equation (2.5) vanishes when $q = 1$, thus displaying the key problem of using S to parametrise the precession cycle. Using the weighted spin difference $\delta\chi$ does not have the same problem (see Gerosa *et al.* (2023) [203]). The spin magnitude S and the spin difference $\delta\chi$ can be written as functions of one another when working in the precession timescale, thus any quantity that varies on the precession timescale can be written as a function of S or $\delta\chi$. The dynamics of the following Chapter parametrise the precession cycle using the total spin S.

The 'effective potential' of $\chi_{\rm eff}$ implies that S oscillates periodically between S_- and S_+. The frequency of this motion we define as $\omega \equiv 2\pi/\tau$, where:

$$\tau = 2\int_{S_-}^{S_+} \frac{{\rm d}S}{|{\rm d}S/{\rm d}t|}\,. \tag{2.6}$$

It is important to note that τ is not equivalent, but is comparable to, the time it takes for the orbital angular momentum $\vec{L}$ to complete its cone of motion around $\vec{J}$. We can now define the precession average of a quantity that varies on the precession timescale, $X(S)$, as:

$$\langle X\rangle \equiv \frac{2}{\tau}\int_{S_-}^{S_+} \frac{X(S)}{|{\rm d}S/{\rm d}t|}{\rm d}S\,. \tag{2.7}$$

In this regime, the azimuthal frequency $\Omega_{\rm L} \equiv {\rm d}\Phi_{\rm L}/{\rm d}t$, can be defined as a function of S only [201, 202]:

$$\begin{aligned}\Omega_{\rm L}(S) = \frac{J}{2r^3}\Bigg(1 &+ \frac{3(1+q)}{2q}\left[1-\chi_{\rm eff}\left(\frac{M}{r}\right)^{1/2}\right]\\ &\times\Big\{1+q-[J^2-(L-S)^2]^{-1}[(L+S)^2-J^2]^{-1}\\ &\times\big[4(1-q)L^2(S_1^2-S_2^2)-(1+q)(J^2-L^2-S^2)\\ &\times(J^2-L^2-S^2-4\eta M^2 L\chi_{\rm eff})\big]\Big\}\Bigg)\,.\end{aligned} \tag{2.8}$$

During a period τ, $\vec{L}$ precesses by an angle $\alpha = \langle \Omega_{\rm L} \rangle \tau$ about $\vec{J}$.

The polar angle between $\vec{L}$ and $\vec{J}$ is given by:

$$\theta_L(S) = \arccos\left(\frac{J^2 + L^2 - S^2}{2JL}\right) . \tag{2.9}$$

The oscillation of S with period τ leads to nutation of $\vec{L}$ with frequency $\omega \equiv 2\pi/\tau$.

Having a procedure to find the precession average, one can then find an equation for the precession averaged inspiral (see Gerosa et al. [202] for the full derivation):

$$\left\langle \frac{\mathrm{d}J}{\mathrm{d}L} \right\rangle_{\rm pre} = \frac{1}{2LJ}(J^2 + L^2 - \langle S^2 \rangle_{\rm pre}) , \tag{2.10}$$

which can be used to evolve binaries from large separations down to $r \sim 10M$ where the PN regime no longer applies. At large separations, BBHs are described by fewer intrinsic parameters and the BBH dynamics are simpler. Large separations are defined as the limit where $r/M \to \infty$, or equivalently where $L/M^2 \to \infty$, as $L \propto r^{1/2}$. In this limit, it is simplest to define a parameter κ, such that:

$$\kappa \equiv \frac{J^2 - L^2}{2L} . \tag{2.11}$$

Unlike J and L, κ asymptotes to a constant at large separation, κ_∞. This can be shown by combining Eqs. (2.10, 2.11) to get:

$$\frac{\mathrm{d}\kappa}{\mathrm{d}L} = -\frac{\langle S^2 \rangle_{\rm pre}}{2L^2} . \tag{2.12}$$

When $L/M^2 \to \infty$, Eq. (2.12) tends to 0, giving a constant κ at large separations, as required. It has been shown in Gerosa *et al.* (2015) [202] that the constant in question is the projection of the total spin onto the orbital angular momentum in the limit of large separations,

$$\kappa_\infty = \lim_{r/M \to \infty} \vec{S} \cdot \hat{L} \,.$$

.

To find the value of κ for a specific BBH, one needs only to integrate Eq. (2.12) to $r/M \to \infty$. At these large separations, spin-orbit coupling dominates over spin-spin coupling, and the black holes' spins $\vec{S_1}$ and $\vec{S_2}$ will precess in cones around the orbital angular momentum $\vec{L}$ with constant opening angles:

$$\cos\theta_{1\infty} \equiv \lim_{r/M \to \infty} \hat{S}_1 \cdot \hat{L} = \frac{-M^2\xi + \kappa_\infty(1+q^{-1})}{S_1(q^{-1}-q)} \,, \tag{2.13a}$$

$$\cos\theta_{2\infty} \equiv \lim_{r/M \to \infty} \hat{S}_2 \cdot \hat{L} = \frac{M^2\xi + \kappa_\infty(1+q)}{S_2(q^{-1}-q)} \,. \tag{2.13b}$$

These opening angles, along with the intrinsic parameters q, S_1 and S_2, are enough to uniquely identify a single BBH without specifying a reference frequency or separation. Using the previous equations, one can now evolve the spins and angular momenta of any binary from infinitely large separations to separations of roughly $10M$, where the PN regime no longer applies.

Chapter 3

Nutation

Abstract

Binary black holes with misaligned spins will generically induce both precession and nutation of the orbital angular momentum $\vec{L}$ about the total angular momentum $\vec{J}$. These phenomena modulate the phase and amplitude of the gravitational waves emitted as the binary inspirals to merger. We introduce a “taxonomy” of binary black-hole spin precession that encompasses all the known phenomenology, then present five new phenomenological parameters that describe generic precession and constitute potential building blocks for future gravitational waveform models. These are the precession amplitude $\langle\theta_{\rm L}\rangle$, the precession frequency $\langle\Omega_L\rangle$, the nutation amplitude $\Delta\theta_L$, the nutation frequency ω, and the precession-frequency variation $\Delta\Omega_L$. We investigate the evolution of these five parameters during the inspiral and explore their statistical properties for sources with isotropic spins. In particular, we find that nutation of $\vec{L}$ is most prominent for binaries with high spins ($\chi \gtrsim 0.5$) and moderate mass ratios ($q \sim 0.6$).

Summary

This chapter is a reformatted version of my joint first-author paper, Gangardt and Steinle *et al.* (2021) [199]. This work was a follow up on a summer project where I studied wide nutations in black hole binaries, as suggested by Davide Gerosa after his work on wide spin configurations in Gerosa *et al.* (2019) [237]. The summary of that project can be found in App. A.1. At the same time, Michael Kesden and Nathan Steinle were studying black-hole dynamics through the perspective of the angle $\theta_{\rm L}$ as opposed to the traditional spin precession angles (see Sec. 2.1). We then combined our results and formulated a new spin precession taxonomy in Gangardt and Steinle *et al.* (2021) [199]. The introduction was written by Nathan Steinle and Davide Gerosa. The taxonomy was formulated by Davide Gerosa. The definition of the five spin precession parameters was given by Michael Kesden and Davide Gerosa. The leading post-Newtonian behaviour was provided by Michael Kesden. I was responsible for Figures 3.3—3.6. The remaining figures were prepared by Nathan Steinle. I described the results concerning Figs. 3.3—3.6, with editorial comments given by Davide Gerosa, Nathan Steinle and Michael Kesden. Nathan Steinle wrote the rest of Sec. 3.3. The conclusions were written by me, then edited by Davide Gerosa.

3.1 Introduction

In Sec. 2.1, I introduced the spin precession parameters $\chi_{\rm eff}$ and $\chi_{\rm P}$. Whilst binary black hole spin precession is often understood through the lens of these two parameters, a variety of configurations where BBH spin dynamics result in peculiar phenomenologies are now known, including transitional precession [232, 238], spin-orbit resonances [202,

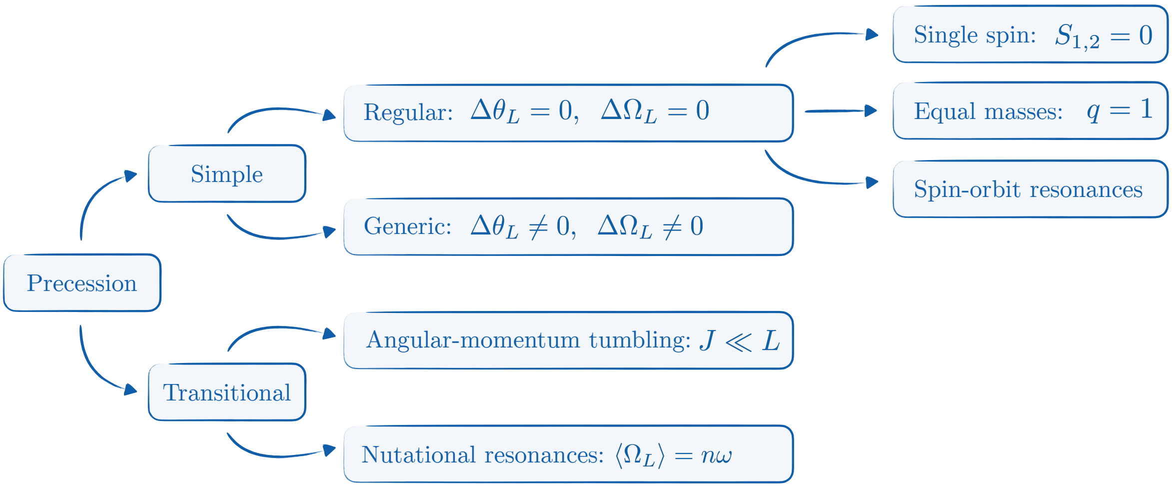

Figure 3.1: Proposed taxonomy of BBH spin precession. Simple (transitional) precession occurs when the direction of the total angular momentum $\vec{J}$ is constant (varying). Simple precession is "regular" when the orbital angular momentum $\vec{L}$ precesses on a cone with fixed opening angle (i.e. $\Delta\theta_{\rm L} = 0$) and frequency (i.e. $\Delta\Omega_{\rm L} = 0$) and is "generic" when nutation causes the opening angle and frequency to vary (i.e. $\Delta\theta_{\rm L} \neq 0$, $\Delta\Omega_{\rm L} \neq 0$). Examples of regular precession include BBHs with a single spin, equal masses, and the spin-orbit resonances of Ref. [239]. Transitional precession occurs for small values of the total angular momentum ($J \ll L$) [232] or at nutational resonances ($\langle\Omega_{\rm L}\rangle = n\omega$) [238].

239, 240], dynamical instabilities [221, 241–243], emergence of new constants of motion [244, 245], and large nutation cycles [237, 246]. This paper attempts to incorporate this richness into a single, comprehensive framework and presents five new parameters that encode the most generic features of BBH spin precession.

Before delving into the details of this study, we introduce a new "taxonomy" of spin precession which encompasses all of the known phenomenology. Our classification is summarised in Fig. 3.1. Additionally, I include Fig. 3.2 which shows the new framework with which we now look at the spin precession problem.

(1) Following Apostolatos *et al.* (1994) [232], we refer to precession as "simple" when the direction of the total angular momentum $\vec{J} = \vec{L} + \vec{S}_1 + \vec{S}_2$ is approximately

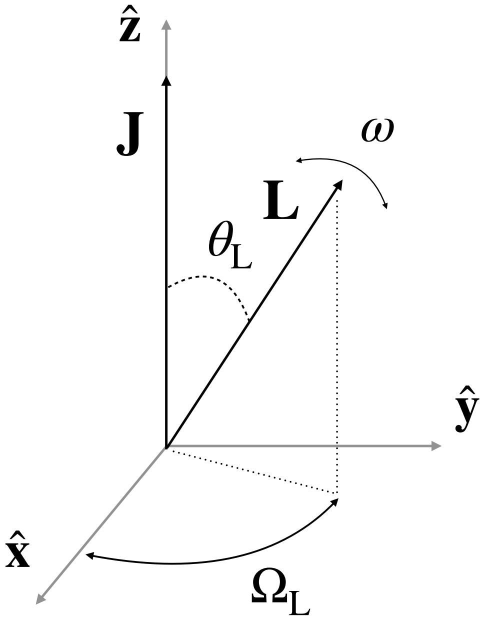

Figure 3.2: The defined coordinate frame set by the assumed to be constant total angular momentum vector direction, $\vec{J}$. During a precession cycle, the precession frequency Ω_{L} will go from 0 to 2π. If the total spin vector $\vec{S}$ does not change, there is no polar motion of $\vec{L}$ and the precession angle θ_{L} will remain constant. If there is a change in the total spin of the system, $\vec{L}$ will nutate with a nutation frequency ω.

constant. In this case, the direction of $\vec{L}$ as it precesses about $\vec{J}$ can be specified by the polar angle θ_L and azimuthal angle Φ_L.

(a) If the total spin magnitude $S = |\vec{S}_1 + \vec{S}_2|$ is conserved on the precession timescale, then θ_{L} and the precession frequency $\Omega_{\mathrm{L}} \equiv d\Phi_L/dt$ are also constant on this timescale. We refer to this uniform precession of $\vec{L}$ on a cone about $\vec{J}$ as "regular" following Landau and Lifshitz (1969) [247]

Cases of regular precession include:

(i) a single nonzero spin [232],

(ii) the equal-mass ($q = 1$) limit [232, 244],

    (iii) the spin-orbit resonances [239].

  (b) In the "generic" case when S is *not* constant on the precession timescale [201, 202], neither are θ_L nor Ω_L, implying that $\vec{L}$ nutates as it precesses about $\vec{J}$.

(2) "Transitional" precession occurs when the direction of $\vec{J}$ is not constant [232]. There are at least two different but related scenarios when this can occur:

  (a) If the ratio of the magnitudes of the total and orbital angular momenta is less than the ratio of the precession and radiation-reaction timescales $J/L \lesssim t_{\rm pre}/t_{\rm RR} \propto (r/M)^{-3/2}$, the direction of $\vec{J}$ tumbles [232].

  (b) At a nutational resonance [238] where the mean precession frequency is an integer multiple of the nutation frequency (i.e. $\langle \Omega_{\rm L} \rangle = n\omega$), coherent GW emission tilts the direction of $\vec{J}$.

The vast majority of the binaries at a given separation r will undergo generic simple precession (1b), as the other three cases are restricted to finely tuned (2a) or lower-dimensional (1a, 2b) portions of BBH parameter space. However, as the precession and nutation frequencies evolve during the inspiral, an order-unity fraction of binaries will pass through one or more nutational resonances for comparable mass ratios ($q \lesssim 1$) [238].

In this paper, we step back from current GW analyses and waveform models and attempt to identify those parameters that most naturally characterise the essential features of the more common simple precession.

Regular precession (1a) of $\vec{L}$ on a cone about $\vec{J}$ can be described by the *precession amplitude* $\theta_{\rm L}$ and the *precession frequency* $\Omega_{\rm L}$ which are constant on the precession timescale.

However, in the generic case (1b), nonzero nutation implies that the precession amplitude and frequency oscillate about their precession-averaged values $\langle\Omega_\mathrm{L}\rangle$ and $\langle\theta_\mathrm{L}\rangle$ with *nutation amplitude* $\Delta\theta_\mathrm{L}$ and *precession-frequency variation* $\Delta\Omega_\mathrm{L}$ at common *nutation frequency* ω. We stress that nutation is a generic feature of BBH spin dynamics and as such deserves further attention. Our five parameters provide a new framework to characterise configurations in which precession and nutation both significantly impact the dynamics and allow us to isolate and analyse their respective contributions. We expect each of these five parameters to imprint a distinct observational signature because of the dominant effect of the direction of $\vec{L}$ on the quadrupole waveform [232], but we leave the characterisation of these signatures and the signal-to-noise ratios needed to observe them to future work.

Our paper is structured as follows. Section 3.2 defines and details the five precession parameters we propose. Section 3.3 explores their behaviour using numerical PN evolutions. Section 3.4 summarises our findings and future prospects. Some details are postponed to Appendices A.1 and A.2. We use geometric units where $G = c = 1$.

3.2 Five precession parameters

3.2.1 Precession parameters

This formalism highlights five promising parameters to describe simple precession:

(1) The precession amplitude given by the average $\langle\theta_\mathrm{L}\rangle$ or median $\overline{\theta}_\mathrm{L} \equiv (\theta_{\mathrm{L}+}+\theta_{\mathrm{L}-})/2$.

(2) The precession frequency given by the average $\langle\Omega_L\rangle$ or median $\overline{\Omega}_\mathrm{L} \equiv (\Omega_{\mathrm{L}+} + \Omega_{\mathrm{L}-})/2$.

(3) The nutation amplitude $\Delta\theta_\mathrm{L} \equiv (\theta_{\mathrm{L}+} - \theta_{\mathrm{L}-})/2$.

(4) The nutation frequency $\omega \equiv 2\pi/\tau$.

(5) The precession-frequency variation $\Delta\Omega_{\rm L} \equiv (\Omega_{\rm L+} - \Omega_{\rm L-})/2$.

The nutation amplitude $\Delta\theta_{\rm L}$ and precession-frequency variation $\Delta\Omega_{\rm L}$ vanish for regular precession (1a); $\theta_{\rm L}$ and $\Omega_{\rm L}$ oscillate with the same nutation frequency ω because S is the only intrinsic parameter varying on the precession timescale.

3.2.2 Leading PN behaviour

We can develop intuition about our five precession parameters by calculating their values at leading PN order ($r/M \to \infty$). In this limit, 1.5PN spin-orbit coupling dominates over 2PN spin-spin coupling [224]. The individual spins $\vec{S}_{1,2}$ precess regularly on cones about the orbital angular momentum $\vec{L}$ with opening angles $\theta_{1\infty}$ and $\theta_{2\infty}$ and frequencies

$$\begin{aligned} \Omega_{1\infty} &= \frac{(4+3q)\eta}{2M}\left(\frac{r}{M}\right)^{-5/2} , \qquad (3.1)\\ \Omega_{2\infty} &= \frac{(4+3/q)\eta}{2M}\left(\frac{r}{M}\right)^{-5/2} . \qquad (3.2)\end{aligned}$$

Defining $\vec{X}_\perp$ as the component of vector $\vec{X}$ perpendicular to the total angular momentum $\vec{J}$, the precession amplitude $\langle\theta_{\rm L}\rangle$ in the limit $r/M \to \infty$ is

$$\begin{aligned} \langle\theta_{\rm L}\rangle_\infty &= \frac{\langle S_\perp\rangle}{L} \\ &= \left\{\left[\left(\frac{\chi_1 \sin\theta_{1\infty}}{q}\right)^2 + (q\chi_2\sin\theta_{2\infty})^2\right]\frac{M}{r}\right\}^{1/2} . \qquad (3.3)\end{aligned}$$

The precession frequency $\langle \Omega_{\rm L} \rangle$ is bimodal in the limit $r/M \to \infty$ and given by

$$\langle \Omega_L \rangle_\infty = \begin{cases} \Omega_{1\infty} & \text{if} \quad S_{1\perp} > S_{2\perp}\,, \\ \Omega_{2\infty} & \text{if} \quad S_{1\perp} < S_{2\perp}\,. \end{cases} \tag{3.4}$$

This result, expressed in a different notation, was first presented in Eqs. (46) and (47) of Ref. [238]. For a population of BBHs with given values of q, χ_1, χ_2 and isotropic spin directions, the fraction of sources with $S_{1\perp} < S_{2\perp}$ is given by [238]:

$$f_< = \begin{cases} \dfrac{|\chi_1^2 - q^4\chi_2^2|}{4q^2\chi_1\chi_2}(\sinh H_C - H_C) & \text{if} \quad S_1 > S_2, \\ \dfrac{|\chi_1^2 - q^4\chi_2^2|}{4q^2\chi_1\chi_2}(\sinh H_S + H_S) & \text{if} \quad S_1 < S_2, \end{cases} \tag{3.5}$$

where

$$H_C = 2\cosh^{-1}\left(\frac{\chi_1}{|\chi_1^2 - q^4\chi_2^2|^{1/2}}\right)\,, \tag{3.6}$$

$$H_S = 2\sinh^{-1}\left(\frac{\chi_1}{|\chi_1^2 - q^4\chi_2^2|^{1/2}}\right)\,. \tag{3.7}$$

The nutation amplitude $\Delta\theta_{\rm L}$ in the limit $r/M \to \infty$ is similarly bimodal and given by

$$\begin{aligned} \Delta\theta_{\rm L\infty} &= \frac{1}{2L}(S_{1\perp} + S_{2\perp} - |S_{1\perp} - S_{2\perp}|) \\ &= \begin{cases} q\chi_2 \sin\theta_{2\infty}\left(\dfrac{M}{r}\right)^{1/2} & \text{if} \quad S_{1\perp} > S_{2\perp}\,, \\ \dfrac{\chi_1}{q}\sin\theta_{1\infty}\left(\dfrac{M}{r}\right)^{1/2} & \text{if} \quad S_{1\perp} < S_{2\perp}\,. \end{cases} \end{aligned} \tag{3.8}$$

The nutation frequency ω in the limit $r/M \to \infty$ is

$$\omega_\infty = \Omega_{2\infty} - \Omega_{1\infty} = \frac{3}{2M}\left(\frac{1-q}{1+q}\right)\left(\frac{r}{M}\right)^{-5/2}, \tag{3.9}$$

which is independent of the BBH spins and vanishes in the equal-mass limit $q \to 1$, consistent with the constancy of S in this limit even at 2PN order [244]. This implies that θ_L and Ω_L are also constant and that Eqs. (3.3), (3.8), and (3.10) are invalid in the precisely equal-mass limit.

The precession frequency $\Omega_{\mathrm{L}\pm}$ at $S = S_\pm$ in the limit $r/M \to \infty$ is

$$\Omega_{\mathrm{L}\pm\infty} = \frac{\chi_1 \sin\theta_{1\infty}\Omega_{1\infty} \pm q^2\chi_2 \sin\theta_{2\infty}\Omega_{2\infty}}{\chi_1 \sin\theta_{1\infty} \pm q^2\chi_2 \sin\theta_{2\infty}}, \tag{3.10}$$

implying that the precession-frequency variation $\Delta\Omega_\mathrm{L}$ in the limit $r/M \to \infty$ is

$$\begin{aligned}\Delta\Omega_{\mathrm{L}\infty} &= \frac{1}{2}(\Omega_{\mathrm{L}+\infty} - \Omega_{\mathrm{L}-\infty}) \\ &= \frac{q^2\chi_1 \sin\theta_{1\infty}\chi_2 \sin\theta_{2\infty}}{\chi_1^2 \sin^2\theta_{1\infty} - q^4\chi_2^2 \sin^2\theta_{2\infty}}\omega_\infty\,. \end{aligned} \tag{3.11}$$

3.3 Numerical evolutions

We now explore the evolution and distribution of our five precession parameters. Numerical integrations are performed with the PRECESSION code [204], which implements 2PN spin-precession equations [207] and 1.5 PN precession-averaged radiation reaction [201, 202]. Sources are evolved from their asymptotic conditions at $r/M \to \infty$ down to $r = 10M$, taken as the threshold for the breakdown of the PN approximation.

3.3.1 Individual sources

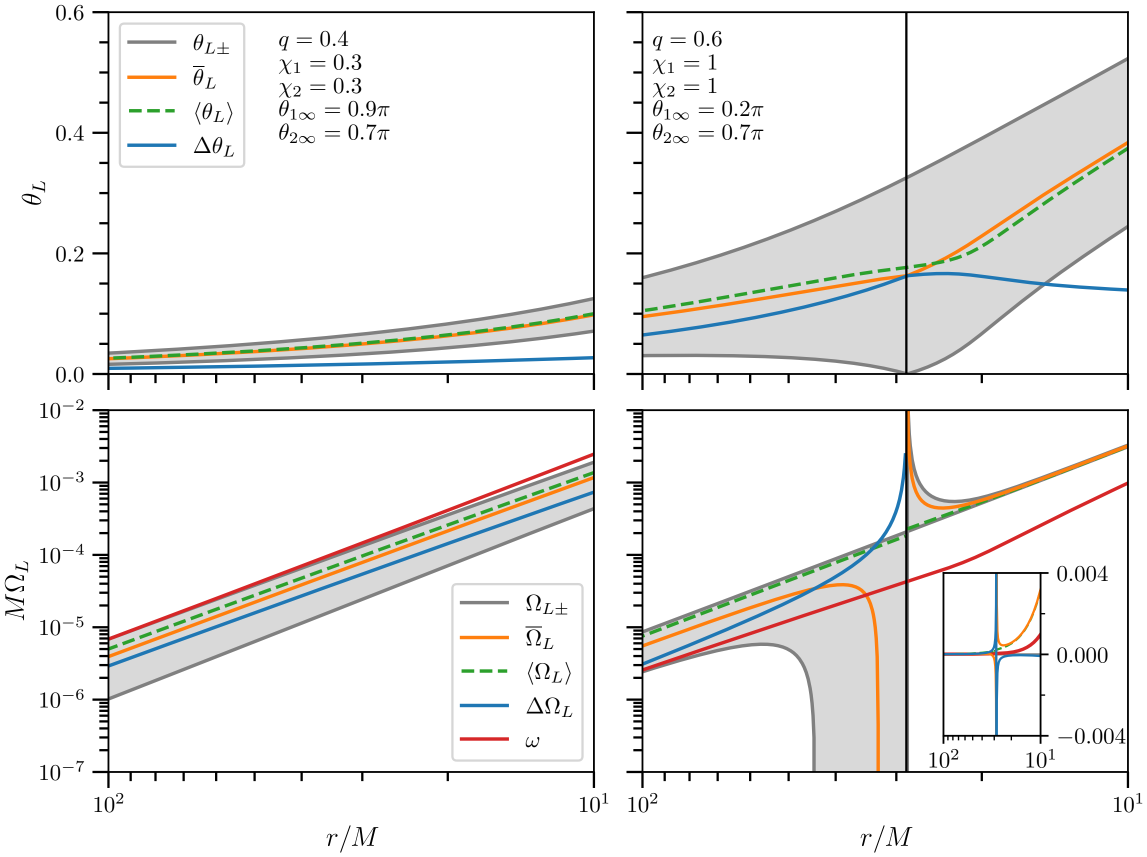

Figure 3.3: Evolution of our five precession parameters for two representative inspirals. These are the precession amplitude $\langle\theta_\mathrm{L}\rangle$ (dashed green, top), the nutation amplitude $\Delta\theta_\mathrm{L}$ (solid blue; top), the precession frequency $\langle\Omega_\mathrm{L}\rangle$ (dashed green, bottom), the precession-frequency variation $\Delta\Omega_\mathrm{L}$ (solid blue, bottom), and the nutation frequency ω (solid red, bottom). We also show the medians $\overline{\theta}_\mathrm{L}$ and $\overline{\Omega}_\mathrm{L}$ (solid orange), as well as the allowed ranges $\theta_{\mathrm{L}\pm}$ and $\Omega_{\mathrm{L}\pm}$ (gray curves and shaded areas). The two binaries shown in this figure are characterised by the values of $q, \chi_1, \chi_2, \theta_{1\infty}$, and $\theta_{2\infty}$ listed in the top panels. The right (left) panels depict a case where $\sin\theta_L$ does (not) reach 0 at some point during the inspiral. This condition is marked by a vertical black line ($r \approx 27M$ for the binary on the right).

Figure 3.3 displays two representative cases for the evolution of our five parameters as functions of the separation r. The key difference between these two systems is whether $\vec{J}$ and $\vec{L}$ align at some point during the inspiral. Because the function $\theta_{\rm L}(S)$ given by Eq. (2.9) is monotonic, the condition $\sin\theta_{\rm L}(S) = 0$ can only be satisfied if either $S_- = |J-L|$ or $S_+ = J+L$, which correspond to $\theta_{\rm L-} = 0$ and $\theta_{\rm L+} = \pi$, respectively [238]. Appendix A.1 shows our proof that these two conditions cannot be satisfied simultaneously, i.e. maximal nutations $\Delta\theta_{\rm L} = \pi$ are forbidden. This is unlike nutations of $\vec{S}_1$ and $\vec{S}_1$ which can have maximal amplitude π during a single period τ [237]. The left panels of Fig. 3.3 show a binary for which $\theta_{\rm L}$ never reaches 0 or π.

The average precession and nutation amplitudes $\langle\theta_{\rm L}\rangle$ and $\Delta\theta_{\rm L}$ are approximately proportional to $(r/M)^{-1/2}$ as suggested by the leading-order behaviour given by Eqs. (3.3) and (3.8), while the three frequencies $\langle\Omega_{\rm L}\rangle$, ω, and $\Delta\Omega_{\rm L}$ are nearly proportional to $(r/M)^{-5/2}$ consistent with the leading-order behaviour given by Eqs. (3.4) and (3.9), and (3.11). The two precession averages $\langle\theta_{\rm L}\rangle$ and $\langle\Omega_{\rm L}\rangle$ are well approximated by the median values $\overline{\theta}_{\rm L}$ and $\overline{\Omega}_{\rm L}$, as one would expect at small nutation amplitude $\Delta\theta_{\rm L}$ where the oscillations are nearly sinusoidal.

The evolution of our five precession parameters is somewhat more complex if $\vec{L}$ and $\vec{J}$ reach co-alignment at some point during the inspiral. The right panels of Fig. 3.3 show an example of such a binary where a cusp-like minimum $\theta_{\rm L-} = 0$ and a corresponding cusp-like local maximum in the nutation amplitude $\Delta\theta_{\rm L}$ occur at $r \approx 27M$. If $\boldsymbol{\Omega}$ is the precession vector, i.e. $d\vec{L}/dt = \boldsymbol{\Omega} \times \vec{L}$, then the precession frequency of Eq. (2.8) is

$$\Omega_{\rm L} = \frac{d\vec{L}}{dt} \cdot \frac{\hat{\vec{J}} \times \hat{\vec{L}}_\perp}{L_\perp} = \boldsymbol{\Omega} \cdot (\hat{\vec{J}} - \hat{\vec{L}}_\perp \cot\theta_{\rm L})\,. \tag{3.12}$$

In Appendix A.2, we show that $\boldsymbol{\Omega} \cdot \hat{\vec{L}}_\perp \neq 0$ for misaligned spins, implying that the second term in Eq. (3.12) diverges and thus $\Omega_{\rm L-}$ approaches $\pm\infty$ as $\theta_{\rm L-}$ approaches zero (or $\theta_{\rm L+}$ approaches π) during the inspiral. As $\vec{L}$ passes through alignment with

$\vec{J}$, $\hat{\vec{L}}_\perp \to -\hat{\vec{L}}_\perp$ and $\Omega_{\rm L-}$ goes to $\mp\infty$ according to Eq. (3.12). This can be seen in the bottom right panel of Fig. 3.3, where $\Omega_{\rm L-}$ jumps from $-\infty$ to $+\infty$ as the binary inspirals through $r \approx 27M$ at which $\theta_{\rm L-} = 0$.

The precession-frequency variation $\Delta\Omega_L$ correspondingly jumps from $+\infty$ to $-\infty$. Integrating Eq. (3.12) with respect to time, we find that this discontinuity causes the precession angle per nutation period $\alpha \equiv \int_0^\tau \Omega_{\rm L}\, dt$ to jump by $\Delta\alpha = \pm 2\pi$ and the average precession frequency $\langle\Omega_{\rm L}\rangle = \alpha/\tau$ to jump by $\Delta\langle\Omega_{\rm L}\rangle = \pm\omega$ as explored by Zhao *et al.* (2017) [238]. Careful examination of the dashed green curve in the bottom right panel of Fig. 3.3 reveals this discontinuity in $\langle\Omega_{\rm L}\rangle$ at the vertical black line. Numerical exploration did not reveal binaries with two or more of such $\vec{L} \parallel \vec{J}$ crossings.

3.3.2 Parameter-space exploration

The dependence of the five precession parameters at $r = 10M$ on the mass ratio q is shown in Fig. 3.4 for three values of the spin magnitudes $\chi_1 = \chi_2 = 1,\ 0.5$, and 0.1. The binaries for which the nutation amplitude $\Delta\theta_{\rm L}$ is largest have high spins but moderate mass ratio $q \sim 0.6$. This counterintuitive result constitutes one of the key findings of this paper. Two-spin effects are, naively, maximised for comparable-mass sources $q \lesssim 1$ because the secondary's spin S_2 vanishes for $q \to 0$. This is *not* the case for nutations. The magnitude S becomes a constant of motion in both the $q \to 0$ and the $q \to 1$ limits, which implies $\Delta\theta_{\rm L} = \Delta\Omega_{\rm L} = 0$. Nutation effects are set by the variation of S and are more prominent for binaries with moderate mass ratios.

As expected, large values of $\Delta\theta_{\rm L}$ are more likely for high χ_1 and χ_2, because large spins can induce greater misalignments between the total and orbital angular momenta (i.e. $\vec{J} - \vec{L} = \vec{S}_1 + \vec{S}_2$). Figure 3.4 also shows that the maximum value of $\Delta\theta_{\rm L}$ occurs at smaller q if $\chi_1 = \chi_2$ increases. This can be understood in terms of the spin-

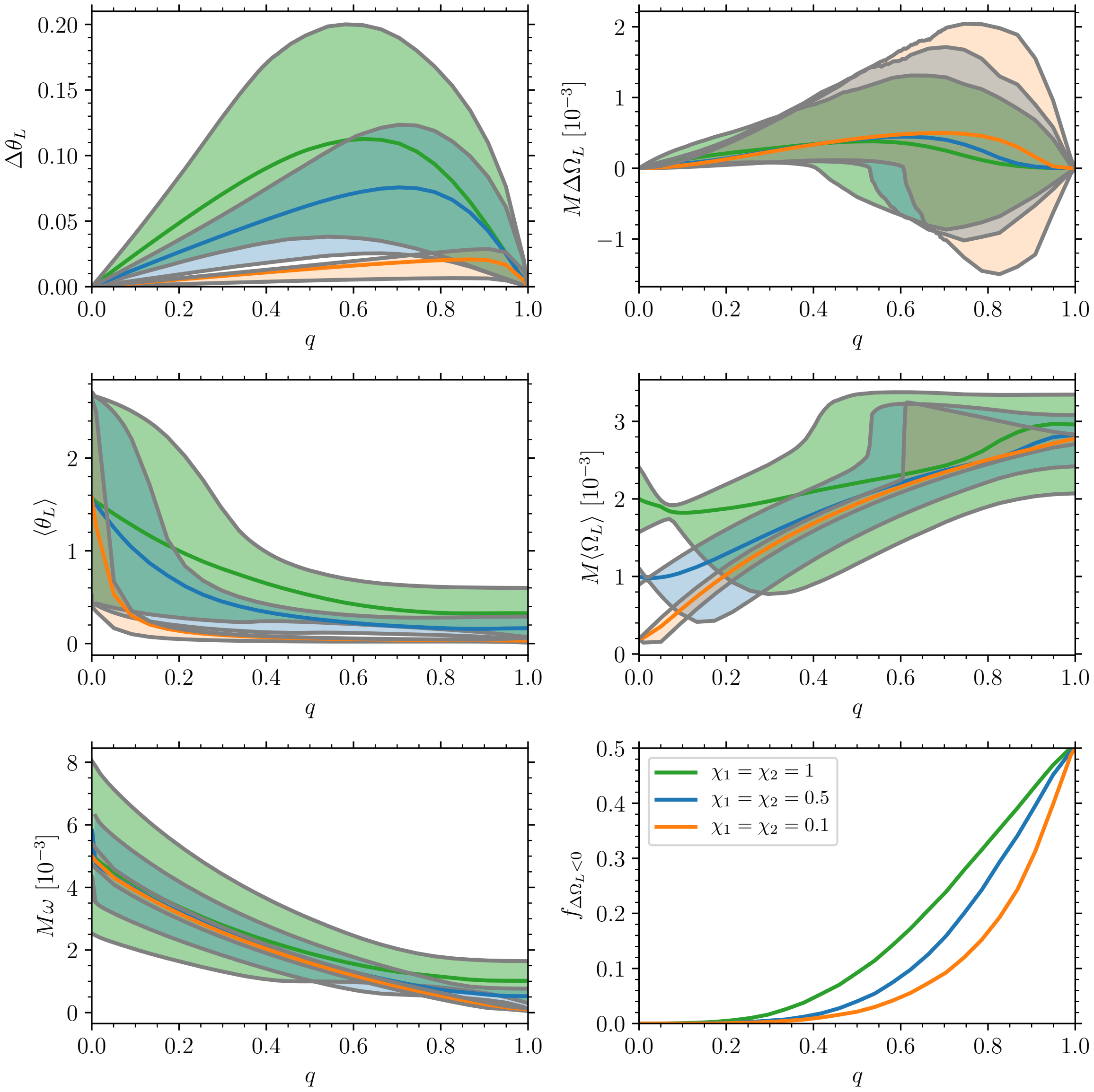

Figure 3.4: Distributions of the precession parameters $\Delta\theta_{\rm L}$ (top left), $\langle\theta_{\rm L}\rangle$ (middle left), ω (bottom left), $\Delta\Omega_{\rm L}$ (top right), and $\langle\Omega_{\rm L}\rangle$ (middle right) as functions of the mass ratio q for isotropic distributions of spin directions at $r = 10M$. The solid orange, blue, and green lines show the median values for spin magnitudes $\chi_1 = \chi_2 = 0.1,\ 0.5$, and 1, while the shaded areas indicate the 90% interval of each distribution. The bottom right panel shows the fraction of binaries with $\Delta\Omega_{\rm L} < 0$ for the same BBHs.

precession morphologies explored in depth in Refs. [201, 202]. Nutation is larger in the circulating morphology than the two librating morphologies in which the spins merely oscillate about the spin-orbit resonances (case 1a.iii of regular precession in our taxonomy detailed in Sec. 3.1). To maximise the nutation amplitude $\Delta\theta_{\mathrm{L}}$ at higher χ_i, the mass ratio q must decrease to suppress spin-spin coupling and maintain a large fraction of binaries in the circulating morphology.

The precession-frequency variation $\Delta\Omega_{\mathrm{L}}$ also reaches its largest values at moderate mass ratios. However, unlike for the nutation amplitude $\Delta\theta_{\mathrm{L}}$, smaller spins produce larger variations $\Delta\Omega_{\mathrm{L}}$. Comparing the leading PN behaviour given by Eqs. (3.8) and (3.11), we see that $\Delta\theta_{\mathrm{L}\infty}$ is linear in the spin magnitudes, while $\Delta\Omega_{\mathrm{L}\infty}$ only depends on their ratio χ_2/χ_1. This ratio is unity for all three spin distributions in Fig. 3.4, but the weaker spin-spin coupling for smaller χ_i again implies a higher fraction of binaries in the circulating morphology and thus larger variations $\Delta\Omega_{\mathrm{L}}$. The sharp decreases in the lower boundaries of the shaded regions (the 5th percentile of each distribution) approximately occur at the values of q at which the fraction of binaries with $\Delta\Omega_{\mathrm{L}} < 0$ reaches 0.05 ($f_{\Delta\Omega_{\mathrm{L}}<0} = 0.05$ in the bottom right panel of Fig. 3.4). In the limit that spin-spin coupling is suppressed, this occurs at $q \simeq 0.62$ where $f_< = 0.05$ according to Eq. (3.5).

This fraction $f_{\Delta\Omega_{\mathrm{L}}<0}$ increases with q for $\chi_1 = \chi_2$, consistent with the leading PN behaviour given by Eq (3.11). This equation also shows that in the equal-mass limit $q \to 1$, $\Delta\Omega_{\mathrm{L}\infty}$ is equally likely to be positive or negative, consistent with our numerical result that $f_{\Delta\Omega_{\mathrm{L}}<0} \to 0.5$ in this limit.

The fraction $f_{\Delta\Omega_{\mathrm{L}}<0}$ is not necessarily maximised at $q = 1$ for $\chi_1 \neq \chi_2$. For example, we find that $f_{\Delta\Omega_{\mathrm{L}}<0}$ reaches a maximum of ~ 0.95 at $q \simeq 0.65$ for $\chi_1 = 0.1$ and $\chi_2 = 1$.

The precession amplitude $\langle\theta_{\mathrm{L}}\rangle$ shown in the middle left panel of Fig. 3.4 decreases monotonically with q and increases monotonically with χ_i. In the extreme mass-ratio limit $q \to 0$, $\vec{L} \to 0$ and $\vec{S} \to \vec{S}_1$, implying that $\langle\theta_{\rm L}\rangle \to \pi/2$ for isotropic spin distributions.

As q increases, the two spins can more effectively cancel each other in the vector sum $\vec{S} = \vec{S}_1 + \vec{S}_2$ leading to smaller precession amplitudes $\theta_{\rm L}$ by Eq. (2.9). Larger spin magnitudes lead to larger precession amplitudes both geometrically by Eq. (2.9) and because enhanced spin-spin coupling increases the fraction of binaries in the precession morphology in which the components of the spins in the orbital plane librate about alignment and thus add constructively.

The average precession frequency $\langle\Omega_{\rm L}\rangle$ is shown in the middle right panel of Fig. 3.4. In the extreme mass-ratio limit $q \to 0$, $\vec{J} \to \vec{S}_1$ and therefore $\Omega_{\rm L} \propto \chi_1$ according to Eq. (2.8). The larger scatter in the distributions for larger spins in this limit follows from the dependence of $\Omega_{\rm L}$ on the projected effective spin $\chi_{\rm eff}$ in this equation which spans a larger range $-\chi_1 \le \chi_{\rm eff} \le +\chi_1$ for higher spins. As q increases, $\langle\Omega_{\rm L}\rangle$ generally increases as well, particularly for small spins where the leading PN approximation of Eq. (3.4) is more accurate. For larger spins, two effects compete at small mass ratios which determine the available $\Omega_{\rm L}$ values: $\Omega_{\rm L} \propto \chi_1$ and $\Omega_{\rm L} \propto -\chi_{\rm eff}$. This creates a 'bottleneck' feature in Fig. 3.4 for the large spin distributions in the ranges of $\Omega_{\rm L}$. The sharp increases in the upper boundaries of the shaded regions (the 95th percentile of each distribution) are essentially the mirror image of the similar features in the lower boundaries of the $\Delta\Omega_{\rm L}$ distributions in the top right panel. This follows from the definitions of these parameters: $\Delta\Omega_{\rm L} \equiv (\Omega_{\rm L+} - \Omega_{\rm L-})/2$ and $\langle\Omega_{\rm L}\rangle \approx \overline{\Omega}_{\rm L} \equiv (\Omega_{\rm L+} + \Omega_{\rm L-})/2$.

The nutation frequency ω decreases monotonically with q, consistent with the factor of $(1-q)/(1+q)$ in Eqs. (2.5) and (3.9). Its median value is largely independent of the spin magnitude, also consistent with Eqs. (2.6) and (3.9). The widths of the ω distributions are roughly proportional to χ_i, which follows from the term proportional to $\chi_{\rm eff}$ in Eq. (2.5), similar to the scatter in $\langle\Omega_{\rm L}\rangle$ in the extreme mass-ratio limit.

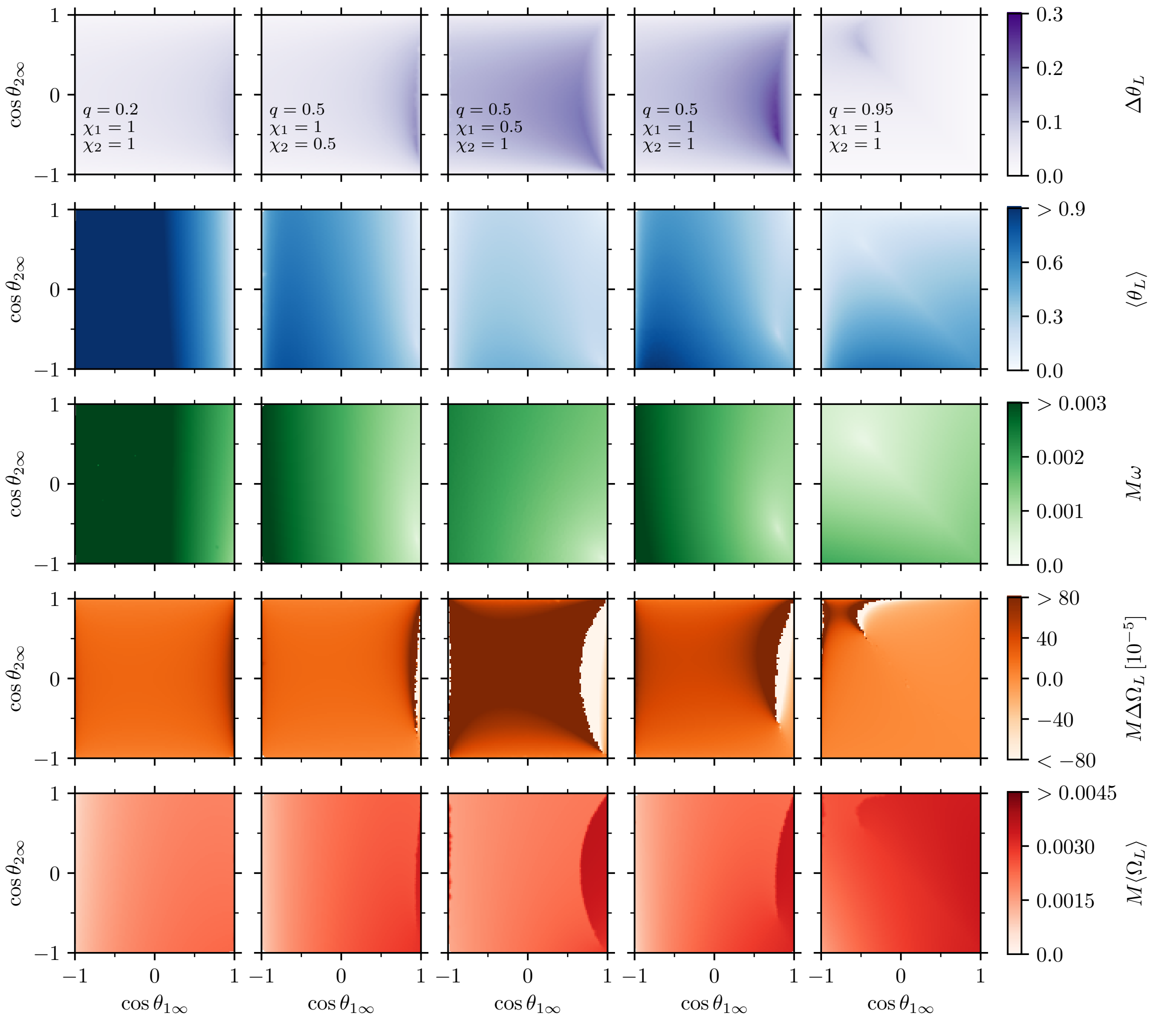

Figure 3.5: Precession parameters $\Delta\theta_{\rm L}$, $\langle\theta_{\rm L}\rangle$, ω, $\Delta\Omega_{\rm L}$, and $\langle\theta_{\rm L}\rangle$ (top to bottom) at $r = 10M$ as a function of the asymptotic spin misalignment angles $\theta_{1\infty}$ and $\theta_{2\infty}$. Each column corresponds to a set of values of mass ratio q and spin magnitudes χ_i. For visualisation purposes, the shading saturates above and below the thresholds indicated in the colour bars.

In Fig. 3.5, we explore how our five precession parameters at $r = 10M$ depend on spin orientation for five choices of mass ratio q and spin magnitudes χ_1 and χ_2. We parametrise the spin orientations by the cosines of the misalignment angles $\cos\theta_{1\infty}$ and $\cos\theta_{2\infty}$ in the limit $r \to \infty$; these parameters fully determine J and $\chi_{\rm eff}$ at all separations as discussed in Ref. [202] and can thus be used to calculate the precession parameters as described in Sec. 3.2. Isotropic spin distributions remain isotropic as they inspiral [248] and are thus specified by flat distributions of $\cos\theta_{1\infty}$ and $\cos\theta_{2\infty}$.

The top row of Fig. 3.5 shows the nutation amplitude $\Delta\theta_{\rm L}$. The boundaries of the plane $(\cos\theta_{1\infty} = \pm 1, \cos\theta_{2\infty} = \pm 1)$ correspond to the spin-orbit resonances [239] that undergo regular precession for which $\Delta\theta_{\rm L} = 0$ (case 1a.iii of our taxonomy). The nutation amplitude increases as one moves inwards from the boundaries and is largest for the three distributions with $q = 0.5$, consistent with Fig. 3.4. All three of these distributions possess distinct crests of large $\Delta\theta_{\rm L}$ that extend from near the bottom right corner of each plot to the top right corner. A line tracing along this crest corresponds to the set of binaries with $\theta_{\rm L-} = 0$ at $r = 10M$; by minimising $\theta_{\rm L-}$, these binaries naturally have large values of the nutation amplitude $\Delta\theta_{\rm L} \equiv (\theta_{\rm L+} - \theta_{\rm L-})/2$ (corresponding to the local maximum of the solid blue curve in the top right panel of Fig. 3.3). We address the consequences of the condition $\vec{J} \parallel \vec{L}$ in greater detail in Sec. 3.3.3.

The second row of Fig. 3.5 shows the precession amplitude $\langle\theta_{\rm L}\rangle$. These plots appear anti-correlated with those in the first row, a consequence of the contribution of $\theta_{\rm L-}$ to these parameters: $\Delta\theta_{\rm L} \equiv (\theta_{\rm L+} - \theta_{\rm L-})/2$ and $\langle\theta_{\rm L}\rangle \approx \overline{\theta}_{\rm L} \equiv (\theta_{\rm L+} + \theta_{\rm L-})/2$. The alternating constructive and destructive addition in the vector sum $\vec{S} = \vec{S}_1 + \vec{S}_2$ that maximises $\Delta\theta_{\rm L}$ suppresses the precession-averaged $\langle\theta_{\rm L}\rangle$.

The precession frequency ω shown in the third row of Fig. 3.5 has the weakest dependence on spin orientation, consistent with the spin-independent leading-order PN result of Eq. (3.9). The higher-order dependence on spin orientation can be largely explained through the term proportional to $\chi_{\rm eff}$ in Eq. (2.5). Another feature of these plots, also apparent in the second row, is the weak dependence on $\cos\theta_{2\infty}$ for small mass ratio q or $\chi_2 \ll \chi_1$.

The fourth and fifth rows of Fig. 3.5 shows the precession-frequency variation $\Delta\Omega_{\rm L}$ and the average precession frequency $\langle\Omega_{\rm L}\rangle$. Both are correlated with the nutation amplitude $\Delta\theta_{\rm L}$ shown in the top row because of the features associated with the set of binaries with $\vec{J} \parallel \vec{L}$ at $r = 10M$.

3.3.3 Role of the $\vec{J} \parallel \vec{L}$ condition and the up-down configuration

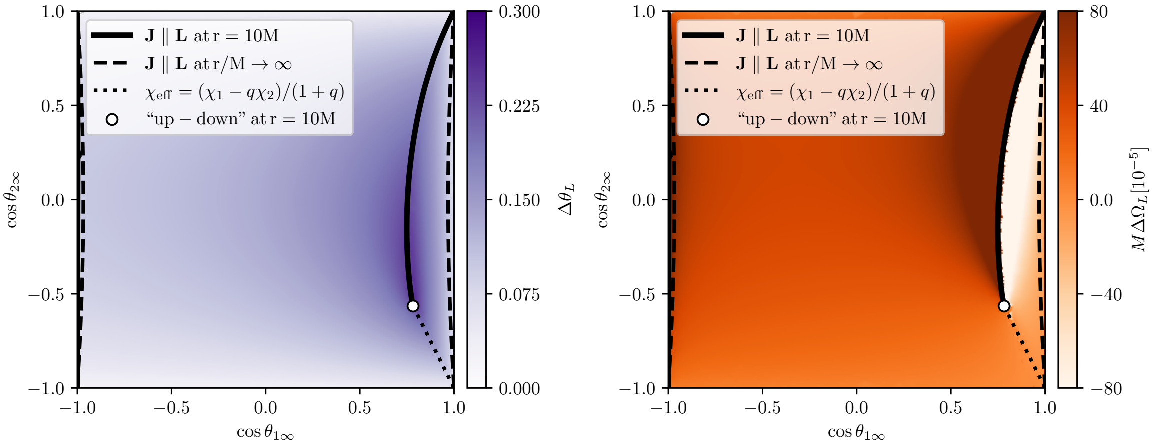

Figure 3.6: The nutation amplitude $\Delta\theta_{\rm L}$ and precession-frequency variation $\Delta\Omega_{\rm L}$ at $r = 10M$ as functions of the cosines of the asymptotic misalignment angles $\cos\theta_{1\infty}$ and $\cos\theta_{2\infty}$ for $q = 0.5$ and $\chi_1 = \chi_2 = 1$. The solid (dashed) black lines depict the asymptotic origin of binaries which are found with $\vec{J} \parallel \vec{L}$ at $r = 10M$ ($r/M \to \infty$). Binaries that precess through the unstable “up-down” configuration (i.e. $\cos\theta_1 = -\cos\theta_2 = 1$) are located on the dotted black line, with the binary in this configuration at $r = r_{ud+}$ ($r = 10M$) in the bottom-right corner (white circle).

Figure 3.6 shows enlarged versions of the first and fourth rows of the fourth column of Fig. 3.5.

The dashed lines show binaries for which $\theta_{\rm L-} = 0$ ($\vec{J} \parallel \vec{L}$) as $r/M \to \infty$. This condition can be expressed analytically by the hyperbola $\chi_1 \sin\theta_{1\infty} = q^2\chi_2 \sin\theta_{2\infty}$. The solid lines show binaries for which $\theta_{\rm L-} = 0$ ($\vec{J} \parallel \vec{L}$) at $r = 10M$.

These lines were determined by setting $\chi_1 \sin\theta_1 = q^2\chi_2 \sin\theta_2$, $\Delta\Phi_{12} = \pi$ at $r = 10M$, then integrating the precession-averaged radiation reaction backwards in time to determine the asymptotic misalignment angles $\theta_{i\infty}$. It is fascinating how the gravitational inspiral (in reverse) breaks the symmetry of this analytic condition.

We denote binaries as being in the "up/down-up/down" configuration if the primary-secondary spin is aligned ("up") or anti-aligned ("down") with the orbital angular momentum $\vec{L}$. The "up-up," "down-up," and "down-down" configurations remain stable throughout the inspiral and can therefore be found at the top right, top left, and bottom left corners, respectively, of the ($\cos\theta_{1\infty} - \cos\theta_{2\infty}$) plane. However, for the parameter choices in Figs. 3.5 and 3.6, the "up-down" configuration becomes unstable during the inspiral [221, 241–243]. The binary in the "up-down" configuration at $S = S_-$ at $r = 10M$ can instead be found on the conserved dotted line in Fig. 3.6,

$$(1+q)\chi_{\rm eff} = \chi_1 \cos\theta_{1\infty} + q\chi_2 \cos\theta_{2\infty} = \chi_1 - q\chi_2 \ , \tag{3.13}$$

at the point denoted by the empty circle.

At this point, the "up-down" configuration is an unstable equilibrium point on the precession time scale implying $\langle\theta_{\rm L}\rangle \to 0$ and $\omega \to 0$; this can seen by the white shading at the location of the empty circle in the second and third rows of the fourth column of Fig. 3.5. The set of binaries with $\vec{J} \parallel \vec{L}$ and $\cos\theta_1 > 0$ at $S = S_-$ and $r = 10M$ is marked by the solid black curve connecting the unstable "up-down" configuration (empty circle) to the stable "up-up" configuration in the top right corner.

The asymmetric inspiral also has the effect of driving binaries with $\vec{J} \parallel \vec{L}$ and

q	χ_1	χ_2	$f_{\vec{J}\|\vec{L}}$
0.2	1	1	0.02
0.5	1	0.5	0.06
0.5	0.5	1	0.16
0.5	1	1	0.15
0.95	1	1	0.40

Table 3.1: The fraction of binaries for which $\vec{J} \parallel \vec{L}$ at some separation $r > 10M$ during the inspiral for BBHs with the same mass ratio q and spin magnitudes $\chi_{1,2}$ as those in Fig. 3.5.

$\cos\theta_1 < 0$ at $S = S_-$ at $r = 10M$ into near complete anti-alignment of the primary spin ($\cos\theta_{1\infty} \simeq -1$) at $r \to \infty$. This makes the second black curve connecting the "down-up" and "down-down" configurations nearly indistinguishable from the left edge of the plots (the divergence in $\Delta\Omega_{\rm L}$ is slightly more pronounced in the third and fifth columns of Fig. 3.5).

As they inspiral through $r = 10M$, all of the binaries on both of these curves experience:

(1) a local maximum in the nutation amplitude $\Delta\theta_{\rm L}$,

(2) a divergence in the precession-frequency variation $\Delta\Omega_{\rm L}$, and

(3) a jump in the average precession frequency $\langle\Omega_{\rm L}\rangle$ by $\pm\omega$.

These features, seen in the first, fourth, and fifth rows of Fig. 3.5, are the same as those that occur at $r \approx 27M$ for the binary in the right panels of Fig. 3.3. The numerical results presented in this paper suggest that, when unstable, the "up-down" configuration maximises the nutation amplitude $\Delta\theta_{\rm L}$ as a function of spin orientation.

BBHs with isotropic spins are uniformly distributed in the ($\cos\theta_{1\infty} - \cos\theta_{2\infty}$) plane. As shown in Fig. 3.6, the set of binaries with $\vec{J} \parallel \vec{L}$ is denoted by two curves within this plane that evolve with binary separation from the dashed lines at $r/M \to \infty$ to the solid lines at $r = 10M$. The fraction of an isotropic population of binaries that pass through such a configuration during the inspiral (and thus experience the three phenomena listed by bullet points in the previous paragraph) is therefore given by the fraction of the area of the $(\cos\theta_{1\infty} - \cos\theta_{2\infty})$ plane bounded by the solid, dashed, and dotted lines in Fig. 3.6. This fraction is given in Table 3.1 for each of the parameter choices corresponding to the five columns in Fig. 3.5. Its increase with mass ratio q can be explained by the following argument. The binary separation [241, 243]

$$\frac{r_{\mathrm{ud}+}}{M} = \frac{\left(\sqrt{\chi_1} + \sqrt{q\chi_2}\right)^4}{(1-q)^2} \tag{3.14}$$

at which the "up-down" configuration becomes unstable increases with mass ratio q, as does the slope of the line of constant χ_{eff} given by Eq. (3.13). This implies that the solid curve in Fig. 3.6 with the white circle (denoting the "up-down" configuration at $r = 10M$) as one of its endpoints can migrate further up and to the left, sweeping out more area in the $(\cos\theta_{1\infty} - \cos\theta_{2\infty})$ plane and thus encompassing a higher fraction of binaries. This is most noticeable in the fourth row, fifth column of Fig. 3.5, where the endpoint of the curve marking divergences in $\Delta\Omega_{\mathrm{L}}$ has nearly reached the top left corner of the plane.

3.3.4 Correlations

Fig. 3.7 shows the marginalised 1D and 2D probability distribution functions (PDFs) for our five precession parameters at $r = 10M$ for a population of BBHs with $q = 0.5$, $\chi_1 = \chi_2 = 1$, and isotropic spins. The 1D PDFs of the average precession amplitude $\langle\theta_{\mathrm{L}}\rangle$ and precession frequency $\langle\Omega_{\mathrm{L}}\rangle$ exhibit distinct bimodality, with subdominant peaks

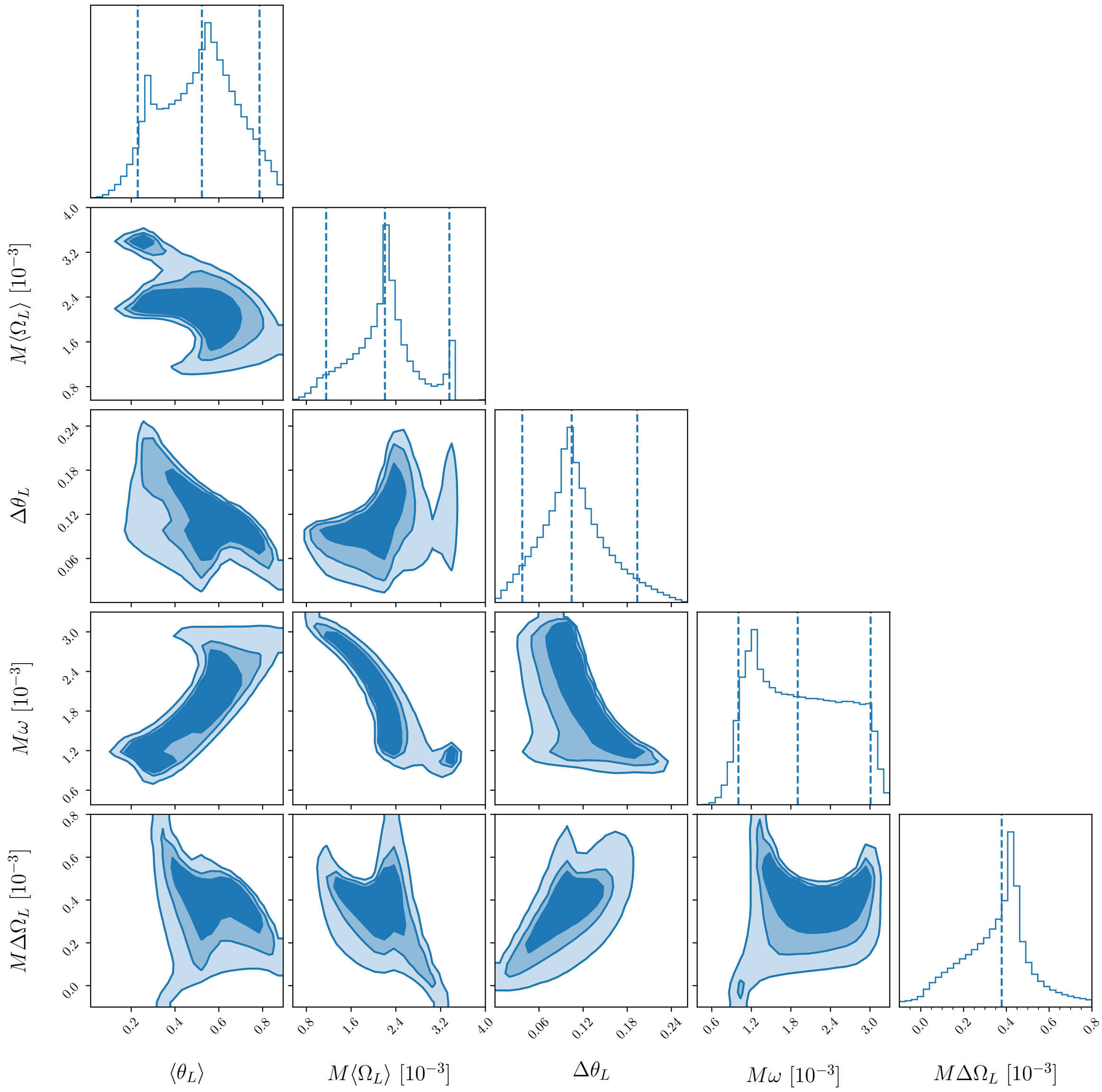

Figure 3.7: Correlations between the five precession parameters assuming a set of BBHs with $q = 0.5$, $\chi_1 = \chi_2 = 1$, $r = 10M$, and isotropic spins. 2D contour levels encompass 50%, 70%, and 90% of the BBHs. Medians and 90% intervals of the marginalised distributions are indicated with vertical dashed lines. Long tails in the $M\Delta\Omega_L$ distribution have been excluded for clarity.

near the 5th percentile of $\langle\theta_\mathrm{L}\rangle$ and the 95th percentile of $\langle\Omega_\mathrm{L}\rangle$. A comparison with the second and fifth rows of the fourth column of Fig. 3.5 reveals that this subpopulation is the $\approx 15\%$ of binaries that have passed through alignment of the orbital and total angular momentum ($\vec{J} \parallel \vec{L}$) during the inspiral. The jump in $\langle\Omega_{\rm L}\rangle$ by the nutation frequency ω as these binaries pass through this alignment is the primary factor that sets this subpopulation apart from the rest of the distribution. The 2D PDFs of $\langle\Omega_{\rm L}\rangle$ with the other three precession parameters reveals that this subpopulation disproportionately contributes to the high $\Delta\theta_{\rm L}$ and low ω tails (like the unstable "up-down" configuration which belongs to the subpopulation). It dominates the negative $\Delta\Omega_{\rm L}$ tail, consistent with the behaviour seen in the bottom right panel of Fig. 3.6.

The main BBH population (those $\approx 85\%$ of binaries that never have $\vec{J} \parallel \vec{L}$ during the inspiral) exhibits many of the correlations previously noted in the discussion of Fig. 3.5. There is a positive correlation between $\Delta\theta_{\rm L}$ and $\Delta\Omega_{\rm L}$, since both increase as the amount of nutation increases. Both of these quantities are anti-correlated with the precession amplitude $\langle\theta_{\rm L}\rangle$, as nutation causes the spins to cancel out in the precession average rather than coherently contribute to misalignment between $\vec{J}$ and $\vec{L}$. The nutation frequency ω is anti-correlated with $\chi_{\rm eff}$ according to Eq. (2.5), implying that it is anti-correlated with J for our isotropic spin distributions. It is thus correlated with $\langle\theta_{\rm L}\rangle$ according to Eq. (2.9) and anti-correlated with $\langle\Omega_{\rm L}\rangle$ according to Eq. (2.8). We also note that the nutation amplitude $\Delta\theta_{\rm L}$ is anti-correlated with the nutation frequency ω and correlated with the average precession frequency $\langle\Omega_{\rm L}\rangle$. This is primarily driven by the binaries near the solid curve in Fig. 3.6 that have not quite reached $\vec{J} \parallel \vec{L}$ by $r = 10M$. Like the unstable "up-down" configuration, such binaries have long nutation periods (small ω) during most of which $\Omega_{\rm L}$ is large because of the smallness of the factor $[(L+S)^2 - J^2]$ in the denominator of Eq. (2.8).

3.4 Conclusions

Spin precession is a prominent feature of the relativistic dynamics of BBHs and a key signature of their astrophysical formation channel. While often simplified using the term "precession," the evolution of the direction of orbital angular momentum $\vec{L}$ is made of a complex superposition of azimuthal (precession) and polar (nutation) motions when defined with respect to a fixed axis such as the direction of the total angular momentum $\vec{J}$. In this work, we have shown that for generic BBHs with misaligned spins, precession and nutation are deeply correlated and occur on the same timescale. Nutation is suppressed only in lower-dimensional regions of the BBH parameter space.

In the construction of gravitational waveforms, the six spin degrees of freedom are often modelled by a reduced set of parameters such as the projected effective spin χ_{eff} [207, 249] and the effective precession spin χ_{P} [206, 210]. These parameters aim to capture the dominant spin effects and reduce the computational cost of GW data analysis. Motivated by the pioneering work of Apostolatos *et al.* (1994) [232] on the effects of spin precession on gravitational waveforms, we choose a different set of parameters that better characterise the precession and nutation of the orbital angular momentum $\vec{L}$ with respect to the total angular momentum $\vec{J}$. The five parameters we propose are: the precession amplitude $\langle\theta_{\text{L}}\rangle$, the nutation amplitude $\Delta\theta_{\text{L}}$, the precession frequency $\langle\Omega_{\text{L}}\rangle$, the nutation frequency ω, and the precession-frequency variation $\Delta\Omega_{\text{L}}$. Reference [250] presented early predictions of the distribution of these parameters in supermassive BBH mergers observable by the LISA mission.

Our numerical investigation indicates that the nutation amplitude $\Delta\theta_{\text{L}}$ is largest for BBHs with:

(1) moderate mass ratios $q \approx 0.6$,

(2) large spin magnitudes $\chi_i \gtrsim 0.5$, and

(3) spin orientations for which $\vec{J} \parallel \vec{L}$ at some point late in the inspiral.

Systems that satisfy condition (3) also experience a divergence in the precession-frequency variation $\Delta\Omega_{\rm L}$. GW events from BBHs satisfying these conditions might offer the best chance to distinguish the effects of precession and nutation and constrain our five parameters observationally.

The next step is to test this hypothesis by exploring the effects of our five precession parameters on the observed gravitational strain $h(t)$. Apostolatos *et al.* (1994) [232] investigated how the changing direction of the orbital angular momentum $\vec{L}$ leads to both frequency and amplitude modulation of the gravitational waveform.

Equation (28) of that paper shows that the time derivative of the precessional correction to the orbital phase $\delta\Phi(t)$ is proportional to $d\hat{\vec{L}}/dt$, which in our notation is given by

$$\frac{d\hat{\vec{L}}}{dt} = \dot{\theta}_L(\cos\theta_{\rm L}\hat{\vec{L}}_\perp - \sin\theta_{\rm L}\hat{\vec{J}}) + \Omega_{\rm L}\sin\theta_{\rm L}(\hat{\vec{J}} \times \hat{\vec{L}}_\perp)\,. \tag{3.15}$$

We see that nutation ($\dot{\theta}_{\rm L} \neq 0$) and precession ($\Omega_{\rm L} \neq 0$) each provide corrections to the orbital and hence GW phase. They also modulate the GW amplitude

by introducing time dependence into the factors of $\hat{\vec{L}}$ and polarisation angle ψ appearing in Eq. (19a) of [232].

In a complementary study, Cutler and Flanagan (1994) [251] investigated the detectability of the lowest-order spin-dependent correction to the GW phase, shown by Kidder *et al.* (1993) [223] to be proportional to

$$\beta \;\equiv\; \left[\frac{113}{12}\vec{S} + \frac{25}{4}\left(q\vec{S}_1 + \frac{1}{q}\vec{S}_2\right)\right] \cdot \frac{\hat{\vec{L}}}{M^2}$$

$$= \frac{19}{6}\frac{J\cos\theta_{\rm L} - L}{M^2} + \frac{25}{4}\chi_{\rm eff}\,. \tag{3.16}$$

Nutation causes $\theta_{\rm L}$ to oscillate with amplitude $\Delta\theta_{\rm L}$ and frequency ω, imprinting an additional signature on the GW phase distinct from that of precession. Although one ultimately wishes to constrain the magnitudes and misalignments of the individual BBH spins, we hypothesise that the five phenomenological parameters presented in this study can be more tightly constrained because of their more direct connection to the waveform amplitude and phase. We will explore these signatures of precession and nutation in greater depth in an upcoming paper [252].

The possibility of measuring our five precession parameters in GW events provides a rich opportunity to identify the astrophysical origin of these systems. Figure 3.7 shows PDFs of these parameters for an isotropic spin distribution as would be expected for BBHs formed in dynamical interactions in dense clusters. An upcoming paper [253] will explore the distributions of these parameters for BBHs formed from isolated stellar binaries [254]. As current and future GW observatories discover an increasing number of BBH systems at higher signal-to-noise ratios, the effects of precession and nutation will be detected unambiguously. We hope that our new precession parameters will aid in the characterisation of these systems and help push the frontiers of GW astronomy.

Chapter 4

Nutations in gravitational wave events

Abstract

We investigate the detectability of sub-dominant spin effects in merging black-hole binaries using current gravitational-wave data. Using a phenomenological model that separates the spin dynamics into precession (azimuthal motion) and nutation (polar motion), we present constraints on the resulting amplitudes and frequencies. We also explore current constraints on the spin morphologies, indicating if binaries are trapped near spin-orbit resonances. We dissect such weak effects from the signals using a sequential prior conditioning approach, where parameters are progressively re-sampled from their posterior distribution. This allows us to investigate whether the data contain additional information beyond what is already provided by quantities that are better measured, namely the masses and the effective spin. For the current catalogue of events, we find no significant measurements of weak spin effects such as nutation and spin-orbit locking. We synthesise a source with a high nutational amplitude and show that near-future detections will allow us to place powerful constraints, hinting that we may be at the cusp of detecting spin nutations in gravitational-wave data.

Summary

This chapter is a reformatted version of my first-author paper Gangardt *et al.* (2022) [255] with corrections from Gangardt *et al.* (2023) [256]. The idea for sequential prior conditioning was given by Michael Kesden. The results were entirely compiled by myself, and the initial draft was written by me. Davide Gerosa, Michael Kesden and Nathan Steinle gave suggestions for this work and its presentation. The data for Fig. 4.10 were provided by Viola De Renzis. The paper received editorial feedback from Davide Gerosa and Michael Kesden.

4.1 Introduction

In Chapter 2, I presented proposed alternative spin-precession estimators that stem directly from PN dynamics [201, 202, 234]. In Gangardt and Steinle *et al.* (2021) [199] (Chapter 3), we split the motion of the orbital angular momentum around the total angular momentum into its nutational (polar) and precessional (azimuthal) components, and used the resulting frequencies and amplitude as indicators of BBH spin precession. In Refs. [201, 202] we illustrated how BBHs can be divided into mutually exclusive "morphologies" based on the shape of their precession cones. These spin morphologies reduce to the known spin-orbit resonances [239] in their zero-amplitude limit, thus generalising the more stringent co-planarity condition of the three spin vectors $\vec{S}_{1,2}$, and $\vec{L}$. Both the phenomenological amplitudes and frequency parameters [234] as well as the spin morphologies [201, 202] have yet to be constrained using the data from current GW event catalogues.

Much like the effective spins, our spin-precession estimators also depend on the masses and spin components of the BBHs in non-trivial ways. The resulting Bayesian posteriors are highly correlated, which can make disentangling effects and interpretation of data somewhat challenging. This is especially true for weak observables such as those due to spin precession, where the data are only mildly informative. A pertinent question to ask in this context is therefore the following:

> Are constraints on the precession parameters providing information beyond what is already encoded in the other observables?

2022PhRvD.106b3019H We tackle this point using sequential prior conditioning. In brief, constructing a conditional prior implies combining the posterior samples of the parameter(s) we are interested in with the uninformative prior distributions of the other parameters. An example of such a procedure in GW astronomy can be seen in fig. 10 of Ref. [80], where the χ_P priors have been conditioned on χ_eff. Prior conditioning is an effective strategy to highlight parameter correlations and show to what extent a given estimator uncovers new information from the data. A more common approach to identifying features in the data is that of calculating odds ratios between analyses where the putative features are included/excluded. While this readily allows one to constrain the joint effect of spin precession and nutation (one needs to compare inference runs with precessing spins against control cases where spins are assumed to be aligned, e.g. [128, 257–259]), current signal models do not isolate one from the other. Our approach aims to be complimentary and seeks to investigate if using more phenomenological parameters can uncover additional information.

Among the intrinsic parameters of a GW event, we expect the BBH masses and the effective spin parameter χ_eff to have a large influence on our posteriors, with the spin precession estimators providing a subdominant contribution. Therefore, events with precession parameters constrained away from their priors conditioned on both the masses and χ_{eff} would provide smoking-gun evidence that new information about the event is being revealed.

In this paper, we systematically employ sequential prior conditioning to investigate if and how the dynamics-based estimators of Refs. [201, 202, 234] can be used to constrain BBH spin precession measured in current GW data. In Sec. 4.2 we briefly review the formulation of the precession/nutation amplitudes and frequencies, as well as the spin morphologies. Section 4.3 details the methodology required to sequentially condition priors on measured parameter posteriors. In Sec. 4.4 we present our results using data from the current GW catalogue. Perhaps unsurprisingly, current evidence is weak. In Sec. 4.5 we present a preliminary analysis from synthetic LIGO/Virgo data and highlight prospects for future observations. Finally, in Sec. 4.6 we draw our conclusions. Some more detailed results are postponed to Appendices A.3 and A.4.

4.2 Spin precession estimators

4.2.1 Five parameters from the decomposition of precession and nutation

Our estimators rely on the PN precession-averaged approach first developed in Refs. [201, 202] and explored at length by both ourselves and other authors [234, 235, 237, 238, 244, 260–263] (summarised in Ch. 2). In particular, the spin dynamics are decomposed into the azimuthal ("precession") and polar ("nutation") motions of the Newtonian orbital angular momentum $\vec{L}$) (see Ch. 3). We only tackle the secular evolution of the spins, which rely on orbit-averaged equations of motions [207]. This implies that we are not sensitive to the dynamics happening on the short orbital timescale (which itself includes nutations, see e.g. [264]).

The five spin-precession parameters are:

(i) The precession amplitude $\langle\theta_{\rm L}\rangle$.

(ii) The precession frequency $\langle\Omega_{\rm L}\rangle$.

(iii) The nutation amplitude $\Delta\theta_{\rm L}$.

(iv) The nutation frequency ω.

(v) The variation of the precession frequency $\Delta\Omega_{\rm L}$.

The astrophysical consequences of these five parameters are explored in Ref. [250] and Ref. [253] for supermassive and stellar-mass BHs, respectively.

4.2.2 Spin morphologies

A complementary categorisation that stems directly from the precession-averaged formalism is that of the spin morphologies. These generalise the notion of the spin-orbit resonances [239], which are non-trivial configurations where nutation vanishes and the four vectors $\mathbf{S_1}$, $\mathbf{S_2}$, $\mathbf{L}$, and $\mathbf{J}$ remain coplanar (see Refs. [45, 236, 240, 265–268] for some of the numerous explorations on the topic, and Ch 2 for more details). There are two families of resonant solutions, characterised by the only two possible configurations that define co-planarity: $\Delta\Phi = 0$ and $\Delta\Phi = \pi$, where $\Delta\Phi$ is the angle between the projections of the two spins onto the orbital plane. Starting from these configurations of regular precession, the entire parameter space of spinning BH binaries can be divided into three mutually exclusive classes where:

(i) Binaries librate in the vicinity of the $\Delta\Phi = 0$ resonance (L0).

(ii) Binaries circulate freely far from either of the two resonances (C).

(iii) Binaries librate in the vicinity of the $\Delta\Phi = \pi$ resonance (Lπ).

Crucially, not all morphologies are available to all binaries: the parameters that are constant on the spin-precession timescale (q, J, S_1, S_2, r, $\chi_{\rm eff}$) can restrict sources to only having certain morphologies [202]. The secular evolution of J and r on the radiation-reaction timescale can cause transitions between the different classes. The spin morphology is thus a quantity that classifies the spin dynamics while being constant on the spin-precession timescale. In the LIGO-Virgo-KAGRA context, this feature could potentially be exploited to probe BH binary formation channels [47, 253, 269].

4.3 Dissecting information

4.3.1 Conditional priors

GW parameter estimation is typically performed within the framework of Bayesian statistics, which explicitly require assuming a prior distribution on the targeted parameters. The standard analyses [80, 90, 270] assume a prior that is uniform in the redshifted component masses m_1 and m_2 (though with cuts in this 2-dimensional parameter space that are informed by the output of the preceding search pipelines), uniform in the spin magnitudes χ_1 and χ_2, and isotropic in the spin directions. This is often referred to as the "uninformative" prior.[1]

Starting from these prior assumptions, stochastic sampling is used to obtain the posterior distribution of the binary parameters. The posterior conveys our best knowledge of the observed BHs. Using public samples from Refs. [80, 92, 270, 271], we select

---

[1] While we use this term for consistency with the literature on the topic, it is a misnomer because the choices behind these prior assumptions are subjectively elicited.

the BBH events that have a probability of astrophysical origin > 0.5. We include BBH events with secondary masses above $2.2\,\mathrm{M}_\odot$ in the source frame; the chosen neutron star threshold reflecting the mass distribution obtained from pulsar observations [272]. Where possible, we use the default samples that combine equally parameter estimation results from the Phenom and EOB waveform families (cf. [80, 92, 270, 271] and references therein). For events where such combined results are unavailable, we use samples from the Phenom waveform family only. We use priors that are uniform in comoving volume and source-frame time.

We re-cast prior and posterior distributions for each event in terms of the five parameters of Ref. [234] and the spin morphologies of Ref. [202] using the PRECESSION code [204]. The necessary quantities for this procedure are the masses, the spins (both magnitudes and directions), and the PN separation of the binary r at the reference frequency of the parameter estimation. LIGO/Virgo parameter estimation samples are reported at a reference frequency of 20 Hz for all events except GW190521, which has a reference frequency of 11 Hz. For each sample, we estimate the orbital separation r using Eq. (4.13) of Ref. [224]; this conversion needs to be performed using detector-frame masses.

When dealing with weak effects in Bayesian statistics, one needs to worry about whether the observed features are data- or prior-driven (see Refs. [273, 274] for GW explorations on this point). Inference on degenerate parameters prompts the question on whether there is truly new information that can be extracted, or whether the data are already saying everything there is to say. In our case, spin precession has a subdominant effect on the waveform and some regions of the parameter space of the spin degrees of freedom are only available to binaries with certain values of the parameters. We address this issue with sequential prior conditioning, which increases the granularity between

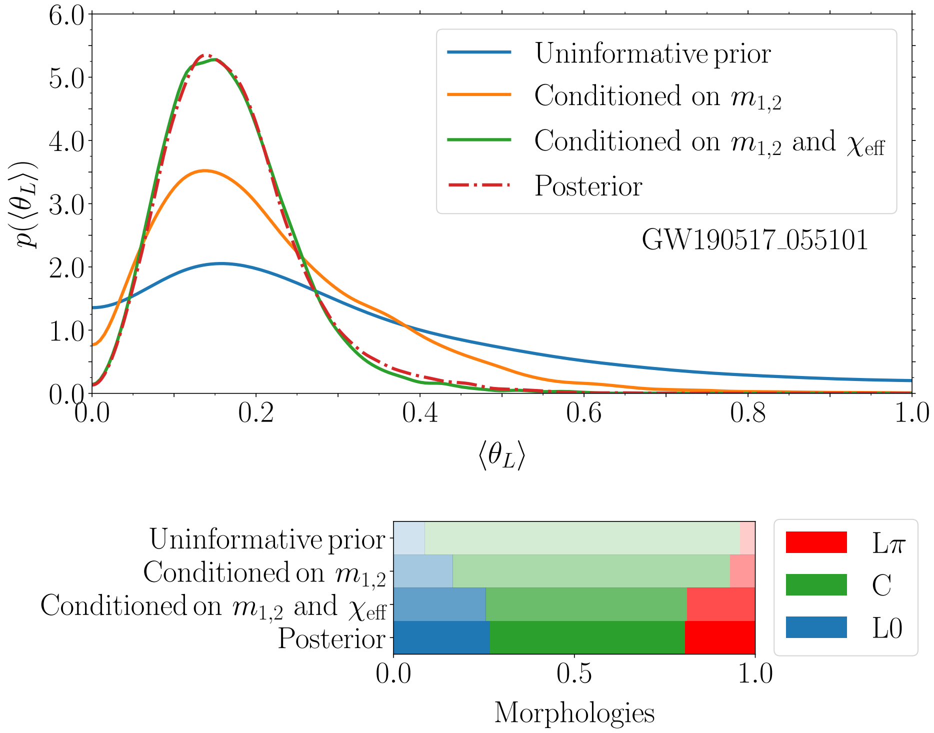

Figure 4.1: Prior and posterior distributions for the precession amplitude $\langle\theta_{\rm L}\rangle$ and the spin morphology of GW190517_055101. In both cases we show the uninformative prior, the prior conditioned on the masses, the prior conditioned both masses and effective spin, and the posterior. For the case of the continuous parameter $\langle\theta_{\rm L}\rangle$, distributions are illustrated using kernel density estimation (top panel). For the case of the spin morphology (bottom panel), we show the fraction of samples in each of the three mutually excluding classes Lπ, C, and L0. In both cases, the prior conditioned on both masses and $\chi_{\rm eff}$ is nearly identical to the posterior distribution, indicating that measurements of those parameters already constrain the precession estimators almost entirely.

prior and posterior, hopefully highlighting where the targeted effects come into play. Prior conditioning has been used in previous analyses when comparing the effective precession parameter $\chi_{\rm P}$ posteriors to priors conditioned on $\chi_{\rm eff}$ [80, 90, 92, 270].

The masses are generically easier to constrain than the spins. Therefore, we first condition our spin inference on the measured values of m_1 and m_2 (or, equivalently, total mass and mass ratio). This is straightforward to implement because the uninformative

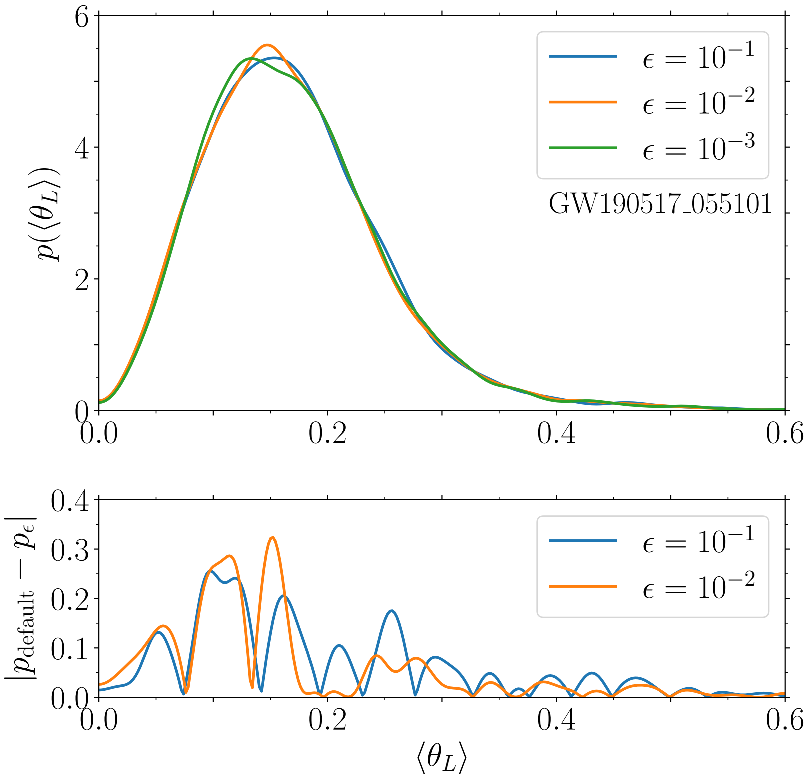

Figure 4.2: Numerical threshold when conditioning on masses and effective spin. The top panel shows the resulting precessional amplitudes $\langle\theta_{\rm L}\rangle$ of GW190517_055101 for three different thresholds $\epsilon = 10^{-1}$ (blue), 10^{-2} (orange) and 10^{-3} (green). The bottom panel shows residuals against the conditioned prior obtained with our default threshold ($\epsilon = 10^{-3}$).

prior assumes that masses and spins are uncorrelated [80, 90, 92, 270]. One can simply take the marginalized posterior distributions of the two masses and combine them with random samples drawn from the uninformative prior for the spins.

Next, it is well known that among the spin degrees of freedom, the combination $\chi_{\rm eff}$ [205, 207] is better measured because it affects the length of the waveform. We thus wish to build a prior that is conditioned on all three parameters m_1, m_2, and $\chi_{\rm eff}$. The implementation here is less trivial because the uninformative prior is posed on m_i and $\mathbf{S}_i$ separately, resulting in a prior on $\chi_{\rm eff}$ that depends on the event-based cuts. We adopt the following numerical approach. For each mass sample in the posterior distribution, we extract a random draw from the uninformative spin prior and compute the resulting $\chi_{\rm eff}$. We then compare this against the posterior's $\chi_{\rm eff}$ and accept the draw if their absolute difference is below a specified threshold $\epsilon = 10^{-3}$. The process is iterated, individually for each sample, until a matching draw is found.

We thus construct four distributions of our spin-precession estimators:

(i) The uninformative prior.

(ii) The prior conditioned on the m_1 and m_2 posteriors.

(iii) The prior conditioned on the m_1, m_2 and $\chi_{\rm eff}$ posterior.

(iv) The posterior.

An example of such sequential conditioning is reported in Fig. 4.1 for GW190517_055101, which is an event with a relatively high value of $\chi_{\rm eff}$ ($\chi_{\rm eff} = 0.54^{+0.19}_{-0.19}$). We show probability distributions for two of our spin estimators, the precession amplitude $\langle\theta_{\rm L}\rangle$ and the spin morphology. This highlights what information on spin precession remains present in the data as one goes from prior to posterior across the two conditionings - we see for both estimators, the prior distributions become increasingly similar to the posterior distribution.

Figure 4.2 shows a convergence study for the numerical threshold ϵ. We test three different thresholds for the nutational amplitude of GW190517_055101. The resulting $\chi_{\rm eff}$ and mass conditioned prior distributions of $\langle\theta_{\rm L}\rangle$ show differences of $\lesssim 0.2$ between our two higher-resolution runs without evident systematics. We have also tested the convergence of all the other estimators and report similar accuracy. GW190517_055101 is the event whose $\chi_{\rm eff}$ posterior distribution is relatively well constrained furthest from

$\chi_{\rm eff} = 0$ (where the uninformative priors tend to be the largest), thus we expect it to be the most sensitive to thresholds in ϵ, making results in Fig. 4.2 conservative and justifying our chosen default threshold of $\Delta\chi_{\rm eff} = 10^{-3}$.

4.3.2 Distance between probability distributions

Some of the more common choices used to compute the difference between two probability distributions include the Kullback-Leibler divergence, its symmetrized extension by Lin (1991) [275], and the Hellinger distance from Hellinger (1909) [276]. Here we employ the latter because it satisfies some very desirable properties including symmetry and unit range (cf. Ref. [277] for a physicists summary). The Hellinger distance between two continuous probability distributions $p(x)$ and $q(x)$ is defined as

$$d_H^2 = 1 - \int \mathrm{d}x \sqrt{p(x)q(x)}. \tag{4.1}$$

For the discrete case where p and q can take N values (as is the case of the spin morphologies) one instead has

$$d_H^2 = 1 - \sum_{i=1}^{N} \sqrt{p_i q_i}. \tag{4.2}$$

The Hellinger distance can take values in the range $[0, 1]$ where $d_H = 0$ for two identical distributions and $d_H = 1$ whenever the supports of p and q do not overlap. For comparison, the Hellinger distance between two identical normal distributions that are offset by n standard deviations is $d_H^2 = 1 - \exp(-n^2/8)$, which implies $d_H \simeq 0.12$ for a 1-σ difference.

4.4 Inference from current data

We now examine the distributions of our estimators across the current GW catalogue. First, we concentrate on a single event for illustrative purposes.

4.4.1 Key behaviour of the nutation parameters

Figure 4.3 shows the distributions of the five precessional and nutational parameters for GW190412 [278]. This is a BH merger with a mass ratio $q = 0.28^{+0.26}_{-0.03}$ that is confidently constrained away from unity and an effective spin $\chi_{\rm eff} = 0.25^{+0.08}_{-0.11}$ that is confidently constrained away from zero. This makes GW190412 ideal to showcase our sequential conditioning approach.

The precessional amplitude $\langle\theta_{\rm L}\rangle$ has a prior distribution with more support for smaller $\langle\theta_{\rm L}\rangle$ values. This is partly because the uninformative priors on masses and spins lead to a preference toward small values of $\langle\theta_{\rm L}\rangle$. Conditioning our priors on the mass parameters results in a broader distribution, retrospectively showing that the uninformative prior's preference for lower $\langle\theta_{\rm L}\rangle$ was indeed due to the uninformative mass priors. Lower values of q allow for larger values of $\langle\theta_{\rm L}\rangle$ [234], which can be seen in the broadening of the $\langle\theta_{\rm L}\rangle$ prior once it is conditioned on GW190412's mass parameters. When we condition our priors on both the masses and $\chi_{\rm eff}$, the range of the distribution becomes considerably smaller and is constrained away from $\langle\theta_{\rm L}\rangle = 0$. GW190412 has a posterior distribution that prefers positive and non-zero values of $\chi_{\rm eff}$ and was reported to show mild evidence of spin precession [278, 279], in agreement with a non-zero precessional amplitude. The marginalised $\langle\theta_{\rm L}\rangle$ posterior is constrained away from all three prior distributions, which can be accounted for by the relatively high network signal-to-noise ratio (SNR) of the event (~ 19) leading to better parameter

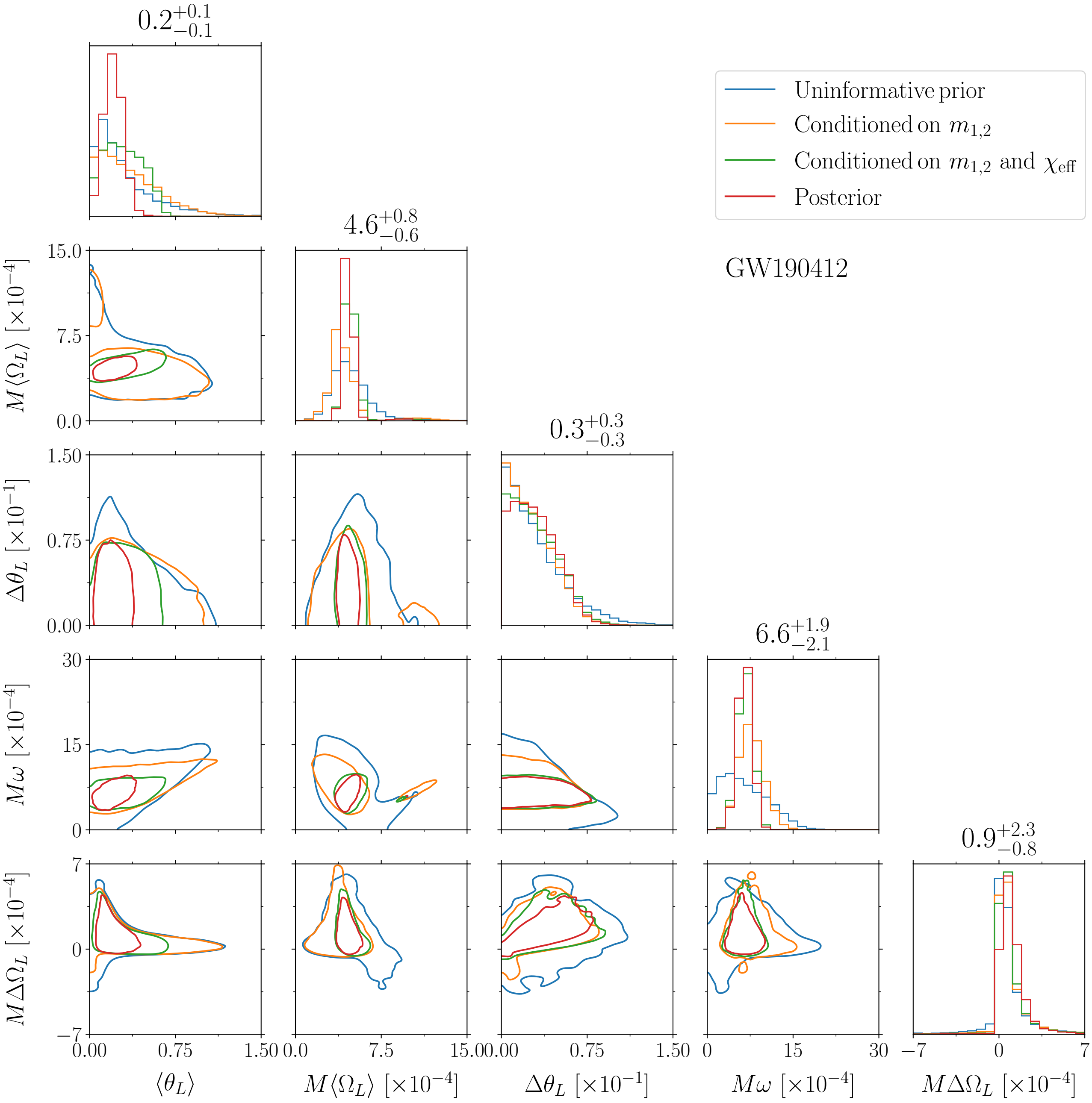

Figure 4.3: Uninformative prior (blue), conditioned priors (orange, green) and posterior (red) distributions of the five phenomenological parameters describing the joint precessional/nutational dynamics for event GW190412. Joint 2D distributions show 90% and 50% confidence levels.

constraints of additional quantities beyond $m_{1,2}$ and $\chi_{\rm eff}$.

Similarly to $\langle\theta_{\rm L}\rangle$, the frequency $\langle\Omega_{\rm L}\rangle$ also has a broad uninformative prior distribution. The mass conditioned prior prefers smaller $\langle\Omega_{\rm L}\rangle$ values, confirming the near-linear relationship between low mass ratio values and $\langle\Omega_{\rm L}\rangle$ explored in Ref. [234]. Conditioning the prior on $\chi_{\rm eff}$ skews it back to the middle and makes it nearly identical to the posterior distribution.

The behaviour of the nutation frequency ω is qualitatively similar to that of $\langle\Omega_{\rm L}\rangle$: the posterior distribution is almost fully described by the information carried by the massed and effective spin. Conditioning on the masses gives a distribution that prefers higher values of ω compared to the uninformative prior because, in general, lower values of q correspond to higher values of ω [234].

For GW190412, the posterior and prior distributions of the nutational parameters $\Delta\theta_{\rm L}$ and $\Delta\Omega_{\rm L}$ are largely compatible, a result we observe for most events across the entire dataset. Nutations are a two-spin effect and as such they are intrinsically harder to measure [210, 280, 281].

4.4.2 Catalogue constraints

Our full results are reported in Table A.1 of Appendix A.4, where we list medians and 90% symmetric credible intervals of the uninformative prior, the conditioned priors, and the posterior for all our estimators ($\langle\theta_{\rm L}\rangle, \langle\Omega_{\rm L}\rangle, \Delta\theta_{\rm L}, \omega$, $\Delta\Omega_{\rm L}$, and the spin morphologies) for each BBH event in the current catalogue. We see across our table that the posterior values typically have narrower credible intervals compared to their prior counterparts, compatible with the non-zero Hellinger distances between the uninformative priors and posteriors for each parameter. As is common practice in the field, we use equal-tailed credible intervals, which, for bound parameters, exclude the extrema by definition. For events with high SNR, such as GW190412 and GW190814, the 90% credible intervals decrease significantly between prior and posterior (from widths of ~ 6 radians to ~ 2 radians) for well-measured parameters such as $\langle\theta_{\rm L}\rangle$, tracing information gain from measurements.

In Fig. 4.4 we summarise the Hellinger distances between the marginalised prior and posterior distributions of the various estimators. As expected, we find that the distance d_H decreases as the conditioning becomes stricter such that the posteriors and conditioned priors approach each other. Events where this is not the case, such as the Hellinger distances for $\Delta\Omega_{\rm L}$ for the event GW200210_092255, are those where the prior and posterior distributions are broad, leading to d_H measurements that overestimate the differences between the distributions. The Hellinger distances for the nutational amplitude $\Delta\theta_{\rm L}$ are small compared to the other four parameters, and conditioning the priors does not affect the d_H values of the events (except for GW190814, whose well measured mass ratio significantly constrains the posterior of $\Delta\theta_{\rm L}$).

The only parameters where the distance d_H between the posterior and the prior conditioned on $m_{1,2}$ and $\chi_{\rm eff}$ is > 0.35 for some events are $\langle\theta_{\rm L}\rangle$, $\langle\Omega_{\rm L}\rangle$ and $\chi_{\rm P}$. This should not be surprising: precession does not require spin-spin couplings and is thus easier to measure than nutation. The nutation frequency ω also shows cases with $d_H > 0.25$, but only between the uninformative prior and the posterior. Much like $\langle\theta_{\rm L}\rangle$, the frequency ω has a strong dependence on the mass ratio q, but for this parameter the leading PN order does not depend on the BBH spins [234]. Therefore, the distance d_H of the ω marginals decreases substantially once the priors are conditioned on the mass parameters.

The event GW200129_065458 has been shown to have hints of spin precession [80, 148, 154]; however, when using the combined posterior samples this spin precession

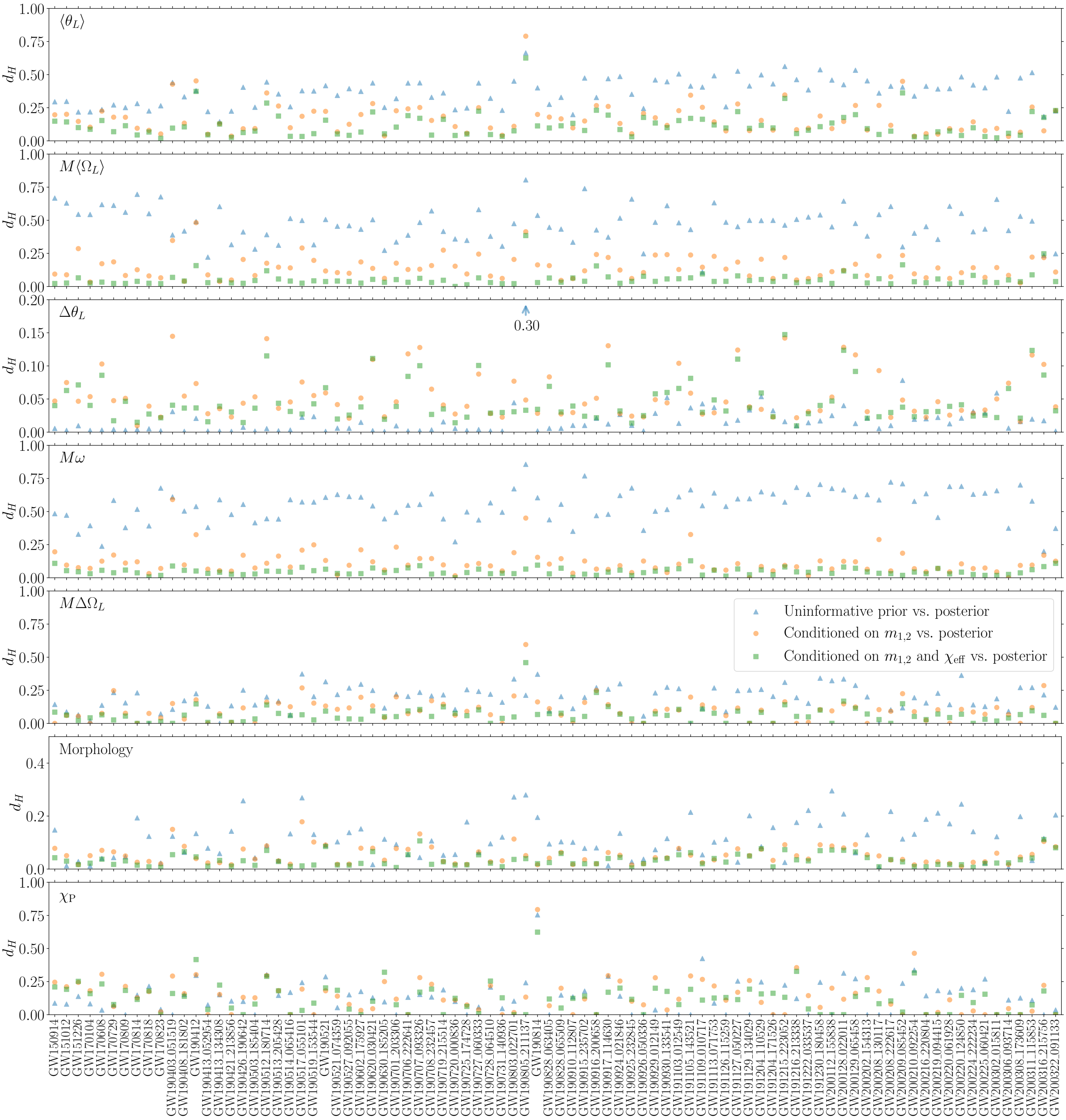

Figure 4.4: Hellinger distances d_H for each of the five phenomenological parameters, spin morphologies, and the effective precession parameter χ_P, comparing the three priors with the posterior for each GW event. Scatter points indicate the distance between posterior vs. uninformative prior (blue triangles), posterior vs. prior conditioned on $m_{1,2}$ (orange circles), and posterior vs. prior conditioned on both $m_{1,2}$ and χ_eff (green squares). Note that the third from the top panel for $\Delta\theta$ and the bottom panel for the morphologies are scaled differently, reflecting the smaller d_H values; GW190814 is an outlier with a distance between posterior and uninformative prior of ~ 0.55 (arrow).

is not evident. Figure 4.5 shows that spin precession is present in the samples from the `IMRPhenomXPHM` waveform family, and is suppressed by the `SEOBNRv4PHM` waveform samples, to a point of non-detection of spin precession when the samples are combined. The `IMRPhenomXPHM` posterior is not only well-constrained away from its uninformed prior in the case of $\chi_{\rm P}$ and $\langle\theta_{\rm L}\rangle$, but it also prohibits non-precession (i.e., $\chi_{\rm P} > 0$ and $\langle\theta_{\rm L}\rangle > 0$). In the case of the nutational amplitude, all three posteriors admit non-nutation for this event ($\Delta\theta_{\rm L} = 0$), although the `IMRPhenomXPHM` posterior appears to have a second peak at higher $\Delta\theta_{\rm L}$ amplitudes of ~ 0.10 radians. The Hellinger distances all decrease in value once the priors are conditioned on the masses of the event.

The event GW190814 has the highest Hellinger distance d_H values between its uninformative prior and posterior for almost all estimators. Its high network SNR of 25 leads to tight constrains on the masses and spins of the two objects, which in turn meant that conditioning our prior on these tightly constrained quantities gave significant changes in the distributions and large distances. In particular, we report $d_H = 0.44$ for $\langle\theta_{\rm L}\rangle$, $d_H = 0.65$ for $\langle\Omega_{\rm L}\rangle$, $d_H = 0.30$ for $\Delta\theta_{\rm L}$, $d_H = 0.73$ for ω, $d_H = 0.05$ for $\Delta\Omega_{\rm L}$, $d_H = 0.28$ for the spin morphology, and $d_H = 0.57$ for $\chi_{\rm P}$, see Table A.1. GW190814 is the only event with a d_H measurement above 0.2 between the uninformative prior and posterior for the nutational amplitude $\Delta\theta_{\rm L}$; however, its low mass ratio of $q = 0.11^{+0.01}_{-0.01}$ and spin posteriors constrain it to have negligible spin precession and nutation.

Informed by the d_H values listed in Table A.1 and Fig. 4.4, we select the ten events with the highest $\langle\theta_{\rm L}\rangle$ Hellinger distances between the posterior and the prior conditioned on both $m_{1,2}$ and $\chi_{\rm eff}$. These are highlighted in Fig. 4.6. Out of this subset of events, only GW190521 has a $\langle\theta_{\rm L}\rangle$ posterior that prefers larger values compared to the conditioned prior. GW190521 is an event with high masses ($m_1 = 98.4^{+33.6}_{-21.7}$,

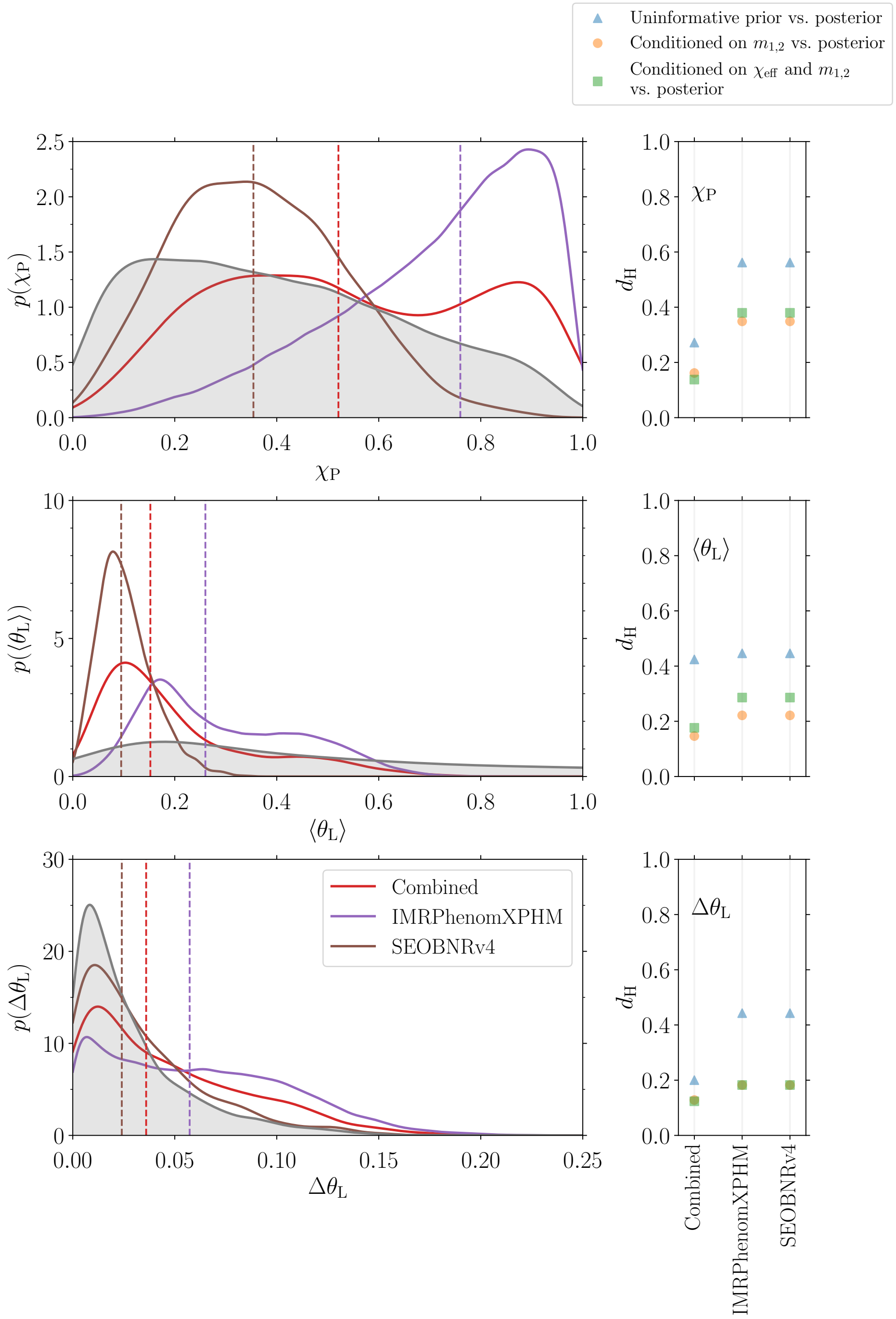

Figure 4.5: The left column shows the posterior distributions for the three spin precession parameters $\chi_{\rm P}$, $\langle\theta_{\rm L}\rangle$, and $\Delta\theta_{\rm L}$, compared to the uninformed prior for the event GW200129_065458, showing results for the `IMRPhenomXPHM` (purple) and `SEOBNRv4PHM` (brown) waveform families and the combined samples (red). Median values for each distribution are displayed as the vertical dashed lines in the corresponding colour. The right column shows the Hellinger distance d_H for each of the three spin precession parameters $\chi_{\rm P}$, $\langle\theta_{\rm L}\rangle$, and $\Delta\theta_{\rm L}$, comparing the three priors with the posterior. Scatter points in the right column indicate the distance between posterior vs. uninformative prior (blue triangles), posterior vs. prior conditioned on $m_{1,2}$ (orange circles), and posterior vs. prior conditioned on both $m_{1,2}$ and $\chi_{\rm eff}$ (green squares).

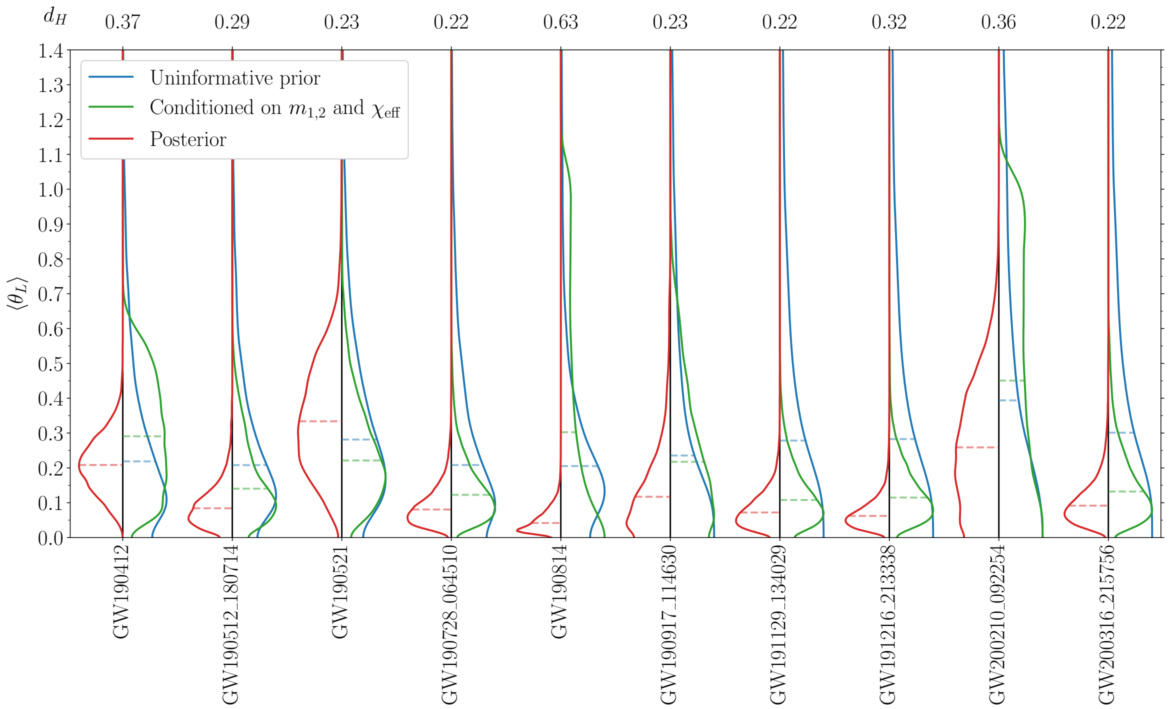

Figure 4.6: Precessional amplitude for the ten GW events with the largest Hellinger distance d_H value between the posterior and prior conditioned on both masses and effective spins. Posteriors (red) are shown on the left-hand side of each violin plot, while the uninformative (blue) and conditioned (green) priors are shown on the right-hand side. Dashed lines indicate the median values of the corresponding distributions. The Hellinger distance d_H value between the posterior and prior conditioned on both masses and effective spin is quoted above each event.

$m_2 = 57.2^{+27.1}_{-30.1}$), contributing to a high network SNR ($\rho \sim 14$). The high network SNR leads to better parameter estimation and thus better-constrained posteriors. While its effective spin was measured to be compatible with 0 ($\chi_{\rm eff} = -0.14^{+0.50}_{-0.45}$), meaningful constraints on the spin misalignments led to claims of spin precession, quantified by an estimate of $\chi_{\rm P} = 0.68^{+0.25}_{-0.37}$ [128]. Evidence of spin precession for GW190521 persists when $\chi_{\rm P}$ is generalised to include all variation over the precession timescale, $\langle\chi_{\rm P}\rangle = 0.70^{+0.56}_{-0.46}$ [210]. Similarly to GW190521, all of the events in Fig. 4.6 but GW200210_092254 and GW190917_114630 are reported to have network SNRs

$\gtrsim 10$. The lower SNR of GW200210_092254 leads to wider prior and posterior distributions. Like for GW190814 and GW190412, the low mass ratio ($q = 0.12^{+0.05}_{-0.05}$) of GW200210_092254 leads to a conditioned prior that prefers a large precessional amplitude, while the posterior is somewhat constrained away from large $\langle\theta_{\rm L}\rangle$; although the lower SNR means that we are unable to place an upper bound on the precession of this event unlike the ones placed for GW190814 and GW190412 (cf. Table A.1). The event GW200129_065458 has the largest median $\chi_{\rm P}$ value in the GW catalogues [80], but after conditioning our priors on just the masses, we do not find significant constraints placed on spin precession or nutation for this event.

Figure 4.7 shows two-dimensional priors and posteriors for the precessional amplitude $\langle\theta_{\rm L}\rangle$ and the nutational amplitude $\langle\Delta\theta_{\rm L}\rangle$ for all BBHs in the catalogue. Colours highlight some events that may be of specific interest. Overall, we find that $\langle\theta_{\rm L}\rangle$ is better constrained than $\Delta\theta_{\rm L}$ for all of the events, highlighting once more that nutation is harder to measure than precession. In particular, all events are consistent with a nutational amplitude of 0 at 90% credible interval. Unlike the nutational amplitude, most of the posteriors for $\langle\theta_{\rm L}\rangle$ are constrained away from zero, something that is seen best with GW190412, cf. Fig. 4.3 above. Current constraints on the nutational amplitude are overall poor, and tend to exclude high values —this is best shown by the event posteriors of systems with large SNR and small q such as GW190412 and GW190814. These constraints on the nutational amplitude are explained by the mass parameters of the events, as the difference between the posterior and the prior conditioned on the masses and the prior conditioned on $\chi_{\rm eff}$ and the masses is negligible ($d_H < 0.15$). The posterior of GW190521 does not show the same behavior in the nutational amplitude because its less extreme mass ratio constrains it away from the single-spin limit that forbids nutations [234, 244], and thus makes large nutational amplitudes possible. The

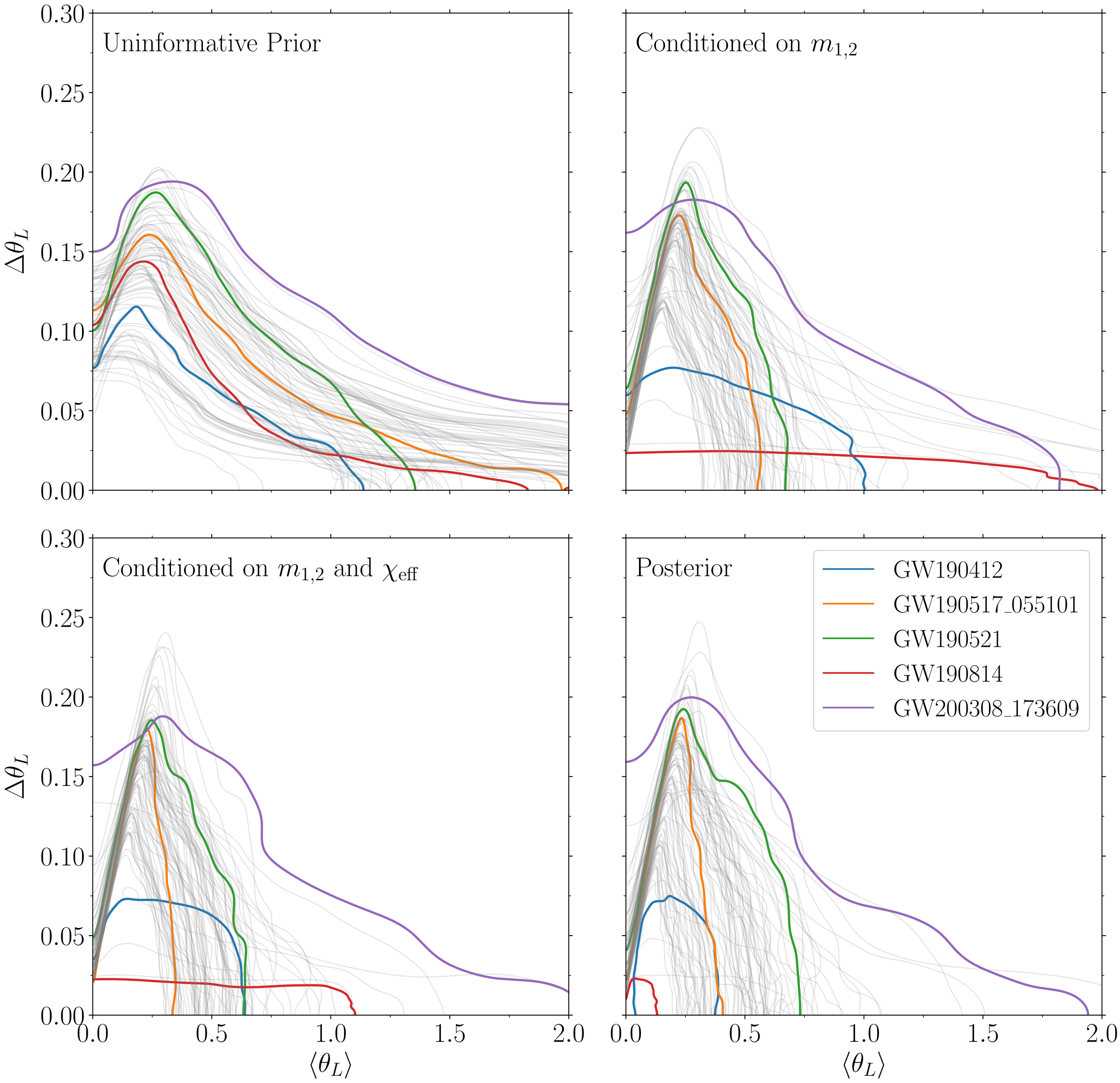

Figure 4.7: Joint prior and posterior marginalized distributions for the precession amplitude $\langle\theta_{\rm L}\rangle$ and the nutational amplitude $\Delta\theta$ for all gravitational wave events, quoted at the 90% credible level. Some events with high Hellinger distance for either of the two amplitudes are highlighted in colour.

event GW200308_173609 has a low SNR of ~ 7.1, and as a consequence its posterior distribution does not move away from its prior even after they are conditioned on the masses and the $\chi_{\rm eff}$ of the event. In general, the gray lines representing the rest of the GW events have posterior distributions that constrain the precessional amplitude $\langle\theta_{\rm L}\rangle$

to be smaller than the distributions given by the uninformative prior. For most of the population, the nutational amplitude posterior distribution remains unconstrained, in agreement with the rest of our findings.

4.4.3 Spin morphologies

We now look at constraining the BBH spin morphology [201, 202]. Our results are presented in Table A.1 and Fig. 4.8.

Events with mass ratios that significantly depart from unity (e.g. GW190412, GW190814) are constrained to be fully in the circular morphology. This is because the parameter space available to binaries in the two librating morphologies shrinks rapidly as $q \to 0$ [202]. Some events present $d_H \gtrsim 0.2$ between their uninformed priors and posteriors, but overall, we find that the morphology of a given event is largely determined once we condition on both masses and effective spin. For events with near equal masses, the uniform priors show an initial preference for the circulating morphology, which is then constrained to be smaller in their posteriors.

Figure 4.9 illustrates the sensitivity of the spin morphologies to sequential prior conditioning. When comparing the fraction of posterior samples in any of the two librating morphologies (L0, Lπ) to the same fraction in the uninformed prior (left panel), for most events these fractions are constrained to be dissimilar, indicating that binaries are somewhat compatible with libration. As expected [202], the fraction of librating samples in the posterior is closely correlated with the mass ratio (color scale). Events with mass ratios below (above) approximately 0.5 present a larger (smaller) fraction of the librating samples in the uninformed prior compared to the posterior. Once we condition the prior samples on the masses only (middle panel), for most events the probability of libration is approximately the same for the conditioned prior and the

Figure 4.8: The fraction of samples in each of the three spin precession morphologies —librating about 0 (L0, blue), librating about π (Lπ, red) and circulating (C, green)— for all GW events. For each event, the fractions in the posterior distribution are shown by the most opaque, leftmost bar, followed by the fractions in each morphology for the prior conditioned on the masses and the effective spin $\chi_{\rm eff}$, then the fractions for the prior conditioned on the masses distribution, and finally the fractions in the uninformative prior to the left. Above each event, we quote the Hellinger distance between the fractions in the uninformative prior distribution and the fractions in the posterior.

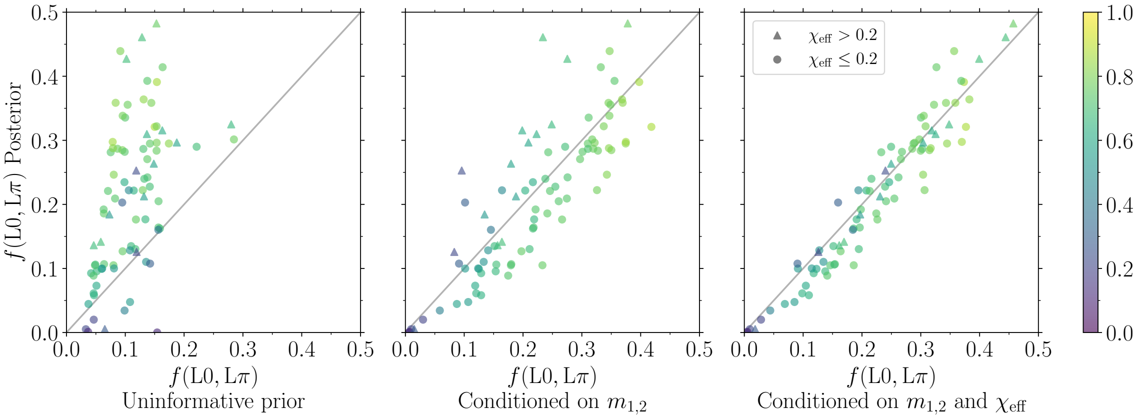

Figure 4.9: The fraction of samples $f(\mathrm{L0},\mathrm{L}\pi)$ in either of the two librating morphologies for all three priors against that for the posterior, progressively increasing the conditioning from left to right. Events are colour-coded by the median value of their mass ratio q. The diagonal grey line indicates the case where the fraction of librating samples is the same for both distributions. Events with a median effective spin parameter χ_{eff} posterior value higher than 0.2 are represented by triangles, while the rest are shown as circles.

posterior. A similar correlation exists between the fraction of librating samples in the posterior and the events' χ_{eff}. When the event priors are conditioned also on χ_{eff} (right panel), we see that events with $\chi_{\mathrm{eff}} > 0.2$ in the posterior (depicted by the triangles) are pushed to the right, implying more event samples are librating in the prior conditioned on both the masses and χ_{eff} than the prior conditioned on the masses alone. Once both of these correlations are taken into account, the spin morphologies are fully described by their mass and χ_{eff} measurements, and no outliers remain in the right panel.

4.5 Synthetic observation

Our investigations show that, overall, the SNR of the current GW catalogue is too moderate to draw accurate constraints on our precession/nutation estimators. We now present a pilot study on synthetic data, showcasing the potential of a putative "golden" event for spin dynamics —a hopeful prediction for the upcoming LIGO/Virgo/KAGRA observing run.

We fine-tune the parameters of a BBH such that spin nutations are manifestly prominent. In particular, we set $q = 0.4$ and spins of magnitude $\chi_{1,2} = 0.95$ directed into the orbital plane ($\theta_{1,2} = \pi/2$) at a reference frequency of 20Hz. The angle between the two black hole spins in the orbital plane is set as $\Delta\phi = 0.1$. This results in an injected signal with $\langle\theta_\mathrm{L}\rangle = 0.59$, $M\langle\Omega_\mathrm{L}\rangle = 1.7\times10^{-3}$ (i.e. 4.6 Hz in the detector frame), $\Delta\theta_\mathrm{L} = 0.20$, $M\omega = 1.5\times10^{-3}$ (4.0 Hz in the detector frame), and $M\Delta\Omega_\mathrm{L} = 4.8\times10^{-4}$ (1.3 Hz in the detector frame), and belongs to the circulating morphology.

The total source-frame mass of the system is set to $70\,\mathrm{M}_\odot$ to maximise the number of GW cycles in band, and the orbital-plane inclination is $\simeq 30°$, close to face-on. The source is placed at a luminosity distance of 500 Mpc; the sky location is $(\mathrm{RA}, \mathrm{DEC}) = (0.75, 0.5)$. We assume noise curves for LIGO and Virgo that are representative of the predicted detector performances during the upcoming the O4 observing run [282]. Signals are injected and recovered using the `IMRPhenomXPHM` waveform model [86]. The injected signal has a SNR of about 45 in LIGO Livingston, 33 in LIGO Hanford, and 25 in Virgo. We sample the resulting posterior using parallel nested sampling [283] as implemented in the BILBY pipeline [271, 284], assuming their standard uninformative priors.

Our full results are reported in Appendix A.3. The distributions of the nutational amplitude $\Delta\theta_\mathrm{L}$ is highlighted in Fig. 4.10. In particular, the posterior is well-constrained from all three prior distributions, providing a confident detection of spin nutation. More specifically we find a $d_H = 0.55$ between the posterior and the uninformative prior, a $d_H = 0.89$ between the posterior and the prior conditioned on $m_{1,2}$, and a $d_H = 0.95$ between the posterior and the prior conditioned on both $m_{1,2}$

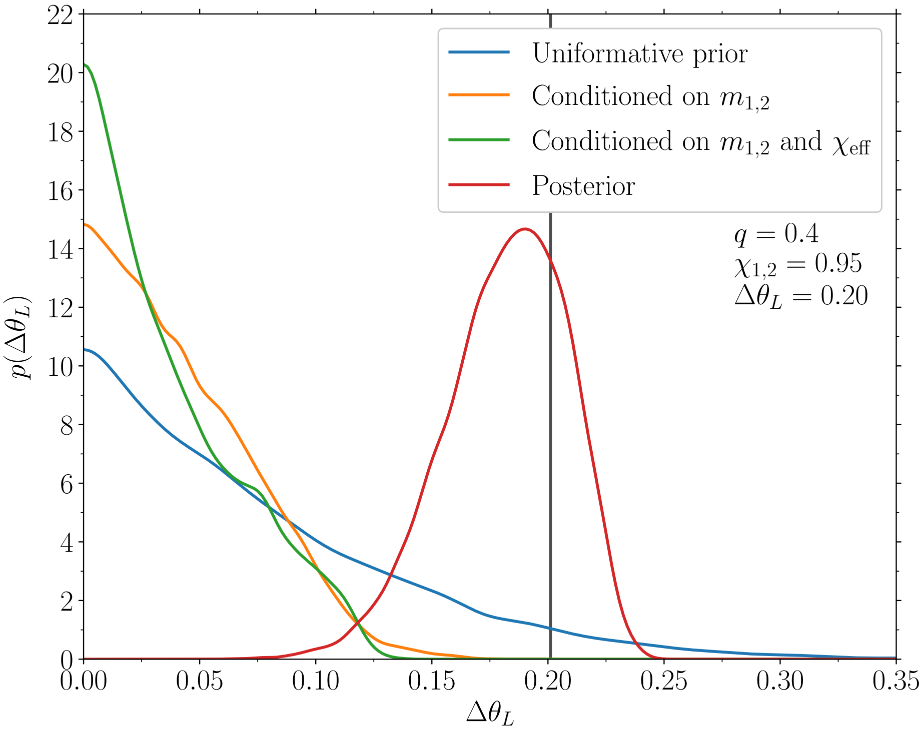

Figure 4.10: Distribution of nutational amplitude $\Delta\theta_{\rm L}$ for a synthesised signal designed to maximise the nutational amplitude. The posterior (red) is well constrained from all the prior distributions (blue, orange, green), even when these are conditioned on masses and effective spin. The vertical black line represents the injected $\Delta\theta_{\rm L}$ value.

and $\chi_{\rm eff}$. Unlike for the GW events in the dataset, as we condition our priors on the masses and then on the masses and $\chi_{\rm eff}$, the distributions are pushed towards low $\Delta\theta_{\rm L}$ values. This is due to the priors on the spin magnitudes preferring low values, while the injected source has $\chi_{1,2} = 0.95$. Since we do not condition our priors directly on the spin magnitudes but only on $\chi_{\rm eff}$, all our distributions but the posteriors present many samples with low $\chi_{1,2}$. On the other hand, nutations require high spins, thus pushing the posterior towards high $\Delta\theta_{\rm L}$ values.

From our posterior distribution we report amplitudes $\langle\theta_{\rm L}\rangle = 0.59^{+0.04}_{-0.04}$, $M\langle\Omega_{\rm L}\rangle = 1.7^{+0.1}_{-0.1} \times 10^{-3}$, $\Delta\theta_{\rm L} = 0.19^{+0.04}_{-0.05}$, $M\omega = 1.55^{+0.01}_{-0.01} \times 10^{-3}$, and $M\Delta\Omega_{\rm L} = 4.5^{+1.1}_{-1.3} \times 10^{-4}$, and a 0.0007/0.9993/0.0 fraction of samples in the L0/C/Lπ morphology, respectively. The prior and posterior distributions of all five precessional parameters are shown in Fig A.1.

While limited to a single case, this exercise serves as a proof of concept, indicating that direct detection of spin nutations is not out of reach. For such a favourable event, our estimators are indeed sensitive to additional information beyond the masses and the dominant spin parameter $\chi_{\rm eff}$.

4.6 Conclusions

Spin precession and nutation are both subtle effects on the waveform. While statements such as *"at least one of the component black holes has spin greater than 0.2"* were possible since the very first GW detections [219], detailed spin dynamics is much harder to extract from the data. In this paper, we exploited previously developed estimators of BBH spin precession and nutation [201, 202, 234] in conjunction with current GW data.

Precisely because spin effects are subdominant, we tackled the interpretation issue on whether indirect constraints from other, easier-to-see parameters are enough to explain features in the data. To this end, we formalised and systematically applied a sequential prior-conditioning approach.

Our analysis does not find strong evidence of either precession or nutation in any individual event using our phenomenological estimators. These results are compatible with those of Refs. [80, 90, 92, 270], which also find no compelling evidence for spin precession in single events. Sequential prior conditioning indicates that, while comparisons between uninformative priors and posteriors could be used to claim evidence for spin precession, their differences are largely re-absorbed when one takes into account measurements of masses and effective spins.

We also presented a pilot injection study, proving that favourable sources at current sensitivities will indeed allow us to disentangle precession and nutation from the coupled motion of the BBH spins. This showcases the potential of our spin estimators parameters to uncover finer details from GW signals, paving the way to deeper explorations in terms of both fundamental physics and astronomy [47, 250, 253, 269].

Chapter A

Appendix for Part I

Additional material for Chs. 3—4 is summarised.

A.1 Maximal $\vec{L}$ nutations are forbidden

In this Appendix, we prove that the nutation amplitude cannot be maximal, i.e. $\Delta\theta_{\mathrm{L}} < \pi$ for all BBH configurations. Our calculation mirrors that of Ref. [237] for $\theta_{1,2}$.

The condition $\Delta\theta_{\mathrm{L}} = \pi$ is possible only if $\cos\theta_{\mathrm{L}-} = 1$ and $\cos\theta_{\mathrm{L}+} = -1$.

In those cases, Eq. (2.9) implies

$$S_{\pm} = |J \pm L|\,.$$

If such a configuration exists, there needs to be values of the constant of motion J and χ_{eff} which can simultaneously satisfy $S_- = |J - L|$ and $S_+ = J + L$. Using Eq. (14) of Ref. [202] (where χ_{eff} is indicated as ξ), these values are

$$J^2 = L^2 + \frac{(S_1^2 - S_2^2)(1-q)}{1+q}, \tag{A.1}$$

and

$$\chi_{\rm eff} = -\left(\frac{r}{M}\right)^{1/2} . \tag{A.2}$$

Equation (A.2) violates the limit $|\chi_{\rm eff}| \leq 1$ in the PN regime $r > M$, implying that $\Delta\theta_{\rm L}$ is strictly smaller than π for all physical BBH configurations.

A.2 $\Omega_{\rm L}$ diverges when $\vec{L}$ and $\vec{J}$ are aligned

At 2PN order, the precession vector is given by (e.g. [207])

$$\begin{aligned} \mathbf{\Omega} = \frac{1}{2r^3}\Bigg\{ &\left[4 + 3q - 3(1+q)\chi_{\rm eff}\left(\frac{M}{r}\right)^{1/2}\right]\vec{S}_1 \\ &+ \left[4 + \frac{3}{q} - \frac{3}{q}(1+q)\chi_{\rm eff}\left(\frac{M}{r}\right)^{1/2}\right]\vec{S}_2\Bigg\} . \end{aligned} \tag{A.3}$$

In the limit $\theta_{\rm L} \to 0$ or π,

$$\vec{S} \cdot \hat{\vec{L}}_\perp = 0 \implies \vec{S}_2 \cdot \hat{\vec{L}}_\perp = -\vec{S}_1 \cdot \hat{\vec{L}}_\perp . \tag{A.4}$$

It follows that

$$\mathbf{\Omega} \cdot \hat{\vec{L}}_\perp = -\frac{3(1-q^2)\vec{S}_1 \cdot \hat{\vec{L}}_\perp}{2qr^3}\left[1 - \chi_{\rm eff}\left(\frac{M}{r}\right)^{1/2}\right] . \tag{A.5}$$

For misaligned spins ($\vec{S}_1 \cdot \hat{\vec{L}}_\perp \neq 0$), this expression does not approach zero as $\theta_{\rm L} \to 0$ or π, implying that the second term in Eq. (3.12) and thus $\Omega_{\rm L}$ diverges in this limit.

A.3 Precessional and nutational parameters of the synthetic signal

Figure A.1 presents the distributions of the five precessional and nutational parameters of the synthetic observation described in Sec. 4.5. The injected value of each parameter is successfully recovered within the 90% credible intervals of the posterior distribution.

A.4 Full results in tabular form

Table A.1 reports results for all distributions and all our estimators across the current GW catalog.

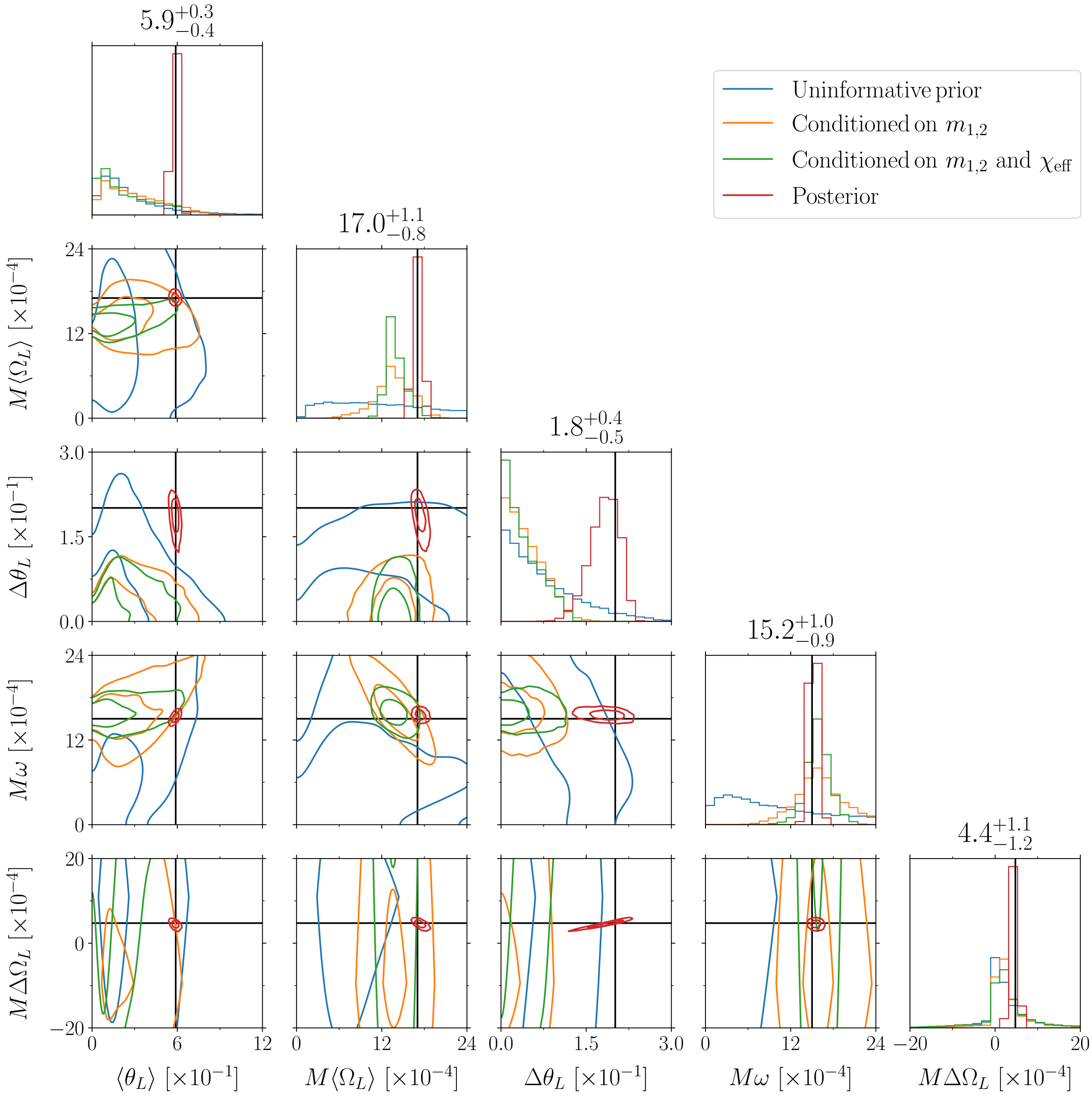

Figure A.1: Uninformative prior (blue), prior conditioned on the masses only (orange), prior conditioned on the masses and on χ_{eff} (green) and posterior (red) distributions of the five precessional and nutational parameters for the synthetic event described in Sec. 4.5. The joint distributions represent the 90% and 50% credible levels. The black vertical and horizontal lines show the injected system. The median value of the posterior for each parameter is displayed above the marginalised distributions.

Event	**Prob.**	$\langle\theta_L\rangle[\times10^{-1}]$	$M\langle\Omega_L\rangle[\times10^{-4}]$	$\Delta\theta_L[\times10^{-1}]$	$M\omega[\times10^{-4}]$	$M\Delta\Omega_L[\times10^{-4}]$	L0/C/Lπ
GW150914	Uninformative Prior	$1.8^{+5.7}_{-1.4}$	$13.8^{+20.4}_{-10.1}$	$2.7^{+6.7}_{-2.5}$	$0.8^{+4.4}_{-0.7}$	$6.7^{+125.8}_{-69.0}$	0.1/0.85/0.05
	Cond. on $m_{1,2}$	$1.6^{+2.0}_{-1.2}$	$17.9^{+3.9}_{-4.0}$	$2.4^{+7.8}_{-2.3}$	$0.4^{+0.4}_{-0.2}$	$0.3^{+51.1}_{-43.5}$	0.29/0.58/0.13
	Cond. on $m_{1,2}$ and $\chi_{\rm eff}$	$1.5^{+1.9}_{-1.2}$	$17.8^{+3.5}_{-3.4}$	$2.3^{+7.9}_{-2.2}$	$0.4^{+0.3}_{-0.3}$	$0.5^{+51.0}_{-39.7}$	0.28/0.62/0.1
	Posterior	$1.1^{+1.8}_{-0.9}$	$17.7^{+3.4}_{-3.2}$	$2.0^{+7.3}_{-1.9}$	$0.3^{+0.4}_{-0.2}$	$0.6^{+54.8}_{-47.1}$	0.24/0.68/0.08
GW151012	Uninformative Prior	$1.8^{+5.8}_{-1.4}$	$14.0^{+20.4}_{-10.2}$	$2.7^{+6.9}_{-2.5}$	$0.8^{+4.4}_{-0.7}$	$6.8^{+118.5}_{-65.5}$	0.11/0.84/0.05
	Cond. on $m_{1,2}$	$1.5^{+2.5}_{-1.1}$	$6.7^{+2.8}_{-1.9}$	$2.9^{+7.0}_{-2.7}$	$0.2^{+0.6}_{-0.1}$	$1.9^{+43.0}_{-33.1}$	0.15/0.78/0.07
	Cond. on $m_{1,2}$ and $\chi_{\rm eff}$	$1.4^{+2.2}_{-1.1}$	$6.8^{+3.1}_{-1.7}$	$2.7^{+7.3}_{-2.5}$	$0.2^{+0.6}_{-0.1}$	$1.5^{+46.9}_{-36.9}$	0.14/0.8/0.05
	Posterior	$1.0^{+1.8}_{-0.8}$	$6.8^{+3.2}_{-1.7}$	$2.3^{+6.4}_{-2.1}$	$0.2^{+0.5}_{-0.1}$	$1.5^{+53.0}_{-44.2}$	0.12/0.84/0.04
GW151226	Uninformative Prior	$1.2^{+4.0}_{-0.9}$	$2.7^{+2.2}_{-1.3}$	$2.0^{+4.8}_{-1.9}$	$0.2^{+0.7}_{-0.2}$	$1.6^{+22.2}_{-14.2}$	0.07/0.89/0.04
	Cond. on $m_{1,2}$	$1.2^{+2.2}_{-0.9}$	$2.1^{+1.0}_{-0.5}$	$2.6^{+5.8}_{-2.4}$	$0.1^{+0.2}_{-0.1}$	$1.0^{+15.8}_{-12.6}$	0.11/0.85/0.04
	Cond. on $m_{1,2}$ and $\chi_{\rm eff}$	$1.2^{+1.8}_{-0.8}$	$2.2^{+0.9}_{-0.3}$	$2.8^{+6.2}_{-2.6}$	$0.1^{+0.1}_{-0.1}$	$0.8^{+15.9}_{-13.0}$	0.11/0.85/0.04
	Posterior	$1.1^{+1.4}_{-0.7}$	$2.2^{+0.8}_{-0.2}$	$2.6^{+5.2}_{-2.4}$	$0.1^{+0.1}_{-0.1}$	$1.0^{+13.5}_{-10.9}$	0.1/0.87/0.04
GW170104	Uninformative Prior	$1.8^{+5.8}_{-1.4}$	$13.9^{+19.9}_{-10.1}$	$2.7^{+6.8}_{-2.5}$	$0.8^{+4.5}_{-0.7}$	$6.6^{+122.1}_{-66.9}$	0.11/0.84/0.05
	Cond. on $m_{1,2}$	$1.7^{+2.4}_{-1.3}$	$12.2^{+4.9}_{-3.8}$	$3.5^{+7.8}_{-3.3}$	$0.5^{+0.6}_{-0.3}$	$3.7^{+79.2}_{-65.6}$	0.15/0.78/0.07
	Cond. on $m_{1,2}$ and $\chi_{\rm eff}$	$1.6^{+2.5}_{-1.2}$	$12.1^{+5.3}_{-3.8}$	$3.2^{+7.9}_{-3.0}$	$0.5^{+0.6}_{-0.3}$	$3.5^{+78.2}_{-66.1}$	0.14/0.81/0.05
	Posterior	$1.4^{+2.1}_{-1.0}$	$12.1^{+5.1}_{-3.9}$	$3.0^{+7.1}_{-2.8}$	$0.5^{+0.5}_{-0.4}$	$3.9^{+81.0}_{-68.1}$	0.12/0.84/0.04
GW170608	Uninformative Prior	$1.0^{+3.4}_{-0.8}$	$1.3^{+1.0}_{-0.6}$	$1.7^{+4.2}_{-1.6}$	$0.1^{+0.3}_{-0.1}$	$0.8^{+10.3}_{-6.5}$	0.07/0.9/0.03
	Cond. on $m_{1,2}$	$1.1^{+1.6}_{-0.8}$	$1.8^{+0.6}_{-0.4}$	$2.4^{+5.8}_{-2.2}$	$0.1^{+0.1}_{-0.1}$	$0.4^{+10.9}_{-8.7}$	0.14/0.8/0.06
	Cond. on $m_{1,2}$ and $\chi_{\rm eff}$	$1.0^{+1.6}_{-0.8}$	$1.8^{+0.6}_{-0.3}$	$2.1^{+6.1}_{-2.0}$	$0.0^{+0.2}_{--0.0}$	$0.3^{+11.3}_{-9.4}$	0.12/0.84/0.04
	Posterior	$0.8^{+1.1}_{-0.6}$	$1.8^{+0.6}_{-0.3}$	$1.8^{+4.9}_{-1.7}$	$0.0^{+0.2}_{--0.0}$	$0.3^{+12.4}_{-10.0}$	0.1/0.87/0.03
GW170729	Uninformative Prior	$2.6^{+5.6}_{-2.0}$	$86.4^{+234.7}_{-71.5}$	$3.7^{+10.0}_{-3.5}$	$5.0^{+11.6}_{-4.4}$	$17.8^{+565.1}_{-403.0}$	0.2/0.72/0.08
	Cond. on $m_{1,2}$	$2.2^{+3.6}_{-1.7}$	$42.4^{+22.5}_{-18.5}$	$4.0^{+9.3}_{-3.8}$	$2.0^{+2.4}_{-1.3}$	$12.9^{+268.5}_{-219.3}$	0.17/0.75/0.08
	Cond. on $m_{1,2}$ and $\chi_{\rm eff}$	$1.9^{+2.3}_{-1.3}$	$49.5^{+22.3}_{-21.2}$	$4.7^{+10.1}_{-4.4}$	$1.8^{+1.5}_{-1.0}$	$-0.0^{+343.2}_{-303.6}$	0.22/0.65/0.13
	Posterior	$1.7^{+2.1}_{-1.1}$	$50.3^{+21.1}_{-22.0}$	$4.5^{+9.8}_{-4.2}$	$1.8^{+1.4}_{-1.1}$	$-0.9^{+366.4}_{-340.1}$	0.21/0.68/0.12
GW170809	Uninformative Prior	$1.8^{+5.8}_{-1.4}$	$14.0^{+20.2}_{-10.3}$	$2.7^{+6.9}_{-2.5}$	$0.8^{+4.5}_{-0.7}$	$6.9^{+121.9}_{-66.8}$	0.11/0.84/0.05
	Cond. on $m_{1,2}$	$1.7^{+2.4}_{-1.3}$	$16.0^{+6.0}_{-4.7}$	$3.4^{+8.2}_{-3.2}$	$0.6^{+0.7}_{-0.4}$	$3.1^{+94.6}_{-76.5}$	0.18/0.74/0.08
	Cond. on $m_{1,2}$ and $\chi_{\rm eff}$	$1.5^{+2.2}_{-1.1}$	$16.7^{+5.9}_{-4.5}$	$3.2^{+8.6}_{-3.0}$	$0.5^{+0.7}_{-0.3}$	$1.5^{+102.3}_{-87.3}$	0.18/0.76/0.06
	Posterior	$1.2^{+1.9}_{-0.9}$	$16.7^{+5.7}_{-4.5}$	$2.8^{+7.9}_{-2.6}$	$0.5^{+0.7}_{-0.3}$	$1.5^{+106.0}_{-96.3}$	0.15/0.8/0.05
GW170814	Uninformative Prior	$1.8^{+5.8}_{-1.4}$	$13.7^{+20.4}_{-9.9}$	$2.7^{+6.9}_{-2.5}$	$0.8^{+4.4}_{-0.7}$	$6.6^{+121.2}_{-69.8}$	0.11/0.85/0.05
	Cond. on $m_{1,2}$	$1.5^{+1.9}_{-1.1}$	$14.0^{+3.1}_{-3.1}$	$2.4^{+7.7}_{-2.3}$	$0.3^{+0.4}_{-0.2}$	$0.3^{+44.7}_{-36.8}$	0.28/0.6/0.12
	Cond. on $m_{1,2}$ and $\chi_{\rm eff}$	$1.4^{+1.7}_{-1.1}$	$14.5^{+2.8}_{-2.7}$	$2.3^{+8.0}_{-2.2}$	$0.3^{+0.3}_{-0.2}$	$-0.0^{+45.7}_{-40.5}$	0.27/0.63/0.1
	Posterior	$1.5^{+1.5}_{-1.1}$	$14.4^{+2.6}_{-2.6}$	$2.3^{+7.9}_{-2.2}$	$0.3^{+0.3}_{-0.2}$	$-0.0^{+39.3}_{-32.7}$	0.29/0.61/0.1
GW170818	Uninformative Prior	$1.8^{+5.8}_{-1.4}$	$14.1^{+20.6}_{-10.3}$	$2.7^{+6.8}_{-2.5}$	$0.8^{+4.5}_{-0.7}$	$6.6^{+121.8}_{-67.9}$	0.11/0.85/0.05
	Cond. on $m_{1,2}$	$1.7^{+2.2}_{-1.3}$	$18.7^{+5.7}_{-5.3}$	$3.1^{+8.4}_{-2.9}$	$0.6^{+0.6}_{-0.4}$	$1.6^{+86.2}_{-71.9}$	0.23/0.68/0.1
	Cond. on $m_{1,2}$ and $\chi_{\rm eff}$	$1.8^{+2.3}_{-1.4}$	$18.0^{+6.2}_{-5.2}$	$3.0^{+8.2}_{-2.8}$	$0.6^{+0.7}_{-0.4}$	$2.8^{+81.1}_{-60.4}$	0.21/0.71/0.08
	Posterior	$1.9^{+2.1}_{-1.3}$	$17.9^{+5.9}_{-5.1}$	$3.1^{+7.6}_{-2.9}$	$0.6^{+0.6}_{-0.4}$	$3.1^{+60.3}_{-45.7}$	0.22/0.7/0.07
GW170823	Uninformative Prior	$2.5^{+5.7}_{-1.9}$	$84.1^{+233.1}_{-69.1}$	$3.7^{+10.1}_{-3.5}$	$4.9^{+11.5}_{-4.3}$	$18.3^{+584.4}_{-411.1}$	0.2/0.72/0.09
	Cond. on $m_{1,2}$	$1.8^{+2.6}_{-1.3}$	$26.4^{+10.2}_{-9.0}$	$3.3^{+8.8}_{-3.1}$	$0.9^{+1.1}_{-0.6}$	$2.9^{+129.0}_{-103.2}$	0.22/0.68/0.1
	Cond. on $m_{1,2}$ and $\chi_{\rm eff}$	$1.7^{+2.3}_{-1.3}$	$27.4^{+10.8}_{-9.4}$	$3.2^{+9.1}_{-3.0}$	$0.8^{+1.0}_{-0.5}$	$1.0^{+138.0}_{-116.0}$	0.22/0.7/0.08
	Posterior	$1.7^{+2.4}_{-1.3}$	$27.6^{+10.1}_{-9.6}$	$3.2^{+9.3}_{-3.0}$	$0.8^{+1.0}_{-0.5}$	$1.1^{+128.4}_{-109.6}$	0.22/0.7/0.08
GW190403_051519	Uninformative Prior	$5.6^{+15.3}_{-4.8}$	$183.3^{+1080.4}_{-148.1}$	$2.7^{+9.3}_{-2.5}$	$29.2^{+221.3}_{-26.7}$	$140.3^{+1349.0}_{-307.8}$	0.08/0.88/0.04
	Cond. on $m_{1,2}$	$5.3^{+12.9}_{-4.4}$	$102.0^{+109.6}_{-69.4}$	$3.2^{+8.5}_{-2.9}$	$16.3^{+13.9}_{-11.4}$	$79.5^{+694.2}_{-204.5}$	0.06/0.9/0.03
	Cond. on $m_{1,2}$ and $\chi_{\rm eff}$	$2.5^{+3.1}_{-1.6}$	$153.7^{+106.5}_{-77.5}$	$5.2^{+9.5}_{-4.8}$	$8.8^{+4.1}_{-4.2}$	$102.2^{+1167.0}_{-1010.7}$	0.12/0.76/0.12

	Posterior	$2.2^{+3.1}_{-1.4}$	$160.7^{+101.8}_{-88.5}$	$4.7^{+9.9}_{-4.3}$	$8.2^{+4.0}_{-3.8}$	$95.0^{+1250.3}_{-1078.4}$	0.17/0.75/0.08
GW190408_181802	Uninformative Prior	$2.1^{+6.2}_{-1.7}$	$8.9^{+8.7}_{-5.0}$	$2.8^{+6.9}_{-2.6}$	$0.8^{+1.2}_{-0.6}$	$6.2^{+70.6}_{-52.0}$	0.08/0.88/0.04
	Cond. on $m_{1,2}$	$1.6^{+2.1}_{-1.2}$	$10.8^{+3.5}_{-3.0}$	$3.2^{+7.9}_{-3.0}$	$0.3^{+0.5}_{-0.2}$	$1.6^{+58.7}_{-46.0}$	0.19/0.73/0.08
	Cond. on $m_{1,2}$ and $\chi_{\rm eff}$	$1.5^{+2.0}_{-1.2}$	$10.7^{+3.8}_{-2.7}$	$2.9^{+8.0}_{-2.7}$	$0.3^{+0.4}_{-0.2}$	$1.7^{+56.8}_{-47.4}$	0.17/0.77/0.06
	Posterior	$1.3^{+1.6}_{-1.0}$	$10.7^{+3.8}_{-2.9}$	$2.6^{+7.4}_{-2.4}$	$0.3^{+0.4}_{-0.2}$	$1.8^{+62.8}_{-53.6}$	0.1/0.82/0.07
GW190412	Uninformative Prior	$2.2^{+6.5}_{-1.8}$	$4.6^{+3.3}_{-2.0}$	$2.4^{+5.7}_{-2.2}$	$0.6^{+0.8}_{-0.5}$	$4.3^{+42.6}_{-24.6}$	0.04/0.93/0.02
	Cond. on $m_{1,2}$	$3.0^{+5.5}_{-2.6}$	$4.0^{+4.3}_{-1.5}$	$2.3^{+3.8}_{-2.1}$	$0.8^{+0.4}_{-0.4}$	$5.3^{+41.4}_{-8.8}$	0.01/0.98/0.01
	Cond. on $m_{1,2}$ and $\chi_{\rm eff}$	$2.9^{+2.8}_{-2.3}$	$4.8^{+1.2}_{-0.9}$	$2.6^{+4.0}_{-2.3}$	$0.7^{+0.2}_{-0.3}$	$5.8^{+35.3}_{-5.6}$	0.01/0.98/0.01
	Posterior	$2.1^{+1.4}_{-1.3}$	$4.6^{+0.8}_{-0.6}$	$2.7^{+3.6}_{-2.4}$	$0.7^{+0.2}_{-0.2}$	$8.6^{+23.9}_{-8.1}$	0.0/0.99/0.0
GW190413_052954	Uninformative Prior	$2.5^{+7.3}_{-2.0}$	$22.5^{+26.4}_{-12.9}$	$3.3^{+8.1}_{-3.1}$	$1.9^{+3.6}_{-1.5}$	$15.2^{+187.1}_{-122.6}$	0.1/0.86/0.04
	Cond. on $m_{1,2}$	$1.9^{+3.1}_{-1.4}$	$26.3^{+14.6}_{-10.5}$	$3.8^{+8.7}_{-3.5}$	$1.1^{+1.5}_{-0.7}$	$7.4^{+169.5}_{-143.2}$	0.18/0.75/0.08
	Cond. on $m_{1,2}$ and $\chi_{\rm eff}$	$1.9^{+2.9}_{-1.4}$	$26.5^{+17.2}_{-11.9}$	$3.6^{+8.8}_{-3.4}$	$1.1^{+1.3}_{-0.7}$	$6.6^{+175.1}_{-135.3}$	0.17/0.76/0.07
	Posterior	$1.7^{+2.8}_{-1.3}$	$27.0^{+16.3}_{-12.2}$	$3.5^{+8.8}_{-3.3}$	$1.1^{+1.2}_{-0.7}$	$5.7^{+180.1}_{-136.9}$	0.16/0.77/0.07
GW190413_134308	Uninformative Prior	$2.9^{+7.6}_{-2.2}$	$96.4^{+201.4}_{-81.5}$	$3.8^{+10.0}_{-3.5}$	$7.2^{+11.6}_{-6.1}$	$34.2^{+661.6}_{-486.6}$	0.15/0.78/0.07
	Cond. on $m_{1,2}$	$2.2^{+3.5}_{-1.6}$	$51.9^{+27.0}_{-23.7}$	$4.0^{+9.7}_{-3.7}$	$2.3^{+2.7}_{-1.5}$	$12.3^{+307.0}_{-300.8}$	0.18/0.73/0.09
	Cond. on $m_{1,2}$ and $\chi_{\rm eff}$	$2.2^{+3.5}_{-1.7}$	$51.2^{+28.2}_{-23.1}$	$3.9^{+9.5}_{-3.7}$	$2.3^{+2.5}_{-1.5}$	$14.0^{+305.4}_{-229.7}$	0.18/0.75/0.06
	Posterior	$2.8^{+3.8}_{-2.1}$	$52.0^{+24.6}_{-22.4}$	$4.0^{+9.7}_{-3.8}$	$2.4^{+2.4}_{-1.6}$	$13.5^{+214.5}_{-161.5}$	0.21/0.71/0.08
GW190421_213856	Uninformative Prior	$2.6^{+7.8}_{-2.0}$	$33.4^{+39.3}_{-21.0}$	$3.5^{+8.6}_{-3.2}$	$2.8^{+4.4}_{-2.1}$	$20.8^{+266.2}_{-181.2}$	0.1/0.85/0.05
	Cond. on $m_{1,2}$	$2.0^{+2.7}_{-1.5}$	$36.8^{+15.2}_{-13.6}$	$3.3^{+9.0}_{-3.1}$	$1.2^{+1.6}_{-0.7}$	$3.4^{+164.9}_{-128.1}$	0.24/0.66/0.1
	Cond. on $m_{1,2}$ and $\chi_{\rm eff}$	$1.9^{+2.8}_{-1.4}$	$36.2^{+16.8}_{-14.1}$	$3.2^{+8.9}_{-3.0}$	$1.2^{+1.5}_{-0.8}$	$4.3^{+160.2}_{-123.5}$	0.22/0.69/0.09
	Posterior	$2.0^{+2.8}_{-1.5}$	$36.6^{+15.7}_{-14.8}$	$3.4^{+9.3}_{-3.2}$	$1.2^{+1.5}_{-0.8}$	$4.4^{+144.3}_{-109.5}$	0.23/0.68/0.09
GW190426_190642	Uninformative Prior	$6.0^{+15.4}_{-5.0}$	$493.1^{+2961.6}_{-427.8}$	$3.4^{+10.7}_{-3.1}$	$67.1^{+501.6}_{-61.5}$	$356.0^{+3757.4}_{-910.3}$	0.1/0.85/0.05
	Cond. on $m_{1,2}$	$2.9^{+5.8}_{-2.1}$	$250.8^{+151.0}_{-125.5}$	$3.9^{+11.4}_{-3.7}$	$11.3^{+22.8}_{-7.2}$	$29.1^{+1133.0}_{-844.5}$	0.25/0.62/0.12
	Cond. on $m_{1,2}$ and $\chi_{\rm eff}$	$2.5^{+3.4}_{-1.7}$	$296.0^{+193.9}_{-148.2}$	$4.2^{+12.3}_{-4.0}$	$11.1^{+11.0}_{-6.9}$	$-3.3^{+1386.9}_{-1314.4}$	0.3/0.54/0.16
	Posterior	$2.7^{+3.8}_{-1.9}$	$298.5^{+202.6}_{-149.4}$	$4.3^{+12.6}_{-4.1}$	$11.3^{+10.5}_{-6.9}$	$-3.1^{+1179.1}_{-1159.5}$	0.34/0.52/0.15
GW190503_185404	Uninformative Prior	$2.5^{+7.4}_{-2.0}$	$21.4^{+26.5}_{-14.0}$	$3.2^{+8.0}_{-2.9}$	$1.9^{+3.1}_{-1.5}$	$14.0^{+174.6}_{-118.4}$	0.09/0.87/0.04
	Cond. on $m_{1,2}$	$1.9^{+3.0}_{-1.4}$	$25.0^{+12.6}_{-10.1}$	$4.0^{+8.7}_{-3.7}$	$1.1^{+1.2}_{-0.7}$	$9.0^{+166.8}_{-153.9}$	0.15/0.78/0.07
	Cond. on $m_{1,2}$ and $\chi_{\rm eff}$	$1.9^{+3.0}_{-1.5}$	$25.0^{+13.7}_{-10.9}$	$3.7^{+8.6}_{-3.4}$	$1.1^{+1.1}_{-0.7}$	$8.1^{+178.2}_{-149.9}$	0.14/0.81/0.05
	Posterior	$1.7^{+2.6}_{-1.3}$	$25.2^{+13.9}_{-11.2}$	$3.4^{+8.3}_{-3.2}$	$1.1^{+1.0}_{-0.7}$	$6.7^{+195.3}_{-174.5}$	0.13/0.82/0.05
GW190512_180714	Uninformative Prior	$2.1^{+6.3}_{-1.7}$	$7.6^{+7.7}_{-4.6}$	$2.6^{+6.9}_{-2.4}$	$0.7^{+1.0}_{-0.5}$	$5.0^{+64.2}_{-40.2}$	0.07/0.89/0.03
	Cond. on $m_{1,2}$	$1.7^{+2.9}_{-1.3}$	$6.4^{+4.0}_{-1.8}$	$3.4^{+6.7}_{-3.1}$	$0.4^{+0.4}_{-0.3}$	$4.9^{+57.3}_{-51.1}$	0.07/0.89/0.03
	Cond. on $m_{1,2}$ and $\chi_{\rm eff}$	$1.4^{+2.6}_{-1.1}$	$6.5^{+4.5}_{-1.3}$	$3.0^{+6.9}_{-2.8}$	$0.4^{+0.3}_{-0.3}$	$4.6^{+63.5}_{-59.9}$	0.06/0.91/0.02
	Posterior	$0.8^{+1.4}_{-0.6}$	$6.6^{+4.9}_{-1.4}$	$2.2^{+5.8}_{-2.0}$	$0.4^{+0.3}_{-0.3}$	$3.2^{+87.8}_{-102.6}$	0.02/0.95/0.02
GW190513_205428	Uninformative Prior	$2.5^{+7.8}_{-2.0}$	$18.0^{+20.6}_{-11.2}$	$3.1^{+7.5}_{-2.9}$	$1.7^{+2.6}_{-1.3}$	$11.9^{+145.1}_{-100.9}$	0.09/0.86/0.04
	Cond. on $m_{1,2}$	$2.0^{+4.1}_{-1.5}$	$14.9^{+10.7}_{-5.5}$	$3.7^{+7.6}_{-3.4}$	$1.1^{+1.1}_{-0.8}$	$11.3^{+134.0}_{-108.3}$	0.09/0.87/0.04
	Cond. on $m_{1,2}$ and $\chi_{\rm eff}$	$1.8^{+3.0}_{-1.4}$	$16.1^{+11.0}_{-5.2}$	$3.7^{+8.0}_{-3.4}$	$1.0^{+0.8}_{-0.7}$	$10.3^{+166.7}_{-128.0}$	0.09/0.87/0.04
	Posterior	$1.3^{+2.0}_{-1.0}$	$16.5^{+10.9}_{-5.7}$	$3.4^{+7.4}_{-3.1}$	$1.0^{+0.7}_{-0.7}$	$10.6^{+202.0}_{-198.5}$	0.07/0.89/0.04
GW190514_065416	Uninformative Prior	$3.3^{+11.2}_{-2.6}$	$60.3^{+91.7}_{-48.6}$	$3.4^{+9.3}_{-3.2}$	$6.2^{+13.4}_{-5.3}$	$34.7^{+521.3}_{-283.5}$	0.1/0.86/0.04
	Cond. on $m_{1,2}$	$2.0^{+3.0}_{-1.5}$	$38.9^{+18.0}_{-15.8}$	$3.5^{+9.3}_{-3.2}$	$1.4^{+2.0}_{-0.9}$	$5.8^{+212.8}_{-161.1}$	0.21/0.69/0.1
	Cond. on $m_{1,2}$ and $\chi_{\rm eff}$	$2.4^{+3.4}_{-1.8}$	$35.2^{+20.9}_{-16.3}$	$3.4^{+8.6}_{-3.2}$	$1.6^{+2.1}_{-1.0}$	$10.3^{+172.6}_{-135.6}$	0.2/0.71/0.09
	Posterior	$2.3^{+3.5}_{-1.7}$	$35.1^{+20.9}_{-16.4}$	$3.5^{+8.5}_{-3.3}$	$1.6^{+2.0}_{-1.0}$	$11.2^{+155.7}_{-110.5}$	0.21/0.71/0.08
GW190517_055101	Uninformative Prior	$2.7^{+10.0}_{-2.2}$	$23.0^{+30.4}_{-15.2}$	$2.9^{+8.2}_{-2.7}$	$2.3^{+4.9}_{-1.8}$	$14.4^{+188.5}_{-101.3}$	0.09/0.87/0.04
	Cond. on $m_{1,2}$	$1.9^{+3.0}_{-1.4}$	$22.1^{+10.2}_{-7.5}$	$3.8^{+8.4}_{-3.5}$	$0.9^{+1.4}_{-0.6}$	$6.7^{+147.4}_{-120.3}$	0.16/0.77/0.07
	Cond. on $m_{1,2}$ and $\chi_{\rm eff}$	$1.6^{+1.5}_{-1.0}$	$26.5^{+9.1}_{-7.6}$	$4.8^{+8.4}_{-4.3}$	$0.9^{+0.7}_{-0.5}$	$-3.3^{+212.6}_{-199.2}$	0.26/0.56/0.19
	Posterior	$1.6^{+1.7}_{-1.0}$	$26.3^{+9.3}_{-7.0}$	$4.5^{+8.8}_{-4.0}$	$0.8^{+0.7}_{-0.4}$	$-2.2^{+170.0}_{-156.0}$	0.27/0.54/0.2

GW190519_153544	Uninformative Prior	$3.1^{+9.1}_{-2.5}$	$65.1^{+63.3}_{-38.5}$	$3.8^{+9.1}_{-3.5}$	$5.9^{+10.4}_{-4.4}$	$42.0^{+512.4}_{-294.8}$	0.11/0.84/0.05
	Cond. on $m_{1,2}$	$2.4^{+3.8}_{-1.8}$	$63.7^{+34.7}_{-27.4}$	$5.0^{+9.9}_{-4.6}$	$3.4^{+2.9}_{-1.9}$	$31.4^{+449.4}_{-413.5}$	0.14/0.8/0.06
	Cond. on $m_{1,2}$ and $\chi_{\rm eff}$	$2.1^{+2.2}_{-1.4}$	$75.9^{+30.8}_{-30.1}$	$6.1^{+11.0}_{-5.6}$	$2.9^{+1.8}_{-1.5}$	$9.1^{+629.1}_{-583.5}$	0.2/0.68/0.11
	Posterior	$2.0^{+2.0}_{-1.3}$	$77.2^{+27.1}_{-32.3}$	$5.8^{+9.8}_{-5.3}$	$2.9^{+1.5}_{-1.4}$	$10.1^{+660.4}_{-622.9}$	0.19/0.68/0.12
GW190521	Uninformative Prior	$2.8^{+7.4}_{-2.2}$	$55.6^{+58.8}_{-32.4}$	$3.9^{+9.4}_{-3.6}$	$4.6^{+8.3}_{-3.6}$	$37.1^{+459.8}_{-308.7}$	0.11/0.84/0.05
	Cond. on $m_{1,2}$	$2.2^{+3.5}_{-1.6}$	$63.5^{+28.1}_{-26.6}$	$3.7^{+9.7}_{-3.5}$	$2.4^{+3.5}_{-1.5}$	$8.5^{+330.9}_{-236.3}$	0.23/0.67/0.1
	Cond. on $m_{1,2}$ and $\chi_{\rm eff}$	$2.2^{+3.2}_{-1.6}$	$65.5^{+32.1}_{-31.2}$	$3.7^{+10.0}_{-3.5}$	$2.4^{+2.8}_{-1.5}$	$7.2^{+318.7}_{-223.2}$	0.23/0.67/0.1
	Posterior	$3.3^{+3.0}_{-2.3}$	$67.1^{+32.3}_{-31.8}$	$4.0^{+10.1}_{-3.8}$	$2.7^{+2.6}_{-1.5}$	$6.4^{+189.4}_{-123.0}$	0.33/0.59/0.08
GW190521_074359	Uninformative Prior	$2.6^{+8.0}_{-2.1}$	$21.7^{+19.0}_{-12.6}$	$3.1^{+7.9}_{-2.9}$	$2.1^{+2.6}_{-1.6}$	$14.5^{+168.9}_{-113.8}$	0.09/0.87/0.04
	Cond. on $m_{1,2}$	$1.8^{+2.4}_{-1.3}$	$27.6^{+7.7}_{-8.0}$	$3.5^{+8.8}_{-3.3}$	$0.9^{+0.8}_{-0.5}$	$2.6^{+126.8}_{-111.2}$	0.23/0.67/0.1
	Cond. on $m_{1,2}$ and $\chi_{\rm eff}$	$1.7^{+1.9}_{-1.3}$	$29.3^{+6.6}_{-8.2}$	$3.4^{+9.3}_{-3.2}$	$0.8^{+0.7}_{-0.5}$	$-0.0^{+135.1}_{-125.2}$	0.23/0.69/0.08
	Posterior	$1.4^{+1.4}_{-1.0}$	$29.6^{+5.9}_{-8.5}$	$3.1^{+7.7}_{-2.9}$	$0.8^{+0.6}_{-0.5}$	$-0.3^{+146.1}_{-148.4}$	0.13/0.78/0.09
GW190527_092055	Uninformative Prior	$3.5^{+12.4}_{-2.9}$	$51.9^{+76.2}_{-41.9}$	$3.0^{+8.9}_{-2.8}$	$5.8^{+13.8}_{-4.9}$	$30.6^{+431.6}_{-225.1}$	0.08/0.89/0.04
	Cond. on $m_{1,2}$	$2.0^{+3.7}_{-1.5}$	$21.2^{+30.0}_{-9.2}$	$3.7^{+8.1}_{-3.4}$	$1.1^{+2.0}_{-0.8}$	$9.1^{+166.4}_{-123.3}$	0.14/0.8/0.06
	Cond. on $m_{1,2}$ and $\chi_{\rm eff}$	$1.8^{+3.1}_{-1.3}$	$22.9^{+32.1}_{-10.4}$	$3.8^{+8.8}_{-3.5}$	$1.1^{+1.7}_{-0.8}$	$7.1^{+195.2}_{-160.6}$	0.14/0.79/0.07
	Posterior	$1.9^{+3.3}_{-1.5}$	$23.4^{+31.6}_{-10.9}$	$3.8^{+8.9}_{-3.5}$	$1.1^{+1.7}_{-0.8}$	$6.2^{+160.6}_{-142.6}$	0.16/0.78/0.06
GW190602_175927	Uninformative Prior	$4.0^{+13.1}_{-3.3}$	$99.4^{+156.8}_{-81.1}$	$3.2^{+9.8}_{-3.0}$	$11.7^{+32.0}_{-10.3}$	$61.3^{+897.3}_{-350.5}$	0.09/0.87/0.04
	Cond. on $m_{1,2}$	$2.4^{+3.8}_{-1.8}$	$82.3^{+39.3}_{-39.2}$	$4.0^{+10.2}_{-3.7}$	$3.5^{+3.9}_{-2.1}$	$15.1^{+432.0}_{-364.4}$	0.21/0.69/0.1
	Cond. on $m_{1,2}$ and $\chi_{\rm eff}$	$2.1^{+3.1}_{-1.6}$	$87.8^{+41.3}_{-41.3}$	$4.1^{+10.8}_{-3.8}$	$3.4^{+3.1}_{-2.1}$	$5.8^{+509.7}_{-442.9}$	0.22/0.7/0.09
	Posterior	$2.0^{+2.8}_{-1.5}$	$89.9^{+39.0}_{-44.6}$	$4.1^{+10.0}_{-3.8}$	$3.4^{+3.0}_{-2.0}$	$3.6^{+516.1}_{-450.7}$	0.2/0.71/0.09
GW190620_030421	Uninformative Prior	$3.3^{+10.6}_{-2.6}$	$62.8^{+91.6}_{-47.9}$	$3.4^{+9.4}_{-3.2}$	$6.5^{+13.3}_{-5.5}$	$36.5^{+570.8}_{-244.8}$	0.09/0.86/0.04
	Cond. on $m_{1,2}$	$2.3^{+4.1}_{-1.7}$	$51.5^{+29.3}_{-24.5}$	$4.4^{+9.5}_{-4.1}$	$2.7^{+3.1}_{-1.7}$	$21.7^{+383.6}_{-269.7}$	0.16/0.78/0.07
	Cond. on $m_{1,2}$ and $\chi_{\rm eff}$	$2.0^{+2.5}_{-1.3}$	$60.9^{+29.0}_{-26.7}$	$5.3^{+10.2}_{-4.9}$	$2.3^{+1.9}_{-1.3}$	$4.3^{+446.3}_{-377.6}$	0.21/0.67/0.12
	Posterior	$1.8^{+2.2}_{-1.2}$	$61.6^{+27.6}_{-28.3}$	$4.9^{+9.6}_{-4.5}$	$2.3^{+1.8}_{-1.2}$	$4.9^{+479.1}_{-447.0}$	0.19/0.69/0.12
GW190630_185205	Uninformative Prior	$2.4^{+7.3}_{-1.9}$	$16.9^{+18.6}_{-11.4}$	$3.1^{+7.7}_{-2.9}$	$1.6^{+3.4}_{-1.4}$	$11.8^{+158.8}_{-85.2}$	0.08/0.88/0.04
	Cond. on $m_{1,2}$	$1.7^{+2.6}_{-1.2}$	$15.3^{+6.4}_{-4.3}$	$3.8^{+8.2}_{-3.5}$	$0.6^{+0.7}_{-0.4}$	$5.1^{+106.8}_{-90.3}$	0.15/0.79/0.06
	Cond. on $m_{1,2}$ and $\chi_{\rm eff}$	$1.6^{+2.1}_{-1.2}$	$16.2^{+6.2}_{-3.9}$	$3.6^{+8.9}_{-3.3}$	$0.6^{+0.6}_{-0.4}$	$2.8^{+116.0}_{-105.5}$	0.14/0.81/0.05
	Posterior	$1.1^{+1.4}_{-0.8}$	$16.4^{+6.4}_{-4.2}$	$2.9^{+6.7}_{-2.7}$	$0.6^{+0.6}_{-0.4}$	$1.6^{+135.2}_{-134.0}$	0.08/0.87/0.05
GW190701_203306	Uninformative Prior	$2.8^{+8.4}_{-2.2}$	$41.3^{+46.2}_{-25.7}$	$3.5^{+8.7}_{-3.3}$	$3.7^{+5.6}_{-2.8}$	$24.9^{+347.1}_{-207.7}$	0.11/0.85/0.05
	Cond. on $m_{1,2}$	$2.1^{+3.0}_{-1.6}$	$50.1^{+20.9}_{-20.6}$	$3.6^{+9.5}_{-3.4}$	$1.8^{+2.1}_{-1.1}$	$6.3^{+246.7}_{-185.8}$	0.23/0.67/0.1
	Cond. on $m_{1,2}$ and $\chi_{\rm eff}$	$2.2^{+3.1}_{-1.7}$	$48.7^{+22.3}_{-20.7}$	$3.4^{+9.4}_{-3.2}$	$1.8^{+2.1}_{-1.1}$	$8.5^{+223.2}_{-164.4}$	0.22/0.7/0.08
	Posterior	$2.0^{+2.9}_{-1.5}$	$48.9^{+22.3}_{-22.0}$	$3.3^{+9.3}_{-3.1}$	$1.8^{+2.0}_{-1.2}$	$8.2^{+236.1}_{-171.8}$	0.2/0.72/0.09
GW190706_222641	Uninformative Prior	$3.1^{+8.4}_{-2.5}$	$85.6^{+121.6}_{-60.9}$	$3.9^{+9.9}_{-3.6}$	$6.9^{+12.1}_{-5.3}$	$45.2^{+651.9}_{-433.4}$	0.13/0.81/0.06
	Cond. on $m_{1,2}$	$2.7^{+4.5}_{-2.1}$	$81.4^{+51.3}_{-42.6}$	$4.9^{+10.1}_{-4.6}$	$4.9^{+4.3}_{-2.9}$	$40.2^{+632.0}_{-474.6}$	0.15/0.79/0.06
	Cond. on $m_{1,2}$ and $\chi_{\rm eff}$	$2.3^{+2.9}_{-1.6}$	$97.3^{+49.5}_{-49.0}$	$5.5^{+11.3}_{-5.0}$	$4.3^{+2.7}_{-2.2}$	$20.3^{+779.2}_{-682.7}$	0.19/0.7/0.11
	Posterior	$1.9^{+2.5}_{-1.3}$	$100.3^{+42.6}_{-54.2}$	$5.1^{+10.4}_{-4.6}$	$4.1^{+2.5}_{-2.2}$	$18.4^{+767.9}_{-706.7}$	0.19/0.7/0.11
GW190707_093326	Uninformative Prior	$1.9^{+6.8}_{-1.5}$	$2.1^{+1.3}_{-0.8}$	$1.9^{+5.0}_{-1.7}$	$0.3^{+0.5}_{-0.3}$	$1.9^{+17.5}_{-8.9}$	0.04/0.94/0.02
	Cond. on $m_{1,2}$	$1.2^{+1.6}_{-0.9}$	$2.3^{+0.8}_{-0.5}$	$2.7^{+6.0}_{-2.5}$	$0.1^{+0.1}_{-0.1}$	$0.7^{+15.1}_{-11.8}$	0.13/0.82/0.05
	Cond. on $m_{1,2}$ and $\chi_{\rm eff}$	$1.1^{+1.6}_{-0.9}$	$2.3^{+0.9}_{-0.4}$	$2.3^{+6.2}_{-2.1}$	$0.1^{+0.1}_{-0.1}$	$0.6^{+14.9}_{-13.7}$	0.12/0.85/0.04
	Posterior	$0.8^{+1.1}_{-0.6}$	$2.3^{+1.0}_{-0.4}$	$1.9^{+5.3}_{-1.8}$	$0.1^{+0.1}_{-0.1}$	$0.6^{+18.5}_{-17.9}$	0.07/0.89/0.03
GW190708_232457	Uninformative Prior	$2.1^{+7.1}_{-1.7}$	$4.3^{+2.9}_{-1.8}$	$2.3^{+5.7}_{-2.1}$	$0.5^{+1.0}_{-0.4}$	$3.6^{+35.6}_{-20.0}$	0.05/0.92/0.03
	Cond. on $m_{1,2}$	$1.3^{+1.9}_{-0.9}$	$5.0^{+1.7}_{-1.0}$	$2.9^{+6.8}_{-2.7}$	$0.2^{+0.2}_{-0.1}$	$1.0^{+29.2}_{-24.2}$	0.16/0.77/0.07
	Cond. on $m_{1,2}$ and $\chi_{\rm eff}$	$1.2^{+1.8}_{-1.0}$	$5.1^{+1.7}_{-0.8}$	$2.5^{+7.3}_{-2.3}$	$0.1^{+0.3}_{-0.1}$	$0.6^{+31.0}_{-24.3}$	0.14/0.81/0.04
	Posterior	$0.8^{+1.5}_{-0.6}$	$5.1^{+1.8}_{-0.8}$	$2.0^{+5.7}_{-1.9}$	$0.1^{+0.3}_{-0.1}$	$0.8^{+31.0}_{-27.7}$	0.06/0.9/0.05
GW190719_215514	Uninformative Prior	$3.0^{+9.3}_{-2.4}$	$64.9^{+88.8}_{-49.7}$	$3.7^{+9.3}_{-3.4}$	$5.8^{+13.8}_{-4.9}$	$39.3^{+560.8}_{-319.5}$	0.1/0.85/0.05
	Cond. on $m_{1,2}$	$2.1^{+4.6}_{-1.6}$	$25.0^{+18.4}_{-11.0}$	$3.7^{+8.5}_{-3.4}$	$1.5^{+2.7}_{-1.1}$	$12.6^{+185.8}_{-177.5}$	0.13/0.82/0.05

	Cond. on $m_{1,2}$ and χ_{eff}	$1.9^{+2.7}_{-1.3}$	$29.0^{+19.9}_{-12.9}$	$4.4^{+9.5}_{-4.0}$	$1.3^{+1.6}_{-0.9}$	$9.2^{+225.5}_{-196.7}$	0.15/0.75/0.1
	Posterior	$1.8^{+2.6}_{-1.3}$	$29.3^{+18.5}_{-13.3}$	$4.3^{+8.6}_{-3.9}$	$1.3^{+1.5}_{-0.9}$	$9.6^{+205.4}_{-198.0}$	0.15/0.74/0.11
GW190720_000836	Uninformative Prior	$2.0^{+7.0}_{-1.7}$	$2.3^{+1.6}_{-0.9}$	$2.0^{+4.9}_{-1.8}$	$0.3^{+0.6}_{-0.3}$	$2.0^{+20.0}_{-10.3}$	0.04/0.94/0.02
	Cond. on $m_{1,2}$	$1.3^{+2.8}_{-1.0}$	$2.3^{+1.3}_{-0.6}$	$2.7^{+5.6}_{-2.5}$	$0.1^{+0.3}_{-0.1}$	$1.5^{+19.3}_{-14.4}$	0.09/0.88/0.04
	Cond. on $m_{1,2}$ and χ_{eff}	$1.3^{+2.2}_{-0.9}$	$2.5^{+1.1}_{-0.4}$	$2.8^{+6.1}_{-2.6}$	$0.1^{+0.2}_{-0.1}$	$1.4^{+18.8}_{-14.7}$	0.09/0.88/0.03
	Posterior	$1.0^{+1.6}_{-0.7}$	$2.5^{+1.2}_{-0.4}$	$2.8^{+5.6}_{-2.6}$	$0.1^{+0.2}_{-0.1}$	$1.7^{+27.6}_{-20.9}$	0.07/0.9/0.03
GW190725_174728	Uninformative Prior	$1.9^{+6.9}_{-1.6}$	$1.8^{+1.6}_{-0.9}$	$1.9^{+4.9}_{-1.8}$	$0.2^{+0.6}_{-0.2}$	$1.5^{+17.0}_{-8.3}$	0.04/0.94/0.02
	Cond. on $m_{1,2}$	$1.4^{+4.1}_{-1.1}$	$1.8^{+1.1}_{-0.5}$	$2.3^{+5.4}_{-2.1}$	$0.1^{+0.4}_{-0.1}$	$1.3^{+15.3}_{-10.9}$	0.07/0.9/0.03
	Cond. on $m_{1,2}$ and χ_{eff}	$1.3^{+3.2}_{-1.0}$	$1.8^{+1.5}_{-0.3}$	$2.2^{+5.3}_{-2.0}$	$0.1^{+0.4}_{-0.1}$	$1.3^{+16.0}_{-12.3}$	0.07/0.91/0.02
	Posterior	$1.2^{+2.7}_{-0.9}$	$1.8^{+1.5}_{-0.3}$	$2.2^{+5.2}_{-2.0}$	$0.1^{+0.3}_{-0.1}$	$1.3^{+17.8}_{-14.3}$	0.08/0.9/0.02
GW190727_060333	Uninformative Prior	$2.5^{+6.7}_{-1.9}$	$29.1^{+28.2}_{-15.8}$	$3.5^{+8.3}_{-3.2}$	$2.4^{+3.9}_{-1.8}$	$19.2^{+230.6}_{-170.6}$	0.1/0.86/0.04
	Cond. on $m_{1,2}$	$1.9^{+2.7}_{-1.4}$	$34.3^{+12.8}_{-12.5}$	$3.3^{+8.9}_{-3.1}$	$1.1^{+1.4}_{-0.7}$	$2.7^{+153.6}_{-114.9}$	0.24/0.65/0.11
	Cond. on $m_{1,2}$ and χ_{eff}	$1.8^{+2.3}_{-1.3}$	$36.1^{+13.6}_{-13.0}$	$3.3^{+9.3}_{-3.1}$	$1.0^{+1.3}_{-0.6}$	$0.1^{+162.6}_{-130.9}$	0.24/0.66/0.1
	Posterior	$1.8^{+2.4}_{-1.4}$	$36.2^{+13.0}_{-12.7}$	$3.2^{+9.4}_{-3.0}$	$1.0^{+1.1}_{-0.6}$	$0.1^{+144.0}_{-105.1}$	0.26/0.64/0.1
GW190728_064510	Uninformative Prior	$2.1^{+6.9}_{-1.8}$	$1.8^{+1.5}_{-0.8}$	$1.8^{+4.7}_{-1.6}$	$0.3^{+0.4}_{-0.3}$	$1.7^{+16.1}_{-7.8}$	0.04/0.95/0.01
	Cond. on $m_{1,2}$	$1.3^{+2.5}_{-1.0}$	$2.3^{+1.0}_{-0.6}$	$2.6^{+5.8}_{-2.4}$	$0.1^{+0.3}_{-0.1}$	$1.0^{+16.9}_{-12.8}$	0.11/0.85/0.05
	Cond. on $m_{1,2}$ and χ_{eff}	$1.2^{+2.1}_{-0.9}$	$2.4^{+1.0}_{-0.3}$	$2.7^{+6.2}_{-2.5}$	$0.1^{+0.2}_{-0.1}$	$0.9^{+16.7}_{-13.6}$	0.1/0.86/0.04
	Posterior	$0.8^{+1.3}_{-0.6}$	$2.4^{+1.1}_{-0.3}$	$2.1^{+5.0}_{-1.9}$	$0.1^{+0.2}_{-0.1}$	$0.8^{+24.0}_{-20.6}$	0.06/0.9/0.03
GW190731_140936	Uninformative Prior	$3.0^{+9.4}_{-2.4}$	$39.0^{+50.9}_{-26.6}$	$3.4^{+8.4}_{-3.2}$	$3.9^{+7.3}_{-3.2}$	$24.6^{+304.2}_{-210.2}$	0.1/0.86/0.04
	Cond. on $m_{1,2}$	$2.0^{+3.2}_{-1.5}$	$36.0^{+17.0}_{-15.9}$	$3.7^{+9.2}_{-3.5}$	$1.5^{+1.6}_{-1.0}$	$7.3^{+202.1}_{-172.7}$	0.19/0.72/0.09
	Cond. on $m_{1,2}$ and χ_{eff}	$1.9^{+2.7}_{-1.5}$	$38.0^{+17.3}_{-17.1}$	$3.7^{+9.5}_{-3.4}$	$1.4^{+1.4}_{-0.9}$	$3.2^{+227.6}_{-193.0}$	0.19/0.74/0.07
	Posterior	$1.7^{+2.7}_{-1.3}$	$38.2^{+16.6}_{-17.7}$	$3.5^{+9.4}_{-3.3}$	$1.4^{+1.3}_{-0.9}$	$4.1^{+229.6}_{-198.9}$	0.16/0.76/0.08
GW190803_022701	Uninformative Prior	$2.7^{+8.0}_{-2.1}$	$30.1^{+36.5}_{-18.7}$	$3.3^{+8.3}_{-3.0}$	$2.7^{+5.0}_{-2.1}$	$19.3^{+258.0}_{-155.7}$	0.09/0.86/0.04
	Cond. on $m_{1,2}$	$1.9^{+2.9}_{-1.4}$	$30.8^{+13.7}_{-12.3}$	$3.4^{+9.0}_{-3.2}$	$1.1^{+1.5}_{-0.7}$	$4.8^{+169.4}_{-123.6}$	0.21/0.7/0.09
	Cond. on $m_{1,2}$ and χ_{eff}	$1.9^{+2.9}_{-1.5}$	$30.9^{+14.9}_{-13.2}$	$3.4^{+8.8}_{-3.2}$	$1.1^{+1.4}_{-0.7}$	$4.8^{+150.6}_{-128.1}$	0.19/0.73/0.07
	Posterior	$1.9^{+2.9}_{-1.4}$	$31.1^{+14.7}_{-13.4}$	$3.4^{+8.8}_{-3.2}$	$1.1^{+1.4}_{-0.7}$	$4.8^{+166.0}_{-122.5}$	0.2/0.73/0.07
GW190805_211137	Uninformative Prior	$5.2^{+15.3}_{-4.4}$	$98.0^{+454.5}_{-74.7}$	$2.4^{+8.6}_{-2.2}$	$16.8^{+105.7}_{-15.3}$	$76.3^{+684.0}_{-168.2}$	0.07/0.9/0.03
	Cond. on $m_{1,2}$	$2.3^{+3.9}_{-1.7}$	$60.4^{+32.1}_{-28.8}$	$4.1^{+9.6}_{-3.8}$	$2.7^{+3.8}_{-1.7}$	$14.3^{+336.5}_{-296.5}$	0.19/0.72/0.09
	Cond. on $m_{1,2}$ and χ_{eff}	$2.0^{+2.3}_{-1.4}$	$70.6^{+33.9}_{-31.8}$	$4.7^{+10.5}_{-4.4}$	$2.5^{+2.0}_{-1.4}$	$-1.2^{+448.0}_{-420.1}$	0.24/0.6/0.16
	Posterior	$2.1^{+2.6}_{-1.4}$	$71.4^{+33.4}_{-31.7}$	$4.8^{+10.6}_{-4.4}$	$2.5^{+1.8}_{-1.4}$	$-1.0^{+359.4}_{-335.4}$	0.29/0.57/0.14
GW190814	Uninformative Prior	$2.1^{+8.6}_{-1.7}$	$9.1^{+25.4}_{-8.2}$	$2.4^{+7.6}_{-2.2}$	$0.8^{+1.2}_{-0.7}$	$3.1^{+79.5}_{-53.4}$	0.11/0.85/0.05
	Cond. on $m_{1,2}$	$5.7^{+11.2}_{-5.1}$	$1.0^{+0.7}_{-0.5}$	$0.8^{+1.2}_{-0.7}$	$0.5^{+0.1}_{-0.1}$	$0.7^{+5.5}_{-0.6}$	0.0/0.99/0.0
	Cond. on $m_{1,2}$ and χ_{eff}	$3.0^{+7.0}_{-2.8}$	$0.8^{+0.7}_{-0.1}$	$0.8^{+1.2}_{-0.7}$	$0.5^{+-0.0}_{-0.1}$	$1.1^{+16.1}_{-1.1}$	0.0/1.0/0.0
	Posterior	$0.4^{+0.8}_{-0.3}$	$0.8^{+4.6}_{-0.1}$	$0.8^{+1.1}_{-0.7}$	$0.5^{+-0.0}_{-0.1}$	$7.3^{+61.0}_{-51.0}$	0.0/1.0/0.0
GW190828_063405	Uninformative Prior	$2.4^{+7.1}_{-1.9}$	$16.9^{+18.0}_{-9.7}$	$3.2^{+7.5}_{-3.0}$	$1.5^{+2.5}_{-1.2}$	$11.5^{+136.0}_{-95.8}$	0.09/0.87/0.04
	Cond. on $m_{1,2}$	$1.7^{+2.2}_{-1.2}$	$21.6^{+6.1}_{-6.0}$	$3.0^{+8.4}_{-2.8}$	$0.6^{+0.6}_{-0.4}$	$0.9^{+81.9}_{-66.4}$	0.26/0.63/0.11
	Cond. on $m_{1,2}$ and χ_{eff}	$1.6^{+1.6}_{-1.1}$	$23.5^{+5.8}_{-6.2}$	$3.1^{+8.7}_{-2.9}$	$0.6^{+0.4}_{-0.4}$	$-1.0^{+89.1}_{-85.7}$	0.27/0.62/0.11
	Posterior	$1.4^{+1.4}_{-1.0}$	$23.4^{+5.4}_{-5.9}$	$2.8^{+8.0}_{-2.6}$	$0.5^{+0.4}_{-0.3}$	$-1.0^{+82.9}_{-87.7}$	0.24/0.64/0.12
GW190828_065509	Uninformative Prior	$2.2^{+7.9}_{-1.8}$	$8.0^{+8.9}_{-4.7}$	$2.5^{+6.8}_{-2.3}$	$0.8^{+1.5}_{-0.6}$	$5.6^{+71.6}_{-43.5}$	0.07/0.9/0.03
	Cond. on $m_{1,2}$	$2.0^{+3.9}_{-1.6}$	$5.4^{+4.5}_{-1.7}$	$3.2^{+5.8}_{-2.9}$	$0.5^{+0.6}_{-0.3}$	$6.0^{+52.1}_{-46.6}$	0.04/0.94/0.02
	Cond. on $m_{1,2}$ and χ_{eff}	$1.6^{+3.3}_{-1.3}$	$5.6^{+4.8}_{-1.0}$	$3.0^{+5.9}_{-2.8}$	$0.5^{+0.4}_{-0.4}$	$6.1^{+64.8}_{-56.5}$	0.03/0.96/0.01
	Posterior	$1.3^{+2.8}_{-1.0}$	$5.5^{+5.0}_{-1.0}$	$2.5^{+5.3}_{-2.3}$	$0.5^{+0.4}_{-0.4}$	$6.1^{+71.3}_{-63.0}$	0.02/0.97/0.01
GW190910_112807	Uninformative Prior	$2.3^{+5.6}_{-1.8}$	$30.5^{+30.8}_{-16.5}$	$3.7^{+8.7}_{-3.4}$	$2.1^{+3.1}_{-1.6}$	$17.1^{+245.2}_{-178.6}$	0.12/0.83/0.05
	Cond. on $m_{1,2}$	$1.9^{+2.3}_{-1.4}$	$33.5^{+10.3}_{-10.1}$	$3.1^{+8.8}_{-2.9}$	$1.0^{+0.9}_{-0.6}$	$1.6^{+129.3}_{-103.8}$	0.26/0.63/0.12
	Cond. on $m_{1,2}$ and χ_{eff}	$1.7^{+2.2}_{-1.3}$	$34.3^{+10.8}_{-10.0}$	$3.0^{+9.0}_{-2.8}$	$0.9^{+0.8}_{-0.6}$	$0.4^{+129.9}_{-110.5}$	0.26/0.66/0.09

	Posterior	$1.5^{+1.7}_{-1.2}$	$34.4^{+9.7}_{-10.1}$	$2.8^{+8.7}_{-2.6}$	$0.8^{+0.8}_{-0.5}$	$0.4^{+129.5}_{-117.8}$	0.19/0.7/0.11
GW190915_235702	Uninformative Prior	$2.3^{+6.6}_{-1.8}$	$15.7^{+15.0}_{-8.7}$	$3.0^{+7.5}_{-2.7}$	$1.3^{+2.1}_{-1.0}$	$10.2^{+113.0}_{-86.4}$	0.09/0.87/0.04
	Cond. on $m_{1,2}$	$1.8^{+2.7}_{-1.3}$	$19.2^{+8.4}_{-6.7}$	$3.6^{+8.5}_{-3.3}$	$0.8^{+1.0}_{-0.5}$	$5.2^{+122.8}_{-103.9}$	0.17/0.76/0.07
	Cond. on $m_{1,2}$ and $\chi_{\rm eff}$	$1.7^{+2.6}_{-1.3}$	$19.7^{+8.7}_{-7.2}$	$3.5^{+8.5}_{-3.3}$	$0.7^{+1.0}_{-0.4}$	$3.9^{+128.2}_{-106.8}$	0.16/0.78/0.06
	Posterior	$2.2^{+2.7}_{-1.6}$	$19.9^{+7.2}_{-7.3}$	$3.8^{+8.8}_{-3.5}$	$0.8^{+0.9}_{-0.5}$	$5.1^{+82.6}_{-60.7}$	0.18/0.76/0.06
GW190916_200658	Uninformative Prior	$5.9^{+15.4}_{-5.0}$	$308.8^{+2175.0}_{-273.4}$	$2.9^{+10.0}_{-2.7}$	$44.9^{+403.5}_{-41.8}$	$226.9^{+2417.7}_{-486.2}$	0.09/0.87/0.04
	Cond. on $m_{1,2}$	$2.4^{+5.6}_{-1.9}$	$37.4^{+36.8}_{-20.5}$	$3.8^{+9.1}_{-3.5}$	$2.5^{+4.0}_{-1.8}$	$19.5^{+302.6}_{-203.6}$	0.13/0.81/0.06
	Cond. on $m_{1,2}$ and $\chi_{\rm eff}$	$2.2^{+3.8}_{-1.7}$	$42.8^{+42.7}_{-24.5}$	$4.1^{+9.6}_{-3.8}$	$2.3^{+2.7}_{-1.6}$	$14.4^{+335.1}_{-269.4}$	0.15/0.77/0.08
	Posterior	$1.8^{+3.2}_{-1.3}$	$43.1^{+41.7}_{-25.4}$	$4.0^{+9.4}_{-3.7}$	$2.3^{+2.5}_{-1.6}$	$15.7^{+416.5}_{-312.3}$	0.13/0.79/0.08
GW190917_114630	Uninformative Prior	$2.4^{+12.2}_{-2.1}$	$0.5^{+0.6}_{-0.2}$	$0.9^{+3.9}_{-0.8}$	$0.1^{+0.4}_{-0.1}$	$0.4^{+3.8}_{-1.1}$	0.02/0.97/0.01
	Cond. on $m_{1,2}$	$2.3^{+5.8}_{-2.0}$	$0.4^{+0.3}_{-0.1}$	$1.2^{+2.7}_{-1.1}$	$0.1^{+0.1}_{-0.1}$	$0.5^{+4.1}_{-0.6}$	0.01/0.99/0.0
	Cond. on $m_{1,2}$ and $\chi_{\rm eff}$	$2.2^{+4.3}_{-1.9}$	$0.4^{+0.3}_{-0.1}$	$1.2^{+2.3}_{-1.1}$	$0.1^{+0.1}_{-0.1}$	$0.5^{+4.7}_{-0.5}$	0.01/0.99/0.0
	Posterior	$1.2^{+3.1}_{-1.0}$	$0.4^{+1.0}_{-0.1}$	$1.2^{+2.3}_{-1.1}$	$0.1^{+0.1}_{-0.1}$	$0.9^{+8.4}_{-2.7}$	0.0/0.99/0.0
GW190924_021846	Uninformative Prior	$2.5^{+12.6}_{-2.2}$	$1.0^{+1.1}_{-0.4}$	$1.1^{+4.3}_{-1.0}$	$0.2^{+0.7}_{-0.2}$	$0.8^{+7.8}_{-2.6}$	0.02/0.96/0.01
	Cond. on $m_{1,2}$	$1.2^{+3.0}_{-0.9}$	$1.0^{+0.6}_{-0.2}$	$2.2^{+5.0}_{-2.0}$	$0.1^{+0.2}_{-0.1}$	$0.7^{+8.6}_{-6.7}$	0.06/0.91/0.03
	Cond. on $m_{1,2}$ and $\chi_{\rm eff}$	$1.1^{+2.6}_{-0.9}$	$1.0^{+0.7}_{-0.1}$	$2.0^{+5.1}_{-1.9}$	$0.1^{+0.1}_{-0.1}$	$0.7^{+9.1}_{-7.3}$	0.05/0.93/0.02
	Posterior	$0.7^{+1.6}_{-0.6}$	$1.0^{+0.7}_{-0.1}$	$1.6^{+3.9}_{-1.5}$	$0.1^{+0.1}_{-0.1}$	$0.7^{+12.2}_{-9.7}$	0.03/0.96/0.02
GW190925_232845	Uninformative Prior	$3.6^{+14.3}_{-3.1}$	$7.5^{+16.3}_{-4.5}$	$1.6^{+5.9}_{-1.5}$	$1.6^{+6.3}_{-1.5}$	$6.0^{+55.8}_{-14.4}$	0.04/0.94/0.02
	Cond. on $m_{1,2}$	$1.4^{+2.1}_{-1.0}$	$6.9^{+2.4}_{-1.7}$	$3.0^{+7.1}_{-2.8}$	$0.2^{+0.4}_{-0.1}$	$1.3^{+41.0}_{-33.0}$	0.17/0.76/0.07
	Cond. on $m_{1,2}$ and $\chi_{\rm eff}$	$1.3^{+1.9}_{-1.0}$	$7.2^{+2.3}_{-1.5}$	$2.9^{+7.6}_{-2.7}$	$0.2^{+0.4}_{-0.1}$	$0.7^{+42.6}_{-36.0}$	0.16/0.78/0.06
	Posterior	$1.2^{+1.6}_{-0.9}$	$7.2^{+2.3}_{-1.5}$	$2.7^{+7.1}_{-2.5}$	$0.2^{+0.3}_{-0.1}$	$0.7^{+50.8}_{-38.3}$	0.12/0.81/0.07
GW190926_050336	Uninformative Prior	$5.3^{+15.3}_{-4.5}$	$132.2^{+722.5}_{-111.7}$	$2.5^{+8.9}_{-2.3}$	$20.7^{+156.7}_{-19.1}$	$99.2^{+977.0}_{-217.3}$	0.07/0.89/0.04
	Cond. on $m_{1,2}$	$2.4^{+5.3}_{-1.9}$	$23.9^{+28.0}_{-12.4}$	$3.7^{+8.3}_{-3.4}$	$1.8^{+2.9}_{-1.2}$	$16.4^{+214.8}_{-161.6}$	0.1/0.86/0.04
	Cond. on $m_{1,2}$ and $\chi_{\rm eff}$	$2.3^{+5.2}_{-1.8}$	$24.0^{+28.6}_{-12.9}$	$3.6^{+8.3}_{-3.3}$	$1.9^{+2.6}_{-1.3}$	$16.5^{+231.9}_{-176.8}$	0.09/0.87/0.04
	Posterior	$2.2^{+5.2}_{-1.8}$	$24.5^{+28.1}_{-13.5}$	$3.5^{+8.3}_{-3.2}$	$1.9^{+2.6}_{-1.3}$	$16.7^{+218.1}_{-170.4}$	0.09/0.87/0.04
GW190929_012149	Uninformative Prior	$3.4^{+10.9}_{-2.8}$	$62.9^{+93.4}_{-48.1}$	$3.4^{+8.9}_{-3.1}$	$6.6^{+13.3}_{-5.6}$	$36.9^{+485.6}_{-298.1}$	0.1/0.86/0.05
	Cond. on $m_{1,2}$	$3.9^{+10.1}_{-3.3}$	$43.0^{+51.5}_{-25.6}$	$3.2^{+8.1}_{-2.9}$	$6.1^{+6.7}_{-4.1}$	$38.0^{+409.7}_{-198.6}$	0.06/0.91/0.03
	Cond. on $m_{1,2}$ and $\chi_{\rm eff}$	$3.7^{+7.8}_{-3.1}$	$43.3^{+58.0}_{-27.2}$	$3.2^{+8.3}_{-2.9}$	$6.4^{+3.9}_{-4.5}$	$36.9^{+394.4}_{-208.3}$	0.06/0.91/0.03
	Posterior	$6.0^{+5.5}_{-5.0}$	$47.8^{+51.8}_{-31.5}$	$3.2^{+8.0}_{-2.9}$	$6.5^{+4.2}_{-4.5}$	$29.5^{+183.8}_{-72.4}$	0.07/0.89/0.03
GW190930_133541	Uninformative Prior	$3.0^{+13.0}_{-2.6}$	$2.0^{+2.8}_{-0.9}$	$1.3^{+4.6}_{-1.2}$	$0.5^{+1.3}_{-0.4}$	$1.7^{+14.9}_{-4.4}$	0.03/0.96/0.01
	Cond. on $m_{1,2}$	$1.3^{+3.7}_{-1.0}$	$2.2^{+1.0}_{-0.6}$	$2.5^{+5.8}_{-2.3}$	$0.1^{+0.5}_{-0.1}$	$1.1^{+15.5}_{-12.0}$	0.09/0.87/0.04
	Cond. on $m_{1,2}$ and $\chi_{\rm eff}$	$1.3^{+2.6}_{-1.0}$	$2.3^{+1.1}_{-0.4}$	$2.5^{+6.1}_{-2.3}$	$0.1^{+0.4}_{-0.1}$	$1.0^{+15.4}_{-12.3}$	0.09/0.88/0.03
	Posterior	$1.0^{+1.8}_{-0.7}$	$2.3^{+1.0}_{-0.4}$	$2.2^{+5.5}_{-2.0}$	$0.1^{+0.4}_{-0.1}$	$1.3^{+18.7}_{-14.8}$	0.06/0.91/0.03
GW191103_012549	Uninformative Prior	$2.8^{+13.1}_{-2.4}$	$1.8^{+2.9}_{-1.0}$	$1.2^{+4.8}_{-1.1}$	$0.4^{+1.5}_{-0.4}$	$1.4^{+13.9}_{-3.7}$	0.03/0.95/0.01
	Cond. on $m_{1,2}$	$1.3^{+2.3}_{-1.0}$	$2.3^{+0.9}_{-0.6}$	$2.6^{+5.8}_{-2.4}$	$0.1^{+0.2}_{-0.1}$	$0.9^{+16.5}_{-12.6}$	0.11/0.84/0.04
	Cond. on $m_{1,2}$ and $\chi_{\rm eff}$	$1.3^{+1.8}_{-0.9}$	$2.4^{+0.8}_{-0.4}$	$3.0^{+6.2}_{-2.8}$	$0.1^{+0.2}_{-0.1}$	$0.8^{+17.4}_{-12.8}$	0.11/0.84/0.05
	Posterior	$1.1^{+1.5}_{-0.8}$	$2.4^{+0.8}_{-0.4}$	$2.6^{+5.5}_{-2.4}$	$0.1^{+0.2}_{-0.1}$	$0.9^{+18.5}_{-14.1}$	0.08/0.86/0.06
GW191105_143521	Uninformative Prior	$2.9^{+13.3}_{-2.5}$	$2.3^{+3.7}_{-1.3}$	$1.3^{+4.9}_{-1.2}$	$0.5^{+1.8}_{-0.5}$	$1.8^{+17.1}_{-4.7}$	0.03/0.95/0.02
	Cond. on $m_{1,2}$	$1.2^{+1.8}_{-0.9}$	$2.1^{+0.8}_{-0.4}$	$2.6^{+5.9}_{-2.4}$	$0.1^{+0.1}_{-0.1}$	$0.7^{+13.0}_{-12.2}$	0.13/0.82/0.05
	Cond. on $m_{1,2}$ and $\chi_{\rm eff}$	$1.1^{+1.7}_{-0.9}$	$2.2^{+0.8}_{-0.4}$	$2.2^{+6.2}_{-2.1}$	$0.1^{+0.1}_{-0.1}$	$0.6^{+14.5}_{-12.8}$	0.11/0.85/0.04
	Posterior	$0.8^{+1.3}_{-0.7}$	$2.2^{+0.9}_{-0.4}$	$1.8^{+5.4}_{-1.7}$	$0.1^{+0.1}_{-0.1}$	$0.5^{+18.9}_{-14.6}$	0.07/0.9/0.04
GW191109_010717	Uninformative Prior	$5.1^{+15.3}_{-4.4}$	$90.3^{+413.8}_{-70.3}$	$2.4^{+8.5}_{-2.2}$	$15.4^{+97.7}_{-14.1}$	$69.9^{+636.4}_{-156.5}$	0.07/0.9/0.03
	Cond. on $m_{1,2}$	$2.2^{+3.0}_{-1.6}$	$58.7^{+26.2}_{-24.9}$	$4.1^{+9.8}_{-3.8}$	$2.2^{+2.0}_{-1.2}$	$9.3^{+293.7}_{-249.8}$	0.22/0.69/0.09
	Cond. on $m_{1,2}$ and $\chi_{\rm eff}$	$3.0^{+3.6}_{-2.2}$	$48.0^{+36.2}_{-25.4}$	$4.0^{+7.7}_{-3.7}$	$2.9^{+2.1}_{-1.8}$	$22.9^{+190.1}_{-93.5}$	0.21/0.7/0.09
	Posterior	$4.1^{+2.9}_{-2.7}$	$48.9^{+40.0}_{-27.2}$	$4.5^{+8.8}_{-4.1}$	$3.4^{+1.7}_{-1.9}$	$18.3^{+162.5}_{-205.9}$	0.27/0.66/0.06

GW191113_071753	Uninformative Prior	$5.1^{+16.4}_{-4.6}$	$5.0^{+26.9}_{-3.1}$	$0.9^{+5.2}_{-0.8}$	$1.8^{+9.8}_{-1.7}$	$3.4^{+24.9}_{-4.7}$	0.03/0.95/0.02
	Cond. on $m_{1,2}$	$3.3^{+9.3}_{-2.9}$	$3.5^{+3.2}_{-1.6}$	$1.7^{+4.2}_{-1.5}$	$0.8^{+0.9}_{-0.6}$	$3.5^{+30.2}_{-5.7}$	0.02/0.97/0.01
	Cond. on $m_{1,2}$ and χ_{eff}	$2.8^{+5.6}_{-2.5}$	$3.3^{+5.1}_{-1.0}$	$1.7^{+4.2}_{-1.6}$	$0.9^{+0.5}_{-0.7}$	$4.0^{+36.9}_{-9.0}$	0.02/0.97/0.01
	Posterior	$1.8^{+4.7}_{-1.5}$	$3.1^{+6.1}_{-0.9}$	$1.8^{+3.8}_{-1.6}$	$0.9^{+0.5}_{-0.7}$	$5.8^{+52.6}_{-16.9}$	0.01/0.98/0.01
GW191126_115259	Uninformative Prior	$3.3^{+13.9}_{-2.9}$	$4.6^{+9.7}_{-3.1}$	$1.4^{+5.6}_{-1.3}$	$1.0^{+4.1}_{-0.9}$	$3.5^{+35.7}_{-8.7}$	0.04/0.94/0.02
	Cond. on $m_{1,2}$	$1.3^{+2.2}_{-1.0}$	$2.8^{+1.2}_{-0.7}$	$2.7^{+6.0}_{-2.5}$	$0.1^{+0.3}_{-0.1}$	$1.1^{+19.3}_{-15.5}$	0.11/0.84/0.05
	Cond. on $m_{1,2}$ and χ_{eff}	$1.3^{+1.7}_{-0.9}$	$3.0^{+1.0}_{-0.5}$	$3.0^{+6.6}_{-2.8}$	$0.1^{+0.2}_{-0.1}$	$0.8^{+20.0}_{-16.0}$	0.12/0.83/0.05
	Posterior	$1.0^{+1.5}_{-0.7}$	$3.0^{+1.1}_{-0.5}$	$2.7^{+5.9}_{-2.5}$	$0.1^{+0.2}_{-0.1}$	$0.8^{+26.5}_{-19.9}$	0.09/0.86/0.06
GW191127_050227	Uninformative Prior	$5.2^{+15.3}_{-4.4}$	$117.7^{+624.2}_{-102.2}$	$2.5^{+8.7}_{-2.3}$	$18.3^{+139.3}_{-17.0}$	$86.1^{+873.3}_{-183.8}$	0.07/0.89/0.04
	Cond. on $m_{1,2}$	$2.8^{+9.4}_{-2.2}$	$37.4^{+48.8}_{-24.0}$	$3.3^{+8.7}_{-3.1}$	$3.2^{+8.8}_{-2.5}$	$20.3^{+269.3}_{-183.5}$	0.12/0.84/0.05
	Cond. on $m_{1,2}$ and χ_{eff}	$2.4^{+6.4}_{-1.8}$	$43.1^{+54.9}_{-29.9}$	$3.4^{+9.8}_{-3.2}$	$2.9^{+7.0}_{-2.3}$	$17.8^{+327.2}_{-230.9}$	0.12/0.81/0.07
	Posterior	$2.9^{+8.1}_{-2.2}$	$45.6^{+54.4}_{-31.9}$	$3.5^{+9.6}_{-3.2}$	$3.0^{+7.2}_{-2.3}$	$16.1^{+270.0}_{-192.1}$	0.15/0.78/0.07
GW191129_134029	Uninformative Prior	$2.8^{+13.0}_{-2.4}$	$1.7^{+2.6}_{-0.8}$	$1.2^{+4.7}_{-1.1}$	$0.4^{+1.3}_{-0.4}$	$1.4^{+12.9}_{-3.7}$	0.03/0.95/0.01
	Cond. on $m_{1,2}$	$1.2^{+2.1}_{-0.9}$	$1.7^{+0.8}_{-0.4}$	$2.6^{+5.5}_{-2.4}$	$0.1^{+0.1}_{-0.1}$	$0.9^{+13.4}_{-10.8}$	0.08/0.88/0.04
	Cond. on $m_{1,2}$ and χ_{eff}	$1.1^{+1.9}_{-0.9}$	$1.7^{+0.9}_{-0.2}$	$2.4^{+5.8}_{-2.2}$	$0.1^{+0.1}_{-0.1}$	$0.8^{+13.8}_{-11.7}$	0.07/0.9/0.03
	Posterior	$0.7^{+1.2}_{-0.5}$	$1.7^{+0.9}_{-0.2}$	$1.9^{+4.5}_{-1.7}$	$0.1^{+0.1}_{-0.1}$	$0.9^{+18.5}_{-15.5}$	0.04/0.94/0.02
GW191204_110529	Uninformative Prior	$4.1^{+14.8}_{-3.5}$	$19.0^{+55.4}_{-13.6}$	$1.9^{+6.8}_{-1.8}$	$3.6^{+17.7}_{-3.3}$	$14.5^{+131.8}_{-35.0}$	0.05/0.92/0.02
	Cond. on $m_{1,2}$	$1.7^{+2.7}_{-1.3}$	$13.2^{+5.5}_{-4.2}$	$3.2^{+8.0}_{-3.0}$	$0.5^{+1.0}_{-0.3}$	$2.8^{+78.2}_{-64.2}$	0.17/0.76/0.07
	Cond. on $m_{1,2}$ and χ_{eff}	$1.6^{+2.4}_{-1.2}$	$13.6^{+5.9}_{-4.2}$	$3.2^{+8.1}_{-3.0}$	$0.4^{+0.9}_{-0.3}$	$2.2^{+81.3}_{-66.7}$	0.17/0.77/0.06
	Posterior	$1.9^{+2.5}_{-1.4}$	$13.7^{+5.4}_{-4.3}$	$3.3^{+8.5}_{-3.1}$	$0.5^{+0.8}_{-0.3}$	$2.0^{+70.6}_{-49.2}$	0.22/0.72/0.06
GW191204_171526	Uninformative Prior	$2.9^{+13.3}_{-2.5}$	$2.1^{+2.9}_{-0.8}$	$1.3^{+4.8}_{-1.2}$	$0.5^{+1.5}_{-0.5}$	$1.7^{+15.0}_{-4.5}$	0.03/0.95/0.02
	Cond. on $m_{1,2}$	$1.2^{+1.7}_{-0.9}$	$2.2^{+0.8}_{-0.5}$	$2.8^{+5.9}_{-2.6}$	$0.1^{+0.1}_{-0.1}$	$0.9^{+15.7}_{-12.6}$	0.11/0.85/0.05
	Cond. on $m_{1,2}$ and χ_{eff}	$1.1^{+1.5}_{-0.7}$	$2.3^{+0.8}_{-0.4}$	$2.9^{+6.3}_{-2.7}$	$0.1^{+0.1}_{-0.1}$	$0.6^{+16.3}_{-14.0}$	0.11/0.85/0.04
	Posterior	$1.0^{+1.2}_{-0.7}$	$2.2^{+0.9}_{-0.3}$	$2.7^{+5.4}_{-2.5}$	$0.1^{+0.1}_{-0.1}$	$1.0^{+18.6}_{-14.0}$	0.05/0.89/0.05
GW191215_223052	Uninformative Prior	$3.9^{+14.8}_{-3.4}$	$13.9^{+34.6}_{-8.5}$	$1.8^{+6.5}_{-1.7}$	$2.8^{+11.9}_{-2.5}$	$11.3^{+101.7}_{-26.3}$	0.05/0.93/0.02
	Cond. on $m_{1,2}$	$1.6^{+2.3}_{-1.2}$	$11.5^{+4.3}_{-3.1}$	$3.3^{+7.9}_{-3.1}$	$0.4^{+0.6}_{-0.3}$	$2.6^{+72.2}_{-52.8}$	0.17/0.75/0.08
	Cond. on $m_{1,2}$ and χ_{eff}	$1.5^{+2.2}_{-1.2}$	$11.5^{+4.6}_{-2.9}$	$3.1^{+8.0}_{-2.9}$	$0.4^{+0.6}_{-0.3}$	$2.5^{+73.1}_{-62.5}$	0.16/0.79/0.06
	Posterior	$1.8^{+2.5}_{-1.4}$	$11.4^{+4.2}_{-2.5}$	$3.1^{+7.9}_{-2.9}$	$0.4^{+0.6}_{-0.3}$	$2.7^{+48.3}_{-40.9}$	0.17/0.78/0.05
GW191216_213338	Uninformative Prior	$2.8^{+13.1}_{-2.4}$	$1.9^{+2.8}_{-0.9}$	$1.2^{+4.8}_{-1.1}$	$0.4^{+1.5}_{-0.4}$	$1.5^{+13.9}_{-4.0}$	0.03/0.95/0.02
	Cond. on $m_{1,2}$	$1.2^{+2.1}_{-0.9}$	$1.8^{+0.9}_{-0.4}$	$2.6^{+5.7}_{-2.4}$	$0.1^{+0.1}_{-0.1}$	$1.0^{+14.3}_{-12.1}$	0.09/0.87/0.04
	Cond. on $m_{1,2}$ and χ_{eff}	$1.1^{+1.9}_{-0.8}$	$1.9^{+0.9}_{-0.3}$	$2.6^{+6.0}_{-2.4}$	$0.1^{+0.1}_{-0.1}$	$0.8^{+14.3}_{-12.5}$	0.08/0.89/0.03
	Posterior	$0.6^{+1.0}_{-0.4}$	$1.9^{+1.0}_{-0.2}$	$1.8^{+4.4}_{-1.6}$	$0.1^{+0.1}_{-0.1}$	$0.6^{+23.1}_{-22.0}$	0.03/0.94/0.02
GW191222_033537	Uninformative Prior	$5.0^{+15.2}_{-4.3}$	$69.2^{+281.0}_{-50.2}$	$2.3^{+8.2}_{-2.1}$	$12.4^{+70.7}_{-11.3}$	$55.2^{+487.8}_{-124.0}$	0.06/0.91/0.03
	Cond. on $m_{1,2}$	$2.0^{+2.9}_{-1.4}$	$43.3^{+17.5}_{-16.0}$	$3.4^{+9.2}_{-3.2}$	$1.4^{+1.8}_{-0.8}$	$3.7^{+190.8}_{-151.0}$	0.24/0.65/0.11
	Cond. on $m_{1,2}$ and χ_{eff}	$2.0^{+2.7}_{-1.5}$	$42.9^{+18.4}_{-16.3}$	$3.2^{+9.1}_{-3.0}$	$1.4^{+1.7}_{-0.9}$	$4.0^{+181.3}_{-150.2}$	0.23/0.69/0.08
	Posterior	$1.8^{+2.7}_{-1.4}$	$42.8^{+18.5}_{-16.9}$	$3.1^{+9.2}_{-2.9}$	$1.3^{+1.9}_{-0.8}$	$4.4^{+197.2}_{-176.9}$	0.19/0.72/0.09
GW191230_180458	Uninformative Prior	$5.2^{+15.3}_{-4.4}$	$106.1^{+528.8}_{-86.9}$	$2.5^{+8.6}_{-2.3}$	$17.2^{+120.1}_{-15.7}$	$80.4^{+779.0}_{-176.8}$	0.07/0.9/0.03
	Cond. on $m_{1,2}$	$2.2^{+3.3}_{-1.7}$	$61.3^{+27.7}_{-25.4}$	$3.5^{+9.5}_{-3.3}$	$2.3^{+2.8}_{-1.5}$	$6.4^{+264.6}_{-236.8}$	0.24/0.65/0.11
	Cond. on $m_{1,2}$ and χ_{eff}	$2.3^{+3.2}_{-1.8}$	$60.5^{+30.4}_{-27.9}$	$3.4^{+9.6}_{-3.2}$	$2.3^{+2.7}_{-1.5}$	$8.5^{+258.2}_{-202.3}$	0.24/0.68/0.09
	Posterior	$2.5^{+3.6}_{-1.9}$	$61.3^{+28.5}_{-27.6}$	$3.6^{+9.8}_{-3.4}$	$2.3^{+2.7}_{-1.5}$	$8.1^{+187.5}_{-153.3}$	0.27/0.64/0.08
GW200112_155838	Uninformative Prior	$4.3^{+14.9}_{-3.7}$	$26.6^{+80.2}_{-17.6}$	$2.0^{+7.2}_{-1.8}$	$5.1^{+24.1}_{-4.6}$	$21.2^{+183.4}_{-48.7}$	0.05/0.92/0.03
	Cond. on $m_{1,2}$	$1.8^{+2.2}_{-1.3}$	$20.9^{+6.3}_{-6.0}$	$3.1^{+8.3}_{-2.9}$	$0.6^{+0.7}_{-0.4}$	$1.7^{+93.6}_{-70.6}$	0.25/0.66/0.1
	Cond. on $m_{1,2}$ and χ_{eff}	$1.6^{+1.9}_{-1.2}$	$21.7^{+6.4}_{-5.7}$	$2.9^{+9.1}_{-2.7}$	$0.6^{+0.6}_{-0.4}$	$0.2^{+102.8}_{-83.5}$	0.22/0.7/0.08
	Posterior	$1.3^{+1.6}_{-1.0}$	$21.6^{+6.3}_{-5.8}$	$2.9^{+8.5}_{-2.7}$	$0.5^{+0.7}_{-0.3}$	$0.3^{+125.4}_{-102.3}$	0.15/0.75/0.1
GW200128_022011	Uninformative Prior	$4.8^{+15.3}_{-4.1}$	$55.9^{+208.5}_{-39.0}$	$2.2^{+8.0}_{-2.0}$	$10.3^{+54.8}_{-9.3}$	$45.6^{+394.4}_{-100.4}$	0.06/0.91/0.03
	Cond. on $m_{1,2}$	$2.0^{+2.6}_{-1.5}$	$41.6^{+17.3}_{-14.8}$	$3.3^{+9.4}_{-3.1}$	$1.4^{+1.6}_{-0.9}$	$3.3^{+194.4}_{-153.1}$	0.24/0.65/0.11

	Cond. on $m_{1,2}$ and χ_{eff}	$1.8^{+2.2}_{-1.3}$	$44.6^{+19.3}_{-16.6}$	$3.4^{+9.7}_{-3.2}$	$1.3^{+1.4}_{-0.8}$	$-0.2^{+186.6}_{-188.1}$	0.25/0.64/0.1
	Posterior	$2.3^{+2.2}_{-1.7}$	$44.6^{+19.1}_{-15.9}$	$3.6^{+10.3}_{-3.4}$	$1.3^{+1.3}_{-0.8}$	$0.0^{+148.7}_{-115.1}$	0.35/0.56/0.09
GW200129_065458	Uninformative Prior	$4.2^{+14.9}_{-3.6}$	$23.9^{+75.9}_{-18.0}$	$1.9^{+7.0}_{-1.8}$	$4.4^{+23.1}_{-4.0}$	$18.0^{+168.1}_{-42.7}$	0.05/0.92/0.03
	Cond. on $m_{1,2}$	$1.7^{+2.6}_{-1.3}$	$18.8^{+5.0}_{-6.3}$	$2.6^{+8.0}_{-2.4}$	$0.5^{+1.0}_{-0.3}$	$1.1^{+68.2}_{-43.5}$	0.27/0.63/0.11
	Cond. on $m_{1,2}$ and χ_{eff}	$1.5^{+2.2}_{-1.1}$	$20.1^{+4.6}_{-6.5}$	$2.5^{+8.0}_{-2.3}$	$0.5^{+0.9}_{-0.3}$	$-0.2^{+72.7}_{-81.7}$	0.25/0.63/0.12
	Posterior	$1.5^{+3.7}_{-1.1}$	$19.5^{+3.9}_{-5.2}$	$3.6^{+8.6}_{-3.4}$	$0.5^{+0.9}_{-0.3}$	$0.2^{+63.9}_{-53.0}$	0.17/0.7/0.12
GW200202_154313	Uninformative Prior	$2.8^{+12.8}_{-2.4}$	$1.6^{+2.3}_{-0.8}$	$1.2^{+4.6}_{-1.1}$	$0.4^{+1.2}_{-0.4}$	$1.3^{+12.1}_{-3.4}$	0.03/0.95/0.01
	Cond. on $m_{1,2}$	$1.1^{+1.7}_{-0.8}$	$1.6^{+0.6}_{-0.3}$	$2.5^{+5.6}_{-2.3}$	$0.1^{+0.1}_{-0.1}$	$0.5^{+10.6}_{-8.9}$	0.12/0.83/0.05
	Cond. on $m_{1,2}$ and χ_{eff}	$1.0^{+1.6}_{-0.8}$	$1.7^{+0.6}_{-0.3}$	$2.2^{+6.0}_{-2.1}$	$0.1^{+0.0}_{-0.1}$	$0.4^{+11.3}_{-9.0}$	0.11/0.86/0.04
	Posterior	$0.7^{+1.1}_{-0.6}$	$1.7^{+0.7}_{-0.3}$	$1.7^{+4.9}_{-1.6}$	$0.1^{+0.0}_{-0.1}$	$0.2^{+13.6}_{-13.0}$	0.06/0.91/0.03
GW200208_130117	Uninformative Prior	$4.4^{+15.0}_{-3.8}$	$31.4^{+99.1}_{-20.9}$	$2.0^{+7.4}_{-1.8}$	$6.0^{+28.9}_{-5.4}$	$25.2^{+214.7}_{-58.4}$	0.06/0.92/0.03
	Cond. on $m_{1,2}$	$1.9^{+2.7}_{-1.4}$	$26.1^{+11.2}_{-9.6}$	$3.6^{+8.8}_{-3.4}$	$1.0^{+1.2}_{-0.6}$	$4.6^{+137.6}_{-123.0}$	0.19/0.73/0.08
	Cond. on $m_{1,2}$ and χ_{eff}	$1.9^{+2.9}_{-1.4}$	$25.5^{+12.8}_{-10.3}$	$3.4^{+8.6}_{-3.2}$	$1.0^{+1.2}_{-0.7}$	$5.6^{+140.5}_{-117.7}$	0.19/0.74/0.07
	Posterior	$1.6^{+2.5}_{-1.2}$	$25.5^{+12.9}_{-10.5}$	$3.2^{+8.2}_{-3.0}$	$0.9^{+1.2}_{-0.6}$	$5.6^{+165.0}_{-131.1}$	0.14/0.79/0.07
GW200208_222617	Uninformative Prior	$5.6^{+15.3}_{-4.8}$	$188.5^{+1187.7}_{-166.5}$	$2.7^{+9.2}_{-2.5}$	$28.1^{+240.8}_{-26.2}$	$137.8^{+1390.5}_{-304.0}$	0.08/0.88/0.04
	Cond. on $m_{1,2}$	$3.6^{+14.9}_{-3.0}$	$19.0^{+82.6}_{-10.8}$	$2.2^{+6.8}_{-2.0}$	$3.8^{+26.8}_{-3.5}$	$18.1^{+184.3}_{-42.9}$	0.05/0.92/0.03
	Cond. on $m_{1,2}$ and χ_{eff}	$2.5^{+4.6}_{-1.8}$	$24.9^{+176.0}_{-14.7}$	$3.0^{+7.7}_{-2.7}$	$2.9^{+9.2}_{-2.6}$	$21.5^{+256.7}_{-70.0}$	0.08/0.87/0.05
	Posterior	$2.6^{+4.5}_{-1.9}$	$24.4^{+178.9}_{-14.3}$	$2.9^{+7.5}_{-2.6}$	$2.9^{+9.3}_{-2.6}$	$20.0^{+222.3}_{-62.3}$	0.08/0.87/0.04
GW200209_085452	Uninformative Prior	$5.0^{+15.2}_{-4.3}$	$77.5^{+346.1}_{-62.3}$	$2.3^{+8.4}_{-2.1}$	$13.0^{+83.9}_{-11.9}$	$58.4^{+545.8}_{-134.0}$	0.07/0.9/0.03
	Cond. on $m_{1,2}$	$1.9^{+2.7}_{-1.4}$	$30.5^{+15.5}_{-12.5}$	$3.2^{+8.9}_{-3.0}$	$1.0^{+1.3}_{-0.6}$	$2.8^{+140.0}_{-112.2}$	0.24/0.65/0.11
	Cond. on $m_{1,2}$ and χ_{eff}	$2.0^{+2.9}_{-1.5}$	$29.1^{+16.6}_{-12.8}$	$3.2^{+8.7}_{-3.0}$	$1.0^{+1.4}_{-0.6}$	$5.5^{+138.6}_{-100.5}$	0.22/0.69/0.09
	Posterior	$2.3^{+3.1}_{-1.8}$	$29.3^{+16.2}_{-12.8}$	$3.2^{+8.4}_{-3.0}$	$1.1^{+1.3}_{-0.7}$	$5.3^{+98.4}_{-69.5}$	0.26/0.66/0.08
GW200210_092254	Uninformative Prior	$3.9^{+16.0}_{-3.5}$	$1.6^{+5.3}_{-0.7}$	$0.8^{+4.5}_{-0.7}$	$0.6^{+2.4}_{-0.6}$	$1.2^{+9.9}_{-2.1}$	0.02/0.96/0.01
	Cond. on $m_{1,2}$	$5.7^{+11.9}_{-5.1}$	$1.4^{+1.3}_{-0.7}$	$0.9^{+1.4}_{-0.8}$	$0.6^{+0.4}_{-0.2}$	$1.1^{+8.2}_{-1.0}$	0.0/0.99/0.0
	Cond. on $m_{1,2}$ and χ_{eff}	$4.5^{+5.5}_{-4.2}$	$1.3^{+1.5}_{-0.4}$	$0.9^{+1.4}_{-0.8}$	$0.6^{+0.3}_{-0.1}$	$1.3^{+12.5}_{-1.2}$	0.0/0.99/0.0
	Posterior	$2.6^{+3.3}_{-2.3}$	$1.2^{+0.9}_{-0.3}$	$0.8^{+1.4}_{-0.7}$	$0.6^{+0.3}_{-0.1}$	$2.0^{+13.9}_{-1.9}$	0.0/1.0/0.0
GW200216_220804	Uninformative Prior	$5.1^{+15.2}_{-4.4}$	$88.4^{+417.5}_{-72.6}$	$2.4^{+8.4}_{-2.2}$	$14.4^{+98.3}_{-13.2}$	$66.6^{+618.9}_{-150.2}$	0.07/0.9/0.03
	Cond. on $m_{1,2}$	$2.4^{+6.1}_{-1.8}$	$48.1^{+37.8}_{-30.5}$	$3.7^{+9.1}_{-3.4}$	$2.7^{+4.3}_{-1.8}$	$17.4^{+308.4}_{-224.8}$	0.15/0.78/0.07
	Cond. on $m_{1,2}$ and χ_{eff}	$2.3^{+4.7}_{-1.7}$	$51.9^{+41.0}_{-34.9}$	$3.8^{+9.6}_{-3.5}$	$2.7^{+3.2}_{-1.8}$	$13.3^{+327.9}_{-263.0}$	0.17/0.75/0.08
	Posterior	$2.3^{+4.9}_{-1.7}$	$52.1^{+40.7}_{-35.1}$	$3.7^{+9.6}_{-3.4}$	$2.7^{+3.1}_{-1.8}$	$13.0^{+371.3}_{-289.8}$	0.16/0.77/0.07
GW200219_094415	Uninformative Prior	$4.6^{+15.2}_{-3.9}$	$44.5^{+160.7}_{-32.6}$	$2.1^{+7.8}_{-1.9}$	$8.1^{+43.9}_{-7.4}$	$34.9^{+308.2}_{-79.4}$	0.06/0.91/0.03
	Cond. on $m_{1,2}$	$2.0^{+2.7}_{-1.5}$	$32.7^{+13.6}_{-13.0}$	$3.4^{+9.0}_{-3.2}$	$1.1^{+1.5}_{-0.7}$	$3.9^{+144.0}_{-139.5}$	0.22/0.68/0.1
	Cond. on $m_{1,2}$ and χ_{eff}	$2.0^{+3.0}_{-1.5}$	$31.6^{+15.2}_{-13.2}$	$3.3^{+8.8}_{-3.1}$	$1.1^{+1.5}_{-0.7}$	$5.9^{+144.5}_{-111.3}$	0.21/0.71/0.07
	Posterior	$2.1^{+2.9}_{-1.6}$	$31.8^{+15.0}_{-13.8}$	$3.4^{+8.9}_{-3.2}$	$1.2^{+1.4}_{-0.8}$	$6.0^{+135.5}_{-104.7}$	0.21/0.71/0.08
GW200220_061928	Uninformative Prior	$6.9^{+15.6}_{-5.9}$	$415.4^{+3448.1}_{-341.3}$	$2.7^{+10.5}_{-2.5}$	$72.8^{+578.8}_{-67.3}$	$303.5^{+2656.2}_{-536.3}$	0.09/0.86/0.05
	Cond. on $m_{1,2}$	$2.9^{+4.9}_{-2.2}$	$214.2^{+136.4}_{-109.7}$	$4.0^{+11.6}_{-3.7}$	$9.5^{+16.6}_{-5.9}$	$27.1^{+991.1}_{-824.3}$	0.25/0.64/0.11
	Cond. on $m_{1,2}$ and χ_{eff}	$2.7^{+4.2}_{-2.0}$	$226.6^{+163.3}_{-121.2}$	$4.1^{+11.7}_{-3.8}$	$9.4^{+11.9}_{-5.6}$	$13.1^{+1143.0}_{-1068.3}$	0.26/0.63/0.11
	Posterior	$2.9^{+4.6}_{-2.1}$	$228.0^{+171.1}_{-125.5}$	$4.4^{+12.0}_{-4.2}$	$9.9^{+11.2}_{-6.2}$	$18.0^{+938.0}_{-700.4}$	0.28/0.61/0.12
GW200220_124850	Uninformative Prior	$5.1^{+15.2}_{-4.4}$	$89.7^{+427.5}_{-74.1}$	$2.4^{+8.4}_{-2.2}$	$14.6^{+100.3}_{-13.4}$	$67.3^{+628.9}_{-151.5}$	0.07/0.9/0.03
	Cond. on $m_{1,2}$	$2.1^{+3.2}_{-1.6}$	$37.1^{+17.0}_{-16.0}$	$3.6^{+9.0}_{-3.4}$	$1.4^{+1.9}_{-0.9}$	$6.3^{+181.4}_{-156.2}$	0.22/0.7/0.08
	Cond. on $m_{1,2}$ and χ_{eff}	$2.1^{+3.2}_{-1.6}$	$35.8^{+19.4}_{-16.5}$	$3.4^{+8.9}_{-3.2}$	$1.4^{+1.9}_{-0.9}$	$7.8^{+188.6}_{-163.9}$	0.2/0.73/0.07
	Posterior	$2.3^{+3.6}_{-1.8}$	$36.1^{+18.4}_{-16.7}$	$3.4^{+9.1}_{-3.2}$	$1.4^{+1.9}_{-0.9}$	$7.4^{+149.0}_{-116.1}$	0.21/0.72/0.07
GW200224_222234	Uninformative Prior	$4.5^{+15.0}_{-3.9}$	$35.0^{+115.0}_{-24.1}$	$2.1^{+7.4}_{-1.9}$	$6.6^{+32.9}_{-6.0}$	$27.8^{+238.3}_{-65.8}$	0.06/0.92/0.03
	Cond. on $m_{1,2}$	$1.8^{+2.4}_{-1.3}$	$29.4^{+8.6}_{-9.3}$	$3.1^{+8.7}_{-2.9}$	$0.8^{+1.0}_{-0.5}$	$1.5^{+112.9}_{-103.6}$	0.26/0.63/0.11
	Cond. on $m_{1,2}$ and χ_{eff}	$1.7^{+2.0}_{-1.3}$	$31.2^{+7.9}_{-9.7}$	$3.1^{+9.3}_{-2.9}$	$0.8^{+0.8}_{-0.5}$	$-0.3^{+117.7}_{-110.9}$	0.26/0.64/0.1

	Posterior	$1.7^{+1.9}_{-1.2}$	$31.1^{+7.2}_{-9.4}$	$3.2^{+9.2}_{-3.0}$	$0.8^{+0.7}_{-0.5}$	$-0.1^{+106.5}_{-90.8}$	0.25/0.64/0.11
GW200225_060421	Uninformative Prior	$3.5^{+14.3}_{-3.0}$	$6.8^{+14.4}_{-3.9}$	$1.6^{+5.8}_{-1.5}$	$1.5^{+5.6}_{-1.4}$	$5.5^{+51.3}_{-13.3}$	0.04/0.94/0.02
	Cond. on $m_{1,2}$	$1.4^{+2.0}_{-1.0}$	$6.3^{+2.2}_{-2.0}$	$3.0^{+7.0}_{-2.8}$	$0.2^{+0.3}_{-0.1}$	$1.4^{+35.9}_{-29.1}$	0.16/0.78/0.06
	Cond. on $m_{1,2}$ and $\chi_{\rm eff}$	$1.5^{+2.2}_{-1.1}$	$6.1^{+2.4}_{-2.2}$	$3.0^{+6.7}_{-2.8}$	$0.2^{+0.3}_{-0.1}$	$2.1^{+34.3}_{-28.1}$	0.15/0.8/0.05
	Posterior	$1.9^{+2.1}_{-1.4}$	$6.0^{+1.9}_{-2.1}$	$2.8^{+6.6}_{-2.6}$	$0.2^{+0.3}_{-0.1}$	$2.2^{+21.6}_{-12.8}$	0.14/0.81/0.05
GW200302_015811	Uninformative Prior	$4.3^{+14.9}_{-3.7}$	$28.6^{+92.9}_{-21.1}$	$2.0^{+7.2}_{-1.8}$	$5.3^{+27.4}_{-4.8}$	$21.8^{+199.0}_{-51.1}$	0.05/0.92/0.03
	Cond. on $m_{1,2}$	$2.0^{+3.7}_{-1.5}$	$15.3^{+12.0}_{-6.3}$	$3.9^{+7.6}_{-3.6}$	$1.0^{+1.0}_{-0.6}$	$11.3^{+137.5}_{-122.5}$	0.09/0.88/0.04
	Cond. on $m_{1,2}$ and $\chi_{\rm eff}$	$1.8^{+3.6}_{-1.4}$	$15.7^{+13.0}_{-6.7}$	$3.7^{+8.0}_{-3.4}$	$1.1^{+0.8}_{-0.7}$	$10.0^{+154.1}_{-127.6}$	0.08/0.89/0.03
	Posterior	$1.7^{+3.4}_{-1.3}$	$15.5^{+12.6}_{-6.6}$	$3.5^{+7.6}_{-3.2}$	$1.1^{+0.7}_{-0.7}$	$11.0^{+149.5}_{-125.3}$	0.07/0.9/0.03
GW200306_093714	Uninformative Prior	$6.0^{+16.1}_{-5.3}$	$45.2^{+376.1}_{-36.9}$	$1.5^{+7.4}_{-1.4}$	$10.9^{+95.5}_{-10.3}$	$31.6^{+251.0}_{-45.7}$	0.05/0.93/0.02
	Cond. on $m_{1,2}$	$2.0^{+5.1}_{-1.5}$	$10.8^{+7.5}_{-5.3}$	$3.2^{+7.3}_{-2.9}$	$0.7^{+1.5}_{-0.5}$	$6.8^{+84.0}_{-64.1}$	0.09/0.87/0.04
	Cond. on $m_{1,2}$ and $\chi_{\rm eff}$	$1.8^{+3.5}_{-1.3}$	$12.7^{+7.1}_{-6.7}$	$3.7^{+8.0}_{-3.4}$	$0.6^{+1.2}_{-0.4}$	$6.3^{+98.7}_{-78.4}$	0.12/0.8/0.07
	Posterior	$1.7^{+3.5}_{-1.2}$	$12.6^{+6.9}_{-6.6}$	$3.6^{+7.7}_{-3.3}$	$0.6^{+1.2}_{-0.4}$	$6.3^{+96.5}_{-83.9}$	0.11/0.82/0.08
GW200308_173609	Uninformative Prior	$6.0^{+15.3}_{-5.0}$	$538.6^{+3027.8}_{-483.2}$	$3.4^{+11.0}_{-3.1}$	$70.2^{+520.6}_{-65.2}$	$370.1^{+4206.4}_{-1003.7}$	0.1/0.84/0.05
	Cond. on $m_{1,2}$	$3.5^{+10.9}_{-2.8}$	$90.7^{+580.9}_{-77.0}$	$3.7^{+9.7}_{-3.4}$	$7.7^{+99.5}_{-6.3}$	$51.7^{+1100.7}_{-385.1}$	0.09/0.85/0.06
	Cond. on $m_{1,2}$ and $\chi_{\rm eff}$	$2.8^{+10.6}_{-2.1}$	$94.3^{+622.9}_{-75.3}$	$4.5^{+9.0}_{-4.1}$	$7.5^{+89.2}_{-6.4}$	$68.2^{+1332.2}_{-570.0}$	0.11/0.82/0.07
	Posterior	$3.0^{+10.2}_{-2.3}$	$98.7^{+645.9}_{-78.8}$	$4.4^{+9.8}_{-4.0}$	$7.3^{+88.7}_{-6.3}$	$49.2^{+1244.3}_{-469.2}$	0.1/0.84/0.06
GW200311_115853	Uninformative Prior	$4.3^{+14.9}_{-3.7}$	$24.9^{+72.9}_{-16.1}$	$1.9^{+7.2}_{-1.7}$	$4.8^{+22.4}_{-4.3}$	$19.9^{+176.6}_{-45.9}$	0.05/0.92/0.03
	Cond. on $m_{1,2}$	$1.7^{+2.1}_{-1.3}$	$19.5^{+5.7}_{-5.7}$	$2.9^{+8.2}_{-2.7}$	$0.5^{+0.7}_{-0.3}$	$1.1^{+78.6}_{-64.1}$	0.24/0.65/0.1
	Cond. on $m_{1,2}$ and $\chi_{\rm eff}$	$1.6^{+2.2}_{-1.2}$	$19.5^{+5.9}_{-5.6}$	$2.8^{+8.4}_{-2.6}$	$0.5^{+0.7}_{-0.3}$	$1.0^{+79.2}_{-66.5}$	0.23/0.68/0.08
	Posterior	$1.6^{+2.1}_{-1.2}$	$19.4^{+5.5}_{-5.6}$	$2.9^{+8.4}_{-2.7}$	$0.5^{+0.6}_{-0.3}$	$1.5^{+75.9}_{-59.2}$	0.19/0.71/0.09
GW200316_215756	Uninformative Prior	$3.0^{+13.6}_{-2.6}$	$2.7^{+4.7}_{-1.4}$	$1.3^{+5.1}_{-1.2}$	$0.6^{+2.2}_{-0.5}$	$2.2^{+20.3}_{-5.7}$	0.03/0.95/0.02
	Cond. on $m_{1,2}$	$1.4^{+3.4}_{-1.1}$	$2.5^{+1.2}_{-0.7}$	$2.6^{+5.9}_{-2.4}$	$0.1^{+0.5}_{-0.1}$	$1.5^{+19.6}_{-14.9}$	0.08/0.88/0.04
	Cond. on $m_{1,2}$ and $\chi_{\rm eff}$	$1.3^{+2.6}_{-1.0}$	$2.6^{+1.2}_{-0.4}$	$2.7^{+6.1}_{-2.5}$	$0.1^{+0.4}_{-0.1}$	$1.4^{+19.4}_{-15.9}$	0.08/0.9/0.03
	Posterior	$0.9^{+1.5}_{-0.6}$	$2.6^{+1.4}_{-0.4}$	$2.4^{+4.9}_{-2.2}$	$0.1^{+0.4}_{-0.1}$	$1.5^{+29.2}_{-26.1}$	0.05/0.93/0.02
GW200322_091133	Uninformative Prior	$7.3^{+15.9}_{-6.4}$	$170.1^{+2642.2}_{-153.5}$	$1.7^{+8.7}_{-1.6}$	$37.8^{+480.4}_{-36.1}$	$120.0^{+1137.3}_{-157.1}$	0.06/0.91/0.03
	Cond. on $m_{1,2}$	$3.8^{+13.0}_{-3.3}$	$45.7^{+336.9}_{-41.8}$	$2.4^{+7.4}_{-2.3}$	$5.1^{+170.8}_{-5.0}$	$30.0^{+939.2}_{-30.0}$	0.09/0.9/0.01
	Cond. on $m_{1,2}$ and $\chi_{\rm eff}$	$2.9^{+14.2}_{-2.6}$	$52.1^{+353.4}_{-48.2}$	$2.1^{+9.2}_{-1.9}$	$4.7^{+100.9}_{-4.6}$	$15.8^{+865.3}_{-53.9}$	0.07/0.84/0.09
	Posterior	$3.9^{+12.4}_{-2.8}$	$56.0^{+905.6}_{-52.2}$	$2.2^{+9.4}_{-2.0}$	$4.5^{+101.2}_{-4.4}$	$19.8^{+291.1}_{-79.5}$	0.16/0.8/0.04

Table A.1: Complete set of results. For each event, each estimator, and each of the four sequential conditioning considered in this paper we indicate the median and 90% credible interval. For the spin morphologies, we indicate the probability mass function at each of the three discrete points.

Part II

Active galactic nuclei and black holes

Chapter 5

Active galactic nuclei

Summary

Gravitational wave science is multifaceted. A key area of research are formation channels and the environments that facilitate BBH mergers. One possible environment for BBH formation are the discs of active galactic nuclei. In Ch. 5, I summarise current knowledge of active galaxies, both from a broad EM observational point of view and their role in the AGN formation channel, using some of the introduction of Gangardt *et al.* (2024) [285]. Additionally, I discuss migration torques in gas discs, which could work as a mechanism for accelerated merger rates. This chapter serves as an introduction for Ch. 6.

5.1 Observations of AGNs

Scattered across the Universe are galaxies with supermassive black holes at their centre, whose luminous signatures are powered by gas accretion onto the central BH as opposed to solely the radiation from their numerous stars. In 1993, Antonucci (1993) [286] proposed the AGN unification model, hypothesising that a wide variety of objects, including quasars and radio-quiet Seyfert galaxies, are all AGNs viewed from different angles which obscured their features [286–288]. AGNs are traditionally identified by the presence of narrow emission lines [289–293] from reprocessed AGN radiation by the host galaxy gas. Additionally, Type I AGN show broad emission lines, thought to originate from the rapidly rotating circumnuclear gas (gas that is gravitationally coupled to the AGN accretion disc). AGN with only narrow emission lines are instead labelled Type II. Quasars are distant and luminous AGN signals; Seyfert galaxies, named after the pioneering work of [294], are AGNs with high-excitation nuclear emission lines but whose host galaxies are visible. Observations of AGN and their various features now cover the entire EM spectrum [287, 295–305] (see Netzer (2015) [288], Padovani *et al.* (2017) [306], Hickox and Alexander (2018) [307], and Bianchi *et al.* (2022) [308] for additional broad reviews on AGN classification).

As briefly described in Ch. 1, the development of radio astronomy lead to large catalogs of quasars, bright radio sources associated with optical point-like sources [309, 310] (see Shields (1999) [311] for a review on the history of AGNs). Their peculiar spectra were shown by Schmidt (1963) [23] to be at relatively high-redshift, originating from extremely bright galactic nuclei. The theory of how astrophysical objects could produce such luminous signals from such distant locations was developed within a year, simultaneously by Zel'dovich (1964) [26] and Salpeter (1964) [25], where it was shown that accretion onto SMBHs was a possible cause of quasars. Nowadays, it is widely accepted that most galaxies go through an AGN phase during their lifecycle, motivating numerous population studies of AGNs and their host galaxies [312–321].

Observations of AGNs reveal them to be strongly correlated with the properties of their host galaxies, suggesting co-evolution of the centrally-located SMBH and its surrounding gas and stars [292, 301, 322]. The SMBHs at the centre of AGNs have been shown to correlate with the properties of the galaxy bulge [323–328], implying a relationship between the SMBH and the galaxy stellar mass. AGN feedback, the process of the AGN disc and its surrounding material interacting through winds and temperature exchanges [322], may also suppress star formation within its galaxy by expelling cold gas from its bulge through accretion winds, or by heating up the interstellar medium (ISM) to temperatures that can no longer collapse into stars [329, 330].

However, interactions of orbits in the galactic nucleus with the gas near the central BH may lead to the shrinking of their orbits [331–338], thus sourcing a population of stars and compact objects inside AGN discs. These pathways mean that despite star formation being suppressed in AGNs, we can expect compact objects to be located within their discs.

5.2 AGNs and GWs

The enriched AGN disc, now saturated with compact objects whose inclinations shrink with respect to the AGN disc with every interaction [331–337], becomes a viable formation channel for binary black hole and compact object mergers [66, 69, 335, 339–344]. The dense gas in the disc can facilitate binary formation, harden the binary and induce chains of hierarchical BH mergers. This makes AGN discs viable sites for compact object mergers [69, 338, 339, 341, 342, 344–350].

Unlike the cluster formation channel or the isolated formation channel, uncertainties in AGN properties and the dynamics of compact objects within AGN discs result in merger rates that span from $\sim 10^{-2}\,\mathrm{Gpc}^{-3}\mathrm{yr}^{-1}$ [351–353] to $\sim 60\,\mathrm{Gpc}^{-3}\mathrm{yr}^{-1}$ [342, 349].

A key predictor of the AGN formation channel is the possibility of strong alignment and anti-alignment of BBH spins, although the BBH may experience several dynamical encounters which may broaden the spin distribution [67, 354–357]. Additionally, the presence of gas in BBH mergers within AGN discs implies EM counterparts to compact object mergers in AGN discs [358–361]; a possible EM counterpart was found in an AGN galaxy for the high mass event GW190521 [362], although this claim is disputed because the large localisation volume of the event made it likely to detect an EM counterpart [363]. Another possible AGN formation channel identifier is a negative q-χ_{eff} relation in the population of BHs [356, 364]. This identifier only manifests in AGNs that have compact object migration in their disc, such that "migration traps" (radial coordinates where the net migration torque is zero) can form. Hierarchical merging in migration traps thus induces a negative q-χ_{eff} relation, which has been observed in the LVK population results [365].

The occurrence of hierarchical mergers in AGN discs crucially depends on the presence of the so-called migration traps, namely locations in the disc where the migration torque changes sign, which is still an open issue in AGN-disc modeling [342, 345, 366].

5.2.1 Migration torques in AGN discs

Migration in gas discs was first proposed based on formulae that considered how spiral-wave structures can be sustained in galaxies [367–370]. An object orbiting in a gas disc exchanges angular momentum with its surroundings, leading to changes in its orbit and thus a net radial migration in the disc [371]. These migration torques were predicted by Goldreich and Tremaine (1979) [369] and used for planets in protoplanetary discs to explain the existence of hot Jupiter-like planets near their host stars formally in Ward (1997) [372] (although see Ward (1986) [373], Ward and Hourigan (1989) [374], Lin and Papaloizou (1993) [375] for some previous studies of radial migration in protoplanetary discs). Migration in gas discs was primarily studied for the case of planets [376–380]; semi-analytical prescriptions for the migration of protoplanets were derived in Tanaka *et al.* (2002) [381], Paardekooper and Mellema (2006) [377], Paardekooper *et al.* (2010) [379]. The planetary migration theory was then applied to AGN discs [69, 331, 339, 345, 382–384]. A key phenomenon emerging from these studies is the potential occurrence of migration traps — locations in the gas disc where the net radial migration torque is zero. Depending on the mass ratio between the migrator, the central object or the disc, the migrator may clear a gap (referred to as Type II migration) or deplete material at the migration trap without clearing a gap (Type I migration) [372].

Migration traps are an effective mechanism for merging stellar-mass BH binaries embedded in AGN discs, especially in a hierarchical manner [66, 69, 345, 350, 356] (see Gerosa and Fishbach (2021) [385] for a review). Earlier works by Bellovary *et al.* (2016) [345] and Grishin *et al.* (2024) [366] showed that the the location of migration traps does not depend on the properties of the migrating object. The location of these migration traps turns out to be a non-trivial function of the AGN disc parameters, ultimately set by the complex interplay of the gradients of the surface density $\Sigma_{\rm g}$ and temperature T.

5.2.2 AGN discs

The phenomenology of AGN gas discs is uncertain, partially due to obscuration from a dusty torus preventing direct observations of the discs. The accretion disc and the gaseous material coupled to its dynamics are collectively referred to as the AGN disc, which is expected to extend to separations of 1-10 pc [288]. Because of high obscurations and uncertainty in observations, the actual size of AGN discs is somewhat unclear but tends to be larger than what is expected from theoretical models [386–388]. Nevertheless, some properties of the AGN disc are known. Due to the deep gravitational well surrounding the central BH, the gas in the accretion disc is expected to reach temperatures of $\sim 10^5$ K and surface densities of $\sim 10^5$ g cm^{-2}. As well as this, AGN discs have been observed to have a rich phenomenology, including high-energy jets, dusty torii, and accreting BHs (see Padovani *et al.* (2017) [306] and references therein).

Early models of AGNs discs consist of one-dimensional, steady-state, semi-analytic solutions utilising parametric prescriptions. Subsequent computational advancements allowed for models capturing more complex physics, such as radiative transfer, gas phase transitions, magnetic fields, and general relativity (eg., Refs. [389–395]). Nevertheless, one-dimensional models remain highly valuable today due to their computational efficiency and insightful perspectives on the structure of AGN discs. This makes them particularly useful in the study of interactions between compact objects and BHs. The first of these one-dimensional approaches dates back to Shakura and Sunyaev (1973) [396], who first model geometrically thin, optically thick discs around a BHs. Building on this seminal work, two models are most commonly used in the field, namely those by Sirko and Goodman (2003) [1] and Thompson *et al.* (2005) [2] (but see also Refs. [366, 383, 397–402]). Both these models assume some heating mechanisms in the disc that marginally support the outer regions from collapsing due to self-gravity and formulate one-dimensional sets of equations for the AGN-disc profile as a function of a number of parameters such as the mass of the central BH and the accretion rate.

Chapter 6

Active galactic nuclei disc models

Abstract

Models of accretion discs surrounding active galactic nuclei (AGNs) find vast applications in high-energy astrophysics. The broad strategy is to parametrise some of the key disc properties such as gas density and temperature as a function of the radial coordinate from a given set of assumptions on the underlying physics. Two of the most popular approaches in this context were presented by Sirko and Goodman (2003) [1] and Thompson *et al.* (2005) [2]. We present a critical reanalysis of these widely used models, detailing their assumptions and clarifying some steps in their derivation that were previously left unsaid. Our findings are implemented in the `pAGN` module for the Python programming language, which is the first public implementation of these accretion-disc models. We further apply `pAGN` to the evolution of stellar-mass black holes embedded in AGN discs, addressing the potential occurrence of migration traps.

6.1 Summary

This chapter is a reformatted version of my first-author paper Gangardt *et al.* (2024) [285]. In Gangardt *et al.* (2024) [285], I present the companion paper to the Python package `pAGN` [403]. I was the first author of the paper, as well as leading co-developer of `pAGN` with Alessandro A. Trani. Some of the coding methodology for `pAGN` was directly provided by Clément Bonnerot. The paper was written by me with editorial feedback from Alessandro A. Trani, Davide Gerosa and Clèment Bonnerot. The package `pAGN` is a Python implementation of two widely-used AGN disc models developed by Sirko and Goodman (2003) [1] and Thompson *et al.* (2005) [2], which is further applied to the migration torque problem described in Ch. 5.

6.2 Introduction

The Sirko and Goodman (2003) [1] and Thompson *et al.* (2005) [2] accretion disc models are widely used and underpin some of the key, qualitative results in the field of AGN-disc physics. Despite that, the underlying parameters and methods are often left unspecified. Achieving a stable numerical implementation of these disc solutions is not straightforward and codes in this area have not been released in the public domain. The goal of this paper is to critically re-analyse the AGN disc models by Sirko and Goodman (2003) [1] and Thompson *et al.* (2005) [2]. In particular, we clarify the model equations one needs to solve (and crucially the order one needs to solve them), highlight the choices one has to make to obtain stable solutions, and provide a highly customisable implementation. Our software is made publicly available in a Python package called `pAGN` (short for “parametric AGNs”, pronounced as “pagan”).

This paper is organised as follows. In Sec. 6.3, we lay out the equations for the Sirko and Goodman (2003) [1] and Thompson *et al.* (2005) [2] models. In Sec. 6.4, we explore some of the input parameter space for both models. In Sec. 6.5, we showcase our implementation, looking in particular at the occurrence of migration traps in either of the two disc models. In Sec. 6.6, we present the public code `pAGN`. In Sec. 6.7, we draw our conclusions and present prospects for future work.

6.3 AGN disc models

We first summarise the AGN disc models by Sirko and Goodman (2003) [1] and Thompson *et al.* (2005) [2]. We refer to the models as SG03 and TQM05, respectively. Both models consist of an inner, thin accretion disc extended to larger radii to explain observed AGN luminosities. In the outer regions, the disc needs to remain marginally stable against fragmentation. With respect to the Shakura and Sunyaev [396] thin-disc solution, the SG03 model additionally assumes the existence of some heating mechanism generating radiation pressure that can support the outer parts of the disc against collapse. The TQM05 model further modifies the SG03 model, with the most notable change being that the mass advection is driven by non-local torques rather than local viscous stresses. Furthermore, the Sirko and Goodman (2003) [1] accretion rate is constant across the disc while that of Thompson *et al.* (2005) [2] varies because it directly takes into account the mass lost to star formation.

We now introduce each model in closer detail and present the key equations one needs to solve to build the resulting disc profiles. For clarity, the parameters entering each model are reported in Table 6.1. A step-by-step guide on how the equations are

Table 6.1: Key parameters entering the Sirko and Goodman (2003) [1] and Thompson *et al.* (2005) [2] AGN-disc models. The third column indicates whether the parameter is an input of the model (I), a fixed value for the entire disc (F), or a profile parameter obtained by running the model (P). The accretion rate $\dot{M}$ is a fixed parameter for the SG03 disc but a profile parameter for the TQM05 disc.

Symbol	**Definition**	**I/F/P**
M	Mass of the central BH	I
R_s	BH Schwarzschild radius	F
L_Edd	Eddington luminosity	F
$\dot{M}_\mathrm{Edd}$	Eddington accretion rate	F
X	Hydrogen abundance in disc	I
κ_es	Electron scattering opacity	F
r	Radial distance from the central BH	P
$\dot{M}$	Mass accretion rate	F or P
r_min	Inner edge of the disc	I
T	Midplane temperature	P
T_eff	Midplane effective temperature	P
ρ	Midplane density	P
h	Height of disc from the midplane	P
Σ_g	Midplane surface density	P
Σ_tot	Midplane total dynamical density	P
f_g	Gas fraction	P
τ_v	Midplane optical depth	P
κ	Midplane opacity	P
c_s	Midpane sound speed	P
p_gas	Gas pressure	P
p_rad	Radiation pressure	P

Sirko and Goodman (2003) [1] parameters

Symbol	**Definition**	**I/F/P**
α	Shakura-Sunyaev viscosity parameter	I
r_max	Outer edge of the disc	I
l_E	Disc Eddington ratio	I
ϵ_S	Radiative efficiency	I
b	Switch for viscosity-pressure relation	I
Q_S	Toomre stability parameter	P
ν	Disc viscosity	P
Ω_S	Rotational velocity	P
β	Gas pressure to total pressure ratio	P

Thompson *et al.* (2005) [2] parameters

Symbol	**Definition**	**I/F/P**
σ	Stellar dispersion velocity	I
r_out	Effective outer edge of the disc	I
$\dot{M}_\mathrm{out}$	Accretion rate at r_out	I
m_T	Global torque efficiency	I
ϵ_T	Star formation efficiency	I
ξ	Supernova radiative efficiency	I
$\dot{\Sigma}_*$	Star formation rate	P
η	Star formation efficiency fraction	P
Q_T	Toomre stability parameter	P
Ω_T	Rotational velocity	P

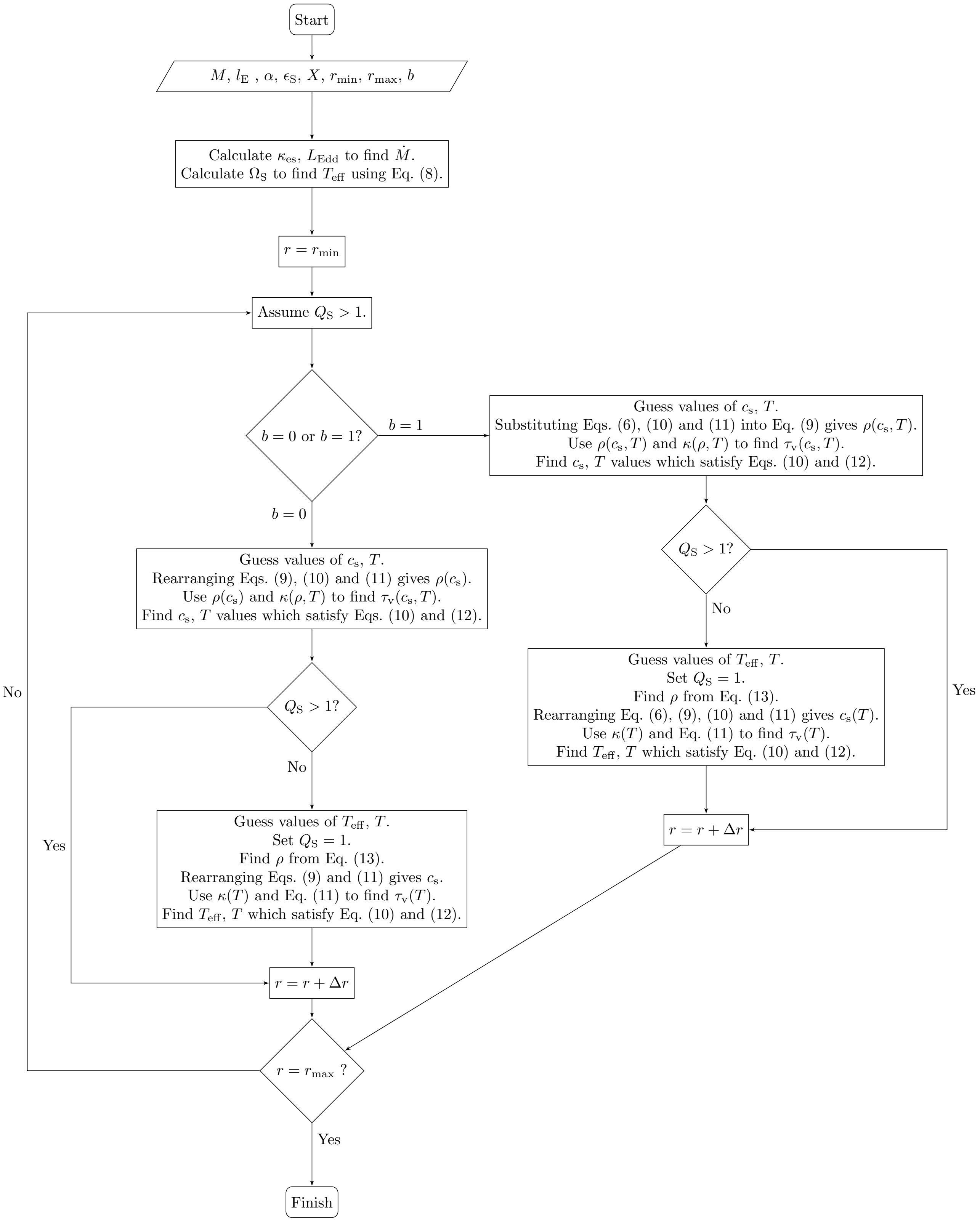

Figure 6.1: Flowchart showing detailing our solution strategy for the SG03 model. Construction proceeds from the inner disc to the outer disc, with initial guesses on the stability parameter $Q_{\rm S}$ which are then checked a-posteriori.

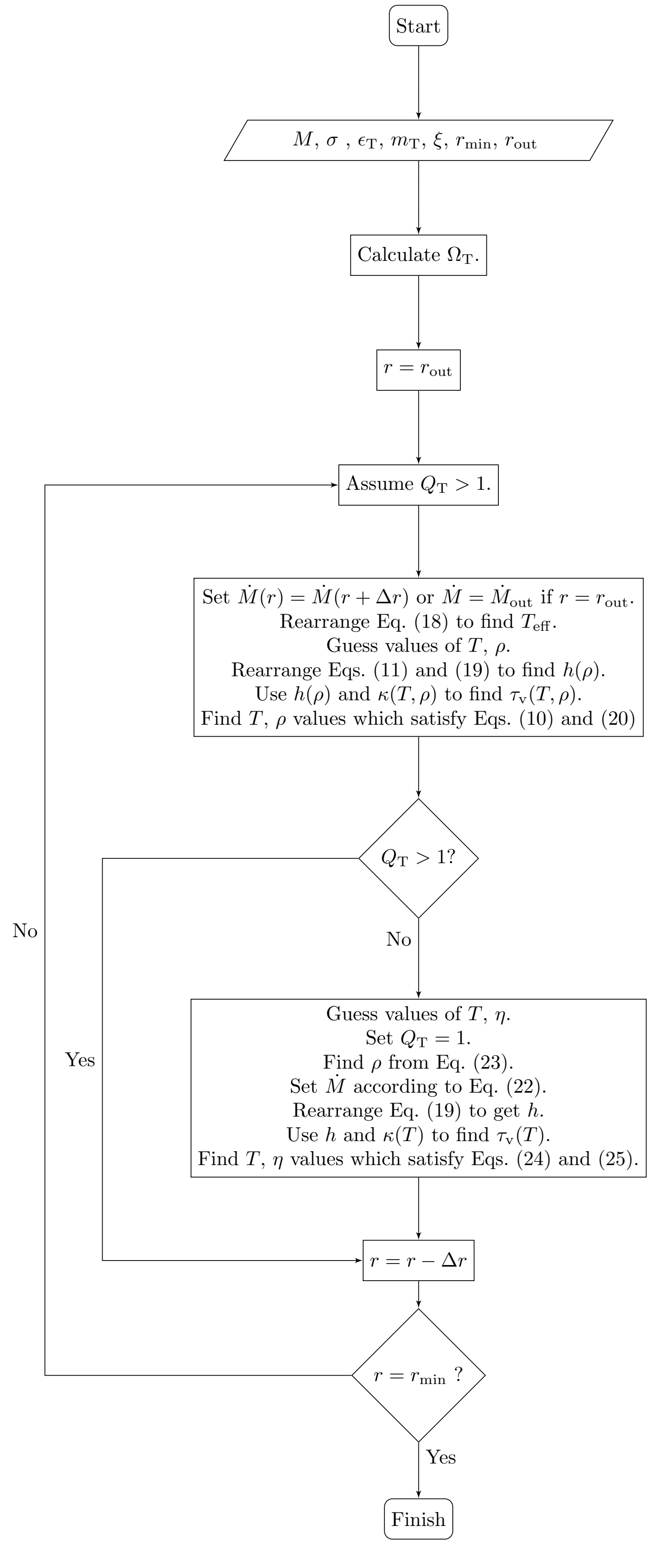

Figure 6.2: Flowchart showing detailing our solution strategy for the TQM05 model. Construction proceeds from the outer disc to the inner disc, with initial guesses on the stability parameter Q_T which are then checked a-posteriori.

solved is provided in Figs. 6.1 and 6.2.

6.3.1 Sirko & Goodman (2003)

Modeling strategy

In the inner regions, the SG03 model assumes a thin and viscous accretion disc to be the source of AGN luminosity (as proposed by Pringle (1981) [404]), similar to the disc model by Shakura and Sunyaev (1973) [396]. Such a self-gravitating disc cannot be extended to large radii, where the gravitational pull in the vertical direction causes disc fragmentation and star formation, thus depleting the disc of gas to sufficiently fuel the inner regions. The SG03 model resolves this by assuming that some auxiliary heating (i.e. heating that does not come from orbital energy) lowers the density of the gas in the outer region gas, thus reducing the gravitational pressure. This heating is most likely sourced by star formation, but this is left unspecified in the SG03 model. The auxiliary heating process is prescribed so that gas supply from the marginally gravitationally stable outer regions keeps fueling the hotter inner regions all under a constant gas accretion rate $\dot{M}$.

The stability of the disc is encoded by the parameter first defined by
Toomre (1964) [405] for circular Keplerian orbits

$$Q_{\mathrm{S}} \equiv \frac{c_{\mathrm{s}}\Omega_{\mathrm{S}}}{\pi G \Sigma_{\mathrm{g}}} \approx \frac{\Omega_{\mathrm{S}}^2}{2\pi G\rho}\,, \tag{6.1}$$

where c_{s} is the speed of sound, $\Omega_{\mathrm{S}} = \sqrt{GM/r^3}$ is the angular velocity of the disc, $\Sigma_{\mathrm{g}} = 2\rho h$ is the midplane mass surface density, ρ is the midplane mass density, and h is the height from the midplane. The disc collapses and fragments whenever $Q_{\mathrm{S}} < 1$. The SG03 model is made of two regimes. In the inner region one has $Q_{\mathrm{S}} \gg 1$: the angular frequency and temperature are high and there is no risk of fragmentation. The outer region instead presents $Q_{\rm S} \sim 1$: the disc is only marginally stable and auxiliary heating sources become necessary to prevent vertical collapse.

The construction of the model proceeds from an inner boundary $r_{\rm min}$ and assumes a zero-torque boundary condition, see Fig. 6.1. Sirko and Goodman (2003) [1] approximate the innermost stable circular orbit to be $r_{\rm min} = R_{\rm s}/4\epsilon_{\rm S}$, where $R_{\rm s} = 2GM/c^2$ is the Schwarzschild radius of the BH and $\epsilon_{\rm S}$ is the radiative efficiency of the BH, which is set to $\epsilon_{\rm S} = 0.1$. For each gas ring at a cylindrical radius r from the central BH, one first assumes that the ring is located in the inner regime where $Q_{\rm S} \gg 1$. The equations presented in Sec. 6.3.1 below are then solved to find $\Omega_{\rm S}$ and ρ. In turn these are used to evaluate $Q_{\rm S}$ from Eq. (6.1). If $Q_{\rm S} < 1$, one switches to the $Q_{\rm S} = 1$ regime and solves the equations from Sec. 6.3.1 instead. This process is then repeated for every value of r until $r = r_{\rm max}$. Unless specified, we set $r_{\rm max}$ to the minimum between $10^7 R_{\rm s}$ and 1 pc. An unreasonably large value of $r_{\rm max}$ leads to a spectral energy distribution that does not match observations (cf. Sirko and Goodman (2003) [1]).

The accretion rate of the SG03 disc is parameterised by the Eddington ratio

$$l_{\rm E} = \frac{\dot{M}\epsilon_{\rm S}c^2}{L_{\rm Edd}}\,, \tag{6.2}$$

where $L_{\rm Edd}$ is the Eddington luminosity and the normalisation is set to the luminosity of a non-self gravitating disc. In turn, the Eddington luminosity is

$$L_{\rm Edd} = \frac{4\pi GMc}{\kappa_{\rm es}}\,, \tag{6.3}$$

where $\kappa_{\rm es} = 0.2(1+X)\,{\rm cm^2 g^{-1}}$ is the electron scattering opacity for a fractional abundance of hydrogen which we assume to be $X = 0.7$. The SG03 model thus depends on the mass of the central BH M through both the angular velocity of the disc $\Omega_{\rm S}$ and the accretion rate $\dot{M}$.

The disc viscosity is prescribed using the Shakura and Sunyaev (1973) [396] dimensionless parameter

$$\alpha = \frac{\nu}{c_{\rm s} h \beta^b} \,, \tag{6.4}$$

where

$$\beta = \frac{p_{\rm gas}}{p_{\rm gas} + p_{\rm rad}} = \frac{p_{\rm gas}}{p_{\rm tot}} \tag{6.5}$$

is the fraction of gas pressure $p_{\rm gas}$ to total pressure $p_{\rm tot}$; the latter contains contributions from both gas and radiation. The parameter $b = \{0, 1\}$ acts as a switch flag to determine how viscosity and pressure relate in the disc. The two cases are often referred to as α-disc ($b = 0$) and β-disc ($b = 1$), see e.g. Haiman *et al.* (2009) [398]. For the gas pressure, we use the ideal gas law

$$p_{\rm gas} = \frac{\rho k_{\rm B} T}{m_{\rm U}} \,, \tag{6.6}$$

where $k_{\rm B}$ is the Boltzmann constant and $m_{\rm U}$ is the atomic-mass constant. The radiation pressure is given by

$$p_{\rm rad} = \frac{\sigma_{\rm SB} \tau_{\rm v}}{2c} T_{\rm eff}^4 \,, \tag{6.7}$$

which is constructed such that in the optically thick regime it recovers $p_{\rm rad} = 4\sigma_{\rm SB} T^4 / 3c$, but retains a dependency on $\tau_{\rm v}$ in the optically thin regime [1]. The source of the radiation pressure is not made explicit by Sirko and Goodman (2003) [1], but is assumed to come from stellar processes such as supernovae and nuclear fusion in stars.

Inner regime

For each value of r, the model first assumes that there is no star formation ($Q_{\rm S} \geq 1$). Each annulus is treated as a black-body with an effective temperature $T_{\rm eff}$. This is found by equating the locally radiated flux to the viscous heating rate per unit area [396]:

$$\sigma_{\rm SB} T_{\rm eff}^4 = \frac{3\Omega_{\rm S}^2}{8\pi} \dot{M} \left(1 - \sqrt{\frac{r_{\rm min}}{r}}\right) = \frac{3\Omega_{\rm S}^2}{8\pi} \dot{M}' \,, \tag{6.8}$$

where $\sigma_{\rm SB}$ is the Stefan-Boltzmann constant and we have defined $\dot{M}' = \dot{M}(1 - \sqrt{r_{\rm min}/r})$. Equation (6.8) assumes that all material below $r = r_{\rm min}$ falls into the BH and cannot energetically interact with the rest of the disc.

Mass conservation relates the viscosity of the gas ring to the accretion rate [1]

$$\beta^b c_{\rm s}^2 \Sigma_{\rm g} = \frac{\dot{M}' \Omega_{\rm S}}{3\pi\alpha} \,, \tag{6.9}$$

which gives two families of solutions: $b = 0$ (where the viscosity is proportional to total pressure) and $b = 1$ (where the viscosity is proportional to the gas pressure only). The sound speed in the disc is defined as

$$c_{\rm s}^2 = \frac{p_{\rm tot}}{\rho} \,. \tag{6.10}$$

In this regime, for each value of r, we look for solutions in $c_{\rm s}$ and T and rearrange all other parameters as functions of $c_{\rm s}$ and T only. The midplane height can be expressed as a function of $c_{\rm s}$ by assuming hydrostatic equilibrium

$$h = \frac{c_{\rm s}}{\Omega_{\rm S}} \,. \tag{6.11}$$

The value of the density as a function of c_{s} and T is then given by substituting $\Sigma_{\mathrm{g}} = 2\rho h$, Eq. (6.10) and Eq. (6.11) into Eq. (6.9) for the $b = 0$ case, and combining them with the equation for the gas pressure [see Eq. (6.6)] for the $b = 1$ case.

The temperature profile in the disc depends on the optical depth $\tau_{\mathrm{v}} = \kappa\rho h$, where $\kappa(\rho, T)$ is the opacity. The latter is obtained using interpolated values by Semenov *et al.* (2003) [406] when $T < 10^4$K and Badnell *et al.* (2005) [407] when $T > 10^4$K, the set of which we refer to as the "combined" opacity. These are newer prescriptions for the opacity compared to those by Iglesias and Rogers (1996) [408] and Alexander and Ferguson (1994) [409] used by Sirko and Goodman (2003) [1]. The opacities in Sirko and Goodman (2003) [1] are calculated for silicate grains; the effect of graphite that is important at temperatures of ∼2000 K and may be responsible for the broad line region in AGN observations (see Baskin and Laor (2018) [410]) is ignored. The inclusion of the effect of graphite in `pAGN` is left to future work. From the opacity and effective temperature, we look for solutions in T by assuming the disc ring is in radiative equilibrium:

$$T^4 = \left(\frac{3}{8}\tau_{\mathrm{v}} + \frac{1}{2} + \frac{1}{4\tau_{\mathrm{v}}}\right) T_{\mathrm{eff}}^4\,, \tag{6.12}$$

where the functional form of the equation was chosen to match the temperature dependence on T_{eff} and τ_{v} across both the optically-thick and optically-thin regimes, cf. Sirko and Goodman (2003) [1]. Finally, one can look for solutions in c_{s} and T by considering Eq. (6.10).

The Toomre stability parameter Q_{S} is calculated from the second expression in Eq. (6.1). If this falls below 1, it is assumed that the ring is in the outer regime and a different set of equations is used, which we present next.

Outer regime

In the outer regions, the model expects the disc to be only marginally gravitationally stable, i.e. $Q_{\mathrm{S}} = 1$. In this case, Eq. (6.8) no longer applies since there is additional auxiliary heating. The density is then given by

$$\rho = \frac{\Omega_{\mathrm{S}}^2}{2\pi G}, \tag{6.13}$$

which is a rearrangement of Eq. (6.1) where $Q_{\mathrm{S}} = 1$. In the inner regime we look for solutions in c_{s} and T; in the outer regime we know the value of the density ρ and instead look for solutions in T and T_{eff}. This is done by rearranging Eq. (6.9) and substituting in Eqs. (6.10), (6.11) and (6.13) to obtain an expression for c_{s} as a function of T. In the $b = 0$ case, c_{s} can be independently determined for a given value of r; in the $b = 1$ case, c_{s} is a function of the temperature T [see Eq. (6.6)]. To find values for T and T_{eff}, we look for solutions that satisfy Eqs. (6.10) and (6.12) simultaneously.

Disc profiles

Figure 6.3 shows the radial profile of some key disc parameters in the SG03 model, tailored to reproducing fig. 2 from Sirko and Goodman (2003) [1]. In particular, the figure shows a $10^8 M_\odot$ BH surrounded by a disc with $\alpha = 0.01$, $l_E = 0.5$ and $\epsilon_{\mathrm{S}} = 0.1$, presenting both the $b = 0$ and $b = 1$ cases.

In fig. 2 in Sirko and Goodman (2003) [1], there are three different solutions for the disc parameters from $r \gtrsim 5 \times 10^5 R_{\mathrm{s}}$. Our implementation recovers the same behaviour, but we only accept the continuous, high-temperature, low-opacity solution. For this case, the midplane temperature of the disc remains above 10^3 K and the opacity drops to 10^{-3} cm^{2}g^{-1} in the outer regime, both of which affect the gas and radiation pressure

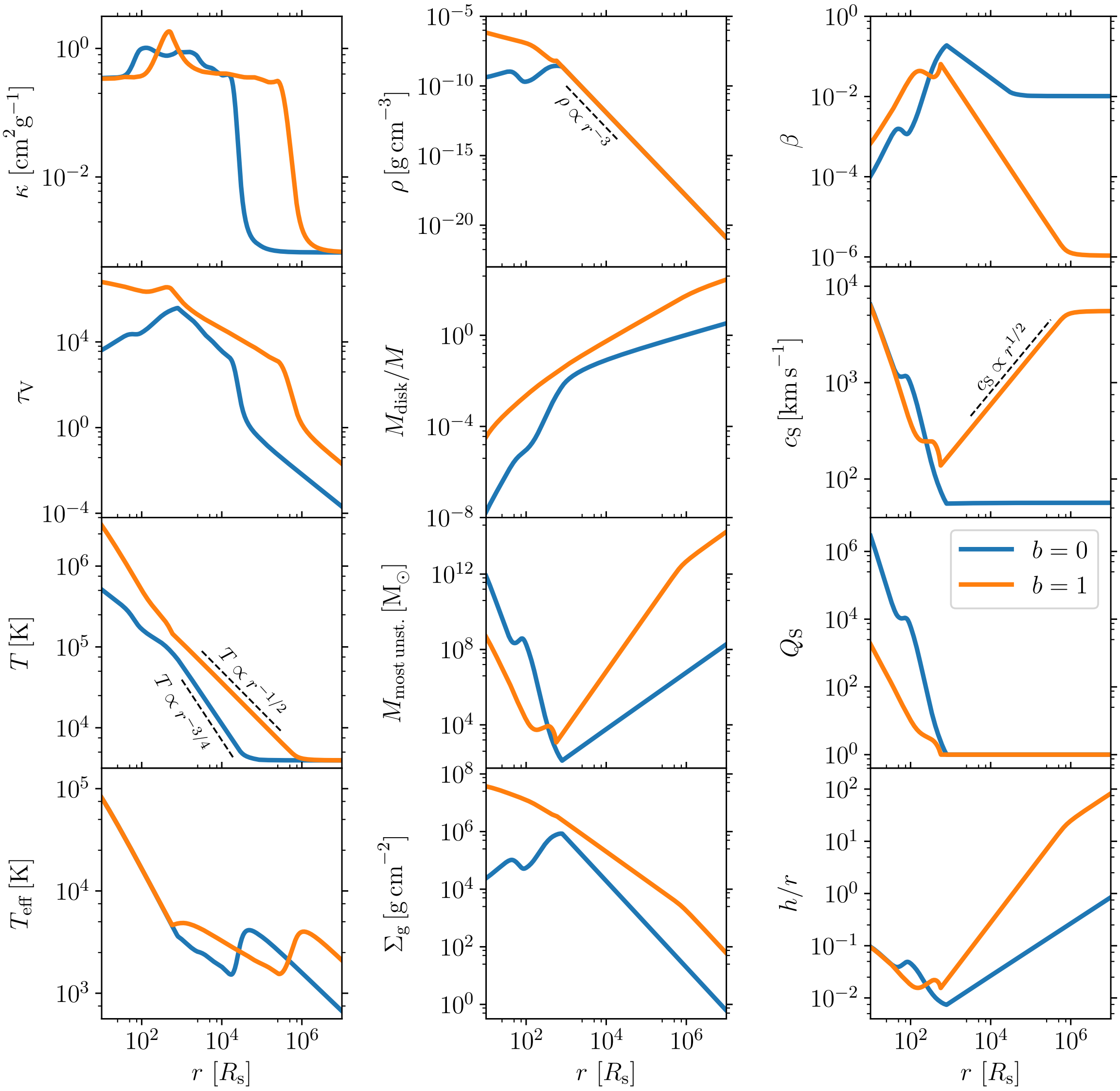

Figure 6.3: Radial profile in the SG03 disc model for the opacity κ, the mass density ρ, the pressure fraction β, the optical depth τ_v, the disc mass $M_{\rm disc}$, the sound speed c_s, the temperature T, the most unstable mass $M_{\rm most\,unst.}$, the Toomre stability parameter Q_S, the effective temperature $T_{\rm eff}$, the surface mass density Σ_g and the half-thickness h. All input values are the same as in fig. 2 by Sirko and Goodman [1]: $M = 10^8 M_\odot$, $\alpha = 0.01$, $l_E = 0.5, \epsilon_S = 0.1$. Blue (orange) curves indicate the case where $b = 0$ ($b = 1$) and the viscosity is proportional to total (gas) pressure.

profiles, as reflected in the parameter β. The transition between the inner and outer disc regimes takes place at $r \approx 10^3\,R_\mathrm{s}$, which is consistent with the original results by Sirko and Goodman (2003) [1].

Figure 6.3 also compares the $b = 0$ case with the $b = 1$ case for the same AGN disc. The difference between the two is that the viscosity is assumed to be proportional to the total and gas pressure, respectively. The $b = 1$ case remains in the optically thick regime out to larger separations, thus also maintaining higher temperatures in those outer regions. For this set of input parameters, the aspect ratio of the disc becomes > 1 at separations as small as $r \approx 5 \times 10^4\,R_\mathrm{s}$, which breaks the thin-disc assumption.

In the outer regime, the density scales as $\rho \propto \Omega_\mathrm{S}^2 \propto r^{-3}$ [see Eq. (6.13)]. Furthermore, the condition $r \gg r_\mathrm{min}$ implies that $\dot{M}'$ is approximately constant. Depending on the value of b, one can use Eq. (6.9) to relate ρ, T and Ω_S. By approximating the system as optically thick ($\tau_\mathrm{v} \gg 1$), Eq. (6.12) gives $T^4 \propto \tau_\mathrm{v} T_\mathrm{eff}^4$. Using Eq. (6.10), one can then find simple power-law scalings for most parameters in the outer regime, as long as the opacity κ is kept constant. These are shown in Fig. 6.3 for the $10^3 R_\mathrm{s} \lesssim r \lesssim 10^5 R_\mathrm{s}$ region. In particular, one has $T \propto r^{-3/4}$ for $b = 0$ and $T \propto r^{-1/2}$ for $b = 1$. From Eq. (6.10), we find that in the optically thick regime, c_s is approximately constant when $b = 0$ and proportional to $r^{1/2}$ when $b = 1$. At $r \gtrsim 10^5 R_\mathrm{s}$, one has $\kappa \ll 1$ and both discs fall back to the optically thin regime. In this case, Eq. (6.12) gives $T^4 \propto T_\mathrm{eff}^4/\tau_\mathrm{v}$, which from Eq. (6.10) gives $T^4 \propto \rho c_\mathrm{s}^2/\tau_\mathrm{v}^2$ for both $b = 0$ and $b = 1$. If we assume κ to be constant, then T will also remain constant for all values of r.

Figure 6.3 shows the "most unstable mass" $M_\text{most unst.} \equiv c_\mathrm{s}^4/G^2\Sigma_\mathrm{g}$ at a given radius. This is the mass enclosed in protostellar clumps with a characteristic radius $r_\mathrm{c} = c_\mathrm{s}^2/G\Sigma_\mathrm{g}$ [405] and corresponds to the maximum mass that can be present in local perturbations and is thus available for star formation. Figure 6.3 shows that, for both the $b = 0$ and $b = 1$ cases, $M_{\mathrm{most\,unst.}}$ has a minimum at $r \approx 10^3 R_\mathrm{s}$, corresponding to high Σ_g values and low c_s values. Below this radius, where $Q > 1$ and star formation ceases, the value of $M_{\mathrm{most\,unst.}}$ no longer provides meaningful information.

6.3.2 Thompson et al. (2005)

Modeling strategy

Thompson *et al.* (2005) [2] proposes an AGN model for which the outer areas of the disc are vertically supported against gravitational collapse by radiation pressure from star formation by-products, dominated in the optically thick regime by dust grains around massive stars. The angular momentum transport in the TQM05 disc is described by global torques instead of a local viscosity mechanism like in the SG03 model, which provides rapid radial advection rates in the outer regions of the disc.

In the TQM05 model, the angular velocity

$$\Omega_\mathrm{T} = \sqrt{\frac{GM}{r^3} + 2\frac{\sigma^2}{r^2}} \tag{6.14}$$

is only approximately Keplerian and includes the effect of the dispersion velocity σ. The dispersion and the central mass are related by the $M-\sigma$ relation from observations. Thompson *et al.* (2005) [2] used the expression by Tremaine *et al.* (2002) [324], while we opted for an updated fit by Gültekin *et al.* (2009) [325]:

$$\log \frac{\sigma}{200\,\mathrm{km/s}} = \frac{1}{4.24}\left(\log \frac{M}{M_\odot} - 8.12\right) , \tag{6.15}$$

which is taken from their full galaxy sample. We stress that both of these expressions were obtained for surveys of non-AGN galaxies, meaning that they do not appropriately account for selection biases [411–413].

The TQM05 model accounts for the star-formation rate per unit area:

$$\dot{\Sigma}_* = \Sigma_{\rm g}\Omega_{\rm T}\eta\,, \tag{6.16}$$

which is parametrized using the fraction η of the disc dynamical timescale. By means of $\dot{\Sigma}_*$, the TQM05 model explicitly tracks changes in the accretion rate $\dot{M}$ throughout the disc due to star formation. The gas accreted onto the central BH is supplied by material outside of a radius $r_{\rm out}$ at a constant rate $\dot{M}_{\rm out}$. As Thompson *et al.* (2005) [2] point out, the AGN disc for the TQM05 model does not have a clear outer boundary because the gas is expected to be fed to the central BH by the surrounding interstellar medium. Unlike $r_{\rm max}$ in the SG03 model, which is a chosen value after which the gas is expected to fragment into stars, here, $r_{\rm out}$ represents a transition point beyond which the accretion rate is constant and within which the accretion rate varies due to star formation. Opposite to the SG03 case, in the TQM05 model one integrates from the outer boundary of the AGN disc $r_{\rm out}$ down to the inner edge of the disc, here set to $r_{\rm min} = 3R_{\rm s}$.

In the TQM05 model, the Toomre (1964) [405] stability criterion is written as

$$Q_{\rm T} = \frac{\kappa_\Omega c_{\rm s}}{\pi G \Sigma_{\rm g}} \approx \frac{\Omega_{\rm T}^2}{\sqrt{2}\pi G\rho}\,, \tag{6.17}$$

where $\kappa_\Omega^2 = 4\Omega_{\rm T}^2 + {\rm d}\Omega_{\rm T}^2/{\rm d}\ln r$ is the epicyclic frequency. To first order in $1/r$, Eq. (6.14) gives ${\rm d}\Omega_{\rm T}/{\rm d}r \approx -\Omega_T/r$ such that $\kappa_\Omega \approx \sqrt{2}\Omega$. When $Q_{\rm T} \gg 1$, we expect conditions to be unfavourable to star formation so that $\dot{\Sigma}_*$ and η are close to zero. In the outer area of the disc where $Q_{\rm T} \approx 1$, stellar feedback plays a key role in stabilizing the disc.

Much like the SG03 model,[1] the TQM05 one also has two regimes according to the value of Q_T, see Fig. 6.2. We initialize our numerical root finder at the outer boundary assuming that the disc is optically thick to its own infrared radiation and that $Q_\mathrm{T} = 1$, thus obtaining initial values for T, ρ and η (see Appendix B.1).

Non star-forming regime

For every value of r under consideration, we first assume that there is no star formation and that $Q_\mathrm{T} > 1$. In this case, the accretion rate is constant and thus the value of $\dot{M}$ is the same as that of the preceding separation, i.e. $\dot{M}(r) = \dot{M}(r + \Delta r)$, where Δr is the numerical radial resolution. At $r = r_\mathrm{out}$, one has the boundary condition $\dot{M}(r_\mathrm{out}) = \dot{M}_\mathrm{out}$. The gas ring at cylindrical radius r is assumed to radiate as a black body with effective temperature:

$$\sigma_\mathrm{SB} T_\mathrm{eff}^4 = \frac{3\Omega_\mathrm{T}^2}{8\pi} \dot{M}' \,, \tag{6.18}$$

which is the same as Eq. (6.8). The TQM05 model assumes that the angular momentum in the disc is transported by global torques, so that the radial velocity of the gas v_r is a fraction m_T of the sound speed c_s. The resulting accretion rate is

$$\dot{M} = 4\pi r \rho h v_\mathrm{r} = 4\pi r \rho h m_\mathrm{T} c_\mathrm{s} = 4\pi r \Omega_\mathrm{T} m_\mathrm{T} \rho h^2 \,, \tag{6.19}$$

where we have assumed hydrostatic equilibrium, $h = c_\mathrm{s}/\Omega_\mathrm{T}$ [see Eq. (6.11)]. Using Eq. (6.19), one can compute the disc half thickness h as a function of the accretion rate and density.

---

[1] For small values of r one has that Ω_T is approximately Keplerian and $Q_\mathrm{T} \approx Q_\mathrm{S}$. Since Q_T is expected to be $\gg 1$ near the BH, the factor $\sqrt{2}$ is negligible.

We then interpolate the opacity tables of our choosing to find the $\kappa(\rho, T)$, which in turn gives us the optical depth $\tau_{\rm v} = \kappa\rho h$ as a function of T and ρ. Notably, Thompson *et al.* (2005) [2] use the opacities by Semenov *et al.* (2003) [406] which are provided for temperatures up to $T \simeq 10^4$K and extrapolate them to higher temperatures by keeping $\kappa(\rho, T)$ constant; in the following we refer to this set as the "Semenov" opacities. In `pAGN`, we instead use the combined set of opacities with values by Semenov *et al.* (2003) [406] up to $T = 10^4$K and then values by Badnell *et al.* (2005) [407] for higher temperatures.

We look for solutions in T and ρ so that the gas ring is in radiative equilibrium and the sound speed is consistently defined. The condition for radiative equilibrium adopted by Thompson *et al.* (2005) [2] is

$$T^4 = \left(\frac{3}{4}\tau_{\rm v} + \frac{1}{2\tau_{\rm v}} + 1\right) T_{\rm eff}^4 \,, \tag{6.20}$$

which is the same as Eq. (6.12) but doubled. The definition of the sound speed $c_{\rm s} = p_{\rm tot}/\rho$ is almost identical to that given in Eq. (6.10) for the SG03 model. The sound speed definition assumes hydrostatic equilibrium and the pressure definitions $p_{\rm gas} = \rho k_{\rm B} T/m_{\rm U}$, $p_{\rm rad} = \sigma_{\rm SB}\tau_{\rm v}T_{\rm eff}^4/c$. The additional factor of 2 in the TQM05 model's definition of $p_{\rm rad}$ ensures that in the optically thick regime using Eq. (6.20) gives $p_{\rm rad} \approx 4\sigma_{\rm SB}T^4/3c$.

Solutions for ρ and T are then found by balancing Eqs. (6.10) and (6.20). One can then compute $Q_{\rm T}$ once more using Eq. (6.17). If $Q_{\rm T} < 1$, the ring at radius r is instead assumed to be in the outer star-forming regime.

Star-forming regime

In the case where there is star formation, the accretion rate is no longer constant. Instead, it is calculated numerically by taking the difference between the initial $\dot{M}_{\mathrm{out}}$ and the integrated accretion rate from star formation down to the current ring:

$$\begin{aligned} \dot{M}(r) &= \dot{M}_{\mathrm{out}} - \int_r^{r_{\mathrm{out}}} 4\pi r \rho h \Omega_{\mathrm{T}} \eta \mathrm{d}r & (6.21) \\ &\approx \dot{M}_{\mathrm{out}} - \sum_{r_j=r}^{r_{\mathrm{out}}} 4\pi r_j \rho_j h_j \Omega_{\mathrm{T},j} \eta_j \Delta r_j \,, & (6.22) \end{aligned}$$

where the subscript j denotes that the given parameter is taken at $r = r_j$. Like in the SG03 model, we assume marginal stability, i.e. $Q_{\mathrm{T}} = 1$. Rearranging Eq. (6.17) for the mass density yields

$$\rho = \frac{\Omega_{\mathrm{T}}^2}{\sqrt{2}\pi G} \,. \tag{6.23}$$

The two parameters we are solving for in this case are the temperature T and the star formation fraction η of the disc ring. One calculates h from Eq. (6.19), interpolates the value of $\kappa(T)$ and finds $\tau_{\mathrm{v}}(T)$, finally calculating $T_{\mathrm{eff}}^4(T)$ using Eq. (6.20).

We now look for solutions in η and T that balance the radiated flux

$$\sigma_{\mathrm{SB}} T_{\mathrm{eff}}^4 = \rho h \Omega_{\mathrm{T}} \eta \epsilon_{\mathrm{T}} c^2 + \frac{3}{8\pi} \dot{M}' \Omega_{\mathrm{T}}^2 \,, \tag{6.24}$$

which now directly accounts for radiation from stars unlike Eqs. (6.8) and (6.18), while assuming hydrostatic equilibrium. One has

$$\rho h^2 \Omega_{\mathrm{T}}^2 = \frac{\rho k_{\mathrm{B}} T}{m_{\mathrm{U}}} + 2\rho h \eta \Omega_{\mathrm{T}} \epsilon_{\mathrm{T}} c \left(\frac{\tau_{\mathrm{v}}}{2} + \xi \right) \,, \tag{6.25}$$

where $\epsilon_{\rm T}$ and ξ are free parameters describing the efficiency of star formation in the disc and the radiative efficiency of supernovae, respectively. In this regime, it is expected that the gas will be optically thin, and therefore radiation pressure from supernovae is included through the ξ parameter. Thompson *et al.* (2005) [2] sets $\epsilon_{\rm T} = 10^{-3}$ and $\xi = 1$. We seek the values of η and T that simultaneously solve Eqs. (6.24) and (6.25).

Accretion criterion

Unlike Sirko and Goodman (2003) [1], the Thompson *et al.* (2005) [2] model presents an accretion rate $\dot{M}$ that changes as a function of the radial separation r. This naturally means that if the accretion rate at the outer boundary is too low, not enough gas is able to reach the central BH to maintain high temperatures and bright AGN luminosities, which are expected to be in the $10^{-3} - 0.5\, L_{\rm Edd}$ range, see [414–417]. This introduces a minimum threshold for $\dot{M}_{\rm out}$. Thompson *et al.* (2005) [2] argue that accretion rates of $\sim 1 - 10\,{\rm M_\odot yr^{-1}}$ at the inner disc boundary $r_{\rm min}$ are sufficient to produce a bright AGN when the central BH mass is $\sim 10^9\,{\rm M_\odot}$. This is equivalent to a minimum BH accretion rate of $\dot{M} \sim 0.2\ \dot{M}_{\rm Edd} = 0.2\ L_{\rm Edd}/(0.1c^2)$ at $r = r_{\rm min}$. Using eq. (47) in Thompson *et al.* (2005) [2], we find that over a wavelength range of $[10^{-8}\,{\rm m}, 10^{-3}\,{\rm m}]$, setting $0.2\ \dot{M}_{\rm Edd}$ gives a disc bolometric luminosity of $2 \times 10^{-4}\, L_{\rm Edd}$.

There is no general expression that relates the accretion rate $\dot{M}_{\rm out}$ and outer radius $r_{\rm out}$ to the BH mass M that would ensure a bright AGN disc. Nonetheless, we can attempt to find such a relationship by considering how the accretion rate at the outer boundary $\dot{M}_{\rm out}$ scales with the size of the disc $r_{\rm out}$ and the central BH mass. Thompson *et al.* (2005) [2] proposes a critical value $\dot{M}_{\rm c}$, obtained by equating the star formation timescale $\tau_* = 1/\eta\Omega$ with the advection timescale $\tau_{\rm adv} = r/v_{\rm r}$ to determine whether enough material reaches the central BH to form a luminous signal. From Eq. (6.19) we find

$$\dot{M}_{\rm c} = 4\pi r^2 \rho h \eta \Omega_{\rm T}\,. \tag{6.26}$$

Together with Eq. (6.26), this result can be used to introduce a dependence on $r_{\rm out}$ and M to $\dot{M}_{\rm out}$. A BH with $M = 10^8\,{\rm M}_\odot$ surrounded by a TQM05 disc that has $r_{\rm out} = 95$ pc, $\dot{M}_{\rm out} = 320\,{\rm M}_\odot{\rm yr}^{-1}$, and $\sigma = 188$ km s^{-1} satisfies $\dot{M}_{\rm out} > \dot{M}_{\rm c}(r = r_{\rm out})$ and has an accretion rate near the central BH of $\approx 1.93\,{\rm M}_\odot{\rm yr}^{-1} = 0.74\dot{M}_{\rm Edd}$ (giving a disc luminosity of $9.61 \times 10^{-4}\,L_{\rm Edd}$). We use these values to keep the ratio of $\dot{M}_{\rm out}/\dot{M}_{\rm c}$ constant. Using Eqs. (6.16), (6.14), (6.26), and assuming the optically thick regime (see Appendix B.1), one can show that $\dot{M}_{\rm c} \propto r\sigma^2$. Therefore, we scale $\dot{M}_{\rm out}$ with the outer boundary of the disc and the dispersion velocity, i.e.

$$\dot{M}_{\rm out} = 320\,{\rm M}_\odot{\rm yr}^{-1} \left(\frac{r_{\rm out}}{95{\rm pc}}\right) \left(\frac{\sigma}{188{\rm kms}^{-1}}\right)^2 . \tag{6.27}$$

However, for high masses, Eq. (6.27) is not enough to fulfill the the $\dot{M}_{\rm out} > \dot{M}_{\rm c}$ criterion. The inability of $\dot{M}_{\rm c}$ to accurately predict whether a bright AGN disc is formed is not surprising, as it compares the timescales for only one value of r. In Thompson *et al.* (2005) [2], it is stated that discs with $\dot{M}_{\rm out} < \dot{M}_{\rm c}(r = r_{\rm out})$ cannot form bright AGNs.

We find that using $\dot{M}_{\rm c}$ from Eq. (6.26) as a threshold is too stringent and often omits signals that produce bright AGN discs. In the following, we use Eq. (6.27) as an initial guess for $\dot{M}_{\rm out}$ but then make adjustments if the accretion rate is not large enough to form a luminous AGN. Developing a full prescription is left to future work. As a precaution to avoid setting an $\dot{M}_{\rm out}$ that is too high, TQM05 suggests a maximum limit for $\dot{M}_{\rm out}$ equal to $\dot{M}_{\rm max} = 8\pi\rho h\sigma^2 r/\epsilon_{\rm T} c = L_{\rm M}/\epsilon_{\rm T} c^2$, where $L_{\rm M}$ is the limiting Eddington-like luminosity below which a galaxy will not have momentum driven winds that are high enough to significantly reduce the gas in the disc [418].

Other authors have used different values for $\dot{M}_{\rm out}$ and $r_{\rm out}$. For instance, Stone *et al.* (2017) [347] scale the AGN disc down to a Milky-Way type galaxy, using $M = 3 \times 10^6\,{\rm M}_\odot$, $\dot{M}_{\rm out} = 15\,\dot{M}_{\rm Edd}$, and $r_{\rm out} = 10\,{\rm pc}$, where the latter was motivated by the radius of the dusty tori from AGN disc observations [419–422].

Disc profiles

Figure 6.4 reproduces fig. 6 in Thompson *et al.* (2005) [2], assuming either the Semenov opacities (as was done by Thompson *et al.* (2005) [2]) or the combined opacities. The input parameters are $\sigma = 300$ km s^{-1}, $M \approx 10^9\,M_\odot$ [instead of Eq. (6.15) we use the M-σ relation by [324] as was done by [2]], $\dot{M}_{\rm out} = 320 M_\odot$ yr^{-1}, $r_{\rm out} = 200$ pc, $m = 0.2$, $\epsilon_{\rm T} = 10^{-3}$, and $\xi = 1$. Our results shown in Fig. 6.4 are generally in agreement with those by Thompson *et al.* (2005) [2].

Our implementation results in disc profiles that diverge when the disc is close to the central BH, around $r \sim 10^{-3}$ pc in this case; this follows from the $r \to r_{\rm min}$ limit in the definition of $\dot{M}'$. We report good agreement between the two opacity implementations, with a noteworthy difference being the presence of the iron opacity bump [423] at a radius of $r \sim 2 \times 10^{-4}$ pc, seen only for the combined opacities. For both sets of opacities, the disc profile presents a sharp feature at $r \sim 5 \times 10^{-1}$ pc where the temperature becomes high enough to leave the so-called opacity gap (the dip in κ for temperatures $10^3\,{\rm K} \lesssim T \lesssim 10^4\,{\rm K}$, see Thompson *et al.* (2005) [2], Sirko and Goodman (2003) [1]). Figure 6.4 shows that for this set of parameters the disc profile is not sensitive to the choice of opacity tables.

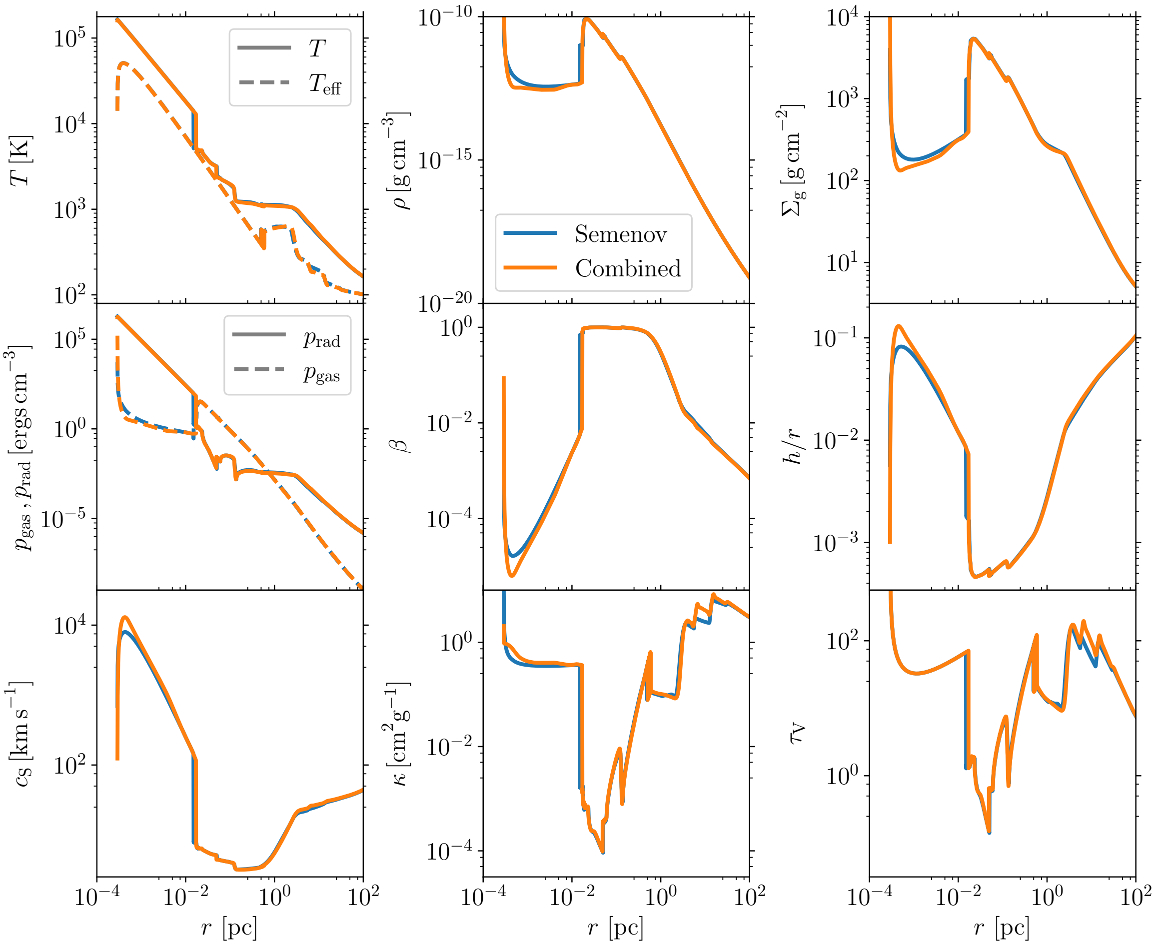

Figure 6.4: Radial profile in TQM05 disc model for the temperature T, the effective temperature $T_{\rm eff}$, the mass density ρ, the surface mass density Σ_g, the gas pressure $p_{\rm gas}$, the radiation pressure $p_{\rm rad}$, the gas pressure fraction β, the half-thickness of the disc h, the sound speed $c_{\rm s}$, the opacity κ and the optical depth $\tau_{\rm v}$. The input values have been chosen to reproduce Fig. 6 in Thompson *et al.* [2]: $\sigma = 300$ km/s, $\epsilon_{\rm T} = 10^{-3}$, $m = 0.2$, $\dot{M}_{\rm out} = 320 M_\odot$ yr^{-1}, and $r_{\rm out} = 200$ pc. Models shown in blue use the opacities by Semenov *et al.* [406], models shown in orange use the combined datasets from Semenov *et al.* [406] and Badnell *et al.* [407].

6.4 Parameter-space exploration

We now present a brief exploration of the phenomenology predicted by the Sirko and Goodman (2003) [1] and Thompson *et al.* (2005) [2] disc models.

6.4.1 Mass dependency

We first investigate the behaviour of both models as a function of the mass of the central BH. Figure 6.5 compares the SG03 and TQM05 discs profiles of four output parameters, namely the disc height from the midplane h, the mass density ρ, the optical depth τ_v, and the temperature T, for three central BH masses: $M = 10^6$, 10^8, and $10^{10}\,\mathrm{M}_\odot$. These five output quantities can be used to fully reconstruct an AGN disc for both models. Results are presented using the combined opacity datasets.

For the Sirko and Goodman (2003) [1] model, we set $\alpha = 0.01$, $l_\mathrm{E} = 0.5$, and only consider the α disc (i.e. $b = 0$). For each disc, we find the solution up to a radius of $10^7 R_\mathrm{s}$, with the $M = 10^6\,\mathrm{M}_\odot$ case having a maximum extension of ∼1 pc, and the $M = 10^{10}\,\mathrm{M}_\odot$ case extending to ∼1 kpc.

The temperature of the SG03 disc is higher at small separations for lower masses. In particular, one has $r \propto R_\mathrm{s} \propto M$ in Fig. 6.5, so that $\Omega_\mathrm{S} \propto M^{-1/2}$, and thus $T \propto M^{-3}$ in the inner region, cf. Eq. (6.12) for the optically-thick regime in the SG03 model. In the outer regions of the SG03 disc, all three models have the same temperature $T \approx 7.5 \times 10^3 K$, which is reached at the separation where the disc becomes optically thin ($\tau_\mathrm{v} < 1$). At large radii, if the disc is dominated by radiation pressure and the gas is optically thin ($T_\mathrm{eff}^4 \propto \tau_\mathrm{v} T^4$), then from Eq. (6.10) we find that $c_\mathrm{s}^2 \propto \tau_\mathrm{v}^2 T^4/\rho$. If κ is independent of r, then $\tau_\mathrm{v} \propto \rho h$, which in hydrostatic equilibrium gives a constant T independent of both r and M.

Figure 6.5 shows that the density ρ is lowest when the central BH mass is highest, with $\rho \propto M^2$ in the inner region of the SG03 disc. The model with $M = 10^{10}\,\mathrm{M}_\odot$ presents the thickest SG03 disc, reaching $h/r > 1$ at $r \gtrsim 10^6\,R_\mathrm{s}$; this is outside the regime of validity of our equations but only applies for large radii suggesting a diffuse envelope of gas around the AGN disc.

The Thompson *et al.* (2005) [2] model shown in Fig. 6.5 uses $m_{\rm T} = 0.2$, $\epsilon_{\rm T} = 10^{-3}$ and $\xi = 1$. In Fig. 6.5, we linearly scale the outer boundary of the disc $r_{\rm out}$ using the Schwarzschild radius so that $r_{\rm out} = 10^7\, R_{\rm s}$ for all three BH masses. We calculate $\dot{M}_{\rm out}$ using Eq. (6.27) for all three BH masses, but find that for the $M = 10^{10}\,{\rm M}_{\odot}$ case the scaled $\dot{M}_{\rm out}$ does not satisfy the $\dot{M}_{\rm out} > \dot{M}_{\rm c}$ condition and the disc profile looks significantly different from the AGN discs with smaller masses (the height ratio h/r monotonically decreases and the temperature in the disc does not reach 10^4 K). Instead, we opt for $\dot{M}_{\rm out} = 1.5 \times 10^6\,{\rm M}_{\odot}{\rm yr}^{-1}$ when $M = 10^{10}\,{\rm M}_{\odot}$ instead. Equation (6.27) gives $\dot{M}_{\rm out} = 0.37\,{\rm M}_{\odot}{\rm yr}^{-1}$ when $M = 10^6\,{\rm M}_{\odot}$ and $\dot{M}_{\rm out} = 322\,{\rm M}_{\odot}{\rm yr}^{-1}$ when $M = 10^8\,{\rm M}_{\odot}$. The AGN disc with $M = 10^8\,{\rm M}_{\odot}$ has an outer boundary of 100 pc, which is about half the size of the model shown in Fig. 6.4.

The $M = 10^6\,{\rm M}_{\odot}$ case in Fig. 6.5 shows an AGN disc with an outer boundary $r_{\rm out} \approx 1$ pc and a BH accretion rate $0.37\,{\rm M}_{\odot}{\rm yr}^{-1}$. Its accretion rate $\dot{M}$ is higher than both the star formation rate and $\dot{M}_{\rm c}$ for all values of r, leading to temperatures as large as $T \sim 10^6\,{\rm K}$ at $r = r_{\rm min}$ and a disc luminosity of $2 \times 10^{-5}\, L_{\rm Edd}$. The radiation pressure in such a high-temperature region leads to a thick disc, with $h/r > 1$ below $r \sim 5 \times 10^2\, R_{\rm s}$. At this aspect ratio, the thin-disc approximation no longer applies and caution must be applied when interpreting our results. In order to reduce h/r in the inner regime, one can decrease $\dot{M}_{\rm out}$ or decrease $m_{\rm T}$.

We find that the model with $M = 10^{10}\,{\rm M}_{\odot}$ also reaches $h/r > 1$ but at $r > 10^5\, R_{\rm s}$. This is due to a combination of low densities, a large optical depth, and a large accretion rate which all increase the radiation pressure at the outer boundary. The $M = 10^{10}\,{\rm M}_{\odot}$ AGN disc extends out to 10 kpc and has an accretion rate of $\sim 10\,{\rm M}_{\odot}{\rm yr}^{-1} = 0.04\,\dot{\rm M}_{\rm Edd}$ at $r = r_{\rm min}$, giving a disc luminosity of $0.07\, L_{\rm Edd}$. For the TQM05 model with $M =$

$10^{10}\,\mathrm{M}_\odot$, the optical depth τ_V shows oscillations at $r \sim 200\,R_\mathrm{s}$ (see Fig. 6.5) which are due to the model switching between the inner and outer regimes back and forth when close to the $Q_\mathrm{T} = 1$ boundary.

6.4.2 Input parameters

The SG03 model has five input parameters: the mass of the central BH M, the luminosity ratio l_E (or alternatively the accretion rate $\dot{M}$), the disc viscosity α, the BH radiative efficiency ϵ_S, and the pressure flag $b = 0, 1$. We consider a fiducial model with $M = 10^8\mathrm{M}_\odot$ $\epsilon_\mathrm{S} = 0.1$, $\alpha = 0.01$, $l_\mathrm{E} = 0.5$ and $b = 0$. Of these parameters, Fig. 6.6 explores the effect of varying α and l_E.

The density ρ in the outer regime is largely independent of α and l_E. The Shakura and Sunyaev (1973) [396] parameter α relates the viscosity to pressure and accretion, cf. Eq. (6.9). A larger α in the Sirko and Goodman (2003) [1] model implies a lower density and lower temperature in the inner regime, cf. Fig. 6.6. In the outer regions, the density is independent of the viscosity and thus independent of α.

We vary the Eddington ratio from $l_\mathrm{E} = 10^{-3}$ to $l_\mathrm{E} = 1$, capturing the range of observed AGNs [414–417]. The Eddington ratio parameterises the accretion rate, which plays a key role in the disc dynamics at all radial distances from the BH. Scaling relations in the optically thick regime far from the disc (see Sec. 6.3.1) indicate that the SG03 model maintains a constant temperature and density at $r \gtrsim 10^5\,R_\mathrm{s}$. Higher accretion rates leads to higher effective temperatures [Eq. (6.8)], higher disc temperatures overall [Eq. (6.12)], and higher total pressure in the disc [Eq. (6.9)], which also implies that h must be higher to maintain hydrostatic equilibrium.

The TQM05 model has six input parameters: the mass M of the SMBH from which we get the velocity dispersion σ using Eq. (6.15), the star formation efficiency ϵ_T, the

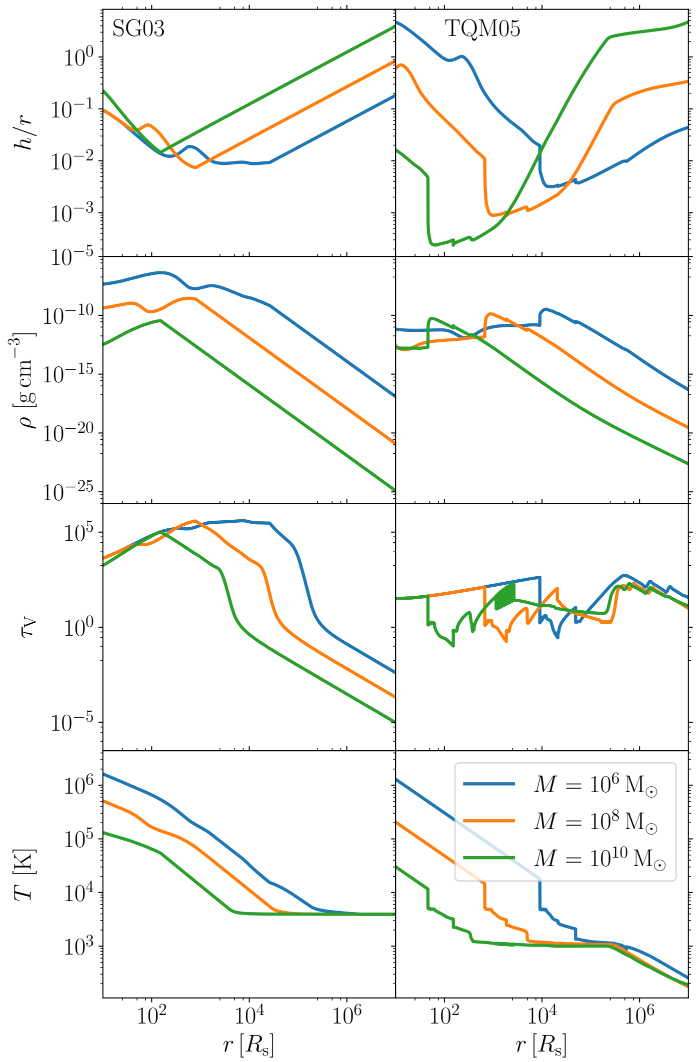

Figure 6.5: Aspect ratio h/r, mass density ρ, optical depth τ_v and midplane temperature T as functions of cylindrical radius r for both the SG03 (left) and TQM05 (right) AGN disc models. We vary the central BH mass $M = 10^6\,\mathrm{M}_\odot$ (blue), $10^8\,\mathrm{M}_\odot$ (orange), and $10^{10}\,\mathrm{M}_\odot$ (green). For the SG03 case, we set $\alpha = 0.01$, $l_\mathrm{E} = 0.5$, and $b = 0$. For the TQM05 case, we set $m = 0.2$, $\epsilon_T = 10^{-3}$ and $\xi = 1$. The outer radius r_out and outer accretion rate $\dot{M}_\mathrm{out}$ are both scaled with the central BH mass such that $r_\mathrm{out} = 95$ pc and $\dot{M}_\mathrm{out} = 320\,\mathrm{M}_\odot\mathrm{yr}^{-1}$ when $M = 10^8\,\mathrm{M}_\odot$, except for the $M = 10^{10}\,\mathrm{M}_\odot$ disc which has an outer accretion rate set to $\dot{M}_\mathrm{out} = 1.5 \times 10^6\,\mathrm{M}_\odot\mathrm{yr}^{-1}$.

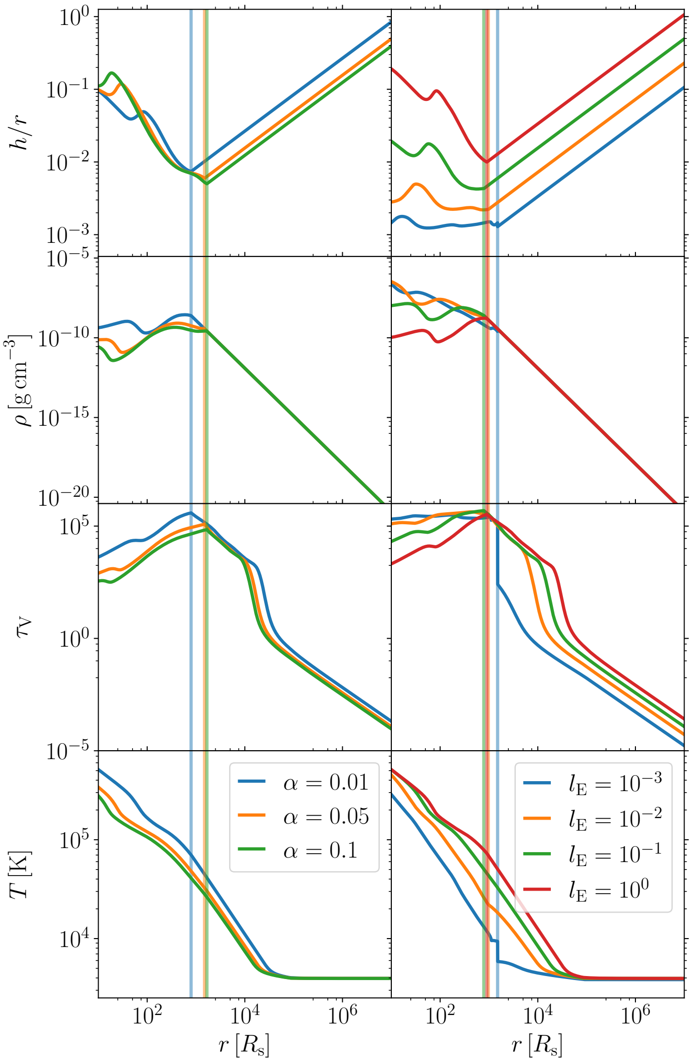

Figure 6.6: Model variations for the SG03 model, showing in particular the aspect ratio h, the midplane mass density ρ, the optical depth τ_v and the midplane temperature T. For both columns, we set $M = 10^8\,\mathrm{M}_\odot$ and $b = 0$. In the left column, we consider AGN discs with an Eddington fraction $l_\mathrm{E} = 0.5$ and vary the viscosity with $\alpha = 0.01$ (blue), $\alpha = 0.05$ (orange) and $\alpha = 0.1$. In the right column, we consider AGN discs where $\alpha = 0.01$, and vary the Eddington ratio $l_\mathrm{E} = 0.001$ (blue), $l_\mathrm{E} = 0.01$ (orange), $l_\mathrm{E} = 0.1$ (green) and $l_\mathrm{E} = 1$ (red). For each disc instance, the radius at which $Q_\mathrm{S} = 1$ is marked by a vertical line.

efficiency of angular momentum transport $m_{\rm T}$ in the disc, the supernovae radiative fraction ξ, the outer boundary of the disc $r_{\rm out}$, and the accretion rate at this outer boundary $\dot{M}_{\rm out}$. Figure 6.7 assumes a fiducial model with $M = 10^8\,{\rm M}_\odot$, $r_{\rm out} = 10^7 R_{\rm s}$, $\epsilon_{\rm T} = 10^{-3}$, $\xi = 1$, $m_{\rm T} = 0.2$ and $\dot{M}_{\rm out} \approx 312\,{\rm M}_\odot{\rm yr}^{-1}$ from Eq. (6.27). Starting from this set of parameters, we explore how the disc profile changes when varying either $\dot{M}_{\rm out}$ or $m_{\rm T}$.

We consider three values of the accretion rate: $\dot{M}_{\rm out} = 15$, 100, $300\,{\rm M}_\odot{\rm yr}^{-1}$. The lowest accretion rate considered, $\dot{M}_{\rm out} = 15\,{\rm M}_\odot{\rm yr}^{-1}$, falls below the critical accretion rate $\dot{M}_{\rm c} \approx 21\,{\rm M}_\odot{\rm yr}^{-1}$ from Eq. (6.26) at $r = r_{\rm out}$. According to this criterion, this model should not produce an AGN that is sufficiently bright. At $r = r_{\rm min}$, the accretion rate for the $\dot{M}_{\rm out} = 15\,{\rm M}_\odot{\rm yr}^{-1}$ case is $\sim 0.58\,{\rm M}_\odot{\rm yr}^{-1} = 0.22\,\dot{\rm M}_{\rm Edd}$, which is below the $1 - 10\,{\rm M}_\odot{\rm yr}^{-1}$ threshold indicated by Thompson *et al.* (2005) [2]. For this case, the disc luminosity is $1.8 \times 10^{-4}\,L_{\rm Edd}$, which still falls in the range of Eddington ratios one might expect for AGN discs. This further shows that $\dot{M}_{\rm c}$ is too strict a criterion for determining whether a TQM05 disc forms an AGN. The disc with such a low accretion rate has a different structure compared to the other two cases, with temperatures that are typically lower. As illustrated in Fig. 6.7, these low temperatures lead to low radiation pressure that fails to effectively counteract the vertical collapse of the disc and thus lower h/r values. On the other hand, for cases where the outer accretion rates clear the $\dot{M}_{\rm c}$ criterion, we find that the profiles become identical when in the inner, non-star forming regime, see the region left of the $Q_{\rm T} = 1$ line in Fig. (6.7). For these cases, the advection timescale and star formation timescale reach an equilibrium at the opacity gap ($\tau_{\rm adv} = \tau_*$ when $T \approx 10^3\,{\rm K}$). This leads to discs of the same temperature, density, aspect ratio and accretion rate ($\dot{M} = 2.23\,{\rm M}_\odot{\rm yr}^{-1}$ at $r = r_{\rm min}$ for both discs).

The global torque efficiency parameter $m_{\rm T}$ is strongly correlated to the behaviour of the disc for all radial distances. Much like α for the SG03 model, here m_{T} parametrizes the relationship between the angular momentum transport and the accretion rate, cf. Eq. (6.19). In the outermost regions of the disc, where the accretion rate $\dot{M} \approx \dot{M}_{\mathrm{out}}$ is roughly constant and $h/r \sim 1$, the total pressure is inversely proportional to m_{T}, see Eq. (6.19) and the definition of c_{s}. This gives a thinner TQM05 disc, with lower values of h/r for higher values of m_{T} at the outer boundary. The density is constant in the marginally stable outer region because of Eq. (6.17), but the low total pressure causes some temperature deviations at $r \approx 10^7\,R_{\mathrm{s}}$ for each disc we consider. These variations contribute to different initial conditions in τ_{v} for each value of m_{T}. The TQM05 disc has similar behaviour for all three m_{T} values once the solutions enter the opacity gap at $r \approx 10^5 R_{\mathrm{s}}$, though differences in the optical depth impact the disc profiles at small values of r. In the innermost regions of the disc, we find that high m_{T} values lead to thick, low density discs due to low radiation pressure (which is proportional to τ_{v} by definition).

6.5 Disc migration

In Sec. 5.2.1 of Ch. 5, I introduce migration torques in gas discs. Several types of migration exist, but in this work, we only consider the case of Type I migration (non gap-forming). Migration traps are an ideal context to showcase our implementation of the Sirko and Goodman (2003) [1] and Thompson *et al.* (2005) [2] disc models. Table 6.2 summarises all parameters used for this section.

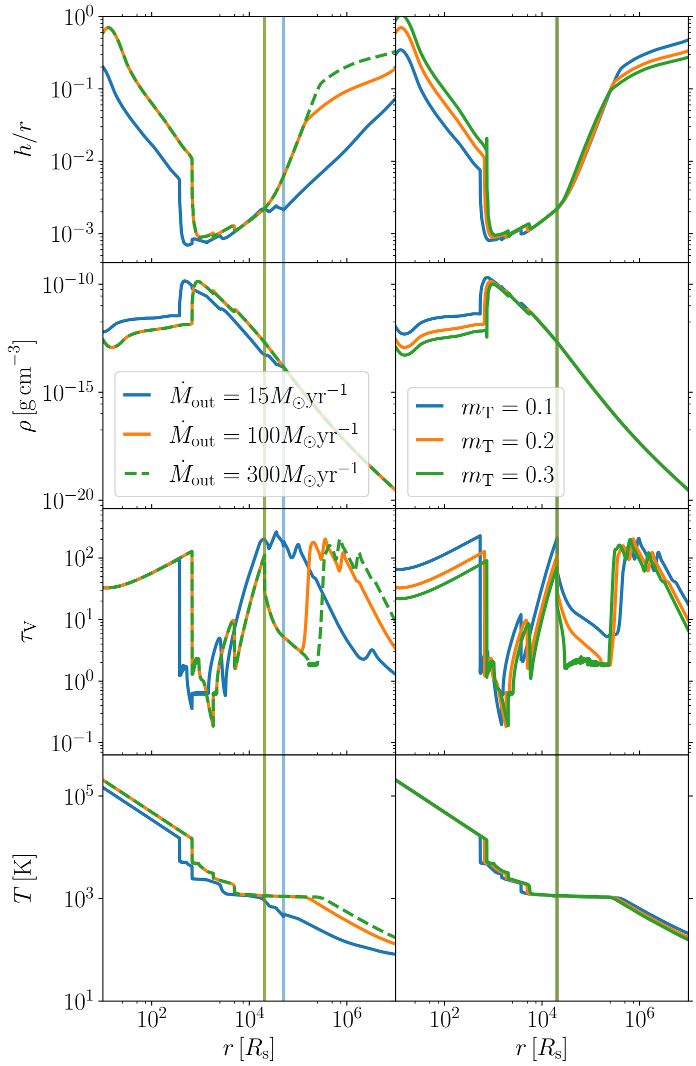

Figure 6.7: Model variations for the TQM05 model, showing in particular the aspect ratio h, the midplane mass density ρ, the optical depth τ_v and the midplane temperature. For both columns, we set $M = 10^8\,\mathrm{M}_\odot$, $\epsilon_\mathrm{T} = 10^{-3}$, $\xi = 1$ and $r_\mathrm{out} = 200$ pc. In the left column, we consider AGN discs with a global torque efficiency of $m_\mathrm{T} = 0.2$ and vary the accretion rate $\dot{M}_\mathrm{out} = 15\,\mathrm{M}_\odot\mathrm{yr}^{-1}$ (blue), $\dot{M}_\mathrm{out} = 100\,\mathrm{M}_\odot\mathrm{yr}^{-1}$ (orange) and $\dot{M}_\mathrm{out} = 300\,\mathrm{M}_\odot\mathrm{yr}^{-1}$ (green, dashed). The $\dot{M}_\mathrm{out} = 300\,\mathrm{M}_\odot\mathrm{yr}^{-1}$ case is dashed to show that parameter profiles are identical to the those of the $\dot{M}_\mathrm{out} = 100\,\mathrm{M}_\odot\mathrm{yr}^{-1}$ case close to the central BH. In the right column, we consider AGN discs with an outer accretion rate $\dot{M}_\mathrm{out} \simeq 312\,\mathrm{M}_\odot\mathrm{yr}^{-1}$ and vary the global torque efficiency $m_\mathrm{T} = 0.1$ (blue), $m_\mathrm{T} = 0.2$ (orange), and $m = 0.3$ (green). For each disc instance, the radius at which $Q_\mathrm{T} = 1$ is marked by a vertical line.

Table 6.2: Summary of the parameter entering our treatment of disc migration explored in Sec. 6.5.

Symbol	Definition
$m_{\rm BH}$	Mass of the migrating object
q	Mass ratio between migrator and central BH
Γ_0	Normalization migration torque
$\Gamma_{\rm I}$	Type I migration torque
γ	Adiabatic index
$C_{\rm L}$	Lindblad torque
χ	Thermal diffusivity of the disc
$\Gamma_{\rm therm}$	Thermal torque
$x_{\rm c}$	Corotation radius of the migrator
λ	Size of the thermal lobes
L	Migrator luminosity from thermal heating
$L_{\rm c}$	Critical migrator luminosity

6.5.1 Torque implementation

In particular, we apply our AGN disc models to the methods by

Grishin *et al.* (2024) [366], adopting their migration torque and thermal torque expressions. Grishin *et al.* (2024) [366] use a simpler AGN disc model where profiles are power laws in M, r and accretion rate $\dot{M}$. Their discs are relatively similar to the SG03 models with $M = 10^6\,{\rm M}_\odot$ and $\alpha = 0.01$. When using migration torques by Paardekooper *et al.* (2010) [379] which assume the disc is locally isothermal, Grishin *et al.* (2024) [366] report the existence of migration traps. However, migration traps disappear when considering the updated migration torque formulas by Jiménez and Masset (2017) [424]. Grishin *et al.* (2024) [366] then add a new type of migratory torque, namely the thermal torque by Masset (2017) [425], and find that migration traps are able to form in their AGN disc model once more. We apply the same methodology and formulas to our more complex AGN models.

Migration induces two over-dense spiral arms in the disc. Each arm will produce a torque acting on the migrating object with a magnitude [426]

$$\Gamma_0 = q^2 \Sigma_{\rm g} r^4 \Omega^2 \left(\frac{h}{r}\right)^{-3} , \tag{6.28}$$

where $q \equiv m_{\rm BH}/M$ is the BH mass ratio and Ω is equal to either $\Omega_{\rm S}$ or $\Omega_{\rm T}$ depending on the AGN disc model. The net torque $\Gamma_{\rm I}$ acting on the migrator in a locally isothermal limit is given by [379]:

$$\Gamma_{\rm I} = \left(-0.85 + 0.9\frac{{\rm d}\ln\Sigma_{\rm g}}{{\rm d}\ln r} + \frac{{\rm d}\ln T}{{\rm d}\ln r}\right)\frac{h}{r}\,\Gamma_0 \,. \tag{6.29}$$

Jiménez and Masset (2017) [424] update the migration torque formula to

$$\Gamma_{\rm I} = \left[C_{\rm L} + \left(0.46 + 0.96\frac{{\rm d}\ln\Sigma_{\rm g}}{{\rm d}\ln r} - 1.8\frac{{\rm d}\ln T}{{\rm d}\ln r}\right)\gamma^{-1}\right]\frac{h}{r}\,\Gamma_0 \,, \tag{6.30}$$

where $\gamma = 5/3$ is the adiabatic index. The parameter

$$C_{\rm L} = \left(-2.34 - 0.1\frac{{\rm d}\ln\Sigma_{\rm g}}{{\rm d}\ln r} + 1.5\frac{{\rm d}\ln T}{{\rm d}\ln r}\right) f_\gamma\left(\frac{\chi}{h^2\Omega}\right) , \tag{6.31}$$

is the Lindblad torque, where

$$f_\gamma(x) = \frac{(x/2)^{1/2} + 1/\gamma}{(x/2)^{1/2} + 1} \tag{6.32}$$

is a function that adds a dependence on the thermal diffusivity for the Lindblad torque and can be approximated to $1/\gamma$ in the case where the diffusivity is small [427]. The thermal diffusivity of the disc is defined as

$$\chi = \frac{16\gamma(\gamma - 1)\sigma_{\rm SB} T^4}{3\kappa\rho^2 h^2 \Omega^2} \,. \tag{6.33}$$

The thermal torque $\Gamma_{\rm therm}$ originates from the temperature build-up around the migrating object due to lack of heat release during its orbital evolution. If heat is trapped around the migrator, two cold and dense lobes are formed in the disc, which leads to inward migration [428]. If the migrator is instead able to release heat back into the disc around it, two hot and under-dense lobes form, leading to outward migration [429]. The total heating torque is [425]:

$$\Gamma_{\rm therm} = 1.61\frac{\gamma-1}{\gamma}\frac{x_{\rm c}}{\lambda}\left(\frac{L}{L_{\rm c}}-1\right)\Gamma_0\,, \tag{6.34}$$

where $x_{\rm c}$ is the corotation radius of the migrating object, λ is the typical size of the lobes, and L is the luminosity generated by the migrator through thermal heating, and

$$L_{\rm c} = \frac{4\pi GqM\rho}{\gamma}\chi \tag{6.35}$$

is the critical luminosity. If $L = L_{\rm c}$, the hot and cold torques acting on the migrator balance out and $\Gamma_{\rm therm} = 0$. We approximate the luminosity of the migrator, L, to be its Eddington luminosity [see Eq. (6.3), replacing the mass M with the mass of the migrator $m_{\rm BH}$]. The size of the lobes λ is given by [366]:

$$\lambda = \sqrt{\frac{2\chi}{3\gamma\Omega}}\,, \tag{6.36}$$

and the corotation radius is [366]:

$$x_{\rm c} = -\frac{h^2}{3\gamma r}\frac{{\rm d}\ln p_{\rm tot}}{{\rm d}\ln r}\,. \tag{6.37}$$

We approximate ${\rm d}\ln p_{\rm tot}/{\rm d}\ln r$ by combining the equation for vertical hydrodynamical equilibrium $p_{\rm tot} \approx \rho h^2\Omega^2$ with the definition of the sound speed $c_{\rm s}^2 = h^2\Omega^2$, resulting in $\mathrm{d}p_{\mathrm{tot}}/\mathrm{d}r \approx \rho c_{\mathrm{s}}^2/r$.

The thermal torque given by Eq. (6.34) is expected to diminish in optically thin discs. Following Grishin *et al.* (2024) [366], we multiply Eq. (6.34) by a factor of $1 - \exp\{-\lambda\tau_{\mathrm{v}}/h\}$. Additionally, when the mass of the migrator exceeds the thermal mass m_{th}, the thermal torque will be reduced Guilera *et al.* [430]. The thermal mass is defined by:

$$\frac{m_{\mathrm{th}}}{m_{\mathrm{BH}}} = \frac{\chi}{c_{\mathrm{s}} R_{\mathrm{B}}}\,, \tag{6.38}$$

where R_{B} is half the Bondi radius

$$R_{\mathrm{B}} = \frac{G m_{\mathrm{BH}}}{c_{\mathrm{s}}^2}\,. \tag{6.39}$$

In the regions where $h < R_{\mathrm{B}}$ we use the disc height h in place of half the Bondi radius R_{B}. To correct for the critical thermal mass, we split Eq. (6.34) into its heating component (the positive L/L_{c} term) and its cooling component (the negative term), which we label as $\Gamma_{\mathrm{therm,\,hot}}$ and $\Gamma_{\mathrm{therm,\,cold}}$ respectively. The total thermal torque is described by Eq. (6.34) unless $\mu_{\mathrm{th}} \equiv m_{\mathrm{th}}/m_{\mathrm{BH}} < 1$. In regions of the disc where $\mu_{\mathrm{th}} < 1$, the thermal torque is instead given by:

$$\Gamma_{\mathrm{therm}} = \Gamma_{\mathrm{therm,\,hot}} \frac{4\mu_{\mathrm{th}}}{1 + 4\mu_{\mathrm{th}}} + \Gamma_{\mathrm{therm,\,cold}} \frac{2\mu_{\mathrm{th}}}{1 + 2\mu_{\mathrm{th}}} \tag{6.40}$$

which is an approximation of numerical fits detailed in Velasco Romero and Masset (2020) [431] and used in Guilera *et al.* (2021) [430] and Grishin *et al.* (2024) [366].

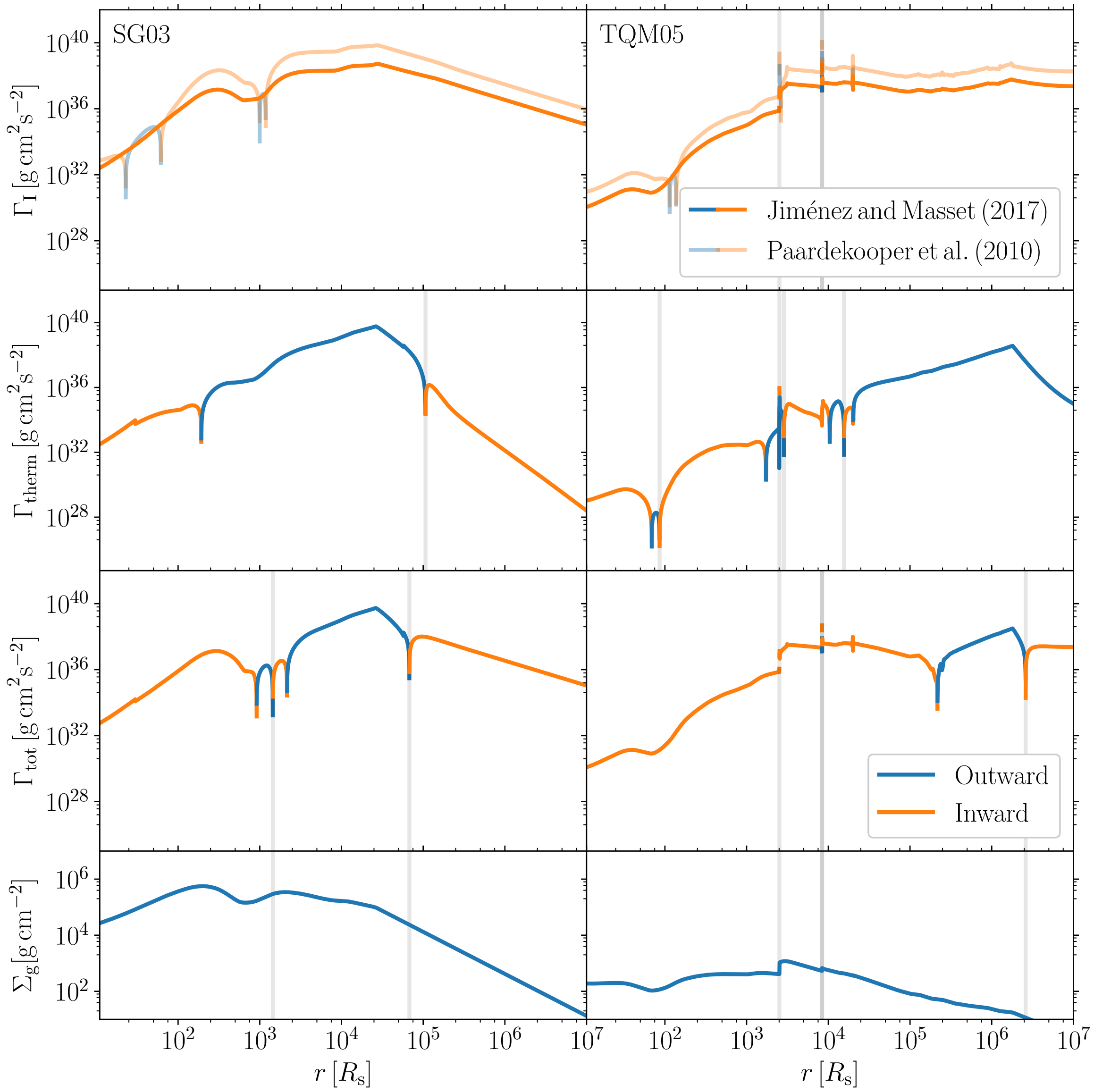

Figure 6.8: The absolute values of the migration torques for a $m_{\rm BH} = 10\,{\rm M}_\odot$ BH orbiting a $M = 10^6\,{\rm M}_\odot$ central BH in AGN discs. The left panels show torque profiles for a SG03 disc with $\epsilon_{\rm S} = 0.1$, $\alpha = 0.01$, $l_{\rm E} = 0.5$ and $b = 0$. The right panels show torque profiles for a TQM05 disc with $\epsilon_{\rm T} = 10^{-3}$, $\xi = 1$, $m = 0.2$, $r_{\rm out} = 10^7\,R_{\rm s}$ and $\dot{M}_{\rm out} = 1.5\times10^{-2}\,{\rm M}_\odot{\rm yr}^{-1}$. Migration torques, thermal torques, and their combination are shown in first three rows from the top, respectively. The bottom panel shows the midplane surface density of the disc for each case. For the Type I migration torques considered in the top row, we show both results using prescriptions by both Paardekooper *et al.* (2010) [379] (light curves) and Jiménez and Masset (2017) [424] (heavy curves). Colours indicate the sign of the torque, with blue referring to inward migration (i.e. positive torques) and orange referring to outward migration (i.e. negative torques). Vertical grey lines indicate the migration traps for all torque prescriptions except for Paardekooper *et al.* (2010) [379] in the top panel.

6.5.2 Migration traps

Figure 6.8 shows the migration-torque profiles for a $M = 10^6\,\mathrm{M}_\odot$ SMBH in both the Sirko and Goodman (2003) [1] and Thompson *et al.* (2005) [2] models. We use $\epsilon_\mathrm{S} = 0.1$, $\alpha = 0.01$, $l_\mathrm{E} = 0.5$ and $b = 0$ for the SG03 AGN disc and $r_\mathrm{out} = 10^7\,R_\mathrm{s}$, $\epsilon_\mathrm{T} = 10^{-3}$, $\xi = 1$, $m_\mathrm{T} = 0.2$, and $\dot{M}_\mathrm{out} = 1.5 \times 10^{-2}\,\mathrm{M}_\odot\mathrm{yr}^{-1}$ for the TQM05 model. The outer accretion rate $\dot{M}_\mathrm{out}$ was set to be smaller than the value given by Eq. (6.27) in order to enforce $h/r < 1$ throughtout the disc, unlike the small mass case in Fig. 6.5. Identifying a migration trap corresponds to regions of the disc where the net migration torque is zero and goes from negative (i.e. inward migration) to positive (i.e. outward migration) as r increases.

The top panel shows the migration torque using both Eq. (6.29) by Paardekooper *et al.* (2010) [379] and Eq. (6.30) by Jiménez and Masset (2017) [424]. When using the former, we find migration traps at $r \approx 22\,R_\mathrm{s}$ and $r \approx 10^3\,R_\mathrm{s}$ for the SG03 model, which is in line with the results reported by both Bellovary *et al.* (2016) [345] and Grishin *et al.* [366]. When using the updated migration torque values by Jiménez and Masset (2017) [424] for the SG03 model, we find that the migration torque is always negative and thus the migrator moves across the disc without being trapped. This result is in agreement with those by Grishin *et al.* (2024) [366]. Once the thermal torque from Eq. (6.34) is added to the updated migration torque of Eq. (6.30), the bottom panel in Fig. 6.8 shows that we again obtain migration traps. In the SG03 AGN disc, we find two migration traps for a $M = 10^6\,\mathrm{M}_\odot$ central BH and a $10\,\mathrm{M}_\odot$ migrator occurring at $r \approx 1.4 \times 10^3\,R_\mathrm{s} = 1.4 \times 10^{-4}$ pc and $r \approx 6.8 \times 10^4\,R_\mathrm{s} = 6.5 \times 10^{-3}$ pc.

When considering the Thompson *et al.* (2005) [2] model, we obtain a larger number of migration traps, irrespective of the torque prescriptions adopted and the inclusion of the thermal torque contribution to the net torque. For the migration torque by Jiménez and Masset (2017) [424] (the top panel in Fig. 6.8), we find migration traps form in the TQM05 disc when the gradient $\mathrm{d}\ln\Sigma_{\mathrm{g}}/\mathrm{d}\ln r$ discretely changes values, as can be seen in the lower panels of Fig. 6.8 at $r \approx 2.5 \times 10^3\,R_{\mathrm{s}}$ and $r \approx 8.3 \times 10^3\,R_{\mathrm{s}}$. When both migration and thermal torques are considered, we find traps at $r \approx 2.5 \times 10^3\,R_{\mathrm{s}}$, $r \approx 8.4 \times 10^3\,R_{\mathrm{s}}$ and $r \approx 2.6 \times 10^6\,R_{\mathrm{s}}$ for the Thompson *et al.* (2005) [2] model.

6.6 Public implementation

Our implementation of both the SG03 and TQM05 models is released publicly in the `pAGN` module for the Python programming language.

`pAGN` is distributed under git version control at

github.com/DariaGangardt/pAGN (code repository)

The documentation is provided at

dariagangardt.github.io/pAGN (documentation)

together with a set of minimal examples.

Our `pAGN` module is available on the Python Package index. The code can be installed with

```
pip install pagn
```

Packages `numpy`, `scipy`, and `matplotlib` are specified as dependencies. The package is imported with

```
import pagn
```

and contains two main classes for the SG03 and TQM05 implementation, respectively:

```
pagn.SirkoAGN
pagn.ThompsonAGN
```

In addition, the code distributions include opacity tables by Semenov *et al.* (2003) [406] and Badnell *et al.* (2005) [407], as well as an interpolation routine. External opacity tables can also be provided by the user. The overall solution strategy follows what is presented in this paper as illustrated in the flowcharts of Figs. 6.1 and 6.2.

6.7 Conclusions

This work presents a critical re-analysis of the AGN disc models by Sirko and Goodman (2003) [1] and Thompson *et al.* (2005) [2]. Our findings are implemented in the public `pAGN` module for the Python programming language [403]. We presented the equations from the original papers and emphasised their solution strategy. Compared to the original model, our results consider updated opacity tables, relate some of the input parameter (most notably the scaling of the outer accretion rate with the central BH mass for TQM05 case), validate AGN discs through limits on the accretion rate at the disc boundaries, and investigate the limits of the thin-disc approximation. While the parameter exploration presented in this work provides valuable insights, there is room for further enhancement to fully explore the predictions of these models across the entire parameter space. An example of such research, Ballantyne [432] presented an observation-motivated study of how the TQM05 input parameters affects the properties of AGN discs in Seyfert-like galaxies with a particular focus on the "starburst" disc regions with high star formation.

As a further example, in this paper we have applied our `pAGN` code to the disc-migration problem, reproducing the analysis by Grishin *et al.* (2024) [366] with the more complex disc profiles by Sirko and Goodman (2003) [1] and Thompson *et al.* (2005) [2]. While we largely confirm previous findings for the SG03 case, our TQM05 disc shows a large number of migration traps, with potential implications for the formation of hierarchical merging stellar-mass BH binaries detectable with current gravitational-wave detectors [385]. This is an interesting avenue for future work.

The AGN disc models by Sirko and Goodman (2003) [1] and Thompson *et al.* (2005) [2] are widely used in the literature. We hope our full, public implementation of these approaches, together with the details of the underlying evolutionary equations, might facilitate further advances in this area while clarifying their underlying limitations. Both the SG03 and TQM05 models can be applied to various problems and compared to newer AGN-disc modeling approaches. The goal of `pAGN` is precisely that to aid further research in the growing field of AGN and gravitational-wave science.

Chapter B

Appendix for Part II

Additional material for Ch. 6.

B.1 Optically Thick Approximation in TQM05

For the TQM05 model, the case where the disc optically thick to its own infrared radiation can be approximated analytically. We assume that the gas is a constant fraction $f_\mathrm{g} \equiv \Sigma_\mathrm{g}/\Sigma_\mathrm{tot}$ of the total dynamical mass

$$\Sigma_\mathrm{tot} = \frac{\sigma^2}{\pi G r}\,. \tag{B.1}$$

These assumption function best at large scales (i.e., $r \gg r_\mathrm{out}$) where the angular frequency is dominated by the velocity dispersion, so that $\Omega_\mathrm{T} \approx \sqrt{2}\sigma/r$. The mass density from Eq. (6.23) reads

$$\rho \approx \frac{\sqrt{2}\sigma^2}{\pi G Q_\mathrm{T} r^2}\,. \tag{B.2}$$

If $f_{\rm g}$ is constant, then the mid-scale height is given by

$$\frac{h}{r} = \frac{f_{\rm g} Q_{\rm T}}{2^{3/2}}\,, \tag{B.3}$$

and the sound speed is

$$\frac{c_{\rm s}}{\sigma} = \frac{f_{\rm g} Q_{\rm T}}{2}\,. \tag{B.4}$$

At large values of r, the disc is mostly radiation-pressure dominated, so that $p_{\rm rad} = 4\sigma_{\rm SB} T^4/3c = \sigma_{\rm SB}\tau_{\rm v} T_{\rm eff}^4/c$. In the optically thick limit, the main contribution to $T_{\rm eff}$ is that of star formation

$$\sigma_{\rm SB} T_{\rm eff}^4 = \frac{1}{2}\epsilon_{\rm T}\dot{\Sigma}_* c^2\,. \tag{B.5}$$

Combining these equations, one can then find the temperature

$$T = \left(\frac{3cQ_{\rm T}}{2^{7/2}\pi G\sigma_{\rm SB}}\right)^{1/4}\left(\frac{f_{\rm g}\sigma^2}{r}\right)^{1/2}\,, \tag{B.6}$$

and the star formation rate

$$\dot{\Sigma}_* = \frac{\sqrt{2} f_{\rm g} Q_{\rm T}}{\epsilon_{\rm T}\kappa c}\frac{\sigma^2}{r}\,. \tag{B.7}$$

Chapter 7

Conclusions

In this thesis, I have covered two broad topics in BBH dynamics - spin precession of BBHs in a vacuum, and the AGN disc models within which BBHs may dynamically form. The two fields are connected by GW astronomy, either by predicting BBH merger signals or by using GW signals to inform their science. Even before the first detection of gravitational waves, black hole physics was a field of great astronomical and theoretical interest (see Ch. 1). Understanding how BHs form, how they evolve and how they merge is essential for GW science. Only by bridging the gaps between astronomy, astrophysics and general relativity, can we paint a full picture of our Universe.

The first chapter of this thesis covers the history of black hole astronomy, from first derivations, to their indirect observations using EM instruments, to the direct detections of black holes merging in GW interferometers. From the general introduction presented in Ch. 1, I briefly explain how the LVK collaboration recovers GW signals, and how these GW signals are used to inform astrophysical BH distributions. Finally, I summarise key LVK results at the end of Ch. 1.

In the second chapter, I summarise the necessary theory to understand the research of Chs. 3-4. The spin precession formalism of this chapter is from Kesden *et al.* (2015) [201] and Gerosa *et al.* (2015) [202], although more recently this was updated in Gerosa *et al.* (2023) [203]. The theory presented in this chapter uses the timescale hierarchy of spin precession in the post-Newtonian order in order to obtain analytical equations for precessing BBHs. The formalism from this chapter, and its updated version, have been used for parameter estimation [433], for phenomenological waveform models [86, 261], and for the study of BBH dynamics (see Refs. [231, 434–436] for some recent examples). It is also this formalism that we use for Chs. 3—4.

Chapter 3 is the article Gangardt and Steinle *et al.* (2021) [199]. Here, we used the spin precession equations stated in Ch. 2 to define new precession parameters, motivated by the motion of the orbital angular momentum around the total angular momentum. These parameters also naturally separate spin precession in BBHs into precession and nutation. We showed that a non-zero nutation amplitude implies that both BHs in the binary are spinning (generic precession). We explored under what conditions nutation can be maximised, and what that maximum value might be. The paper clarifies precession dynamics in BBHs, through a precession taxonomy (Fig. 3.1) and five parameters that best capture it.

Chapter 4 uses the five precession and nutation parameters from Ch. 3 and looks for them in the GW events reported by the LVK collaboration for the first three runs. It also searches for the spin morphologies defined in Ch. 2 in the same GW events. Our results agree with current catalog results [80]; specifically, we identify the same events that have significant χ_P measurements also have significant precession amplitude $\langle\theta_\mathrm{L}\rangle$ measurements. We use sequential prior conditioning to identify how much of the precession/nutation information is constrained from our measurements of mass parameters and χ_eff. We then conclude with an idealised injection of a highly-nutating event, and demonstrate that with future detectors we would confidently constrain nutation (i.e., two spin effects) in GW data.

The work summarised in Chapters 3 and 4 has since its publication received some follow up. Steinle and Kesden (2022) [253] explored the five spin precession parameters for the isolated BBH formation channel, and in Johnson-McDaniel *et al.* (2023) [436] the GW catalogues are also studied using the spin morphologies defined in Ch. 2. An unexplored avenue is the independent detection of the five spin precession parameters. As hinted at in the conclusions of Ch. 3 and Gangardt *et al.* (2021) [234], the five precessional parameters may leave distinct imprints on the gravitational waveform - constructing waveforms that, for example, include and exclude nutation ($\Delta\theta_{\rm L} = 0$), then running source parameter inference on a GW waveform using both waveform families would extend the results presented in Gangardt *et al.* (2022) [255] by robustly identifying whether we can detect nutation or not. As a companion to the work in Steinle and Kesden (2022) [253], a study exploring different dynamical formation channels and their predicted distributions of the five spin precession parameters would be complimentary and interesting work.

The second part of the thesis, Ch. 5-6, takes a step away from the dynamics of BBHs and instead looks at the dynamical environment of active galactic nuclei. Chapter 5 serves as an introduction to the field of AGNs, both from a broad observational perspective and from a gravitational wave science point of view.

The thesis' final chapter, Ch. 6, presents the theory behind the software package `pAGN` [403]. We implement the equations behind two widely used one-dimensional disc models, the Sirko and Goodman (2003) [1] and Thompson *et al.* (2005) [2] disc models. These two models have multiple input parameters, which we study the effect on the AGN disc profiles. We found that, as expected, the mass of the SMBH at the centre of the AGN plays a dominant role in the disc dynamics. We also apply `pAGN` to the migration torque problem, studying how a stellar mass black hole would move through the disc of a $10^6\,\mathrm{M}_\odot$ SMBH. AGN disc theory is essential for predicting compact object populations in AGN discs, and already the presence of a reliable Python code that implements and clarifies the Sirko and Goodman (2003) [1] and Thompson *et al.* (2005) [2] models has been used in a few articles [344, 437].

The package `pAGN` is a piece of software that must be maintained in order to guarantee its usefulness. Therefore, some next steps would be to update the customisability of the code, and test it for different opacities. Applying updated opacity tables such as the ones used in Baskin and Laor (2018) [410] and exploring their effects on the SG03 and TQM05 AGN disc would be a simple next step for this work. The project was initially motivated by a study of black hole orbits in AGN discs; using the package to explore what BH populations may look like within AGN discs would be interesting. An ambitious project would be to explore the spin precession dynamics of BBHs located within either AGN disc, even more so by using the parameters of the first part of this thesis.

Overall, this thesis, which can be considered in two parts, aims to demonstrate some interesting areas of black hole dynamics. The first part explored using new parameters to describe BBH spin precession and unravel it in current LVK data, the second part looked at setting up a tool for the AGN formation channel and studies of AGN discs. The field of GW science is rapidly advancing, and soon we'll enter the "big data" era of the field as we start detecting thousands of BBH mergers. This will mean at least better population constraints on spin precession, if not more precise individual event measurements. Alongside, the acceleration of GW science will also tell us more about AGN discs, informing us about their fraction in the universe and some of their composition. Step by step, simulation by simulation, observation by observation, we advance our knowledge of the observable Universe and the gravity that holds it together.

Bibliography

[1] E. Sirko and J. Goodman, MNRAS **341**, 501 (2003), arXiv:astro-ph/0209469 [astro-ph].

[2] T. A. Thompson, E. Quataert, and N. Murray, ApJ **630**, 167 (2005), arXiv:astro-ph/0503027 [astro-ph].

[3] J. Michell, Philosophical Transactions of the Royal Society of London Series I **74**, 35 (1784).

[4] S. Laplace, Paris: Courcier (1808).

[5] C. Montgomery, W. Orchiston, and I. Whittingham, Journal of Astronomical History and Heritage **12**, 90 (2009).

[6] S. Chandrasekhar, MNRAS **91**, 456 (1931).

[7] J. R. Oppenheimer and G. M. Volkoff, Phys. Rev. **55**, 374 (1939).

[8] J. R. Oppenheimer and H. Snyder, Phys. Rev. **56**, 455 (1939).

[9] A. Einstein, Sitzungsberichte der Königlich Preußischen Akademie der Wissenschaften (Berlin , 778 (1915).

[10] A. Einstein, Sitzungsberichte der Königlich Preußischen Akademie der Wissenschaften (Berlin , 831 (1915).

[11] A. Einstein, Sitzungsberichte der Königlich Preußischen Akademie der Wissenschaften (Berlin , 844 (1915).

[12] K. Schwarzschild, in *Sitzungsberichte der Königlich Preussischen Akademie der Wissenschaften zu Berlin* (1916) pp. 424–434.

[13] A. Einstein, Annals of Mathematics **40**, 922 (1939).

[14] R. Penrose, Phys. Rev. Lett. **14**, 57 (1965).

[15] W. Israel, Phys. Rev. **164**, 1776 (1967).

[16] B. Carter, Phys. Rev. Lett. **26**, 331 (1971).

[17] S. W. Hawking, Communications in Mathematical Physics **25**, 152 (1972).

[18] D. C. Robinson, Phys. Rev. Lett. **34**, 905 (1975).

[19] P. O. Mazur, Journal of Physics A Mathematical General **15**, 3173 (1982).

[20] R. P. Kerr, Phys. Rev. Lett. **11**, 237 (1963).

[21] R. H. Boyer and R. W. Lindquist, Journal of Mathematical Physics **8**, 265 (1967).

[22] R. Penrose, Nuovo Cimento Rivista Serie **1**, 252 (1969).

[23] M. Schmidt, Nature **197**, 1040 (1963).

[24] F. Wang, J. Yang, X. Fan, J. F. Hennawi, A. J. Barth, E. Banados, F. Bian, K. Boutsia, T. Connor, F. B. Davies, et al., ApJ **907**, L1 (2021), arXiv:2101.03179 [astro-ph.GA].

[25] E. E. Salpeter, ApJ **140**, 796 (1964).

[26] Y. B. Zel'dovich, Sov. Phys. Dokl. **9**, 195 (1964).

[27] B. Balick and R. L. Brown, ApJ **194**, 265 (1974).

[28] A. Hewish, S. J. Bell, J. D. H. Pilkington, P. F. Scott, and R. A. Collins, Nature **217**, 709 (1968).

[29] T. Gold, Nature **218**, 731 (1968).

[30] B. L. Webster and P. Murdin, Nature **235**, 37 (1972).

[31] C. T. Bolton, Nature **235**, 271 (1972).

[32] A. M. Ghez, B. L. Klein, M. Morris, and E. E. Becklin, ApJ **509**, 678 (1998), arXiv:astro-ph/9807210 [astro-ph].

[33] R. Genzel, C. Pichon, A. Eckart, O. E. Gerhard, and T. Ott, MNRAS **317**, 348 (2000), arXiv:astro-ph/0001428 [astro-ph].

[34] Event Horizon Telescope Collaboration, K. Akiyama, A. Alberdi, W. Alef, K. Asada, R. Azulay, A.-K. Baczko, D. Ball, M. Baloković, J. Barrett, et al., ApJ **875**, L1 (2019), arXiv:1906.11238 [astro-ph.GA].

[35] Event Horizon Telescope Collaboration, K. Akiyama, A. Alberdi, W. Alef, J. C. Algaba, R. Anantua, K. Asada, R. Azulay, U. Bach, A.-K. Baczko, et al., ApJ **930**, L12 (2022).

[36] H. A. Bethe and G. E. Brown, ApJ **506**, 780 (1998), arXiv:astro-ph/9802084 [astro-ph].

[37] M. Dominik, K. Belczynski, C. Fryer, D. E. Holz, E. Berti, T. Bulik, I. Mandel, and R. O'Shaughnessy, ApJ **759**, 52 (2012), arXiv:1202.4901 [astro-ph.HE].

[38] K. Belczynski, S. Repetto, D. E. Holz, R. O'Shaughnessy, T. Bulik, E. Berti, C. Fryer, and M. Dominik, ApJ **819**, 108 (2016), arXiv:1510.04615 [astro-ph.HE].

[39] J. J. Eldridge and E. R. Stanway, MNRAS **462**, 3302 (2016), arXiv:1602.03790 [astro-ph.HE].

[40] S. Stevenson, A. Vigna-Gómez, I. Mandel, J. W. Barrett, C. J. Neijssel, D. Perkins, and S. E. de Mink, Nature Communications **8**, 14906 (2017), arXiv:1704.01352 [astro-ph.HE].

[41] N. Giacobbo and M. Mapelli, MNRAS **480**, 2011 (2018), arXiv:1806.00001 [astro-ph.HE].

[42] A. Duquennoy and M. Mayor, A&A **248**, 485 (1991).

[43] D. A. Fischer and G. W. Marcy, ApJ **396**, 178 (1992).

[44] P. P. Eggleton and A. A. Tokovinin, MNRAS **389**, 869 (2008), arXiv:0806.2878 [astro-ph].

[45] D. Gerosa, M. Kesden, E. Berti, R. O'Shaughnessy, and U. Sperhake, Phys. Rev. D **87**, 104028 (2013), arXiv:1302.4442 [gr-qc].

[46] D. Wysocki, D. Gerosa, R. O'Shaughnessy, K. Belczynski, W. Gladysz, E. Berti, M. Kesden, and D. E. Holz, Phys. Rev. D **97**, 043014 (2018), arXiv:1709.01943 [astro-ph.HE].

[47] D. Gerosa, E. Berti, R. O'Shaughnessy, K. Belczynski, M. Kesden, D. Wysocki, and W. Gladysz, Phys. Rev. D **98**, 084036 (2018), arXiv:1808.02491 [astro-ph.HE].

[48] T. A. Callister, W. M. Farr, and M. Renzo, (2020), arXiv:2011.09570 [astro-ph.HE].

[49] Z. Barkat, G. Rakavy, and N. Sack, Phys. Rev. Lett. **18**, 379 (1967).

[50] S. E. Woosley, ApJ **836**, 244 (2017), arXiv:1608.08939 [astro-ph.HE].

[51] K. Takahashi, ApJ **863**, 153 (2018), arXiv:1807.05373 [astro-ph.HE].

[52] R. Farmer, M. Renzo, S. E. de Mink, M. Fishbach, and S. Justham, ApJ **902**, L36 (2020), arXiv:2006.06678 [astro-ph.HE].

[53] S. F. Portegies Zwart and S. L. W. McMillan, ApJ **576**, 899 (2002), arXiv:astro-ph/0201055 [astro-ph].

[54] A. Sadowski, K. Belczynski, T. Bulik, N. Ivanova, F. A. Rasio, and R. O'Shaughnessy, ApJ **676**, 1162 (2008), arXiv:0710.0878 [astro-ph].

[55] J. M. B. Downing, M. J. Benacquista, M. Giersz, and R. Spurzem, MNRAS **407**, 1946 (2010), arXiv:0910.0546 [astro-ph.SR].

[56] J. Samsing, M. MacLeod, and E. Ramirez-Ruiz, ApJ **784**, 71 (2014), arXiv:1308.2964 [astro-ph.HE].

[57] B. M. Ziosi, M. Mapelli, M. Branchesi, and G. Tormen, MNRAS **441**, 3703 (2014), arXiv:1404.7147 [astro-ph.GA].

[58] C. L. Rodriguez, M. Morscher, B. Pattabiraman, S. Chatterjee, C.-J. Haster, and F. A. Rasio, Phys. Rev. Lett. **115**, 051101 (2015).

[59] C. L. Rodriguez, S. Chatterjee, and F. A. Rasio, Phys. Rev. D **93**, 084029 (2016), arXiv:1602.02444 [astro-ph.HE].

[60] F. Antonini and F. A. Rasio, ApJ **831**, 187 (2016), arXiv:1606.04889 [astro-ph.HE].

[61] A. Askar, M. Szkudlarek, D. Gondek-Rosińska, M. Giersz, and T. Bulik, MNRAS **464**, L36 (2017), arXiv:1608.02520 [astro-ph.HE].

[62] J. Samsing and E. Ramirez-Ruiz, ApJ **840**, L14 (2017), arXiv:1703.09703 [astro-ph.HE].

[63] V. Kalogera, ApJ **541**, 319 (2000), arXiv:astro-ph/9911417 [astro-ph].

[64] I. Mandel and R. O'Shaughnessy, Class. Quantum Gravity **27**, 114007 (2010), arXiv:0912.1074 [astro-ph.HE].

[65] C. Talbot and E. Thrane, Phys. Rev. D **96**, 023012 (2017), arXiv:1704.08370 [astro-ph.HE].

[66] Y. Yang, I. Bartos, V. Gayathri, K. E. S. Ford, Z. Haiman, S. Klimenko, B. Kocsis, S. Márka, Z. Márka, B. McKernan, et al., Phys. Rev. Lett. **123**, 181101 (2019), arXiv:1906.09281 [astro-ph.HE].

[67] H. Tagawa, Z. Haiman, I. Bartos, and B. Kocsis, ApJ **899**, 26 (2020), arXiv:2004.11914 [astro-ph.HE].

[68] M. C. Miller and D. P. Hamilton, MNRAS **330**, 232 (2002), arXiv:astro-ph/0106188 [astro-ph].

[69] B. McKernan, K. E. S. Ford, W. Lyra, and H. B. Perets, MNRAS **425**, 460 (2012), arXiv:1206.2309 [astro-ph.GA].

[70] M. Fishbach, D. E. Holz, and B. Farr, ApJ **840**, L24 (2017), arXiv:1703.06869 [astro-ph.HE].

[71] D. Gerosa and E. Berti, Phys. Rev. D **95**, 124046 (2017).

[72] J. M. Ezquiaga and D. E. Holz, ApJ **909**, L23 (2021).

[73] C. Kimball, C. Talbot, C. P. L. Berry, M. Carney, M. Zevin, E. Thrane, and V. Kalogera, ApJ **900**, 177 (2020), arXiv:2005.00023 [astro-ph.HE].

[74] M. Zevin, S. S. Bavera, C. P. L. Berry, V. Kalogera, T. Fragos, P. Marchant, C. L. Rodriguez, F. Antonini, D. E. Holz, and C. Pankow, ApJ **910**, 152 (2021), arXiv:2011.10057 [astro-ph.HE].

[75] K. W. K. Wong, K. Breivik, K. Kremer, and T. Callister, Phys. Rev. D **103**, 083021 (2021), arXiv:2011.03564 [astro-ph.HE].

[76] A. Q. Cheng, M. Zevin, and S. Vitale, ApJ **955**, 127 (2023), arXiv:2307.03129 [astro-ph.HE].

[77] B. P. Abbott, R. Abbott, T. D. Abbott, M. R. Abernathy, F. Acernese, K. Ackley, C. Adams, T. Adams, P. Addesso, R. X. Adhikari, et al., Phys. Rev. Lett. **116**, 061102 (2016), arXiv:1602.03837 [gr-qc].

[78] LIGO Scientific Collaboration, J. Aasi, B. P. Abbott, R. Abbott, T. Abbott, M. R. Abernathy, K. Ackley, C. Adams, T. Adams, P. Addesso, et al., Class. Quantum Gravity **32**, 074001 (2015), arXiv:1411.4547 [gr-qc].

[79] T. Akutsu, M. Ando, K. Arai, Y. Arai, S. Araki, A. Araya, N. Aritomi, Y. Aso, S. Bae, Y. Bae, et al., Progress of Theoretical and Experimental Physics **2021**, 05A101 (2021), arXiv:2005.05574 [physics.ins-det].

[80] R. Abbott, T. D. Abbott, F. Acernese, K. Ackley, C. Adams, N. Adhikari, R. X. Adhikari, V. B. Adya, C. Affeldt, D. Agarwal, et al., Physical Review X **13**, 041039 (2023), arXiv:2111.03606 [gr-qc].

[81] B. P. Abbott, R. Abbott, T. D. Abbott, S. Abraham, F. Acernese, K. Ackley, C. Adams, V. B. Adya, C. Affeldt, M. Agathos, et al., Class. Quantum Gravity **37**, 055002 (2020), arXiv:1908.11170 [gr-qc].

[82] L. Blackburn, L. Cadonati, S. Caride, S. Caudill, S. Chatterji, N. Christensen, J. Dalrymple, S. Desai, A. Di Credico, G. Ely, et al., Class. Quantum Gravity **25**, 184004 (2008), arXiv:0804.0800 [gr-qc].

[83] B. P. Abbott, R. Abbott, T. D. Abbott, M. R. Abernathy, F. Acernese, K. Ackley, M. Adamo, C. Adams, T. Adams, P. Addesso, et al., Classical and Quantum Gravity **33**, 134001 (2016), arXiv:1602.03844 [gr-qc].

[84] M. Cabero, A. Lundgren, A. H. Nitz, T. Dent, D. Barker, E. Goetz, J. S. Kissel, L. K. Nuttall, P. Schale, R. Schofield, et al., Class. Quantum Gravity **36**, 155010 (2019), arXiv:1901.05093 [physics.ins-det].

[85] E. Payne, S. Hourihane, J. Golomb, R. Udall, D. Davis, and K. Chatziioannou, Phys. Rev. D **106**, 104017 (2022), arXiv:2206.11932 [gr-qc].

[86] G. Pratten, C. García-Quirós, M. Colleoni, A. Ramos-Buades, H. Estellés, M. Mateu-Lucena, R. Jaume, M. Haney, D. Keitel, J. E. Thompson, et al., Phys. Rev. D **103**, 104056 (2021), arXiv:2004.06503 [gr-qc].

[87] S. Ossokine, A. Buonanno, S. Marsat, R. Cotesta, S. Babak, T. Dietrich, R. Haas, I. Hinder, H. P. Pfeiffer, M. Pürrer, et al., Phys. Rev. D **102**, 044055 (2020), arXiv:2004.09442 [gr-qc].

[88] S. A. Usman, A. H. Nitz, I. W. Harry, C. M. Biwer, D. A. Brown, M. Cabero, C. D. Capano, T. Dal Canton, T. Dent, S. Fairhurst, et al., Class. Quantum Gravity **33**, 215004 (2016), arXiv:1508.02357 [gr-qc].

[89] S. Sachdev, S. Caudill, H. Fong, R. K. L. Lo, C. Messick, D. Mukherjee, R. Magee, L. Tsukada, K. Blackburn, P. Brady, et al., arXiv e-prints , arXiv:1901.08580 (2019), arXiv:1901.08580 [gr-qc].

[90] B. P. Abbott et al. (LIGO and Virgo Collaborations), Phys. Rev. X **9**, 031040 (2019), arXiv:1811.12907 [astro-ph.HE].

[91] R. Abbott et al. (LIGO and Virgo Collaborations), (2020), arXiv:2010.14527 [gr-qc].

[92] R. Abbott, T. D. Abbott, F. Acernese, K. Ackley, C. Adams, N. Adhikari, R. X. Adhikari, V. B. Adya, C. Affeldt, D. Agarwal, et al., Phys. Rev. D **109**, 022001 (2024), arXiv:2108.01045 [gr-qc].

[93] W. M. Farr, J. R. Gair, I. Mandel, and C. Cutler, Phys. Rev. D **91**, 023005 (2015), arXiv:1302.5341 [astro-ph.IM].

[94] B. P. Abbott, R. Abbott, T. D. Abbott, M. R. Abernathy, F. Acernese, K. Ackley, C. Adams, T. Adams, P. Addesso, R. X. Adhikari, et al., ApJ **833**, L1 (2016), arXiv:1602.03842 [astro-ph.HE].

[95] A. H. Nitz, C. Capano, A. B. Nielsen, S. Reyes, R. White, D. A. Brown, and B. Krishnan, ApJ **872**, 195 (2019), arXiv:1811.01921 [gr-qc].

[96] A. H. Nitz, T. Dent, G. S. Davies, S. Kumar, C. D. Capano, I. Harry, S. Mozzon, L. Nuttall, A. Lundgren, and M. Tápai, ApJ **891**, 123 (2020), arXiv:1910.05331 [astro-ph.HE].

[97] T. Venumadhav, B. Zackay, J. Roulet, L. Dai, and M. Zaldarriaga, Phys. Rev. D **101**, 083030 (2020), arXiv:1904.07214 [astro-ph.HE].

[98] A. H. Nitz, C. D. Capano, S. Kumar, Y.-F. Wang, S. Kastha, M. Schäfer, R. Dhurkunde, and M. Cabero, ApJ **922**, 76 (2021), arXiv:2105.09151 [astro-ph.HE].

[99] A. H. Nitz, S. Kumar, Y.-F. Wang, S. Kastha, S. Wu, M. Schäfer, R. Dhurkunde, and C. D. Capano, ApJ **946**, 59 (2023), arXiv:2112.06878 [astro-ph.HE].

[100] A. Trovato (Ligo Scientific, Virgo), PoS **Asterics2019**, 082 (2020).

[101] The LIGO Scientific Collaboration, the Virgo Collaboration, and the KAGRA Collaboration, arXiv e-prints , arXiv:2404.04248 (2024), arXiv:2404.04248 [astro-ph.HE].

[102] R. Abbott et al. (LIGO and Virgo Collaborations), ApJ **896**, L44 (2020), arXiv:2006.12611 [astro-ph.HE].

[103] B. P. Abbott, R. Abbott, T. D. Abbott, M. R. Abernathy, F. Acernese, K. Ackley, C. Adams, T. Adams, P. Addesso, R. X. Adhikari, et al., Phys. Rev. Lett. **116**, 221101 (2016), arXiv:1602.03841 [gr-qc].

[104] M. Isi, M. Giesler, W. M. Farr, M. A. Scheel, and S. A. Teukolsky, Phys. Rev. Lett. **123**, 111102 (2019), arXiv:1905.00869 [gr-qc].

[105] J. C. Bustillo, P. D. Lasky, and E. Thrane, Phys. Rev. D **103**, 024041 (2021).

[106] R. Cotesta, G. Carullo, E. Berti, and V. Cardoso, Phys. Rev. Lett. **129**, 111102 (2022), arXiv:2201.00822 [gr-qc].

[107] E. Finch and C. J. Moore, Phys. Rev. D **106**, 043005 (2022), arXiv:2205.07809 [gr-qc].

[108] B. P. Abbott, R. Abbott, T. D. Abbott, F. Acernese, K. Ackley, C. Adams, T. Adams, P. Addesso, R. X. Adhikari, V. B. Adya, et al., Phys. Rev. Lett. **119**, 161101 (2017), arXiv:1710.05832 [gr-qc].

[109] D. A. Coulter, R. J. Foley, C. D. Kilpatrick, M. R. Drout, A. L. Piro, B. J. Shappee, M. R. Siebert, J. D. Simon, N. Ulloa, D. Kasen, et al., Science **358**, 1556 (2017), arXiv:1710.05452 [astro-ph.HE].

[110] S. Allam, J. Annis, E. Berger, D. J. Brout, D. Brown, R. E. Butler, H. Y. Chen, R. Chornock, E. Cook, P. Cowperthwaite, et al., GRB Coordinates Network **21530**, 1 (2017).

[111] S. Yang, S. Valenti, E. Cappellaro, D. J. Sand, L. Tartaglia, A. Corsi, D. E. Reichart, J. Haislip, and V. Kouprianov, ApJ **851**, L48 (2017), arXiv:1710.05864 [astro-ph.HE].

[112] S. Valenti, D. J. Sand, S. Yang, E. Cappellaro, L. Tartaglia, A. Corsi, S. W. Jha, D. E. Reichart, J. Haislip, and V. Kouprianov, ApJ **848**, L24 (2017), arXiv:1710.05854 [astro-ph.HE].

[113] I. Arcavi, C. McCully, G. Hosseinzadeh, D. A. Howell, S. Vasylyev, D. Poznanski, M. Zaltzman, D. Maoz, L. Singer, S. Valenti, et al., ApJ **848**, L33 (2017), arXiv:1710.05842 [astro-ph.HE].

[114] M. Soares-Santos, D. E. Holz, J. Annis, R. Chornock, K. Herner, E. Berger, D. Brout, H. Y. Chen, R. Kessler, M. Sako, et al., ApJ **848**, L16 (2017), arXiv:1710.05459 [astro-ph.HE].

[115] B. P. Abbott, R. Abbott, T. D. Abbott, F. Acernese, K. Ackley, C. Adams, T. Adams, P. Addesso, R. X. Adhikari, V. B. Adya, et al., ApJ **848**, L12 (2017), arXiv:1710.05833 [astro-ph.HE].

[116] N. R. Tanvir, A. J. Levan, A. S. Fruchter, J. Hjorth, R. A. Hounsell, K. Wiersema, and R. L. Tunnicliffe, Nature **500**, 547 (2013), arXiv:1306.4971 [astro-ph.HE].

[117] V. Connaughton, GBM-LIGO Group, L. Blackburn, M. S. Briggs, J. Broida, E. Burns, J. Camp, T. Dal Canton, N. Christensen, A. Goldstein, et al., GRB Coordinates Network **21506**, 1 (2017).

[118] A. Goldstein, P. Veres, E. Burns, M. S. Briggs, R. Hamburg, D. Kocevski, C. A. Wilson-Hodge, R. D. Preece, S. Poolakkil, O. J. Roberts, et al., ApJ **848**, L14 (2017), arXiv:1710.05446 [astro-ph.HE].

[119] A. Goldstein, P. Veres, E. Burns, L. Blackburn, M. S. Briggs, N. Christensen, W. H. Cleveland, V. Connaughton, T. Dal Canton, R. Hamburg, et al., ApJ **846**, L5 (2017), arXiv:1706.00199 [astro-ph.HE].

[120] V. Savchenko, C. Ferrigno, E. Kuulkers, A. Bazzano, E. Bozzo, S. Brandt, J. Chenevez, T. J. L. Courvoisier, R. Diehl, A. Domingo, et al., ApJ **848**, L15 (2017), arXiv:1710.05449 [astro-ph.HE].

[121] I. Arcavi, G. Hosseinzadeh, D. A. Howell, C. McCully, D. Poznanski, D. Kasen, J. Barnes, M. Zaltzman, S. Vasylyev, D. Maoz, et al., Nature **551**, 64 (2017), arXiv:1710.05843 [astro-ph.HE].

[122] V. M. Lipunov, E. Gorbovskoy, V. G. Kornilov, N. . Tyurina, P. Balanutsa, A. Kuznetsov, D. Vlasenko, D. Kuvshinov, I. Gorbunov, D. A. H. Buckley, et al., ApJ **850**, L1 (2017), arXiv:1710.05461 [astro-ph.HE].

[123] N. R. Tanvir, A. J. Levan, C. González-Fernández, O. Korobkin, I. Mandel, S. Rosswog, J. Hjorth, P. D'Avanzo, A. S. Fruchter, C. L. Fryer, et al., ApJ **848**, L27 (2017), arXiv:1710.05455 [astro-ph.HE].

[124] B. P. Abbott, R. Abbott, T. D. Abbott, F. Acernese, K. Ackley, C. Adams, T. Adams, P. Addesso, R. X. Adhikari, V. B. Adya, et al., Nature **551**, 85 (2017), arXiv:1710.05835 [astro-ph.CO].

[125] H.-Y. Chen, M. Fishbach, and D. E. Holz, Nature **562**, 545 (2018), arXiv:1712.06531 [astro-ph.CO].

[126] G. Efstathiou, MNRAS **505**, 3866 (2021), arXiv:2103.08723 [astro-ph.CO].

[127] W. L. Freedman, ApJ **919**, 16 (2021), arXiv:2106.15656 [astro-ph.CO].

[128] R. Abbott et al. (LIGO and Virgo Collaboration), Phys. Rev. Lett. **125**, 101102 (2020), arXiv:2009.01075 [gr-qc].

[129] A. E. Reines, J. E. Greene, and M. Geha, ApJ **775**, 116 (2013), arXiv:1308.0328 [astro-ph.CO].

[130] V. F. Baldassare, A. E. Reines, E. Gallo, and J. E. Greene, ApJ **809**, L14 (2015), arXiv:1506.07531 [astro-ph.GA].

[131] R. Abbott et al. (LIGO and Virgo Collaborations), ApJ **900**, L13 (2020), arXiv:2009.01190 [astro-ph.HE].

[132] V. De Luca, G. Franciolini, P. Pani, and A. Riotto, J. Cosmology Astropart. Phys. **2020**, 044 (2020), arXiv:2005.05641 [astro-ph.CO].

[133] V. De Luca, V. Desjacques, G. Franciolini, P. Pani, and A. Riotto, Phys. Rev. Lett. **126**, 051101 (2021), arXiv:2009.01728 [astro-ph.CO].

[134] J. C. Bustillo, N. Sanchis-Gual, A. Torres-Forné, and J. A. Font, Phys. Rev. Lett. **126**, 201101 (2021), arXiv:2009.01066 [gr-qc].

[135] I. Romero-Shaw, P. D. Lasky, E. Thrane, and J. Calderón Bustillo, ApJ **903**, L5 (2020), arXiv:2009.04771 [astro-ph.HE].

[136] M. Mapelli, M. Spera, E. Montanari, M. Limongi, A. Chieffi, N. Giacobbo, A. Bressan, and Y. Bouffanais, ApJ **888**, 76 (2020), arXiv:1909.01371 [astro-ph.HE].

[137] H. Müller and B. D. Serot, Nucl. Phys. A **606**, 508 (1996), arXiv:nucl-th/9603037 [nucl-th].

[138] LIGO Scientific Collaboration and Virgo Collaboration, Phys. Rev. X **9**, 011001 (2019), arXiv:1805.11579 [gr-qc].

[139] C. D. Bailyn, R. K. Jain, P. Coppi, and J. A. Orosz, ApJ **499**, 367 (1998), arXiv:astro-ph/9708032 [astro-ph].

[140] F. Özel, D. Psaltis, R. Narayan, and J. E. McClintock, ApJ **725**, 1918 (2010), arXiv:1006.2834 [astro-ph.GA].

[141] W. M. Farr, N. Sravan, A. Cantrell, L. Kreidberg, C. D. Bailyn, I. Mandel, and V. Kalogera, ApJ **741**, 103 (2011), arXiv:1011.1459 [astro-ph.GA].

[142] L. Kreidberg, C. D. Bailyn, W. M. Farr, and V. Kalogera, ApJ **757**, 36 (2012), arXiv:1205.1805 [astro-ph.HE].

[143] A. Nathanail, E. R. Most, and L. Rezzolla, ApJ **908**, L28 (2021), arXiv:2101.01735 [astro-ph.HE].

[144] Y.-P. Li, Z.-L. Chen, D.-B. Lin, and E.-W. Liang, ApJ **968**, 104 (2024), arXiv:2404.19340 [astro-ph.HE].

[145] R. Abbott, T. D. Abbott, S. Abraham, F. Acernese, K. Ackley, A. Adams, C. Adams, R. X. Adhikari, V. B. Adya, C. Affeldt, et al., ApJ **915**, L5 (2021), arXiv:2106.15163 [astro-ph.HE].

[146] F. Foucart, L. Buchman, M. D. Duez, M. Grudich, L. E. Kidder, I. MacDonald, A. Mroue, H. P. Pfeiffer, M. A. Scheel, and B. Szilagyi, Phys. Rev. D **88**, 064017 (2013), arXiv:1307.7685 [gr-qc].

[147] P. Kumar, M. Pürrer, and H. P. Pfeiffer, Phys. Rev. D **95**, 044039 (2017), arXiv:1610.06155 [gr-qc].

[148] M. Hannam, C. Hoy, J. E. Thompson, S. Fairhurst, V. Raymond, M. Colleoni, D. Davis, H. Estellés, C.-J. Haster, A. Helmling-Cornell, et al., Nature **610**, 652 (2022), arXiv:2112.11300 [gr-qc].

[149] M. Fasano, K. W. K. Wong, A. Maselli, E. Berti, V. Ferrari, and B. S. Sathyaprakash, Phys. Rev. D **102**, 023025 (2020), arXiv:2005.01726 [astro-ph.HE].

[150] F. Pannarale, Phys. Rev. D **88**, 104025 (2013), arXiv:1208.5869 [gr-qc].

[151] F. Foucart, T. Hinderer, and S. Nissanke, Phys. Rev. D **98**, 081501 (2018), arXiv:1807.00011 [astro-ph.HE].

[152] F. Pannarale, A. Tonita, and L. Rezzolla, ApJ **727**, 95 (2011), arXiv:1007.4160 [astro-ph.HE].

[153] V. Paschalidis, M. Ruiz, and S. L. Shapiro, ApJ **806**, L14 (2015), arXiv:1410.7392 [astro-ph.HE].

[154] T. Islam, A. Vajpeyi, F. H. Shaik, C.-J. Haster, V. Varma, S. E. Field, J. Lange, R. O'Shaughnessy, and R. Smith, arXiv e-prints , arXiv:2309.14473 (2023), arXiv:2309.14473 [gr-qc].

[155] B. P. Abbott et al. (LIGO and Virgo Collaborations), Living Rev. Relativ. **23**, 3 (2020).

[156] F. Acernese, M. Agathos, K. Agatsuma, D. Aisa, N. Allemandou, A. Allocca, J. Amarni, P. Astone, G. Balestri, G. Ballardin, et al., Class. Quantum Gravity **32**, 024001 (2015), arXiv:1408.3978 [gr-qc].

[157] Kagra Collaboration, Nat. Astron. **3**, 35 (2019), arXiv:1811.08079 [gr-qc].

[158] M. Saleem, J. Rana, V. Gayathri, A. Vijaykumar, S. Goyal, S. Sachdev, J. Suresh, S. Sudhagar, A. Mukherjee, G. Gaur, et al., Class. Quantum Gravity **39**, 025004 (2022), arXiv:2105.01716 [gr-qc].

[159] P. Amaro-Seoane et al. (LISA Core Team), (2017), arXiv:1702.00786 [astro-ph.IM].

[160] eLISA Consortium, P. Amaro Seoane, S. Aoudia, H. Audley, G. Auger, S. Babak, J. Baker, E. Barausse, S. Barke, M. Bassan, et al., arXiv e-prints , arXiv:1305.5720 (2013), arXiv:1305.5720 [astro-ph.CO].

[161] S. R. Taylor, arXiv e-prints , arXiv:2105.13270 (2021), arXiv:2105.13270 [astro-ph.HE].

[162] A. Afzal, G. Agazie, A. Anumarlapudi, A. M. Archibald, Z. Arzoumanian, P. T. Baker, B. Bécsy, J. J. Blanco-Pillado, L. Blecha, K. K. Boddy, et al., ApJ **951**, L11 (2023), arXiv:2306.16219 [astro-ph.HE].

[163] EPTA Collaboration, InPTA Collaboration, J. Antoniadis, P. Arumugam, S. Arumugam, S. Babak, M. Bagchi, A. S. Bak Nielsen, C. G. Bassa, A. Bathula, et al., A&A **678**, A50 (2023), arXiv:2306.16214 [astro-ph.HE].

[164] D. J. Reardon, A. Zic, R. M. Shannon, G. B. Hobbs, M. Bailes, V. Di Marco, A. Kapur, A. F. Rogers, E. Thrane, J. Askew, et al., ApJ **951**, L6 (2023), arXiv:2306.16215 [astro-ph.HE].

[165] H. Xu, S. Chen, Y. Guo, J. Jiang, B. Wang, J. Xu, Z. Xue, R. Nicolas Caballero, J. Yuan, Y. Xu, et al., Research in Astronomy and Astrophysics **23**, 075024 (2023), arXiv:2306.16216 [astro-ph.HE].

[166] M. Punturo et al., Class. Quantum Gravity **27**, 194002 (2010).

[167] M. Maggiore, C. Van Den Broeck, N. Bartolo, E. Belgacem, D. Bertacca, M. A. Bizouard, M. Branchesi, S. Clesse, S. Foffa, J. García-Bellido, et al., J. Cosmology Astropart. Phys. **2020**, 050 (2020), arXiv:1912.02622 [astro-ph.CO].

[168] D. Reitze et al., BAAS **51**, 35 (2019), arXiv:1907.04833 [astro-ph.IM].

[169] M. Evans, R. X. Adhikari, C. Afle, S. W. Ballmer, S. Biscoveanu, S. Borhanian, D. A. Brown, Y. Chen, R. Eisenstein, A. Gruson, et al., arXiv e-prints , arXiv:2109.09882 (2021), arXiv:2109.09882 [astro-ph.IM].

[170] K. K. Y. Ng, S. Vitale, W. M. Farr, and C. L. Rodriguez, ApJ **913**, L5 (2021), arXiv:2012.09876 [astro-ph.CO].

[171] F. Iacovelli, M. Mancarella, S. Foffa, and M. Maggiore, ApJ **941**, 208 (2022), arXiv:2207.02771 [gr-qc].

[172] M. Mancarella, F. Iacovelli, and D. Gerosa, Phys. Rev. D **107**, L101302 (2023), arXiv:2303.16323 [gr-qc].

[173] V. Kalogera, B. S. Sathyaprakash, M. Bailes, M.-A. Bizouard, A. Buonanno, A. Burrows, M. Colpi, M. Evans, S. Fairhurst, S. Hild, et al., arXiv e-prints , arXiv:2111.06990 (2021), arXiv:2111.06990 [gr-qc].

[174] M. Mould and D. Gerosa, Phys. Rev. D **105**, 024076 (2022), arXiv:2110.05507 [astro-ph.HE].

[175] S. Biscoveanu, T. A. Callister, C.-J. Haster, K. K. Y. Ng, S. Vitale, and W. M. Farr, ApJ **932**, L19 (2022), arXiv:2204.01578 [astro-ph.HE].

[176] F. S. Broekgaarden, S. Stevenson, and E. Thrane, ApJ **938**, 45 (2022), arXiv:2205.01693 [astro-ph.HE].

[177] C. Talbot and J. Golomb, MNRAS **526**, 3495 (2023), arXiv:2304.06138 [astro-ph.IM].

[178] J. Golomb, M. Isi, and W. Farr, arXiv e-prints , arXiv:2312.03973 (2023), arXiv:2312.03973 [astro-ph.HE].

[179] A. Toubiana, M. L. Katz, and J. R. Gair, MNRAS **524**, 5844 (2023), arXiv:2305.08909 [gr-qc].

[180] A. M. Farah, B. Edelman, M. Zevin, M. Fishbach, J. María Ezquiaga, B. Farr, and D. E. Holz, ApJ **955**, 107 (2023), arXiv:2301.00834 [astro-ph.HE].

[181] A. M. Farah, T. A. Callister, J. María Ezquiaga, M. Zevin, and D. E. Holz, arXiv e-prints , arXiv:2404.02210 (2024), arXiv:2404.02210 [astro-ph.CO].

[182] A. Boesky, F. S. Broekgaarden, and E. Berger, arXiv e-prints , arXiv:2405.01623 (2024), arXiv:2405.01623 [astro-ph.HE].

[183] I. Magaña Hernandez and A. Ray, arXiv e-prints , arXiv:2404.02522 (2024), arXiv:2404.02522 [astro-ph.CO].

[184] K. Leyde, S. R. Green, A. Toubiana, and J. Gair, Phys. Rev. D **109**, 064056 (2024), arXiv:2311.12093 [gr-qc].

[185] B. P. Abbott et al. (LIGO and Virgo Collaborations), ApJ **882**, L24 (2019), arXiv:1811.12940 [astro-ph.HE].

[186] R. Abbott et al. (LIGO and Virgo Collaborations), (2020), arXiv:2010.14533 [astro-ph.HE].

[187] R. Abbott, T. D. Abbott, F. Acernese, K. Ackley, C. Adams, N. Adhikari, R. X. Adhikari, V. B. Adya, C. Affeldt, D. Agarwal, et al., Physical Review X **13**, 011048 (2023), arXiv:2111.03634 [astro-ph.HE].

[188] J. Abadie, B. P. Abbott, R. Abbott, M. Abernathy, T. Accadia, F. Acernese, C. Adams, R. Adhikari, P. Ajith, B. Allen, et al., Class. Quantum Gravity **27**, 173001 (2010), arXiv:1003.2480 [astro-ph.HE].

[189] I. Mandel and F. S. Broekgaarden, Living Rev. Relativ. **25**, 1 (2022), arXiv:2107.14239 [astro-ph.HE].

[190] A. Boesky, F. S. Broekgaarden, and E. Berger, arXiv e-prints , arXiv:2405.01630 (2024), arXiv:2405.01630 [astro-ph.HE].

[191] F. S. Broekgaarden, S. Banagiri, and E. Payne, arXiv e-prints , arXiv:2303.17628 (2023), arXiv:2303.17628 [astro-ph.HE].

[192] I. Mandel, W. M. Farr, A. Colonna, S. Stevenson, P. Tiňo, and J. Veitch, MNRAS **465**, 3254 (2017), arXiv:1608.08223 [astro-ph.HE].

[193] V. Tiwari and S. Fairhurst, ApJ **913**, L19 (2021), arXiv:2011.04502 [astro-ph.HE].

[194] K. W. K. Wong, G. Franciolini, V. De Luca, V. Baibhav, E. Berti, P. Pani, and A. Riotto, Phys. Rev. D **103**, 023026 (2021), arXiv:2011.01865 [gr-qc].

[195] S. Rinaldi and W. Del Pozzo, MNRAS **509**, 5454 (2022), arXiv:2109.05960 [astro-ph.IM].

[196] A. Ray, I. M. Hernandez, S. Mohite, J. Creighton, and S. Kapadia, ApJ **957**, 37 (2023), arXiv:2304.08046 [gr-qc].

[197] J. Heinzel, S. Vitale, and S. Biscoveanu, Phys. Rev. D **109**, 103006 (2024), arXiv:2312.00993 [astro-ph.HE].

[198] A. Ray, I. Magaña Hernandez, K. Breivik, and J. Creighton, arXiv e-prints , arXiv:2404.03166 (2024), arXiv:2404.03166 [astro-ph.HE].

[199] T. A. Callister and W. M. Farr, Phys. Rev. X **14**, 021005 (2024), arXiv:2302.07289 [astro-ph.HE].

[200] J. Sadiq, T. Dent, and M. Gieles, ApJ **960**, 65 (2024).

[201] M. Kesden, D. Gerosa, R. O'Shaughnessy, E. Berti, and U. Sperhake, Phys. Rev. Lett. **114**, 081103 (2015), arXiv:1411.0674 [gr-qc].

[202] D. Gerosa, M. Kesden, U. Sperhake, E. Berti, and R. O'Shaughnessy, Phys. Rev. D **92**, 064016 (2015), arXiv:1506.03492 [gr-qc].

[203] D. Gerosa, G. Fumagalli, M. Mould, G. Cavallotto, D. P. Monroy, D. Gangardt, and V. De Renzis, Phys. Rev. D **108**, 024042 (2023), arXiv:2304.04801 [gr-qc].

[204] D. Gerosa and M. Kesden, Phys. Rev. D **93**, 124066 (2016), arXiv:1605.01067 [astro-ph.HE].

[205] T. Damour, Phys. Rev. D **64**, 124013 (2001), arXiv:gr-qc/0103018 [gr-qc].

[206] P. Schmidt, F. Ohme, and M. Hannam, Phys. Rev. D **91**, 024043 (2015), arXiv:1408.1810 [gr-qc].

[207] É. Racine, Phys. Rev. D **78**, 044021 (2008), arXiv:0803.1820 [gr-qc].

[208] C. Reisswig, S. Husa, L. Rezzolla, E. N. Dorband, D. Pollney, and J. Seiler, Phys. Rev. D **80**, 124026 (2009), arXiv:0907.0462 [gr-qc].

[209] M. Campanelli, C. O. Lousto, and Y. Zlochower, Phys. Rev. D **74**, 041501 (2006), arXiv:gr-qc/0604012 [gr-qc].

[210] D. Gerosa, M. Mould, D. Gangardt, P. Schmidt, G. Pratten, and L. M. Thomas, Phys. Rev. D **103**, 064067 (2021), arXiv:2011.11948 [gr-qc].

[211] V. De Renzis, D. Gerosa, G. Pratten, P. Schmidt, and M. Mould, Phys. Rev. D **106**, 084040 (2022), arXiv:2207.00030 [gr-qc].

[212] L. M. Thomas, P. Schmidt, and G. Pratten, Phys. Rev. D **103**, 083022 (2021), arXiv:2012.02209 [gr-qc].

[213] M. Kramer, ApJ **509**, 856 (1998), arXiv:astro-ph/9808127 [astro-ph].

[214] R. P. Breton, V. M. Kaspi, M. Kramer, M. A. McLaughlin, M. Lyutikov, S. M. Ransom, I. H. Stairs, R. D. Ferdman, F. Camilo, and A. Possenti, Science **321**, 104 (2008), arXiv:0807.2644 [astro-ph].

[215] R. N. Manchester, M. Kramer, I. H. Stairs, M. Burgay, F. Camilo, G. B. Hobbs, D. R. Lorimer, A. G. Lyne, M. A. McLaughlin, C. A. McPhee, et al., ApJ **710**, 1694 (2010), arXiv:1001.1483 [astro-ph.GA].

[216] E. Fonseca, I. H. Stairs, and S. E. Thorsett, ApJ **787**, 82 (2014), arXiv:1402.4836 [astro-ph.HE].

[217] G. Desvignes, M. Kramer, K. Lee, J. van Leeuwen, I. Stairs, A. Jessner, I. Cognard, L. Kasian, A. Lyne, and B. W. Stappers, Science **365**, 1013 (2019), arXiv:1909.06212 [astro-ph.HE].

[218] C. S. Reynolds, ARA&A **59**, 117 (2021), arXiv:2011.08948 [astro-ph.HE].

[219] B. P. Abbott et al. (LIGO and Virgo Collaboration), Phys. Rev. Lett. **116**, 241103 (2016), arXiv:1606.04855 [gr-qc].

[220] M. Boyle, D. Hemberger, D. A. B. Iozzo, G. Lovelace, S. Ossokine, H. P. Pfeiffer, M. A. Scheel, L. C. Stein, C. J. Woodford, A. B. Zimmerman, et al., Classical and Quantum Gravity **36**, 195006 (2019), arXiv:1904.04831 [gr-qc].

[221] V. Varma, M. Mould, D. Gerosa, M. A. Scheel, L. E. Kidder, and H. P. Pfeiffer, Phys. Rev. D **103**, 064003 (2021), arXiv:2012.07147 [gr-qc].

[222] L. Blanchet, Living Rev. Relativ. **17**, 2 (2014), arXiv:1310.1528 [gr-qc].

[223] L. E. Kidder, C. M. Will, and A. G. Wiseman, Phys. Rev. D **47**, R4183 (1993), arXiv:gr-qc/9211025 [gr-qc].

[224] L. E. Kidder, Phys. Rev. D **52**, 821 (1995), arXiv:gr-qc/9506022 [gr-qc].

[225] É. É. Flanagan and T. Hinderer, Phys. Rev. D **77**, 021502 (2008), arXiv:0709.1915 [astro-ph].

[226] T. Binnington and E. Poisson, Phys. Rev. D **80**, 084018 (2009), arXiv:0906.1366 [gr-qc].

[227] N. Gupte, A. Ramos-Buades, A. Buonanno, J. Gair, M. C. Miller, M. Dax, S. R. Green, M. Pürrer, J. Wildberger, J. Macke, et al., arXiv e-prints , arXiv:2404.14286 (2024), arXiv:2404.14286 [gr-qc].

[228] I. M. Romero-Shaw, D. Gerosa, and N. Loutrel, MNRAS **519**, 5352 (2023), arXiv:2211.07528 [astro-ph.HE].

[229] P. C. Peters and J. Mathews, Phys. Rev. **131**, 435 (1963).

[230] G. Fumagalli and D. Gerosa, Phys. Rev. D **108**, 124055 (2023), arXiv:2310.16893 [gr-qc].

[231] G. Fumagalli, I. Romero-Shaw, D. Gerosa, V. De Renzis, K. Kritos, and A. Olejak, arXiv e-prints , arXiv:2405.14945 (2024), arXiv:2405.14945 [astro-ph.HE].

[232] T. A. Apostolatos, C. Cutler, G. J. Sussman, and K. S. Thorne, Phys. Rev. D **49**, 6274 (1994).

[233] L. Blanchet, T. Damour, B. R. Iyer, C. M. Will, and A. G. Wiseman, Phys. Rev. Lett. **74**, 3515 (1995), arXiv:gr-qc/9501027 [gr-qc].

[234] D. Gangardt, N. Steinle, M. Kesden, D. Gerosa, and E. Stoikos, Phys. Rev. D **103**, 124026 (2021), arXiv:2103.03894 [gr-qc].

[235] A. Klein, arXiv e-prints , arXiv:2106.10291 (2021), arXiv:2106.10291 [gr-qc].

[236] V. Varma, S. Biscoveanu, M. Isi, W. M. Farr, and S. Vitale, Phys. Rev. Lett. **128**, 031101 (2022), arXiv:2107.09693 [astro-ph.HE].

[237] D. Gerosa, A. Lima, E. Berti, U. Sperhake, M. Kesden, and R. O'Shaughnessy, Class. Quantum Gravity **36**, 105003 (2019), arXiv:1811.05979 [gr-qc].

[238] X. Zhao, M. Kesden, and D. Gerosa, Phys. Rev. D **96**, 024007 (2017), arXiv:1705.02369 [gr-qc].

[239] J. D. Schnittman, Phys. Rev. D **70**, 124020 (2004), arXiv:astro-ph/0409174 [astro-ph].

[240] C. Afle, A. Gupta, B. Gadre, P. Kumar, N. Demos, G. Lovelace, H. G. Choi, H. M. Lee, S. Mitra, M. Boyle, et al., Phys. Rev. D **98**, 083014 (2018), arXiv:1803.07695 [gr-qc].

[241] D. Gerosa, M. Kesden, R. O'Shaughnessy, A. Klein, E. Berti, U. Sperhake, and D. Trifirò, Phys. Rev. Lett. **115**, 141102 (2015), arXiv:1506.09116 [gr-qc].

[242] C. O. Lousto and J. Healy, Phys. Rev. D **93**, 124074 (2016), arXiv:1601.05086 [gr-qc].

[243] M. Mould and D. Gerosa, Phys. Rev. D **101**, 124037 (2020), arXiv:2003.02281 [gr-qc].

[244] D. Gerosa, U. Sperhake, and J. Vošmera, Class. Quantum Gravity **34**, 064004 (2017), arXiv:1612.05263 [gr-qc].

[245] S. Tanay, L. C. Stein, and J. T. Gálvez Ghersi, Phys. Rev. D **103**, 064066 (2021), arXiv:2012.06586 [gr-qc].

[246] C. O. Lousto, J. Healy, and H. Nakano, Phys. Rev. D **93**, 044031 (2016), arXiv:1506.04768 [gr-qc].

[247] L. D. Landau and E. M. Lifshitz, *Mechanics* (1969).

[248] T. Bogdanović, C. S. Reynolds, and M. C. Miller, ApJ **661**, L147 (2007), arXiv:astro-ph/0703054 [astro-ph].

[249] K. K. Y. Ng, S. Vitale, A. Zimmerman, K. Chatziioannou, D. Gerosa, and C.-J. Haster, Phys. Rev. D **98**, 083007 (2018), arXiv:1805.03046 [gr-qc].

[250] M. Sayeb, L. Blecha, L. Z. Kelley, D. Gerosa, M. Kesden, and J. Thomas, MNRAS **501**, 2531 (2021), arXiv:2006.06647 [astro-ph.GA].

[251] C. Cutler and É. E. Flanagan, Phys. Rev. D **49**, 2658 (1994), arXiv:gr-qc/9402014 [gr-qc].

[252] E. Stoikos, N. Steinle, and M. Kesden, in preparation.

[253] N. Steinle and M. Kesden, Phys. Rev. D **106**, 063028 (2022), arXiv:2206.00391 [astro-ph.HE].

[254] N. Steinle and M. Kesden, Phys. Rev. D **103**, 063032 (2021), arXiv:2010.00078 [astro-ph.HE].

[255] D. Gangardt, D. Gerosa, M. Kesden, V. De Renzis, and N. Steinle, Phys. Rev. D **106**, 024019 (2022), arXiv:2204.00026 [gr-qc].

[256] D. Gangardt, D. Gerosa, M. Kesden, V. De Renzis, and N. Steinle, Phys. Rev. D **107**, 109901 (2023).

[257] G. Pratten, P. Schmidt, R. Buscicchio, and L. M. Thomas, Phys. Rev. Res. **2**, 043096 (2020), arXiv:2006.16153 [gr-qc].

[258] C. Hoy, C. Mills, and S. Fairhurst, Phys. Rev. D **106**, 023019 (2022), arXiv:2111.10455 [gr-qc].

[259] M. Colleoni, M. Mateu-Lucena, H. Estellés, C. García-Quirós, D. Keitel, G. Pratten, A. Ramos-Buades, and S. Husa, Phys. Rev. D **103**, 024029 (2021), arXiv:2010.05830 [gr-qc].

[260] K. Chatziioannou, A. Klein, N. Yunes, and N. Cornish, Phys. Rev. D **95**, 104004 (2017), arXiv:1703.03967 [gr-qc].

[261] S. Khan, K. Chatziioannou, M. Hannam, and F. Ohme, Phys. Rev. D **100**, 024059 (2019), arXiv:1809.10113 [gr-qc].

[262] L. Reali, M. Mould, D. Gerosa, and V. Varma, Class. Quantum Gravity **37**, 225005 (2020), arXiv:2005.01747 [gr-qc].

[263] N. K. Johnson-McDaniel, S. Kulkarni, and A. Gupta, Phys. Rev. D **106**, 023001 (2022), arXiv:2107.11902 [astro-ph.HE].

[264] S. Ossokine, M. Boyle, L. E. Kidder, H. P. Pfeiffer, M. A. Scheel, and B. Szilágyi, Phys. Rev. D **92**, 104028 (2015), arXiv:1502.01747 [gr-qc].

[265] D. Gerosa, R. O'Shaughnessy, M. Kesden, E. Berti, and U. Sperhake, Phys. Rev. D **89**, 124025 (2014), arXiv:1403.7147 [gr-qc].

[266] A. Gupta and A. Gopakumar, Class. Quantum Gravity **31**, 105017 (2014), arXiv:1312.0217 [gr-qc].

[267] D. Trifirò, R. O'Shaughnessy, D. Gerosa, E. Berti, M. Kesden, T. Littenberg, and U. Sperhake, Phys. Rev. D **93**, 044071 (2016), arXiv:1507.05587 [gr-qc].

[268] A. C. M. Correia, MNRAS **457**, L49 (2016), arXiv:1511.01890 [gr-qc].

[269] D. Gerosa, S. Ma, K. W. K. Wong, E. Berti, R. O'Shaughnessy, Y. Chen, and K. Belczynski, Phys. Rev. D **99**, 103004 (2019), arXiv:1902.00021 [astro-ph.HE].

[270] R. Abbott et al. (LIGO and Virgo Collaboration), Phys. Rev. X **11**, 021053 (2021), arXiv:2010.14527 [gr-qc].

[271] I. M. Romero-Shaw, C. Talbot, S. Biscoveanu, V. D'Emilio, et al., MNRAS **499**, 3295 (2020), arXiv:2006.00714 [astro-ph.IM].

[272] J. Alsing, H. O. Silva, and E. Berti, MNRAS **478**, 1377 (2018), arXiv:1709.07889 [astro-ph.HE].

[273] S. Vitale, D. Gerosa, C.-J. Haster, K. Chatziioannou, and A. Zimmerman, Phys. Rev. Lett. **119**, 251103 (2017), arXiv:1707.04637 [gr-qc].

[274] I. M. Romero-Shaw, E. Thrane, and P. D. Lasky, PASA **39**, e025 (2022), arXiv:2202.05479 [astro-ph.IM].

[275] J. Lin, IEEE Transactions on Information theory **37**, 145 (1991).

[276] E. Hellinger, Journal für die reine und angewandte Mathematik **1909**, 210 (1909).

[277] C. J. Moore and D. Gerosa, Phys. Rev. D **104**, 083008 (2021), arXiv:2108.02462 [gr-qc].

[278] R. Abbott et al. (LIGO and Virgo Collaborations), Phys. Rev. D **102**, 043015 (2020).

[279] D. Gerosa, S. Vitale, and E. Berti, Phys. Rev. Lett. **125**, 101103 (2020), arXiv:2005.04243 [astro-ph.HE].

[280] S. Vitale, R. Lynch, J. Veitch, V. Raymond, and R. Sturani, Phys. Rev. Lett. **112**, 251101 (2014), arXiv:1403.0129 [gr-qc].

[281] M. Pürrer, M. Hannam, and F. Ohme, Phys. Rev. D **93**, 084042 (2016), arXiv:1512.04955 [gr-qc].

[282] B. P. Abbott et al. (LIGO, Virgo, and KAGRA Collaboration), Living Rev. Relativ. **21**, 3 (2018), arXiv:1304.0670 [gr-qc].

[283] R. J. E. Smith, G. Ashton, A. Vajpeyi, and C. Talbot, MNRAS **498**, 4492 (2020), arXiv:1909.11873 [gr-qc].

[284] G. Ashton, M. Hübner, P. D. Lasky, C. Talbot, K. Ackley, S. Biscoveanu, Q. Chu, A. Divakarla, P. J. Easter, B. Goncharov, et al., ApJS **241**, 27 (2019), arXiv:1811.02042 [astro-ph.IM].

[285] D. Gangardt, A. A. Trani, C. Bonnerot, and D. Gerosa, MNRAS **530**, 3689 (2024), arXiv:2403.00060 [astro-ph.HE].

[286] R. Antonucci, ARA&A **31**, 473 (1993).

[287] C. M. Urry and P. Padovani, PASP **107**, 803 (1995), arXiv:astro-ph/9506063 [astro-ph].

[288] H. Netzer, ARA&A **53**, 365 (2015), arXiv:1505.00811 [astro-ph.GA].

[289] J. A. Baldwin, M. M. Phillips, and R. Terlevich, PASP **93**, 5 (1981).

[290] L. J. Kewley, M. A. Dopita, R. S. Sutherland, C. A. Heisler, and J. Trevena, ApJ **556**, 121 (2001), arXiv:astro-ph/0106324 [astro-ph].

[291] M. J. Meyer, M. J. Drinkwater, S. Phillipps, and W. J. Couch, MNRAS **324**, 343 (2001).

[292] G. Kauffmann, T. M. Heckman, C. Tremonti, J. Brinchmann, S. Charlot, S. D. M. White, S. E. Ridgway, J. Brinkmann, M. Fukugita, P. B. Hall, et al., MNRAS **346**, 1055 (2003), arXiv:astro-ph/0304239 [astro-ph].

[293] J. Stern and A. Laor, MNRAS **426**, 2703 (2012), arXiv:1207.5543 [astro-ph.CO].

[294] C. K. Seyfert, ApJ **97**, 28 (1943).

[295] K. Chen and J. P. Halpern, ApJ **344**, 115 (1989).

[296] M. Lacy, L. J. Storrie-Lombardi, A. Sajina, P. N. Appleton, L. Armus, S. C. Chapman, P. I. Choi, D. Fadda, F. Fang, D. T. Frayer, et al., ApJS **154**, 166 (2004), arXiv:astro-ph/0405604 [astro-ph].

[297] D. Stern, P. Eisenhardt, V. Gorjian, C. S. Kochanek, N. Caldwell, D. Eisenstein, M. Brodwin, M. J. I. Brown, R. Cool, A. Dey, et al., ApJ **631**, 163 (2005), arXiv:astro-ph/0410523 [astro-ph].

[298] T. H. Jarrett, M. Cohen, F. Masci, E. Wright, D. Stern, D. Benford, A. Blain, S. Carey, R. M. Cutri, P. Eisenhardt, et al., ApJ **735**, 112 (2011).

[299] D. Stern, R. J. Assef, D. J. Benford, A. Blain, R. Cutri, A. Dey, P. Eisenhardt, R. L. Griffith, T. H. Jarrett, S. Lake, et al., ApJ **753**, 30 (2012), arXiv:1205.0811 [astro-ph.CO].

[300] R. J. Assef, D. Stern, C. S. Kochanek, A. W. Blain, M. Brodwin, M. J. I. Brown, E. Donoso, P. R. M. Eisenhardt, B. T. Jannuzi, T. H. Jarrett, et al., ApJ **772**, 26 (2013), arXiv:1209.6055 [astro-ph.CO].

[301] T. M. Heckman and P. N. Best, ARA&A **52**, 589 (2014), arXiv:1403.4620 [astro-ph.GA].

[302] M. Lacy, S. E. Ridgway, A. Sajina, A. O. Petric, E. L. Gates, T. Urrutia, and L. J. Storrie-Lombardi, ApJ **802**, 102 (2015), arXiv:1501.04118 [astro-ph.GA].

[303] W. N. Brandt and D. M. Alexander, A&A Rev. **23**, 1 (2015), arXiv:1501.01982 [astro-ph.HE].

[304] P. Padovani, A&A Rev. **24**, 13 (2016), arXiv:1609.00499 [astro-ph.GA].

[305] C. Tadhunter, A&A Rev. **24**, 10 (2016), arXiv:1605.08773 [astro-ph.GA].

[306] P. Padovani, D. M. Alexander, R. J. Assef, B. De Marco, P. Giommi, R. C. Hickox, G. T. Richards, V. Smolčić, E. Hatziminaoglou, V. Mainieri, et al., A&A Rev. **25**, 2 (2017), arXiv:1707.07134 [astro-ph.GA].

[307] R. C. Hickox and D. M. Alexander, ARA&A **56**, 625 (2018), arXiv:1806.04680 [astro-ph.GA].

[308] S. Bianchi, V. Mainieri, and P. Padovani, Handbook of X-ray and Gamma-ray Astrophysics **4**, 4 (2022).

[309] D. O. Edge, J. R. Shakeshaft, W. B. McAdam, J. E. Baldwin, and S. Archer, MmRAS **68**, 37 (1959).

[310] A. S. Bennett, MmRAS **68**, 163 (1962).

[311] G. A. Shields, PASP **111**, 661 (1999), arXiv:astro-ph/9903401 [astro-ph].

[312] A. Soltan, MNRAS **200**, 115 (1982).

[313] J. Binney and G. Tabor, MNRAS **276**, 663 (1995).

[314] L. Ciotti and J. P. Ostriker, ApJ **487**, L105 (1997), arXiv:astro-ph/9706281 [astro-ph].

[315] P. Valageas and J. Silk, A&A **350**, 725 (1999), arXiv:astro-ph/9907068 [astro-ph].

[316] J. Silk and M. J. Rees, A&A **331**, L1 (1998), arXiv:astro-ph/9801013 [astro-ph].

[317] M. J. Page, MNRAS **328**, 925 (2001), arXiv:astro-ph/0108389 [astro-ph].

[318] D. M. Alexander and R. C. Hickox, New A Rev. **56**, 93 (2012), arXiv:1112.1949 [astro-ph.GA].

[319] A. Marconi, G. Risaliti, R. Gilli, L. K. Hunt, R. Maiolino, and M. Salvati, MNRAS **351**, 169 (2004), arXiv:astro-ph/0311619 [astro-ph].

[320] C. M. Harrison, T. Costa, C. N. Tadhunter, A. Flütsch, D. Kakkad, M. Perna, and G. Vietri, Nat. Astron. **2**, 198 (2018), arXiv:1802.10306 [astro-ph.GA].

[321] C. M. Harrison and C. Ramos Almeida, Galaxies **12**, 17 (2024), arXiv:2404.08050 [astro-ph.GA].

[322] A. C. Fabian, ARA&A **50**, 455 (2012), arXiv:1204.4114 [astro-ph.CO].

[323] J. Magorrian, S. Tremaine, D. Richstone, R. Bender, G. Bower, A. Dressler, S. M. Faber, K. Gebhardt, R. Green, C. Grillmair, et al., AJ **115**, 2285 (1998), arXiv:astro-ph/9708072 [astro-ph].

[324] S. Tremaine, K. Gebhardt, R. Bender, G. Bower, A. Dressler, S. M. Faber, A. V. Filippenko, R. Green, C. Grillmair, L. C. Ho, et al., ApJ **574**, 740 (2002), arXiv:astro-ph/0203468 [astro-ph].

[325] K. Gültekin, D. O. Richstone, K. Gebhardt, T. R. Lauer, S. Tremaine, M. C. Aller, R. Bender, A. Dressler, S. M. Faber, A. V. Filippenko, et al., ApJ **698**, 198 (2009), arXiv:0903.4897 [astro-ph.GA].

[326] N. J. McConnell and C.-P. Ma, ApJ **764**, 184 (2013), arXiv:1211.2816 [astro-ph.CO].

[327] J. Kormendy and L. C. Ho, ARA&A **51**, 511 (2013), arXiv:1304.7762 [astro-ph.CO].

[328] A. E. Reines and M. Volonteri, ApJ **813**, 82 (2015), arXiv:1508.06274 [astro-ph.GA].

[329] M. J. Hardcastle and J. H. Croston, New A Rev. **88**, 101539 (2020), arXiv:2003.06137 [astro-ph.HE].

[330] G. Vietri, B. Garilli, M. Polletta, S. Bisogni, L. P. Cassarà, P. Franzetti, M. Fumana, A. Gargiulo, D. Maccagni, C. Mancini, et al., A&A **659**, A129 (2022), arXiv:2111.08730 [astro-ph.GA].

[331] D. Syer, C. J. Clarke, and M. J. Rees, MNRAS **250**, 505 (1991).

[332] M. Morris, ApJ **408**, 496 (1993).

[333] K. P. Rauch, MNRAS **275**, 628 (1995).

[334] M. MacLeod and D. N. C. Lin, ApJ **889**, 94 (2020), arXiv:1909.09645 [astro-ph.SR].

[335] G. Fabj, S. S. Nasim, F. Caban, K. E. S. Ford, B. McKernan, and J. M. Bellovary, MNRAS **499**, 2608 (2020), arXiv:2006.11229 [astro-ph.GA].

[336] S. S. Nasim, G. Fabj, F. Caban, A. Secunda, K. E. S. Ford, B. McKernan, J. M. Bellovary, N. W. C. Leigh, and W. Lyra, MNRAS **522**, 5393 (2023), arXiv:2207.09540 [astro-ph.GA].

[337] A. Generozov and H. B. Perets, MNRAS **522**, 1763 (2023), arXiv:2212.11301 [astro-ph.GA].

[338] H. Whitehead, C. Rowan, T. Boekholt, and B. Kocsis, MNRAS **531**, 4656 (2024), arXiv:2309.11561 [astro-ph.GA].

[339] B. McKernan, K. E. S. Ford, W. Lyra, H. B. Perets, L. M. Winter, and T. Yaqoob, MNRAS **417**, L103 (2011), arXiv:1108.1787 [astro-ph.CO].

[340] F. Antonini and H. B. Perets, ApJ **757**, 27 (2012), arXiv:1203.2938 [astro-ph.GA].

[341] A. Secunda, J. Bellovary, M.-M. Mac Low, K. E. S. Ford, B. McKernan, N. W. C. Leigh, W. Lyra, and Z. Sándor, A&A **878**, 85 (2019), arXiv:1807.02859 [astro-ph.HE].

[342] H. Tagawa, Z. Haiman, and B. Kocsis, ApJ **898**, 25 (2020), arXiv:1912.08218 [astro-ph.GA].

[343] A. A. Trani, S. Quaini, and M. Colpi, A&A **683**, A135 (2024), arXiv:2312.13281 [astro-ph.HE].

[344] M. Dodici and S. Tremaine, arXiv e-prints , arXiv:2404.08138 (2024), arXiv:2404.08138 [astro-ph.GA].

[345] J. M. Bellovary, M.-M. Mac Low, B. McKernan, and K. E. S. Ford, ApJ **819**, L17 (2016), arXiv:1511.00005 [astro-ph.GA].

[346] I. Bartos, Z. Haiman, Z. Marka, B. D. Metzger, N. C. Stone, and S. Marka, Nature Communications **8**, 831 (2017), arXiv:1701.02328 [astro-ph.HE].

[347] N. C. Stone, B. D. Metzger, and Z. Haiman, MNRAS **464**, 946 (2017), arXiv:1602.04226 [astro-ph.GA].

[348] B. McKernan, K. E. S. Ford, and R. O'Shaughnessy, MNRAS **498**, 4088 (2020), arXiv:2002.00046 [astro-ph.HE].

[349] V. Gayathri, D. Wysocki, Y. Yang, V. Delfavero, R. O'Shaughnessy, Z. Haiman, H. Tagawa, and I. Bartos, ApJ **945**, L29 (2023), arXiv:2301.04187 [gr-qc].

[350] M. P. Vaccaro, M. Mapelli, C. Périgois, D. Barone, M. C. Artale, M. Dall'Amico, G. Iorio, and S. Torniamenti, A&A **685**, A51 (2024), arXiv:2311.18548 [astro-ph.HE].

[351] B. McKernan, K. E. S. Ford, J. Bellovary, N. W. C. Leigh, Z. Haiman, B. Kocsis, W. Lyra, M. M. Mac Low, B. Metzger, M. O'Dowd, et al., ApJ **866**, 66 (2018), arXiv:1702.07818 [astro-ph.HE].

[352] M. Gröbner, W. Ishibashi, S. Tiwari, M. Haney, and P. Jetzer, A&A **638**, A119 (2020), arXiv:2005.03571 [astro-ph.GA].

[353] K. E. S. Ford and B. McKernan, MNRAS **517**, 5827 (2022), arXiv:2109.03212 [astro-ph.HE].

[354] B. Liu and D. Lai, ApJ **846**, L11 (2017), arXiv:1706.02309 [astro-ph.HE].

[355] A. Vajpeyi, E. Thrane, R. Smith, B. McKernan, and K. E. Saavik Ford, ApJ **931**, 82 (2022), arXiv:2111.03992 [gr-qc].

[356] A. Santini, D. Gerosa, R. Cotesta, and E. Berti, Phys. Rev. D **108**, 083033 (2023), arXiv:2308.12998 [astro-ph.HE].

[357] B. McKernan and K. E. S. Ford, arXiv e-prints , arXiv:2309.15213 (2023), arXiv:2309.15213 [astro-ph.HE].

[358] M. J. Graham, S. G. Djorgovski, A. J. Drake, D. Stern, A. A. Mahabal, E. Glikman, S. Larson, and E. Christensen, MNRAS **470**, 4112 (2017), arXiv:1706.03079 [astro-ph.GA].

[359] B. McKernan, K. E. S. Ford, I. Bartos, M. J. Graham, W. Lyra, S. Marka, Z. Marka, N. P. Ross, D. Stern, and Y. Yang, ApJ **884**, L50 (2019), arXiv:1907.03746 [astro-ph.HE].

[360] H. Tagawa, S. S. Kimura, Z. Haiman, R. Perna, and I. Bartos, ApJ **950**, 13 (2023), arXiv:2301.07111 [astro-ph.HE].

[361] H. Tagawa, S. S. Kimura, Z. Haiman, R. Perna, and I. Bartos, ApJ **966**, 21 (2024), arXiv:2310.18392 [astro-ph.HE].

[362] M. J. Graham, K. E. S. Ford, B. McKernan, N. P. Ross, D. Stern, K. Burdge, M. Coughlin, S. G. Djorgovski, A. J. Drake, D. Duev, et al., Phys. Rev. Lett. **124**, 251102 (2020), arXiv:2006.14122 [astro-ph.HE].

[363] A. Palmese, M. Fishbach, C. J. Burke, J. Annis, and X. Liu, ApJ **914**, L34 (2021), arXiv:2103.16069 [astro-ph.HE].

[364] B. McKernan, K. E. S. Ford, T. Callister, W. M. Farr, R. O'Shaughnessy, R. Smith, E. Thrane, and A. Vajpeyi, MNRAS **514**, 3886 (2022), arXiv:2107.07551 [astro-ph.HE].

[365] T. A. Callister, C.-J. Haster, K. K. Y. Ng, S. Vitale, and W. M. Farr, ApJ **922**, L5 (2021), arXiv:2106.00521 [astro-ph.HE].

[366] E. Grishin, S. Gilbaum, and N. C. Stone, MNRAS **530**, 2114 (2024), arXiv:2307.07546 [astro-ph.HE].

[367] D. Lynden-Bell and A. J. Kalnajs, MNRAS **157**, 1 (1972).

[368] S. I. Feldman and C. C. Lin, Stud. Appl. Math. **52**, 1 (1973).

[369] P. Goldreich and S. Tremaine, ApJ **233**, 857 (1979).

[370] D. N. C. Lin and J. Papaloizou, MNRAS **186**, 799 (1979).

[371] P. J. Armitage, *Astrophysics of planet formation* (Cambridge University Press, 2020).

[372] W. R. Ward, Icarus **126**, 261 (1997).

[373] W. R. Ward, Icarus **67**, 164 (1986).

[374] W. R. Ward and K. Hourigan, ApJ **347**, 490 (1989).

[375] D. N. C. Lin and J. C. B. Papaloizou, in *Protostars and Planets III*, edited by E. H. Levy and J. I. Lunine (1993) p. 749.

[376] R. P. Nelson, J. C. B. Papaloizou, F. Masset, and W. Kley, MNRAS **318**, 18 (2000), arXiv:astro-ph/9909486 [astro-ph].

[377] S. J. Paardekooper and G. Mellema, A&A **459**, L17 (2006), arXiv:astro-ph/0608658 [astro-ph].

[378] W. Kley and A. Crida, A&A **487**, L9 (2008), arXiv:0806.2990 [astro-ph].

[379] S. J. Paardekooper, C. Baruteau, A. Crida, and W. Kley, MNRAS **401**, 1950 (2010), arXiv:0909.4552 [astro-ph.EP].

[380] W. Lyra, S.-J. Paardekooper, and M.-M. Mac Low, ApJ **715**, L68 (2010), arXiv:1003.0925 [astro-ph.EP].

[381] H. Tanaka, T. Takeuchi, and W. R. Ward, ApJ **565**, 1257 (2002).

[382] P. Artymowicz, D. N. C. Lin, and E. J. Wampler, ApJ **409**, 592 (1993).

[383] Y. Levin, arXiv e-prints , astro-ph/0307084 (2003), arXiv:astro-ph/0307084 [astro-ph].

[384] A. Derdzinski and L. Mayer, MNRAS **521**, 4522 (2023), arXiv:2205.10382 [astro-ph.GA].

[385] D. Gerosa and M. Fishbach, Nat. Astron. **5**, 749 (2021), arXiv:2105.03439 [astro-ph.HE].

[386] V. K. Jha, R. Joshi, H. Chand, X.-B. Wu, L. C. Ho, S. Rastogi, and Q. Ma, MNRAS **511**, 3005 (2022), arXiv:2109.05036 [astro-ph.GA].

[387] W.-J. Guo, Y.-R. Li, Z.-X. Zhang, L. C. Ho, and J.-M. Wang, ApJ **929**, 19 (2022), arXiv:2201.08533 [astro-ph.GA].

[388] H. Guo, A. J. Barth, and S. Wang, ApJ **940**, 20 (2022), arXiv:2207.06432 [astro-ph.GA].

[389] J. R. Wilson, ApJ **173**, 431 (1972).

[390] J. F. Hawley, L. L. Smarr, and J. R. Wilson, ApJ **277**, 296 (1984).

[391] S. A. E. G. Falle, MNRAS **250**, 581 (1991).

[392] M. Schartmann, K. Meisenheimer, M. Camenzind, S. Wolf, and T. Henning, A&A **437**, 861 (2005), arXiv:astro-ph/0504105 [astro-ph].

[393] M. Schartmann, K. Meisenheimer, M. Camenzind, S. Wolf, K. R. W. Tristram, and T. Henning, A&A **482**, 67 (2008), arXiv:0802.2604 [astro-ph].

[394] K. Wada, P. P. Papadopoulos, and M. Spaans, ApJ **702**, 63 (2009), arXiv:0906.5444 [astro-ph.GA].

[395] F. Huško and C. G. Lacey, MNRAS **520**, 5090 (2023), arXiv:2205.08884 [astro-ph.GA].

[396] N. I. Shakura and R. A. Sunyaev, A&A **24**, 337 (1973).

[397] J. Goodman, MNRAS **339**, 937 (2003), arXiv:astro-ph/0201001 [astro-ph].

[398] Z. Haiman, B. Kocsis, and K. Menou, ApJ **700**, 1952 (2009), arXiv:0904.1383 [astro-ph.CO].

[399] M. Cantiello, A. S. Jermyn, and D. N. C. Lin, ApJ **910**, 94 (2021), arXiv:2009.03936 [astro-ph.SR].

[400] S. Gilbaum and N. C. Stone, ApJ **928**, 191 (2022), arXiv:2107.07519 [astro-ph.HE].

[401] P. F. Hopkins, J. Squire, K.-Y. Su, U. P. Steinwandel, K. Kremer, Y. Shi, M. Y. Grudic, S. Wellons, C.-A. Faucher-Giguere, D. Angles-Alcazar, et al., The Open Journal of Astrophysics **7**, 19 (2024), arXiv:2310.04506 [astro-ph.HE].

[402] P. F. Hopkins, J. Squire, E. Quataert, N. Murray, K.-Y. Su, U. P. Steinwandel, K. Kremer, C.-A. Faucher-Giguere, and S. Wellons, The Open Journal of Astrophysics **7**, 20 (2024), arXiv:2310.04507 [astro-ph.HE].

[403] D. Gangardt and A. A. Trani, doi.org/10.5281/zenodo.10723301, github.com/DariaGangardt/pAGN (2024).

[404] J. E. Pringle, ARA&A **19**, 137 (1981).

[405] A. Toomre, ApJ **139**, 1217 (1964).

[406] D. Semenov, T. Henning, C. Helling, M. Ilgner, and E. Sedlmayr, A&A **410**, 611 (2003), arXiv:astro-ph/0308344 [astro-ph].

[407] N. R. Badnell, M. A. Bautista, K. Butler, F. Delahaye, C. Mendoza, P. Palmeri, C. J. Zeippen, and M. J. Seaton, MNRAS **360**, 458 (2005), arXiv:astro-ph/0410744 [astro-ph].

[408] C. A. Iglesias and F. J. Rogers, ApJ **464**, 943 (1996).

[409] D. R. Alexander and J. W. Ferguson, ApJ **437**, 879 (1994).

[410] A. Baskin and A. Laor, MNRAS **474**, 1970 (2018), arXiv:1711.00025 [astro-ph.GA].

[411] E. Barausse, F. Shankar, M. Bernardi, Y. Dubois, and R. K. Sheth, MNRAS **468**, 4782 (2017), arXiv:1702.01762 [astro-ph.GA].

[412] F. Shankar, M. Bernardi, and R. K. Sheth, MNRAS **466**, 4029 (2017), arXiv:1701.01732 [astro-ph.GA].

[413] N. Menci, F. Fiore, F. Shankar, L. Zanisi, and C. Feruglio, A&A **674**, A181 (2023), arXiv:2304.08273 [astro-ph.GA].

[414] T. M. Heckman, G. Kauffmann, J. Brinchmann, S. Charlot, C. Tremonti, and S. D. M. White, ApJ **613**, 109 (2004), arXiv:astro-ph/0406218 [astro-ph].

[415] J. A. Kollmeier, C. A. Onken, C. S. Kochanek, A. Gould, D. H. Weinberg, M. Dietrich, R. Cool, A. Dey, D. J. Eisenstein, B. T. Jannuzi, et al., ApJ **648**, 128 (2006), arXiv:astro-ph/0508657 [astro-ph].

[416] H. Suh, G. Hasinger, C. Steinhardt, J. D. Silverman, and M. Schramm, ApJ **815**, 129 (2015), arXiv:1511.01092 [astro-ph.GA].

[417] M. Kong and L. C. Ho, ApJ **859**, 116 (2018), arXiv:1804.09852 [astro-ph.GA].

[418] N. Murray, E. Quataert, and T. A. Thompson, ApJ **618**, 569 (2005), arXiv:astro-ph/0406070 [astro-ph].

[419] W. Jaffe, K. Meisenheimer, H. J. A. Röttgering, C. Leinert, A. Richichi, O. Chesneau, D. Fraix-Burnet, A. Glazenborg-Kluttig, G. L. Granato, U. Graser, et al., Nature **429**, 47 (2004).

[420] L. Burtscher, K. Meisenheimer, K. R. W. Tristram, W. Jaffe, S. F. Hönig, R. I. Davies, M. Kishimoto, J. U. Pott, H. Röttgering, M. Schartmann, et al., A&A **558**, A149 (2013), arXiv:1307.2068 [astro-ph.CO].

[421] S. García-Burillo, F. Combes, C. Ramos Almeida, A. Usero, A. Alonso-Herrero, L. K. Hunt, D. Rouan, S. Aalto, M. Querejeta, S. Viti, et al., A&A **632**, A61 (2019), arXiv:1909.00675 [astro-ph.GA].

[422] A. Sajina, M. Lacy, and A. Pope, Universe **8**, 356 (2022), arXiv:2210.02307 [astro-ph.GA].

[423] Y.-F. Jiang, S. W. Davis, and J. M. Stone, ApJ **827**, 10 (2016), arXiv:1601.06836 [astro-ph.HE].

[424] M. A. Jiménez and F. S. Masset, MNRAS **471**, 4917 (2017), arXiv:1707.08988 [astro-ph.EP].

[425] F. S. Masset, MNRAS **472**, 4204 (2017), arXiv:1708.09807 [astro-ph.EP].

[426] D. G. Korycansky and J. B. Pollack, Icarus **102**, 150 (1993).

[427] F. S. Masset and J. Casoli, ApJ **723**, 1393 (2010), arXiv:1009.1913 [astro-ph.EP].

[428] E. Lega, A. Crida, B. Bitsch, and A. Morbidelli, MNRAS **440**, 683 (2014), arXiv:1402.2834 [astro-ph.EP].

[429] P. Benítez-Llambay, F. Masset, G. Koenigsberger, and J. Szulágyi, Nature **520**, 63 (2015), arXiv:1510.01778 [astro-ph.EP].

[430] O. M. Guilera, M. M. Miller Bertolami, F. Masset, J. Cuadra, J. Venturini, and M. P. Ronco, MNRAS **507**, 3638 (2021), arXiv:2108.04880 [astro-ph.EP].

[431] D. A. Velasco Romero and F. S. Masset, MNRAS **495**, 2063 (2020), arXiv:2004.13422 [astro-ph.EP].

[432] D. R. Ballantyne, ApJ **685**, 787 (2008), arXiv:0806.2863 [astro-ph].

[433] C. Henshaw, R. O'Shaughnessy, and L. Cadonati, Class. Quantum Gravity **39**, 125003 (2022), arXiv:2201.05220 [gr-qc].

[434] K. Kritos, V. Strokov, V. Baibhav, and E. Berti, arXiv e-prints , arXiv:2210.10055 (2022), arXiv:2210.10055 [astro-ph.HE].

[435] V. De Renzis, D. Gerosa, M. Mould, R. Buscicchio, and L. Zanga, Phys. Rev. D **108**, 024024 (2023), arXiv:2304.13063 [gr-qc].

[436] N. K. Johnson-McDaniel, K. S. Phukon, N. V. Krishnendu, and A. Gupta, Phys. Rev. D **108**, 103003 (2023), arXiv:2301.10125 [astro-ph.HE].

[437] M. Epstein-Martin, H. Tagawa, Z. Haiman, and R. Perna, arXiv e-prints , arXiv:2405.09380 (2024), arXiv:2405.09380 [astro-ph.HE].